Combining spin-orbit coupling and multi-orbital interactions: a recipe for novel magnetism and superconductivity

Lena Engström

Department of Physics

McGill University, Montréal

July, 2023

A thesis submitted to McGill University in partial fulfillment of the requirements of the degree of Doctor of Philosophy

Abstract

This thesis explores a multi-orbital model with a strong spin-orbit coupling where interactions are tuned via a compressive strain. The platform used to explore this type of physics is the perovskite iridate Sr_2IrO_4. Undoped and unstrained, this iridate compound is a spin-orbit coupled antiferromagnet. Under doping, Sr_2IrO_4 has been predicted to host superconductivity. Applying a compressive strain to the compound tunes the dispersion of electrons in each orbital and consequently the interactions between electrons. In a model considering strain and doping, iridate physics is shown to encompass the two cases of either the interacting order being dominated by spin-orbit physics or multi-orbital interactions and spin-orbit coupling being of comparable size. This thesis focuses on modeling magnetism and superconductivity. Firstly, the magnetic order parameters are modeled with a mean field approximation. For undoped Sr_2IrO_4 under compressive strain the multi-orbital nature of the order is determined, and a strain-induced phase transition takes place. An external magnetic field is included to further determine signatures of the order. Secondly, superconductivity is modeled with an effective interaction calculated via the random phase approximation (RPA). For realistic parameter values for doped Sr_2IrO_4 a strain-induced superconducting order is found to be possible. Considering a wider range of parameters reveals a theoretical phase diagram rich with magnetic and superconducting orders. As the compressive strain is increased, several types of magnetic fluctuations compete. For the found novel superconducting orders a classification of symmetries as well as determination of topological properties is performed. Strain in the iridates is thus not only shown to be a useful tool to expand a possible superconducting region at high spin-orbit coupling. It is also a good tool to explore the complex system of underlying interactions.

Résumé

Cette thèse explore un modèle multi-orbital avec un fort couplage spin-orbite où les interactions sont modifiées par des contraintes de compression. La plateforme utilisée pour explorer cette physique est la pérovskite iridate Sr_2IrO_4. Si cet iridate n'est pas dopé ou compress, c'est un composé antiferromagnétique couplé spin-orbite. Il a été prédit que Sr_2IrO_4 pourrait devenir un supraconducteur s'il était dopé. L'application d'une compression au composé modifie la dispersion des électrons dans chaque orbitale et par conséquent les interactions entre électrons. Dans un modèle prenant en compte la compression et le dopage, la physique des iridates englobe les deux cas où soit l'ordre d'interaction est dominé par la physique spin-orbite, soit les interactions multi-orbitales et le couplage spin-orbite sont de taille comparable. Cette thèse s'intéresse à la modélisation du magnétisme et de la supraconductivité. Premièrement, les paramètres d'ordre magnétique sont modélisés avec une approximation du champ moyen. Pour Sr_2IrO_4 non dopé sous compression, la nature multi-orbitale de l'ordre est déterminée et on trouve une transition de phase induite par la compression. Un champ magnétique externe est inclus pour déterminer plus en détail les signatures de l'ordre magnétique. Deuxièmement, la supraconductivité est modélisée avec une interaction effective calculée via le RPA (Random Phase Approximation). Pour des valeurs de paramètres réalistes pour Sr_2IrO_4 sous dopage, un ordre supraconducteur induit par la compression est possible. La prise en compte d'une plus large gamme de paramètres révèle un diagramme de phase théorique riche en ordres magnétiques et supraconducteurs. Lorsque la compression augmente, plusieurs types de fluctuations magnétiques entrent en compétition. Pour les nouveaux ordres supraconducteurs trouvés, une classification des symétries ainsi qu'une détermination des propriétés topologiques sont effectuées. La contrainte en compression dans les iridates ne se

révèle donc pas seulement être un bon outil pour étendre une éventuelle région supraconductrice à fort couplage spin-orbite. C'est aussi un bon outil pour explorer le système complexe d'interactions sous-jacentes.

Acknowledgements

There are many people that have greatly contributed to the completion of this thesis. I would first like to thank my supervisors, Tami Pereg-Barnea and William Witczak-Krempa. Your support, feedback, and advice has shaped me into a better physicist. It has been a pleasure to work with you both. To the other graduate students that have been my fellow group members, both at McGill University and Universié de Montréal: it has been a privilege to be accompanied by you. Thank you, Ben, Bill, Éric, Kunal, Gabrielle, Melina, Ivan, Liuke, Dounia, Amir, James, Alex, Etienne, Louis, Gabriel, Stéphane, Simon, Brett, Juliette, Muath, and Leo, as well as postdocs Sergueï, Ranjani, Rufus, Chia-Chuan, Ren-Bo, Clément, and Gilles. Getting to discuss physics with you and hearing about your research has been a wonderfully enriching experience. Finally, this thesis would not exist were it not for the love and support from friends and family. I am thankful for my parents, who have always been there for me.

Contribution to original knowledge

The original contributions of this thesis are contained in Chapters 5 and 6. The original contributions of Chapter 5 are:

- A multi-orbital model of magnetism formulated for Sr_2IrO_4 with increasing compressive strain and a Zeeman field.
- A numerical calculation performed to find all 42 complex on-site mean field order parameters in a two-site basis. This work therefore provides a rigorous study of how each orbital and total angular momentum states contributes to the magnetic order.

The original contributions of Chapter 6 are:

- The first study of multi-orbital superconductivity in Sr_2IrO_4 in a lattice with staggered rotations. Superconductivity could thus be modelled for the combination of compressive strain and doping. Such a study was performed for spin-fluctuation mediated superconductivity.
- Phase diagrams for spin-fluctuation mediated superconductivity were calculated both in the limit of strong spin-orbit coupling and in the limit of spin-orbit coupling, Hubbard interactions, and Hund's coupling being of comparable size.
- A prediction for strain-induced superconductivity for realistic model parameters in doped Sr_2IrO_4.
- A prediction of new superconducting orders in the wider phase diagram of the multi-orbital model.

Contribution of Authors

This thesis is written in the manuscript based format. Chapters 5 and 6 are manuscripts of papers published during my candidature. I am the principal author of these papers and the sole author of this thesis. The contributions of the other authors to Chapters 5 and 6 are listed here.

Chapter 5: Modeling multiorbital effects in Sr_2IrO_4 under strain and a Zeeman field

Lena Engström Performed all analytical and numerical analyses. Compiled and interpreted the results. Wrote and co-edited the manuscript.

Tami Pereg-Barnea Co-proposed the original idea for the work. Supervised the research, providing critical insight, feedback, and interpretation of results. Co-edited the manuscript.

William Witczak-Krempa Co-proposed the original idea for the work. Supervised the research, providing critical insight, feedback, and interpretation of results. Co-edited the manuscript.

Chapter 6: Strain-induced superconductivity in Sr_2IrO_4

Lena Engström Co-proposed the idea for the work. Performed all analytical and numerical analyses. Compiled and interpreted the results. Wrote and co-edited the manuscript.

Chia-Chuan Liu Provided feedback and interpretation of results.

William Witczak-Krempa Co-proposed the idea for the work. Supervised the research, providing critical insight, feedback, and interpretation of results. Co-edited the manuscript.

Tami Pereg-Barnea Co-proposed the idea for the work. Supervised the research, providing critical insight, feedback, and interpretation of results. Co-edited the manuscript.

Contents

List of Figures

List of Tables

List of Acronyms

AFM	Antiferromagnet.
ARPES	Angle-resolved photoemission spectroscopy.
BCS	Bardeen–Cooper–Schrieffer.
BdG	Bogoliubov-de Gennes.
BZ	Brilluoin zone.
cAFM	Canted antiferromagnet.
CDW	Charge density wave.
cFM	Canted ferromagnet.
FM	Ferromagnet.
FS	Fermi surface.
MF	Mean field.
ODW	Orbital density wave.
PM	Paramagnet.
RIXS	Resonant inelastic X-ray scattering.
RPA	Random phase approximation.
SDW	Spin density wave.
SOC	Spin-orbit coupling.
SODW	Spin-orbit density wave.
TRS	Time-reversal symmetry.

Chapter 1

Introduction

The collective effort within physics to understand unconventional superconductivity has led to its observation in multiple families of compounds. The Ruddlesden-Popper perovskite iridates is one family which has been predicted to host superconductivity. However, experiments have not been able to confirm that there is a superconducting order in the predicted regime of the electron doped Sr_2IrO_4. In this thesis I present theoretical work modeling magnetic and superconducting orders in Sr_2IrO_4, with the addition of compressive strain and an external magnetic field. The multi-orbital interactions combined with the strong spin-orbit coupling can result in a rich collection of phases. The motivation for the approach taken by this thesis is the experimental observation that the magnetism is exceptionally sensitive to compressive epitaxial strain in Sr_2IrO_4. Consequently, if superconductivity is mediated by magnetic fluctuations, strain is a powerful tool for tuning the system, i.e. by suppressing the magnetic order to allow for superconductivity to form. A compressive strain could be used as a tuning parameter to explore whether the predicted superconducting regions can be expanded. In several families of multi-orbital superconductors, in particular the iron pnictides and the ruthenates, there are multiple types of interactions present as well as a non-negligible spin-orbit coupling. Models of these compounds often approach the problem from the limit of a small SOC.

The iridates are in a unique position as possible multi-orbital superconductors with a strong spin-orbit coupling. A model of doped and strained Sr_2IrO_4 could therefore approach the problem of multiple competing energy scales, Hubbard interactions, Hund's coupling,

and spin-orbit coupling, from a different limit.

1.1 Thesis objective

In the following chapters, this thesis will show how a multi-orbital interacting model, with large spin-orbit coupling, can be tuned between a rich variety of competing phases by modifying the hopping amplitudes of each orbital via compressive strain. In particular, the relevance of this model will be shown for potentially superconducting iridates. This is particularly important as even with large spin-orbit coupling a simplified model, which focuses on one total angular momentum sector, is only valid in parts of the phase diagram.

The objective of the thesis is thus to use the iridate Sr_2IrO_4 to describe the states that contribute to the magnetic order and to determine if a magnetic insulator/superconductor transition is possible. To fully capture the breadth of iridate physics the most realistic parameter values are to be considered as well as an extension to a broader range of values that could potentially be achieved in the doped compound. The first step is to understand what degrees of freedom are necessary to describe the bandstructure and interacting order of Sr_2IrO_4 under compressive strain, as well as a potential phase transition. The second step is to expand the study to both doing and compressive epitaxial strain and thus to see if a stain-induced superconducting order is possible for realistic values. The final step is to explore a wider region of parameter to determine the symmetry of the order in any possible superconducting region.

1.2 Thesis organization

This thesis is organized around the two manuscripts in Chapters 5 and 6. The necessary background is covered in Chapters 2-4, where Chapter 2 is an overview of the iridates as a family of compounds with a particular focus on the properties of Sr_2IrO_4. Chapter 3 introduces the multi-orbital model and how compressive strain is taken into account. In Chapter 4 the Hubbard-Kanamori interactions are introduced and the difference between the approximations used in this work is outlined. The first manuscript, in Chapter 5, is

a mean field study of the magnetic orders in a multi-orbital model of undoped Sr_2IrO_4 under compressive strain and a Zeeman field. The second manuscript, in Chapter 6, is aimed at modeling superconductivity while considering Sr_2IrO_4 under compressive strain and doping. Effective interactions are calculated via the random phase approximation (RPA). A discussion of the results and the relevance of this thesis is covered in Chapter 7. Limitations to the study and proposed directions for future studies are covered as well. Chapter 8 is the conclusion of the thesis.

Chapter 2

Iridates

To understand the interest in Sr_2IrO_4 we want to start with the experiments that have generated it. As a family of compounds, the iridates provide a unique environment of multiple orbitals, spin-orbit coupling, and moderately strong interactions. They are a group of iridium-based transition metal oxides. Strontium iridate compounds can form a perovskite structure, where the single layer configuration Sr_2IrO_4 has a band structure close to the Fermi level that can be described by a cuprate-like effective model [1, 2]. Just like the single band models for cuprates capture a d-wave superconducting order when doped, doping of this iridate has been predicted to host the same type of superconductivity [1, 3, 4, 5, 6, 7].

What distinguishes the iridates, which have $5d$ orbitals, from the well-studied superconducting families of the cuprates and the ruthenate is the strength of the spin-orbit coupling (SOC). The strength of the spin-orbit coupling λ generally scales with atom number Z as Z^4 [8]. However, for heavy atoms the outer electron, which will be considered in the models, the effect scales as Z^2 [9]. For comparison copper has $Z = 29$ while iridium has $Z = 77$. This ends up placing the iridates in a regime where SOC, crystal field effects (CF), and Coulomb interactions (U) are of roughly equal size $\lambda \sim CF \sim U$.

In the case of the weak interactions, Hubbard U and the Hund's coupling J_{H} being small, such that $\lambda \gg U, J_{\mathrm{H}}$, we can easily find the ground state of the system. Under some approximations iridate compounds can be placed in this limit. However, when $\lambda \sim U, J_{\mathrm{H}}$ more exotic magnetic ground states are possible, as predicted in other studies on d^4 and d^5 compounds [10, 11, 12, 13, 14, 15]. For example, small changes to the parameters induce

magnetic phase transitions between different total angular momentum states [11]. As this thesis goes on to explore, a comparable scale of all these parameters can also lead to a wide range of superconducting orders.

2.1 Perovskite structure

The Ruddlesden-Popper series of perovskite iridates, $Sr_{n+1}Ir_nO_{3n+1}$, are of interest for studying their magnetic and possibly superconducting orders. A compound's number n in the series is determined by how many quasi-2d layers, of iridium atoms surrounded by an oxygen octahedra at each site, that is required to describe the structure. The compound of the series described by a single layer is Sr_2IrO_4, which has a tetragonal structure with space-group $I41/acd$ (No. 142) with $a = b = 5.4846$Å and $c = 25.804$ Å at 13 K [16], as shown in Fig. 2.1a). Within each layer the iridium sites form a square lattice, as shown in Fig. 2.1b). At each site the oxygen octahedra are rotated by a staggered rotation angle ϕ. A two-Ir-site unit cell within a layer thus describes the lattice geometry. The angle is measured to $\phi \approx \pm 12°$ [17].

The ground state of Sr_2IrO_4 is an insulating antiferromagnet, with an energy gap $\Delta \leq 0.62$eV [18, 19] and a relatively small magnetic coupling energy of $60 - 100$meV [18]. A magnetic order persists until the Néel temperature $T_N = 240$K [20, 16, 21]. However, when increasing the temperature further the compound was found to be insulating up to at least 600K and no anomaly in the transport is seen at the Néel temperature [21, 22, 23]. This is the case for both in the in-plane direction ρ_a and between layers ρ_c. This is one of the unexpected behaviors which has raised questions about the exact nature of the insulating state. Various studies have tried to determine if it is either Mott [24, 25] or Slater [26] insulator physics. Alternative proposed descriptions are both behaviors coexisting [27, 28, 29, 3, 30] or a correlated band insulator [31].

In the antiferromagnetic (AFM) order the magnetic moment has the nature of a total angular momentum $j = 1/2$ state [32, 33, 34]. From x-ray scattering and neutron diffraction investigations the ordered magnetic moments are found to be 0.202 and 0.049 μ_B per Ir-site along the a- and b-axis respectively [35]. This corresponds to a canted AFM (cAFM)

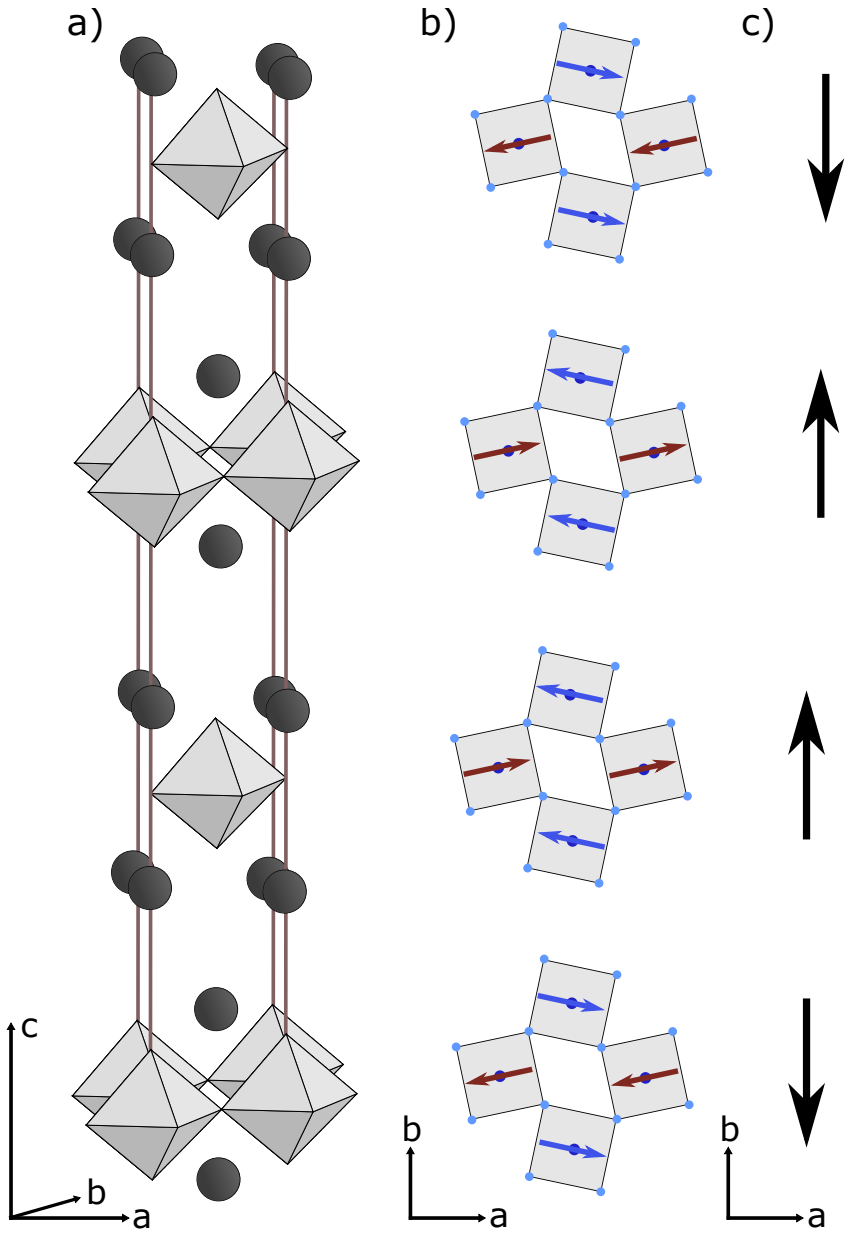

Figure 2.1: a) Perovskite structure of Sr_2IrO_4, where sites surrounded by oxygen octahedra are stacked in quasi-2d layers. Strontium, Sr, atoms are located in between layers. b) Top view of the IrO-layers where the staggered rotations in-plane of the octahedra are shown. The magnetic moment forms a canted antiferromagnetic order that follows the staggered rotations in each plane. c) The net moment from the canting within each layer has a stacking pattern between 4 layers.

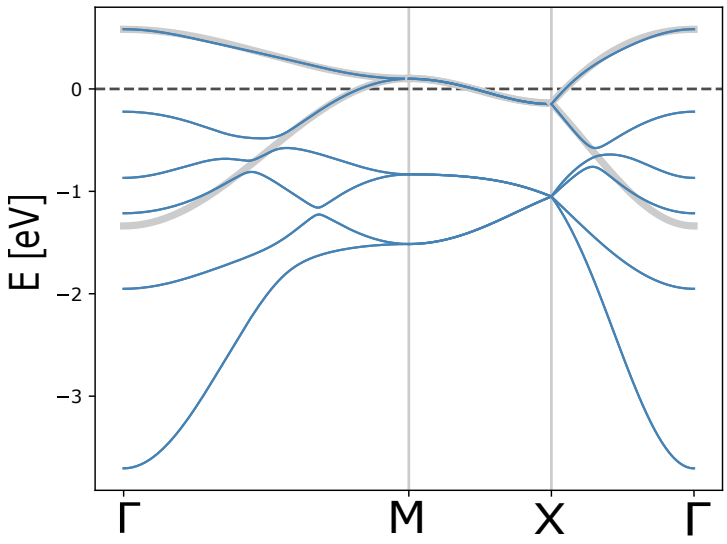

Figure 2.2: The 6 band bandstructure (blue) is shown for an non-interacting model of Sr_2IrO_4, with a strong spin-orbit coupling $\lambda = 0.7$eV. Overlain with the bands closest to the Fermi level is the dispersion for an effective model (gray) for the $j = 1/2$ states.

order where the magnetic moment follows the staggered rotations of the sites as shown in Fig. 2.1b). Within each layer the cAFM has a net ferromagnetic (FM) moment along the b-axis. As shown in Fig. 2.1c) the direction of the net moment is stacked between layers in a $\downarrow\uparrow\uparrow\downarrow$ pattern. This 4-layer pattern form a centrosymmetric order, and non-centrosymmetric stacking patterns can be possible for synthesizing Sr_2IrO_4 under high pressure [36, 37]. As the inter-layer coupling between magnetic moments is much smaller than the in-layer, a fair approximation for the model of this compound is to consider only one layer.

2.2 The prediction of superconductivity in Sr_2IrO_4

The perovskite structure and antiferromagnetic insulator as a ground state is similar to that of the superconductor parent compound La_2CuO_4. An effective cuprate isotropic Hubbard model is often given the parameters: nearest neighbor $t \approx 0.2$eV, next-nearest neighbor $t' \approx t/4$, 3rd n.n. $t'' \approx -t/10$, and $U \approx 10$t. The iridate is a Sr_2IrO_4 has multiple orbitals close to the Fermi level. However, due to the strong SOC each band has the character of mainly one of the total angular momentum states. In Fig. 2.2 a non-interacting bandstructure

is shown for the compound, for both a 3 orbital model and a total angular momentum $j = 1/2$ effective model. For the effective model, the full multi-orbital hopping parameters are projected onto the $j = 1/2$ state. The effective model has roughly the same parameters as the cuprate Hubbard model, except overall $t \to t/2$, and with the opposite sign of t'/t. The models would therefore be on the same form if the particle and hole degrees of freedom were to be switched, as this brings $t \to t$ and $t' \to -t'$. An electron doping of Sr_2IrO_4 is thus expected to have a similar superconducting region as hole-doped cuprates. As shown in Ref. [1] that terms arising in this simplified model from the staggered rotations of the oxygen octahedra can be gauged out, and are thus not significant to describe the physics within the band.

Multiple experiments have been carried out on doped Sr_2IrO_4. As of yet, no study has been able to fully confirm the existence of a superconducting region. In 2016 the authors of Ref. [38] were able to observe an order with d-wave symmetry by electron doping via oxygen deposition. However, the order could not be determined to be superconducting as no measurement of the Meissner effect or of transport properties was possible. Electron doping can also be achieved by chemical doping with lanthanum (La) [38, 39, 40, 41]. For La doping the long-range antiferromagnetic order eventually disappears. However, the same d-wave order is not observed. Instead a possible incommensurate spin density wave appears with a pseudogap at higher temperatures [41]. It should also be noted that high quality samples are difficult to achieve for higher La concentrations [42, 43].

There have been previous attempts to model superconductivity in doped Sr_2IrO_4 by also taking the multi-orbital nature into account. These works consider a three orbital model using variational Monte Carlo [3], functional renormalization group [4], dynamical mean-field theory [5], and random phase approximation [7]. When considering multiple orbitals a value for the inter-orbital Hund's coupling J_H must be chosen. A range of possible values can be approximated from experiments. For Hund's coupling in the lower end of that range, all studies find a d-wave order at electron doping. Quasiparticle interference calculations find that this order has a similar signature to that in cuprates [6]. However, at a sufficient value of J_H the d-wave order is no longer favorable. On the other hand, for a high J_H and hole doping either a multi-band $s_\pm$-wave [4, 7] or an odd parity p-wave order [5] can be favored.

Previous multi-orbital studies did not take the staggered lattice rotations into account. The first study to do so is Chapter 6 of this thesis.

Models that study the $j = 1/2$ states and take other effects into account, do such with staggered rotation and the titling of octahedra that can occur in thin films [44], possible heterostructures with Sr_2IrO_4 [45, 46, 47, 48] or additional effects like antisymmetric SOC [36] or inter-pseudospin hopping in $j = 1/2$ bands [49].

2.3 Epitaxial strain

The staggered rotations of the oxygen octahedra are not expected to change the pairing symmetry in the predicted $j = 1/2$ states. However, the in-plane magnetic order has shown to be sensitive to changes in the rotation angle, as the magnetic moments closely follow the rotations. When Sr_2IrO_4 is grown on a substrate with mismatched lattice parameters it experiences compressive $\epsilon < 0$ or tensile $\epsilon > 0$ strain. The strain ϵ describes the change in the lattice parameter a between sites in terms of percent change. As the oxygen octahedra remains largely rigid; they rotate closer or further from each other as a result. In the following section a multi-orbital model is introduced. It describes how each orbital is affected by the change in lattice geometry due to the epitaxial strain.

Bibliography

[1] F. Wang and T. Senthil, "Twisted Hubbard Model for Sr_2IrO_4 : Magnetism and Possible High Temperature Superconductivity," *Physical Review Letters*, vol. 106, p. 136402, mar 2011.

[2] J. Kim, D. Casa, M. H. Upton, T. Gog, Y.-J. Kim, J. F. Mitchell, M. van Veenendaal, M. Daghofer, J. van den Brink, G. Khaliullin, and B. J. Kim, "Magnetic Excitation Spectra of Sr_2IrO_4 Probed by Resonant Inelastic X-Ray Scattering: Establishing Links to Cuprate Superconductors," *Phys. Rev. Lett.*, vol. 108, p. 177003, Apr 2012.

[3] H. Watanabe, T. Shirakawa, and S. Yunoki, "Monte Carlo Study of an Unconventional Superconducting Phase in Iridium Oxide $J_{\mathrm{eff}} = 1/2$ Mott Insulators Induced by Carrier Doping," *Physical Review Letters*, vol. 110, p. 027002, jan 2013.

[4] Y. Yang, W.-S. Wang, J.-g. Liu, H. Chen, J.-h. Dai, and Q.-h. Wang, "Superconductivity in doped Sr_2IrO_4: A functional renormalization group study," *Physical Review B*, vol. 89, p. 094518, mar 2014.

[5] Z. Y. Meng, Y. B. Kim, and H.-Y. Y. Kee, "Odd-Parity triplet superconducting phase in multiorbital materials with a strong spin-orbit coupling: Application to doped Sr_2IrO_4," *Physical Review Letters*, vol. 113, pp. 1–5, apr 2014.

[6] Y. Gao, T. Zhou, H. Huang, and Q. H. Wang, "Possible superconductivity in Sr_2IrO_4 probed by quasiparticle interference," *Scientific Reports*, vol. 5, pp. 1–7, 2015.

[7] K. Nishiguchi, T. Shirakawa, H. Watanabe, R. Arita, and S. Yunoki, "Possible Superconductivity Induced by a Large Spin–Orbit Coupling in Carrier Doped Iridium Oxide Insulators: A Weak Coupling Approach," *Journal of the Physical Society of Japan*, vol. 88, p. 094701, sep 2019.

[8] G. Cao and P. Schlottmann, "The challenge of spin–orbit-tuned ground states in iridates: a key issues review," *Reports on Progress in Physics*, vol. 81, p. 042502, apr 2018.

[9] K. V. Shanavas, Z. S. Popović, and S. Satpathy, "Theoretical model for Rashba spin-orbit interaction in d electrons," *Phys. Rev. B*, vol. 90, p. 165108, Oct 2014.

[10] G. Chen, L. Balents, and A. P. Schnyder, "Spin-Orbital Singlet and Quantum Critical Point on the Diamond Lattice: $FeSc_2S_4$," *Phys. Rev. Lett.*, vol. 102, p. 096406, Mar 2009.

[11] O. N. Meetei, W. S. Cole, M. Randeria, and N. Trivedi, "Novel magnetic state in d^4 Mott insulators," *Phys. Rev. B*, vol. 91, p. 054412, Feb 2015.

[12] S. Bhowal, S. Baidya, I. Dasgupta, and T. Saha-Dasgupta, "Breakdown of $J = 0$ nonmagnetic state in d^4 iridate double perovskites: A first-principles study," *Phys. Rev. B*, vol. 92, p. 121113, Sep 2015.

[13] J. C. Wang, J. Terzic, T. F. Qi, F. Ye, S. J. Yuan, S. Aswartham, S. V. Streltsov, D. I. Khomskii, R. K. Kaul, and G. Cao, "Lattice-tuned magnetism of $Ru^{4+}(4d^4)$ ions in single crystals of the layered honeycomb ruthenates Li_2RuO_3 and Na_2RuO_3," *Phys. Rev. B*, vol. 90, p. 161110, Oct 2014.

[14] A. J. Kim, H. O. Jeschke, P. Werner, and R. Valentí, "**J** Freezing and Hund's Rules in Spin-Orbit-Coupled Multiorbital Hubbard Models," *Phys. Rev. Lett.*, vol. 118, p. 086401, Feb 2017.

[15] C. Svoboda, M. Randeria, and N. Trivedi, "Effective magnetic interactions in spin-orbit coupled d^4 Mott insulators," *Phys. Rev. B*, vol. 95, p. 014409, Jan 2017.

[16] M. K. Crawford, M. A. Subramanian, R. L. Harlow, J. A. Fernandez-Baca, Z. R. Wang, and D. C. Johnston, "Structural and magnetic studies of Sr_2IrO_4," *Phys. Rev. B*, vol. 49, pp. 9198–9201, Apr 1994.

[17] S. Boseggia, H. C. Walker, J. Vale, R. Springell, Z. Feng, R. S. Perry, M. Moretti Sala, H. M. Rønnow, S. P. Collins, and D. F. McMorrow, "Locking of iridium magnetic moments to the correlated rotation of oxygen octahedra in Sr_2IrO_4 revealed by x-ray resonant scattering," *Journal of Physics: Condensed Matter*, vol. 25, p. 422202, oct 2013.

[18] S. Fujiyama, H. Ohsumi, T. Komesu, J. Matsuno, B. J. Kim, M. Takata, T. Arima, and H. Takagi, "Two-Dimensional Heisenberg Behavior of $J_{\text{eff}} = 1/2$ Isospins in the Paramagnetic State of the Spin-Orbital Mott Insulator Sr_2IrO_4," *Phys. Rev. Lett.*, vol. 108, p. 247212, Jun 2012.

[19] J. Dai, E. Calleja, G. Cao, and K. McElroy, "Local density of states study of a spin-orbit-coupling induced Mott insulator Sr_2IrO_4," *Phys. Rev. B*, vol. 90, p. 041102, Jul 2014.

[20] Q. Huang, J. Soubeyroux, O. Chmaissem, I. Sora, A. Santoro, R. Cava, J. Krajewski, and W. Peck, "Neutron Powder Diffraction Study of the Crystal Structures of Sr_2RuO_4 and Sr_2IrO_4 at Room Temperature and at 10 K," *Journal of Solid State Chemistry*, vol. 112, no. 2, pp. 355–361, 1994.

[21] G. Cao, J. Bolivar, S. McCall, J. E. Crow, and R. P. Guertin, "Weak ferromagnetism, metal-to-nonmetal transition, and negative differential resistivity in single-crystal Sr_2IrO_4," *Phys. Rev. B*, vol. 57, pp. R11039–R11042, May 1998.

[22] M. Ge, T. F. Qi, O. B. Korneta, D. E. De Long, P. Schlottmann, W. P. Crummett, and G. Cao, "Lattice-driven magnetoresistivity and metal-insulator transition in single-layered iridates," *Phys. Rev. B*, vol. 84, p. 100402, Sep 2011.

[23] S. Chikara, O. Korneta, W. P. Crummett, L. E. DeLong, P. Schlottmann, and G. Cao, "Giant magnetoelectric effect in the $J_{\text{eff}} = \frac{1}{2}$ Mott insulator Sr_2IrO_4," *Phys. Rev. B*, vol. 80, p. 140407, Oct 2009.

[24] B. Xu, P. Marsik, E. Sheveleva, F. Lyzwa, A. Louat, V. Brouet, D. Munzar, and C. Bernhard, "Optical Signature of a Crossover from Mott- to Slater-Type Gap in $Sr_2Ir_{1-x}Rh_xO_4$," *Phys. Rev. Lett.*, vol. 124, p. 027402, Jan 2020.

[25] P. Foulquier, M. Civelli, M. Rozenberg, A. Camjayi, J. Bobadilla, D. Colson, A. Forget, P. Thuéry, F. Bertran, P. L. Fèvre, and V. Brouet, "Evolution of the spectral lineshape at the magnetic transition in Sr_2IrO_4 and $Sr_3Ir_2O_7$," *The European Physical Journal B*, vol. 96, p. 42, apr 2023.

[26] R. Arita, J. Kuneš, P. Augustinský, A. V. Kozhevnikov, A. G. Eguiluz, and M. Imada, "Mott versus Slater-Type Metal-Insulator Transition in Sr_2IrO_4 and Ba_2IrO_4," in *Proceedings of the International Conference on Strongly Correlated Electron Systems (SCES2013)*, Journal of the Physical Society of Japan, jun 2014.

[27] Q. Li, G. Cao, S. Okamoto, J. Yi, W. Lin, B. C. Sales, J. Yan, R. Arita, J. Kuneš, A. V. Kozhevnikov, A. G. Eguiluz, M. Imada, Z. Gai, M. Pan, and D. G. Mandrus, "Atomically resolved spectroscopic study of Sr_2IrO_4: Experiment and theory," *Scientific Reports*, vol. 3, p. 3073, oct 2013.

[28] J. M. Carter and H. Y. Kee, "Microscopic theory of magnetism in $Sr_3Ir_2O_7$," *Physical Review B - Condensed Matter and Materials Physics*, vol. 87, no. 1, pp. 1–5, 2013.

[29] D. Hsieh, F. Mahmood, D. H. Torchinsky, G. Cao, and N. Gedik, "Observation of a metal-to-insulator transition with both Mott-Hubbard and Slater characteristics in Sr_2IrO_4 from time-resolved photocarrier dynamics," *Phys. Rev. B*, vol. 86, p. 035128, Jul 2012.

[30] I. V. Solovyev, V. V. Mazurenko, and A. A. Katanin, "Validity and limitations of the superexchange model for the magnetic properties of Sr_2IrO_4 and Ba_2IrO_4 mediated by the strong spin-orbit coupling," *Phys. Rev. B*, vol. 92, p. 235109, Dec 2015.

[31] D. Choi, C. Yue, D. Azoury, Z. Porter, J. Chen, F. Petocchi, E. Baldini, B. Lv, M. Mogi, Y. Su, S. D. Wilson, M. Eckstein, P. Werner, and N. Gedik, "Light-induced insulator-metal transition in Sr_2IrO_4 reveals the nature of the insulating ground state," 2023.

[32] B. J. Kim, H. Jin, S. J. Moon, J.-Y. Kim, B.-G. Park, C. S. Leem, J. Yu, T. W. Noh, C. Kim, S.-J. Oh, J.-H. Park, V. Durairaj, G. Cao, and E. Rotenberg, "Novel $J_{\text{eff}} = 1/2$ Mott State Induced by Relativistic Spin-Orbit Coupling in Sr_2IrO_4," *Physical Review Letters*, vol. 101, p. 076402, aug 2008.

[33] B. J. Kim, H. Ohsumi, T. Komesu, S. Sakai, T. Morita, H. Takagi, and T. Arima, "Phase-Sensitive Observation of a Spin-Orbital Mott State in Sr_2IrO_4," *Science*, vol. 323, no. 5919, pp. 1329–1332, 2009.

[34] S. J. Moon, H. Jin, K. W. Kim, W. S. Choi, Y. S. Lee, J. Yu, G. Cao, A. Sumi, H. Funakubo, C. Bernhard, and T. W. Noh, "Dimensionality-Controlled Insulator-Metal Transition and Correlated Metallic State in 5*d* Transition Metal Oxides $Sr_{n+1}Ir_nO_{3n+1}$ ($n = 1$, 2, and ∞)," *Phys. Rev. Lett.*, vol. 101, p. 226402, Nov 2008.

[35] F. Ye, S. Chi, B. C. Chakoumakos, J. A. Fernandez-Baca, T. Qi, and G. Cao, "Magnetic and crystal structures of Sr_2IrO_4: A neutron diffraction study," *Phys. Rev. B*, vol. 87, p. 140406, Apr 2013.

[36] S. Sumita, T. Nomoto, and Y. Yanase, "Multipole Superconductivity in Nonsymmorphic Sr_2IrO_4," *Physical Review Letters*, vol. 119, no. 2, pp. 1–6, 2017.

[37] H. Wang, M. Marshall, Z. Wang, K. W. Plumb, M. Greenblatt, Y. Zhu, D. Walker, and W. Xie, "Non-centrosymmetric Sr_2IrO_4 obtained under High Pressure," 2023.

[38] Y. K. Kim, N. H. Sung, J. D. Denlinger, and B. J. Kim, "Observation of a d-wave gap in electron-doped Sr_2IrO_4," *Nature Physics*, vol. 12, no. 1, pp. 37–41, 2016.

[39] X. Chen, T. Hogan, D. Walkup, W. Zhou, M. Pokharel, M. Yao, W. Tian, T. Z. Ward, Y. Zhao, D. Parshall, C. Opeil, J. W. Lynn, V. Madhavan, and S. D. Wilson, "Influence of electron doping on the ground state of $(Sr_{1-x}La_x)_2IrO_4$," *Phys. Rev. B*, vol. 92, p. 075125, Aug 2015.

[40] I. Battisti, K. M. Bastiaans, V. Fedoseev, A. de la Torre, N. Iliopoulos, A. Tamai, E. C. Hunter, R. S. Perry, J. Zaanen, F. Baumberger, and M. P. Allan, "Universality of pseudogap and emergent order in lightly doped Mott insulators," *Nature Physics*, vol. 13, pp. 21–25, jan 2017.

[41] X. Chen, J. L. Schmehr, Z. Islam, Z. Porter, E. Zoghlin, K. Finkelstein, J. P. Ruff, and S. D. Wilson, "Unidirectional spin density wave state in metallic $(Sr_{1-x}La_x)_2IrO_4$," *Nature Communications*, vol. 9, no. 1, 2018.

[42] N. H. Sung, H. Gretarsson, D. Proepper, J. Porras, M. L. Tacon, A. V. Boris, B. Keimer, and B. J. Kim, "Crystal growth and intrinsic magnetic behaviour of Sr_2IrO_4," *Philosophical Magazine*, vol. 96, no. 4, pp. 413–426, 2016.

[43] J. M. Guevara, Z. Sun, E. M. Pärschke, S. Sykora, K. Manna, J. Schoop, A. Maljuk, S. Wurmehl, J. van den Brink, B. Büchner, and C. Hess, "Spin-polaron ladder spectrum of the spin-orbit-induced Mott insulator Sr_2IrO_4 probed by scanning tunneling spectroscopy," *Phys. Rev. B*, vol. 99, p. 121114, Mar 2019.

[44] A. W. Lindquist and H.-Y. Kee, "Odd-parity superconductivity driven by octahedra rotations in iridium oxides," *Physical Review B*, vol. 100, p. 054512, aug 2019.

[45] Y. Chen and H. Y. Kee, "Helical Majorana fermions at the interface of Weyl semimetal and d-wave superconductor: Application to Iridates and high-Tc Cuprates," *arXiv*, vol. 085155, pp. 1–8, 2017.

[46] M. Horsdal and T. Hyart, "Robust semi-Dirac points and unconventional topological phase transitions in doped superconducting Sr_2IrO_4 tunnel coupled to t_{2g} electron systems," *SciPost Physics*, vol. 3, p. 041, dec 2017.

[47] A. M. Petrzhik, K. Y. Constantinian, G. A. Ovsyannikov, A. V. Shadrin, Y. V. Kislinskii, G. Cristiani, and G. Logvenov, "Superconducting Current in Mesa Structures with Interlayer of Strontium Iridate, a Material Having Strong Spin-Orbit Interaction," *Journal of Surface Investigation: X-ray, Synchrotron and Neutron Techniques*, vol. 14, pp. 547–550, may 2020.

[48] H. Pandey, M. Kumar, D. Tripathi, and S. Pandey, "Superconducting Properties of $La_{1.85}Sr_{0.15}CuO_4$-Sr_2IrO_4 multilayers," 2021.

[49] M.-H. Zare, M. Biderang, and A. Akbari, "Mixed-pairing superconductivity in 5*d* Mott insulators with antisymmetric exchange: Application to Sr_2IrO_4," *Physical Review B*, vol. 96, p. 205156, nov 2017.

Chapter 3

A spin-orbit coupled tight-binding model

3.1 Ir-d orbitals

In Sr_2IrO_4 the iridium sites are filled by $5d^5$ electrons. For a free ion the five orbitals, the t_{2g} and e_g orbitals, are degenerate. By placing the Ir-atom in the surrounding oxygen octahedra introduces a O_h symmetry, which splits the subspace with angular momentum $L = 0, 1$ to a lower energy than the $L = 2$ subspace. In Fig. 3.1 it is shown that only the three orbitals d_{yz}, d_{xz}, d_{xy} in the t_{2g} subspace are located close to the Fermi level, as they are filled by 5 electrons in 6 bands. If the atomic spin-orbit coupling (SOC) of the iridium is included a new basis describes the new energy levels. That is the basis of total angular momentum $j = \frac{1}{2}, \frac{3}{2}$, and the projection along the z-axis $j_z = \pm\frac{1}{2}, \pm\frac{3}{2}$. The strength of the SOC, λ, separates the $(j, j_z) = \left(\frac{1}{2}, \pm\frac{1}{2}\right)$ from the other states, as shown in Fig. 3.1.

3.1.1 Tetragonal splitting

An additional symmetry breaking and splitting of energy levels is shown in Fig. 3.1. In Sr_2IrO_4, the oxygen octahedra are compressed along the c-axis. To see how this tetragonal symmetry breaking splits the energy levels one considers the angular momentum of the orbitals. The d-orbitals can be written with spherical harmonics $Y_{lm_l}(\theta, \phi)$ for $l = 2$. The

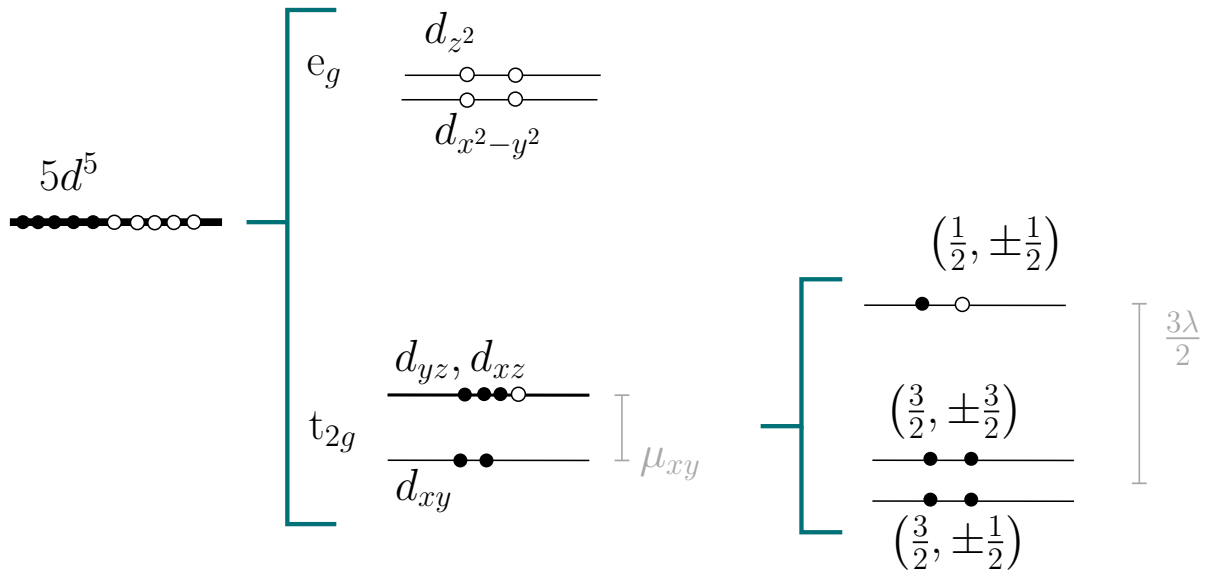

Figure 3.1: The atomic energy levels for the the iridium d^5 orbitals, where the levels are filled by 5 electrons. The 5 d-orbitals are split into two subspaces by the O_h symmetry of the oxygen octahedron. When tetragonal symmetry is broken d_{xy} is separated from the rest of the t_{2g} orbitals by μ_{xy}. The energy levels are split further by the SOC λ.

tetragonal symmetry breaking shifts the energy levels according to $\propto m_l^2$. The e_g subsector has a vanishing orbital momentum m_l

$$d_{z^2} = Y_{2,0}, \qquad d_{x^2-y^2} = \frac{1}{\sqrt{2}}\left(Y_{2,2} + Y_{2,-2}\right) \tag{3.1}$$

while the t_{2g} subsector has a non-zero m_l

$$d_{yz} = \frac{1}{i\sqrt{2}}\left(Y_{2,1} - Y_{2,-1}\right), \qquad d_{xz} = \frac{1}{\sqrt{2}}\left(Y_{2,1} + Y_{2,-1}\right), \qquad d_{xy} = \frac{1}{i\sqrt{2}}\left(Y_{2,2} - Y_{2,-2}\right) \tag{3.2}$$

We can observe that if we operate on the orbitals in the t_{2g} subsector with the angular momentum ladder operators L_z^+, L_z^- they effectively form a three level system as

$$\begin{aligned} L_z^+ d_{xy} &\propto Y_{2,-1}, \qquad & L_z^- d_{xy} &\propto Y_{2,+1}, \\ L_z^+ Y_{2,-1} &= 0, \qquad & L_z^- Y_{2,+1} &= 0 \end{aligned} \tag{3.3}$$

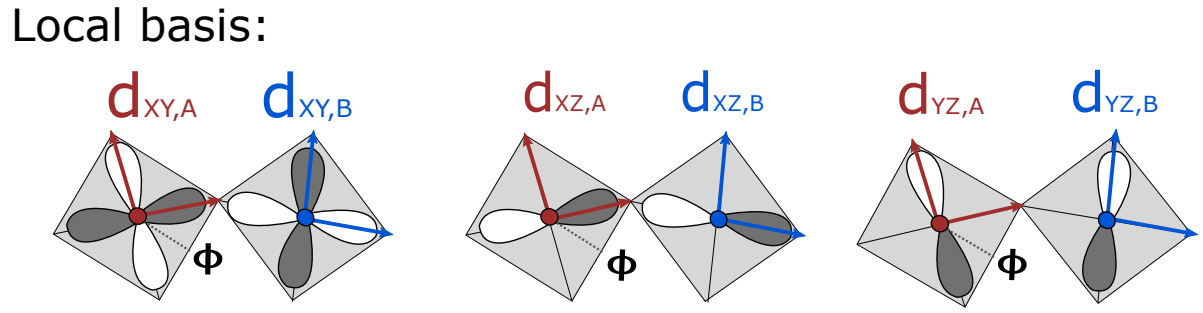

Figure 3.2: In the two-site basis the orbitals are defined in the local staggered basis. The orbitals in sublattice $s = A, B$ are rotated by $\phi \approx 12°$.

So the states $Y_{2,-1}, d_{xy}, Y_{2,+1}$ forms an effective system with $l_{\text{eff}} = -1$ and $m_{l,\text{eff}} = 1, 0, -1$ respectively. In Sr_2IrO_4 the tetragonal distortion bring the symmetry group at a site from O_h to D_{4h}. For compression of the octahedra this should place the d_{xy} higher in energy than the d_{yz}, d_{xz} orbitals. However, the observed spectra of Sr_2IrO_4, as well as *ab initio* calculations, shows d_{xy} as being lower in energy. Additional hybridization of the p-orbitals of the oxygen atoms with the d-orbitals can explain this discrepancy and results in the energy splitting in Fig. 3.1.

3.1.2 Local rotated basis

As introduced in Section 2.1 each layer in the perovskite structure has a staggered rotations of the oxygen octahedra surrounding the iridium sites. To take into account the staggered rotations we model a two-site basis. A global basis has global axes x, y along the crystallographic a- and b-axes. With the staggered rotations ϕ, $\phi_A = \phi$ and $\phi_B = -\phi$, the orbitals on each site are rotated through the coordinate transformation

$$X_s = x\cos\phi_i + y\sin\phi_s, \qquad Y_s = -x\sin\phi_s + y\cos\phi_i \tag{3.4}$$

in a local basis X_s, Y_s. The orbitals follow the rotations and are defined in the local basis, as shown in Fig. 3.2. The spins are however defined along the global axes. The quantization axis is given such that the spin-direction $\uparrow$ is given along $+z$ and spin-$\downarrow$ along $-z$.

3.2 Tight binding model

A tight binding model for hopping in the square lattice with three orbitals $\alpha = yz, xz, xy$, two spins $\sigma = \uparrow, \downarrow$, and two sublattices $s = A, B$ can be written as

$$H_{\text{kin}} = \sum_{\alpha,\beta,\sigma,\sigma'} \sum_{s,s'} \sum_{i,\delta} \left[t^{\delta}_{(\alpha,s)(\beta,s')} c^{\dagger}_{i,s,\alpha,\sigma} c_{i+\delta,s',\beta,\sigma} + \text{h.c.} \right] \tag{3.5}$$

Here i are unit cells in the lattice and δ connects nearest neighbor or next nearest neighbor sites. Without staggered rotations the hopping only occurs within the same orbital and spin. From the spread of each orbital, the overlap of wavefunction between sites is significantly larger between orbitals with the same geometry. For the nearest neighbor hopping along each axis is t^{x}_{ab} and t^{y}_{ab}, with the labels $a = (\alpha, s)$ containing the orbital α and sublattice s degrees of freedom. The hopping takes place between sublattices and the terms have the form

$$H^{x}_{\text{kin,no rot}} = \sum_{\alpha,\sigma} t^{x}_{(\alpha A)(\alpha B)} c^{\dagger}_{i,A,\alpha,\sigma} c_{i+x,B,\alpha,\sigma} + t^{x}_{(\alpha B)(\alpha A)} c^{\dagger}_{i,B,\alpha,\sigma} c_{i+x,A,\alpha,\sigma} \tag{3.6}$$

3.2.1 Slater-Koster approach

The hopping integrals for the d-orbitals under rotation can be calculated with the Slater-Koster approach [1, 2]. The hopping integrals can be derived from the hopping $(t_{dd\sigma}, t_{dd\pi}, t_{dd\delta})$. They each represent the hopping along the z-direction between states Y^{m}_{l}, where the labels represent the projection along the z-axis as $\sigma : m = 0$, $\pi : m = \pm 1$, and $\delta : m = \pm 2$. The usual ratio between the hoppings is given by $t_{dd\sigma} : t_{dd\pi} : t_{dd\delta} = \frac{3}{2} : -1 : \frac{1}{4}$ [3, 4]. The standard Slater-Koster hopping for the five states of the d-orbitals are given by the matrix

$$t_{SK} = \begin{pmatrix} t_{dd\delta} & 0 & 0 & 0 & 0 \\ 0 & t_{dd\pi} & 0 & 0 & 0 \\ 0 & 0 & t_{dd\sigma} & 0 & 0 \\ 0 & 0 & 0 & t_{dd\pi} & 0 \\ 0 & 0 & 0 & 0 & t_{dd\delta} \end{pmatrix} \tag{3.7}$$

in the basis $m = (-2, -1, 0, 1, 2)$. The hopping along a given direction can be derived by rotating the z-axis into a given direction. This means that we can write down the general form for the resulting hopping for an in-plane staggered rotations ϕ. A general rotation matrix is given by

$$\mathcal{R}(\alpha, \beta, \gamma) = e^{-i\alpha J_z} e^{-i\beta J_y} e^{-i\gamma J_z}. \tag{3.8}$$

α, β, γ are here the Euler angles rotated in the directions $z - y - z$. If each orbital state is quantized along the z-axis as $|l, m\rangle$. The Wigner D-matrix representation is the overlap between two states with the general rotation matrix [5]:

$$\mathcal{D}^l_{m,m'}(\alpha, \beta, \gamma) = \langle lm|\mathcal{R}(\alpha, \beta, \gamma)|lm'\rangle = e^{-i\alpha m'} d^j_{mm'}(\beta) e^{-i\gamma m} \tag{3.9}$$

as J_z is diagonal in the basis $|lm\rangle$. The rotation β around the y-axis is the overlap between in the d-orbitals, with the five possible states in $l = 2$:

$$d^l_{mm'}(\beta) = \langle lm|e^{-i\beta J_y}|lm'\rangle \tag{3.10}$$

So to get a rotation into a local basis with a rotation $\pm\phi$ of each site, a rotation matrix defined for the angles is given as $R_{loc}(\phi) = D(-\pi/4, 0, \pi/4 + \phi)$. To calculate the hopping in a given direction the bonds are rotated as well, for example in the x-direction $R_{bond} = D(0, -\pi/2, 0)$. So for the basis of staggered rotations $\phi = \pm 12°$:

$$\tilde{t}^x_{SK} = \psi^\dagger R^\dagger_{loc}(\phi, 0) R^\dagger_{bond} t_{SK} R_{bond} R_{loc}(-\phi, 0)\psi \tag{3.11}$$

where one sublattice is rotated with $R_{loc}(-\phi, 0)$ and the other with $R_{loc}(\phi, 0)$. Here the matrix ψ transforms the 5 $l = 2$ into the 3 t_{2g} orbitals as in section 3.1.1 and in this basis

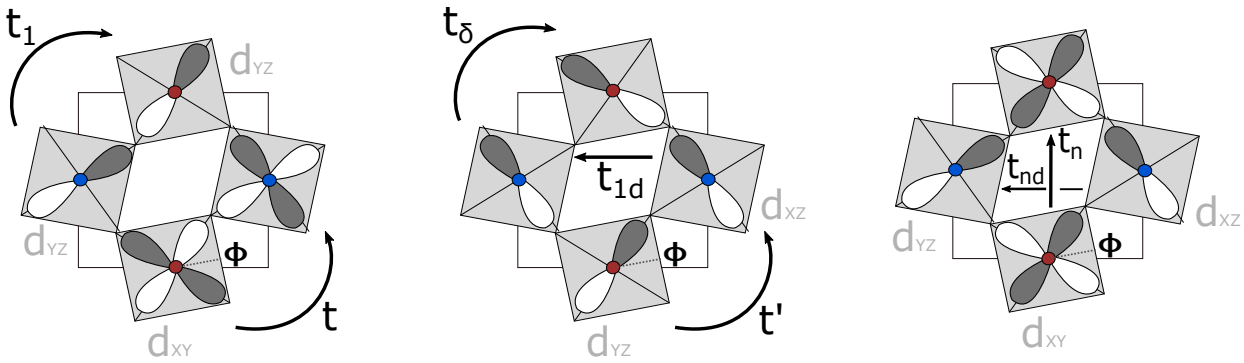

Figure 3.3: Nearest and next nearest neighbor hopping terms are shown for each orbital in the lattice with staggered rotations. The hopping $t_1 \gg t_\delta$ as the orbitals d_{yz} and d_{xz} have a quasi-1d overlap n-plane with neighboring sites.

the hopping has the form

$$\tilde{t}^x_{SK} = \begin{pmatrix} \cos^2\phi t_{dd\delta} - \sin^2\phi t_{dd\pi} & -\frac{1}{2}\sin 2\phi\,(t_{dd\delta} + t_{dd\pi}) & 0 \\ \frac{1}{2}\sin 2\phi\,(t_{dd\delta} + t_{dd\pi}) & \cos^2\phi t_{dd\pi} - \sin^2\phi t_{dd\delta} & 0 \\ 0 & 0 & \cos^2 2\phi t_{dd\pi} - \frac{3}{4}\sin^2 2\phi t_{dd\sigma} - \frac{1}{4}\sin^2 2\phi t_{dd\delta} \end{pmatrix} \tag{3.12}$$

in the basis (d_{yz}, d_{xz}, d_{xy}). For the expected value $\phi = 12°$ and $t_{dd\sigma} : t_{dd\pi} : t_{dd\delta} = \frac{3}{2} : -1 : \frac{1}{4}$

$$\tilde{t}^x_{SK} = \begin{pmatrix} 0.27 & 0.15 & 0 \\ -0.15 & -0.94 & 0 \\ 0 & 0 & -1 \end{pmatrix} t_{dd\pi} \tag{3.13}$$

We define the hopping with the parameters

$$\tilde{t}^x_{SK} = \begin{pmatrix} t_\delta & t' & 0 \\ -t' & t_1 & 0 \\ 0 & 0 & t \end{pmatrix}, \qquad \tilde{t}^y_{SK} = \begin{pmatrix} t_1 & t' & 0 \\ -t' & t_\delta & 0 \\ 0 & 0 & t \end{pmatrix} \tag{3.14}$$

where the bond along the y-direction is calculated at $R_{bond} = D(0, -\pi/2, \pi/2)$. In Fig. 3.3 each hopping term is shown in the lattice.

n.n.n. hopping

The next-nearest neighbor (n.n.n.) hopping is scaled by 0.2 with respect to the corresponding n.n. hopping as in Ref. [2] and now takes place between sites belonging to the same sublattice. The rotation terms from the sublattice therefore cancel out and the hopping terms are calculated as

$$\tilde{t}_{SK}^{+x,+y} = 0.2\psi^{\dagger} R_{bond}^{\dagger} t_{SK} R_{bond} \psi \tag{3.15}$$

The bond angle along $+x, +y$ with $R_{bond} = D(0, -\pi/2, \pi/4)$:

$$\tilde{t}_{SK}^{+x,+y} = \begin{pmatrix} -0.07 & 0.12 & 0 \\ 0.12 & -0.07 & 0 \\ 0 & 0 & 0.23 \end{pmatrix} t_{dd\pi} \tag{3.16}$$

The set of n.n.n. terms are defined as

$$\tilde{t}_{SK}^{+x,+y} = \begin{pmatrix} t_{1d} & -t_{nd} & 0 \\ -t_{nd} & t_{1d} & 0 \\ 0 & 0 & t_n \end{pmatrix}, \qquad \tilde{t}_{SK}^{+x,-y} = \begin{pmatrix} t_{1d} & t_{nd} & 0 \\ t_{nd} & t_{1d} & 0 \\ 0 & 0 & t_n \end{pmatrix} \tag{3.17}$$

In Eq.s (3.14) & (3.17) only direct hopping between Ir-d orbitals are considered. One additional type of hopping not considered here is the contributions from oxygen mediated hopping. The strength of the hybridization between iridium d-orbitals and oxygen p-orbitals determines the size of this effect.

3.3 Modeling compressive strain

When a layer of Sr_2IrO_4 is compressed the main effect is the oxygen octahedra rotate closer to each other by increasing the staggered angle ϕ. As a first approximation the effect of a compressive strain could be modeled by increasing the staggered angle in the Slater-Koster model. However, an additional expected effect is the compression of the axes. To accurately capture the size of the two effects we must have information about Sr_2IrO_4. If the hopping parameters as in Eq.s (3.14) & (3.17) are modeled to change linearly with compressive strain

$\epsilon < 0$, that change can follow values fitted for strain up to $\epsilon = -1.9\%$ [6]. A significant difference from the Slater-Koster approach is a larger increase of the nearest neighbor $d_{xy}-d_{xy}$ and $d_{yz} - d_{xz}$ hopping.

One additional aspect to be noted is that tensile strain $\epsilon > 0$ could be considered as an extrapolation of the same linearization. However, that does not agree with the experimental values for undoped samples of Sr_2IrO_4 under tensile strain. For example, the effect of a lowered critical temperature for the magnetic order is seen both for compressive and tensile strain. For consistency with experiment, the works included in this thesis only consider compressive strain.

The strain has two types of effects. Firstly, the strain can increase or decrease the overall bandwidth or the resulting band structure. For compressive strain in Sr_2IrO_4 the bandwidth increases. Secondly, the bandwidth for different bands changes in different amounts. As shown in the next section, the bands will have different orbital contributions for which the hopping parameters change in different amounts.

3.4 Momentum space

The non-interacting tight binding model is considered in a periodic lattice and can thus be diagonalized in momentum space. The transformation is defined as

$$c_{\boldsymbol{j},a} = \frac{1}{\sqrt{N}} \sum_{\boldsymbol{k}} e^{i\boldsymbol{k}\cdot\boldsymbol{j}} c_{\boldsymbol{j},a}, \qquad c^\dagger_{\boldsymbol{j},a} = \frac{1}{\sqrt{N}} \sum_{\boldsymbol{k}} e^{-i\boldsymbol{k}\cdot\boldsymbol{j}} c^\dagger_{\boldsymbol{j},a} \tag{3.18}$$

where N is the number of sites in the lattice and the lattice spacing is set to 1. The model contains 12 operators: $N_\sigma = 2$ (spins $\sigma = \uparrow, \downarrow$), $N_o = 3$ (orbitals $\alpha = yz, xz, yz$), and $N_s = 2$ (sublattices $s = A, B$). The 12 eigenvalues of the Hamiltonian thus form 12 bands $E_{n,\boldsymbol{k}}$. As hopping terms mix sublattice and orbital degrees of freedom and the SOC couples different spin sectors, we cannot block diagonalize the Hamiltonian in these degrees of freedom. The non-interacting Hamiltonian in momentum space is divided into two parts:

$$H = H_{\text{kin}} + H_{\text{SOC}} \tag{3.19}$$

The kinetic part contains the hopping terms, the Fourier transform of the terms in Eq.s (3.14) & (3.17). In the basis $\boldsymbol{c_k} = (c_{\boldsymbol{k},A,yz,\uparrow}, c_{\boldsymbol{k},A,yz,\downarrow}, c_{\boldsymbol{k},A,xz,\uparrow}, c_{\boldsymbol{k},A,xz,\downarrow}, c_{\boldsymbol{k},A,xy,\uparrow}, c_{\boldsymbol{k},A,xy,\downarrow}, c_{\boldsymbol{k},B,yz,\uparrow}, c_{\boldsymbol{k},B,yz,\downarrow}, c_{\boldsymbol{k},B,xz,\uparrow}, c_{\boldsymbol{k},B,xz,\downarrow}, c_{\boldsymbol{k},B,xy,\uparrow}, c_{\boldsymbol{k},B,xy,\downarrow})$ the 12×12 Hamiltonian has the form:

$$H_{\text{kin}} = \sum_{\boldsymbol{k}} \boldsymbol{c}_{\boldsymbol{k}}^{\dagger} \begin{pmatrix} H_{AA} & e^{ik_x} H_{AB} \\ e^{-ik_x} H_{AB}^{\dagger} & H_{BB} \end{pmatrix} \boldsymbol{c_k} \tag{3.20}$$

$$H_{AA} = \begin{pmatrix} \epsilon_d & \epsilon_{1d} & 0 \\ \epsilon_{1d} & \epsilon_d & 0 \\ 0 & 0 & \epsilon_d^{xy} \end{pmatrix}, H_{AB} = \begin{pmatrix} \epsilon_{yz} & -\epsilon_{rot} & 0 \\ \epsilon_{rot} & \epsilon_{xz} & 0 \\ 0 & 0 & \epsilon_{xy} \end{pmatrix} \tag{3.21}$$

with $H_{BB} = H_{AA}$. With the Fourier transform each term becomes

$$\begin{aligned} \epsilon_{xy} &= 2t\,(\cos k_x + \cos k_y) \\ \epsilon_{yz} &= 2\,(t_\delta \cos k_x + t_1 \cos k_y) \\ \epsilon_{xz} &= 2\,(t_1 \cos k_x + t_\delta \cos k_y) \\ \epsilon_{rot} &= 2t'\,(\cos k_x + \cos k_y) \\ \epsilon_d^{xy} &= 4t_n \cos k_x \cos k_y + \mu_{xy} \\ \epsilon_{1d} &= 4t_{1d} \sin k_x \sin k_y \\ \epsilon_d &= 4t_{nd} \cos k_x \cos k_y \end{aligned} \tag{3.22}$$

where the hopping values are specified in Chapters 5 and 6. The atomic spin-orbit coupling is an on-site coupling $\boldsymbol{L} \cdot \boldsymbol{S}$:

$$H_{\text{SOC}} = \frac{\lambda}{2} \sum_{\boldsymbol{j},s} \sum_{i=x,y,z} \sum_{\alpha\beta,\sigma\sigma'} L^i_{\alpha\beta} \sigma^i_{\sigma\sigma'} c^{\dagger}_{\boldsymbol{j}s\alpha\sigma} c_{\boldsymbol{j}s\beta\sigma'} = \frac{\lambda}{2} \sum_{\boldsymbol{k},s} \sum_{i=x,y,z} \sum_{\alpha\beta,\sigma\sigma'} L^i_{\alpha\beta} \sigma^i_{\sigma\sigma'} c^{\dagger}_{\boldsymbol{k}s\alpha\sigma} c_{\boldsymbol{k}s\beta\sigma'} \tag{3.23}$$

where $\boldsymbol{\sigma} = (\sigma^x, \sigma^y, \sigma^z)$ are the Pauli matrices in the spin basis, and the matrices

$$\boldsymbol{L} = \left(\begin{bmatrix} 0 & 0 & 0 \\ 0 & 0 & -i \\ 0 & i & 0 \end{bmatrix}, \begin{bmatrix} 0 & 0 & i \\ 0 & 0 & 0 \\ -i & 0 & 0 \end{bmatrix}, \begin{bmatrix} 0 & -i & 0 \\ i & 0 & 0 \\ 0 & 0 & 0 \end{bmatrix} \right) \tag{3.24}$$

which are the Gell-Mann matrices $\lambda_2, \lambda_5.\lambda_7$, as defined in Appendix A. In Fig. 3.4 the orbital contributions of the bands at the Fermi surface are shown. There is a clear orbital texture of the bands. Due to the geometry of the orbitals, the hopping $t_1 \gg t_\delta$ and the hopping of the yz is almost entirely in the y-direction. The same is true for the xz, which has a dispersion mainly in the x-direction. The hopping within these orbitals is thus quasi-1d while the xy-orbital has a dispersion which is equal in both directions.

3.4.1 J-state basis

When a strong spin-orbit coupling is included the quantum states are better described in a total angular momentum basis. The total angular momentum is, as usual, the sum of the orbital and spin momenta $\hat{J} = \hat{L} + \hat{S}$. For the allowed quantum numbers the following projections along the z-axis are allowed for the states

$$\begin{aligned} m_s &\in \{-s, -s+1, \ldots, s-1, s\}, \\ m_l &\in \{-l, -l+1, \ldots, l-1, l\}, \quad l \in \{0, 1, \ldots, n-1\} \\ j_z &\in \{-j, -j+1, \ldots, j-1, j\} \end{aligned} \tag{3.25}$$

as $j_z = m_s + m_l$ and $j = l + s$ The t_{2g} subspace has $l = 0, 1$. As the spin $s = 1/2$ the values $j = 1/2$ and $j = 3/2$ are possible. These states are also the eigenstates of the SOC Hamiltonian Eq. (3.23) and can be written as

$$\begin{aligned} |\frac{1}{2}, \pm\frac{1}{2}\rangle &= \frac{1}{\sqrt{3}} \left(|yz, \downarrow / \uparrow\rangle \mp i|xz, \downarrow / \uparrow\rangle + |xy, \uparrow / \downarrow\rangle\right) \\ |\frac{3}{2}, \pm\frac{1}{2}\rangle &= \frac{1}{\sqrt{6}} \left(\mp|yz, \downarrow / \uparrow\rangle - i|xz, \downarrow / \uparrow\rangle - 2|xy, \uparrow / \downarrow\rangle\right) \\ |\frac{3}{2}, \pm\frac{3}{2}\rangle &= \frac{1}{\sqrt{2}} \left(\pm|yz, \downarrow / \uparrow\rangle - i|xz, \downarrow / \uparrow\rangle\right) \end{aligned} \tag{3.26}$$

As the full non-interacting Hamiltonian contains additional terms from H_{kin} the basis of j-states in Eq. (3.26) are no longer eigenstates. However, for a large SOC parameter, λ, each band consists mainly of two j-states. This can be observed in Fig. 3.4, where the Fermi surface is shown with the projection onto each state. As λ is decreased the j-states are more mixes within each band. However, the shift in energy splitting $3\lambda/2$ between $j = 1/2$ and

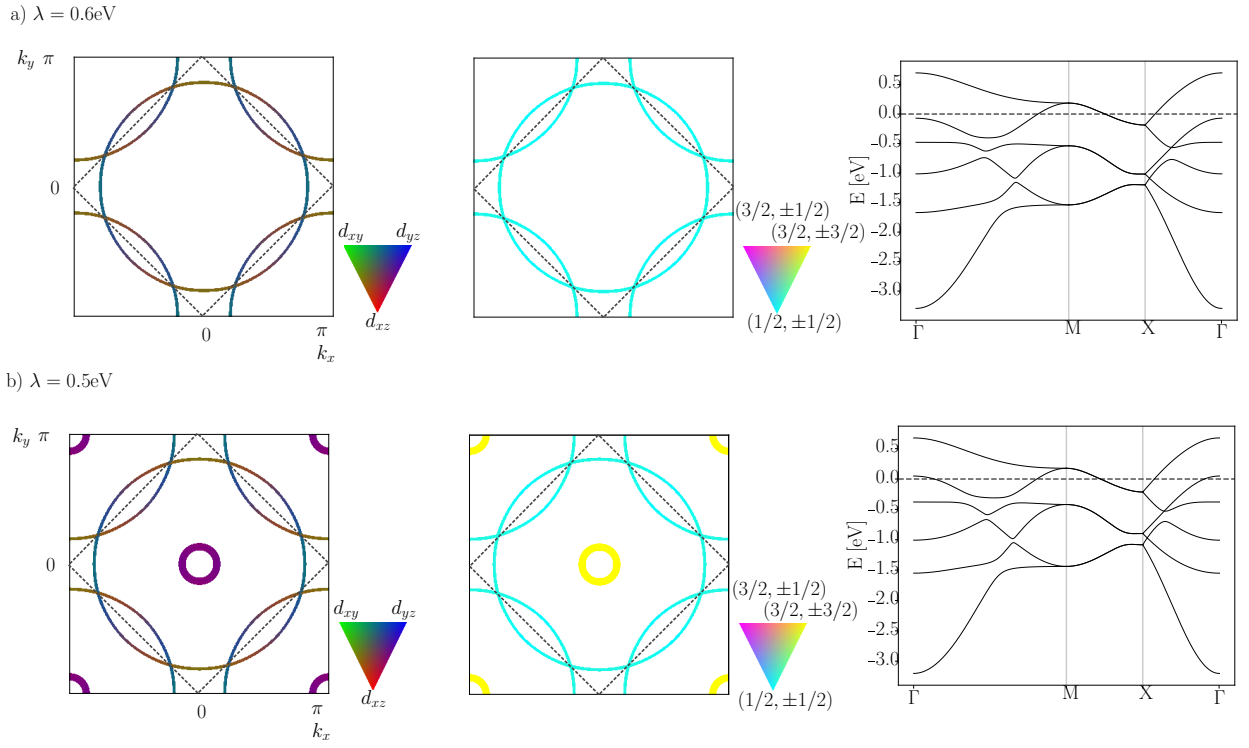

Figure 3.4: For two values of the spin-orbit coupling the Fermi surface (in the extended Brillouin zone) and bandstructure is shown for the non-interacting model with electron filling $n = 5$. For the Fermi surface the density of the orbital and j-states are shown in two different plots. The color of a point at the FS represents the contribution from each state to the eigenvector for that band.

$j = 3/2$ bands is the larger energy scale that changes with the strength of the SOC. The mixing of orbital and spin degrees of freedom means that there are bands with sections of multiple orbital and spin characters at the Fermi surface. The validity of only considering physics in the $j = 1/2$ bands is therefore dependent on the interactions in the model. The interactions are introduced in the next Chapter 4.

3.5 Green's functions

The single-particle (particle-hole) Green's function is defined as

$$G_{ab}(k) = -\int_0^\beta d\tau e^{i\omega_n \tau} \langle T_\tau c_{\boldsymbol{k}a}(\tau) c^\dagger_{\boldsymbol{k}b}(0) \rangle \tag{3.27}$$

for two sublattice (s), orbital (α), and spin (σ), indices $a = (s, \alpha, \sigma)$. The non-interacting Green's function can be calculated for the non-interacting Hamiltonian. The eigenvalues ($\xi_{\boldsymbol{k},n}$) and eigenvectors ($\tilde{c}_{\boldsymbol{k},n}$) of the Hamiltonian are

$$H_0(\boldsymbol{k}) = \sum_{\boldsymbol{k},ab} c^\dagger_{\boldsymbol{k},a} \mathcal{H}_{\boldsymbol{k},ab} c_{\boldsymbol{k},b} = \sum_{\boldsymbol{k},n} \tilde{c}^\dagger_{\boldsymbol{k},n} \xi_{\boldsymbol{k},n} \tilde{c}_{\boldsymbol{k},n} = \sum_{\boldsymbol{k},a,b} \sum_n \left(\tilde{c}^\dagger_{\boldsymbol{k},n} U^\dagger_{na}\right) \left(U_{bn} \xi_{\boldsymbol{k},n} U^\dagger_{nb}\right) \left(U_{bn} \tilde{c}_{\boldsymbol{k},n}\right) \quad (3.28)$$

where $U_{\boldsymbol{k}}$ are unitary matrices such that $c_{\boldsymbol{k},a} = \sum_n U_{\boldsymbol{k},an} \tilde{c}_{\boldsymbol{k},n}$. Now one element of the Green function (for a given eigenvalue $\xi_{\boldsymbol{k},n}$)

$$G^{(0)}_n(k) = \left[i\omega_m - \xi_{\boldsymbol{k},n}\right]^{-1} \quad (3.29)$$

We cannot that for the non-interacting Green's function $\bar{G}_{0ab}(k) = -G_{0ba}(-k)$. For a combination of states a, b:

$$G^{(0)}_{ab}(k) = \sum_n U_{\boldsymbol{k},an} G^{(0)}_n(k) U^\dagger_{\boldsymbol{k},nb} \quad (3.30)$$

Bibliography

[1] J. C. Slater and G. F. Koster, "Simplified LCAO Method for the Periodic Potential Problem," *Phys. Rev.*, vol. 94, pp. 1498–1524, Jun 1954.

[2] J. M. Carter and H. Y. Kee, "Microscopic theory of magnetism in $Sr_3Ir_2O_7$," *Physical Review B - Condensed Matter and Materials Physics*, vol. 87, no. 1, pp. 1–5, 2013.

[3] O. Andersen, "Simple approach to the band-structure problem," *Solid State Communications*, vol. 13, no. 2, pp. 133–136, 1973.

[4] M. Finnis, *Interatomic Forces in Condensed Matter*. Oxford University Press, 10 2003.

[5] E. Wigner, *Gruppentheorie und ihre Anwendung auf die Quantenmechanik der Atomspektren*, vol. 39. Wiesbaden: Vieweg+Teubner Verlag, 1931.

[6] A. Seo, P. P. Stavropoulos, H. H. Kim, K. Fürsich, M. Souri, J. G. Connell, H. Gretarsson, M. Minola, H. Y. Kee, and B. Keimer, "Compressive strain induced enhancement of exchange interaction and short-range magnetic order in Sr_2IrO_4 investigated by Raman spectroscopy," *Physical Review B*, vol. 100, no. 16, pp. 1–7, 2019.

Chapter 4

Multi-orbital interactions

In the non-interacting multi-orbital model, introduced in Chapter 3, there are already multiple types of terms coupling spin, orbital, and sublattice degrees of freedom. When considering Coulomb interactions in the system no exact solution can be found and approximations must be made to treat the interactions. In the manuscripts of Chapters 5 and 6 two approximations are used to study the magnetic and superconducting orders: a mean field approximation and the random phase approximation (RPA). In the following sections the derivation for the self-consistency equations used to calculate the order parameters is outlined and the approximations are compared.

4.1 Hubbard-Kanamori interactions

Any model of interactions between electrons in a solid is an effective description of Coulomb interactions. In a d-orbital each electron feels the effects from the iridium nuclei and the electrons filling the other orbitals. In a crystalline solid the tight binding model, with hopping between discrete sites, is often a sufficient description of the electrostatic potential landscape created by the full system, as experienced by electrons close to the Fermi level. For interactions between the electrons, an on-site interaction can be introduced as the bare interactions in our effective Hubbard model.

In a multi-orbital system several types of interactions are present. Here they are screened Coulomb interaction from the t_{2g} orbitals. For Coulomb interaction between two electrons

located at $\boldsymbol{r}$ and $\boldsymbol{r}'$, $V_c(\boldsymbol{r},\boldsymbol{r}')$, the wavefunction will screen the electrons. An electron in the t_{2g} orbital $\alpha \in [yz, xz, xy]$ has the wavefunction $\phi_\alpha(\boldsymbol{r})$. The three types of screened interactions: the intra-orbital U, the inter-orbital ($\alpha \neq \alpha'$) U', and the Hund's coupling J_{H}, given by

$$\begin{aligned} U &= \int d\boldsymbol{r}d\boldsymbol{r}'|\phi_\alpha(\boldsymbol{r})|^2 V_c(\boldsymbol{r},\boldsymbol{r}')|\phi_\alpha(\boldsymbol{r}')|^2 \\ U' &= \int d\boldsymbol{r}d\boldsymbol{r}'|\phi_\alpha(\boldsymbol{r})|^2 V_c(\boldsymbol{r},\boldsymbol{r}')|\phi_{\alpha'}(\boldsymbol{r}')|^2 \\ J_{\mathrm{H}} &= \int d\boldsymbol{r}d\boldsymbol{r}'\phi^*_\alpha(\boldsymbol{r})\phi^*_{\alpha'}(\boldsymbol{r})V_c(\boldsymbol{r},\boldsymbol{r}')\phi_\alpha(\boldsymbol{r}')\phi_{\alpha'}(\boldsymbol{r}') \end{aligned} \tag{4.1}$$

The wavefunctions $\phi_\alpha(\boldsymbol{r})$ van be chosen to be real and thus the last integral is the same for pair-hopping and spin-exchange terms, both giving the same value of J_{H}. For the tight binding model introduced in section 3.2 the Hubbard-Kanamori interaction [1] becomes

$$\begin{aligned} H_{\mathrm{I}} = \; & U\sum_{\boldsymbol{j},\alpha} n_{\boldsymbol{j}\alpha\uparrow}n_{\boldsymbol{j}\alpha\downarrow} \\ & + \sum_{\boldsymbol{j},\alpha\neq\beta} J_{\mathrm{H}}\left[c^\dagger_{\boldsymbol{j}\alpha\uparrow}c^\dagger_{\boldsymbol{j}\beta\downarrow}c_{\boldsymbol{j}\alpha\downarrow}c_{\boldsymbol{j}\beta\uparrow} + c^\dagger_{\boldsymbol{j}\alpha\uparrow}c^\dagger_{\boldsymbol{j}\alpha\downarrow}c_{\boldsymbol{j}\beta\downarrow}c_{\boldsymbol{j}\beta\uparrow}\right] \\ & + \sum_{\boldsymbol{j},\alpha<\beta,\sigma}\left[U' n_{\boldsymbol{j}\alpha\sigma}n_{\boldsymbol{j}\beta\bar{\sigma}} + (U'-J_{\mathrm{H}})\, n_{\boldsymbol{j}\alpha\sigma}n_{\boldsymbol{j}\beta\sigma}\right] \end{aligned} \tag{4.2}$$

The interactions can be set to be rotationally invariant, meaning that they have the full $U(1)_c \otimes SU(2)_s \otimes SO(3)_o$ symmetry [2]. This is achieved by setting $U' = U - 2J_{\mathrm{H}}$ [1].

4.2 Mean field theory

The interactions can be treated to the lowest order with the mean field approximation. In Chapter 5 such an approximation is done for the Hubbard-Kanamori interactions in Eq. (4.2), to consider on-site magnetic order parameters. A mean field decoupling of a Hamiltonian is done by defining a set of order parameters around which fluctuations are assumed to be small. We can always write a set of parameters as the mean value and fluctuations around that mean:

$$c_a c_b = (c_a c_b - \langle c_a c_b\rangle) + \langle c_a c_b\rangle = \delta\,(c_a c_b) + \langle c_a c_b\rangle \tag{4.3}$$

for any two operators c_a, c_b. A general term of the interaction can be expressed as

$$H_V^{abcd} = V^{abcd} c_a^\dagger c_b c_c^\dagger c_d \tag{4.4}$$

If the order parameters $o_{ab} = \langle c_a^\dagger c_b \rangle$ with fluctuations $\delta o_{ab} = c_a^\dagger c_b - \langle c_a^\dagger c_b \rangle$ are inserted into the Hamiltonian

$$\begin{aligned} H_V^{abcd} = & \quad V^{abcd}(\delta o_{ab} + o_{ab})(\delta o_{cd} + o_{cd}) \\ = & \quad V^{abcd}(\delta o_{ab}\delta o_{cd} + o_{ab}\delta o_{cd} + o_{cd}\delta o_{ab} + o_{ab}o_{cd}) \end{aligned} \tag{4.5}$$

If the fluctuations are sufficiently small, we assume $\mathcal{O}((\delta o)^2) \approx 0$:

$$H_V^{abcd} \approx V^{abcd}(o_{ab} c_c^\dagger c_d + o_{cd} c_a^\dagger c_b - o_{ab} o_{cd}) \tag{4.6}$$

It is however also the case that an equally valid decomposition is

$$H_V^{abcd} \approx V^{abcd}(o_{cb} c_a^\dagger c_d + o_{ad} c_c^\dagger c_b - o_{cb} o_{ad}) \tag{4.7}$$

As an example, let us consider the intra-orbital interaction per orbital α

$$H_U = \sum_{j,\alpha} U c_{j,\alpha,\uparrow}^\dagger c_{j,\alpha,\uparrow} c_{j,\alpha,\downarrow}^\dagger c_{j,\alpha,\downarrow} \tag{4.8}$$

The two possible ways to decompose the Hamiltonian can then be combined as

$$\begin{aligned} H_U \approx & \frac{U}{2} \sum_{j,\alpha} (n_{j,\alpha,\downarrow} c_{j,\alpha,\uparrow}^\dagger c_{j,\alpha,\uparrow} + n_{j,\alpha,\uparrow} c_{j,\alpha,\downarrow}^\dagger c_{j,\alpha,\downarrow} - n_{j,\alpha,\uparrow} n_{j,\alpha,\downarrow}) \\ & + \frac{U}{2} \sum_{j,\alpha} (\langle c_{j,\alpha,\uparrow}^\dagger c_{j,\alpha,\downarrow} \rangle c_{j,\alpha,\downarrow}^\dagger c_{j,\alpha,\uparrow} + \langle c_{j,\alpha,\downarrow}^\dagger c_{j,\alpha,\uparrow} \rangle c_{j,\alpha,\uparrow}^\dagger c_{j,\alpha,\downarrow} - \langle c_{j,\alpha,\downarrow}^\dagger c_{j,\alpha,\uparrow} \rangle \langle c_{j,\alpha,\uparrow}^\dagger c_{j,\alpha,\downarrow} \rangle) \end{aligned} \tag{4.9}$$

with spin-diagonal $n_{j,\alpha,\sigma}$ and spin-off-diagonal $\langle c_{j,\alpha,\uparrow}^\dagger c_{j,\alpha,\downarrow} \rangle$ operators. This can be written using spin and density operators

$$n_{j,\alpha,\uparrow} = n_{j,\alpha} + S_{j,\alpha}^z, \qquad n_{j,\alpha,\downarrow} = n_{j,\alpha} - S_{j,\alpha}^z, \qquad \langle c_{j,\alpha,\uparrow}^\dagger c_{j,\alpha,\downarrow} \rangle = S_{j,\alpha}^x + i S_{j,\alpha}^y. \tag{4.10}$$

By Fourier transforming the Hamiltonian the decomposition in momentum space is

$$\begin{aligned} H_U \approx & \frac{U}{2N^2} \sum_{k,k',\alpha} (n_{k',s,\alpha,\downarrow} c^\dagger_{k,s,\alpha,\uparrow} c_{k,s,\alpha,\uparrow} + n_{k',s\alpha,\uparrow} c^\dagger_{k,s,\alpha,\downarrow} c_{k,s,\alpha,\downarrow} - n_{k',s,\alpha,\uparrow} n_{k,s,\alpha,\downarrow} \\ & + (S^x_{k',\alpha} + iS^y_{k',\alpha}) c^\dagger_{k,\alpha,\downarrow} c_{k,\alpha,\uparrow} + (S^x_{k',\alpha} - iS^y_{k',\alpha}) c^\dagger_{k,\alpha,\uparrow} c_{k,\alpha,\downarrow} - (S^x_{k',\alpha} + iS^y_{k',\alpha})(S^x_{k,\alpha} - iS^y_{k,\alpha})) \end{aligned} \tag{4.11}$$

We will further assume that all on-site order parameters are equal at all sites belonging to the same sublattice, therefore allowing for a uniform order or an order which is staggered between sublattices. $\langle c^\dagger_{j,\alpha,\downarrow} c_{j,\alpha,\uparrow} \rangle = \langle c^\dagger_{s,\alpha,\downarrow} c_{s,\alpha,\uparrow} \rangle$, for $s = A, B$. This mean value is then defined as

$$\langle c^\dagger_{s,\alpha,\downarrow} c_{s,\alpha,\uparrow} \rangle = \frac{1}{N} \sum_{k'} \langle c^\dagger_{k',s,\alpha,\downarrow} c_{k',s,\alpha,\uparrow} \rangle \tag{4.12}$$

which is a self-consistency equation for the order parameter and where the mean is taken with respect to the eigenstates of the mean field decoupled Hamiltonian:

$$\begin{aligned} H_{\mathrm{MF}} = & \frac{U}{2N} \sum_{k,\alpha} (n_{s,\alpha,\downarrow} c^\dagger_{k,s,\alpha,\uparrow} c_{k,s,\alpha,\uparrow} + n_{s\alpha,\uparrow} c^\dagger_{k,s,\alpha,\downarrow} c_{k,s,\alpha,\downarrow} - n_{s,\alpha,\uparrow} n_{s,\alpha,\downarrow} \\ & + (S^x_\alpha + iS^y_\alpha) c^\dagger_{k,\alpha,\downarrow} c_{k,\alpha,\uparrow} + (S^x_\alpha - iS^y_\alpha) c^\dagger_{k,\alpha,\uparrow} c_{k,\alpha,\downarrow} - (S^x_\alpha + iS^y_\alpha)(S^x_\alpha - iS^y_\alpha)) \end{aligned} \tag{4.13}$$

We can now solve the quadratic mean field Hamiltonian to get eigenvalues and eigenstates. The expectation values in the self-consistency equation Eq. (4.12) can be calculated as

$$\langle c^\dagger_a c_b \rangle = \frac{1}{N} \sum_{\boldsymbol{k}} \sum_n U^\dagger_{an} U_{nb} f(E_n(\boldsymbol{k}), T). \tag{4.14}$$

where the energy $E_n(\boldsymbol{k})$ is the eigenvalue to the mean field Hamiltonian $H_{\mathrm{kin}} + H_{\mathrm{MF}}$. U_{nb} is the matrix transforming the spin-orbital basis into the eigenstates at a momentum $\boldsymbol{k}$. $f(E_n(\boldsymbol{k}), T)$ is the Fermi-Dirac distribution at a temperature T:

$$f(E_n(\boldsymbol{k}), T) = \frac{1}{e^{E_n(\boldsymbol{k})/k_{\mathrm{B}}T} + 1} \tag{4.15}$$

4.2.1 Self-consistency equations

The Hubbard-Kanamori interactions, Eq. (4.2), can be decomposed into a large set of order parameters per site. In the spin and orbital basis, there are densities $n_{s,\alpha}$, spin densities

$S^i_{s,\alpha}$, orbital angular momentum $L^i_{s,\sigma}$, and operators renormalizing the spin-orbit coupling Λ^i_s. The directions are $i = x, y, z$ and the self-consistency equations are

$$S^i_{s,\alpha} = \sum_{\sigma,\sigma'} S^i_{\sigma\sigma'} \langle c^\dagger_{s\alpha\sigma} c_{s\alpha\sigma'} \rangle \tag{4.16}$$

$$L^i_{s,\sigma} = \sum_{\alpha,\beta} L^i_{\alpha\beta} \langle c^\dagger_{\alpha\sigma} c_{\beta\sigma} \rangle \tag{4.17}$$

$$\Lambda^i_s = \sum_{\alpha,\beta} \sum_{\sigma,\sigma'} L^i_{\alpha\beta} S^i_{\sigma\sigma'} \langle c^\dagger_{s\alpha\sigma} c_{s\beta\sigma'} \rangle \tag{4.18}$$

where S^i are the Pauli matrices $i = x, y, z$ and L^i are three of the Gell-Mann matrices corresponding to $l = 1$ orbital angular momentum operators, as defined in Appendix A. As all on-site parameters are considered for two sublattices, and the Hamiltonian must remain Hermitian, there are 42 complex order parameters. An alternative definition of order parameters is to decompose the Hamiltonian in the total angular momentum j-states. This definition results in the same amount of order parameters, which instead has momentum contributions from intra- or inter-J operators:

$$J^i_{s,m} = \sum_{\tau,\tau'} S^i_{\tau\tau'} \langle \tilde{c}^\dagger_{sm\tau} \tilde{c}_{sm\tau'} \rangle \tag{4.19}$$

$$J^i_{s,mn} = \sum_{\tau,\tau'} S^i_{\tau\tau'} \langle \tilde{c}^\dagger_{sm\tau} \tilde{c}_{sn\tau'} \rangle \tag{4.20}$$

where $m \in [(1/2, \pm 1/2), (3/2, \pm 1/2), (3/2, \pm 3/2)]$ are the j-states and $\tau = +, -$ is the projection along the z-axis. The total magnetic moment per sublattice is

$$\boldsymbol{m}_s = (\boldsymbol{L}_{s,\uparrow} + \boldsymbol{L}_{s,\downarrow})/2 + g\boldsymbol{S}_s = (\boldsymbol{L}_{s,\uparrow} + \boldsymbol{L}_{s,\downarrow})/2 + g \sum_\alpha \boldsymbol{S}_{s,\alpha} \tag{4.21}$$

and the staggered AFM and net FM moments are respectively

$$\boldsymbol{m}_{s,AFM} = (\boldsymbol{m}_A - \boldsymbol{m}_B)/2, \qquad \boldsymbol{m}_{s,FM} = (\boldsymbol{m}_A + \boldsymbol{m}_B)/2 \tag{4.22}$$

In Fig. 4.1 the magnetic moment of a mean field solution is shown. The solution is the canted AFM state of Sr_2IrO_4, along with the different components.

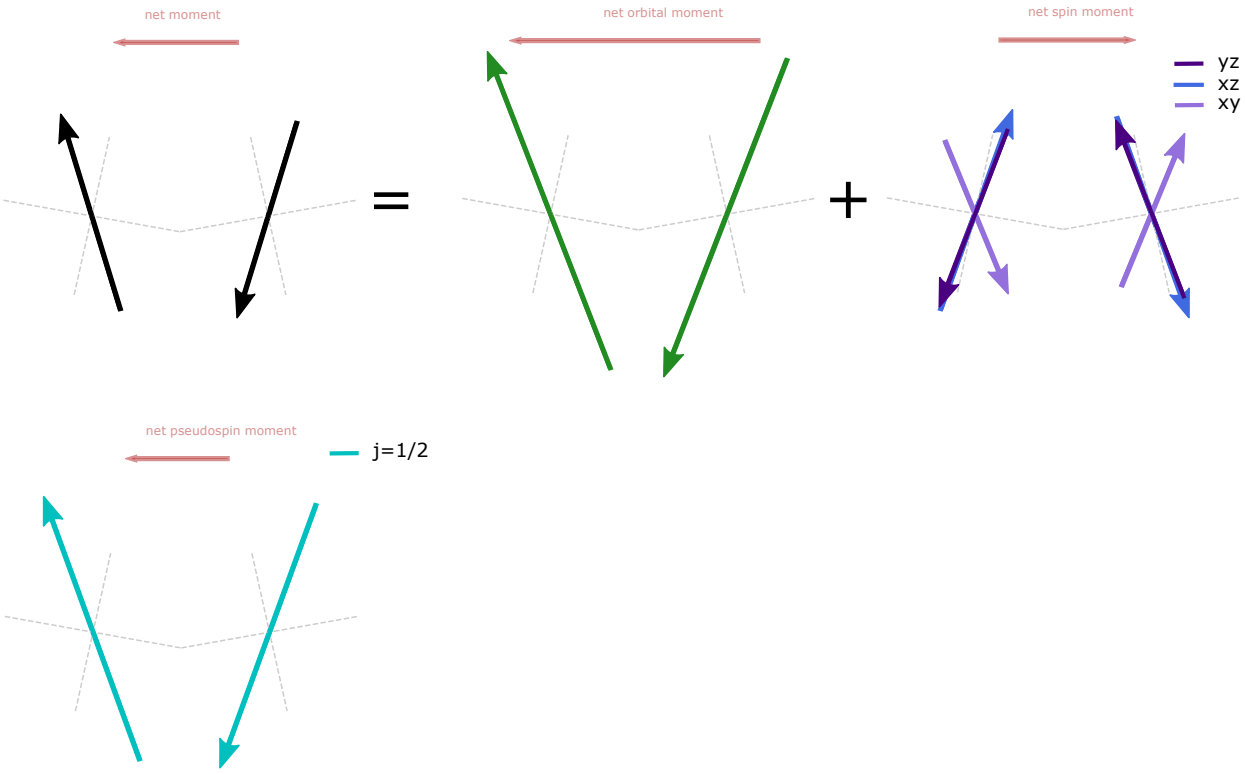

Figure 4.1: The mean field solution for the canted AFM ground state is shown in terms of total magnetic moment, Eq. (4.21), per sublattice. The components per orbital Eq. (4.16) and spin Eq. (4.17) magnetic moment are shown as well. On the bottom row the magnetic moment per site from Eq. (4.19) for the $j = 1/2$ state is shown.

Parameters to describe Sr_2IrO_4

The undoped Sr_2IrO_4, with 5 d electrons $n = 5$, has bands of mostly $j = 1/2$ character at the Fermi surface and the magnetic moment consists mostly of a $j = 1/2$ pseudospin. The question is then: is it sufficient to just include the $j = 1/2$ moment, Eq. (4.19), as an order parameter? The answer is in general no. The accuracy of the $j = 1/2$ approximation depends on where we are in the phase diagram. What the order parameters solely in the $j = 1/2$ bands are missing are the effects from the order parameters describing the renormalized SOC and the density per orbital. These two types of terms will determine the overall placement of the $j = 1/2$ bands in the band structure and therefore which states are present at the Fermi surface.

Depending on the strength of the SOC and the interactions terms U, J_{H}, the multi-orbital Hamiltonian can form a large number of orders. By including all on-site order parameters in a two-site basis several types of staggered orders are allowed. A charge density wave (CDW) is a staggered filling of all orbitals per site $n_s = \sum_{\alpha,\sigma} n_{s,\alpha,\sigma}$. A spin density wave (SDW) is a staggered spin, either in-plane or out-of-plane, between sites. An orbital density wave (ODW) has a staggered orbital angular momentum of one or several of the orbitals per site. Finally, a spin-orbit density wave (SODW) is a staggered order in any of the order parameters in Eq. (4.18). This order mixes spin and orbital components and thus contains a type of hidden SDW. For example, terms of the forms

$$L^x S^x : \langle c^\dagger_{sxy\uparrow} c_{sxz\downarrow} \rangle - \langle c^\dagger_{sxz\uparrow} c_{sxy\downarrow} \rangle + \langle c^\dagger_{sxy\downarrow} c_{sxz\uparrow} \rangle - \langle c^\dagger_{sxz\downarrow} c_{sxy\uparrow} \rangle \tag{4.23}$$

and

$$L^z S^z : \langle c^\dagger_{syz\uparrow} c_{sxz\uparrow} \rangle - \langle c^\dagger_{sxz\uparrow} c_{syz\uparrow} \rangle - \left(\langle c^\dagger_{syz\downarrow} c_{sxz\downarrow} \rangle - \langle c^\dagger_{sxz\downarrow} c_{syz\downarrow} \rangle \right). \tag{4.24}$$

In Chapter 5 this full set of parameters are considered for the magnetic order of Sr_2IrO_4 under compressive strain.

4.2.2 BCS theory

Superconductivity can similarly be treated on a mean field level. To consider a superconducting order parameter $\langle c_a c_b \rangle$, we can formulate the Nambu basis $\left(c_{\boldsymbol{k}}, c^\dagger_{-\boldsymbol{k}}\right)^{\mathrm{T}}$. The full Hamiltonian is then the Bogoliubov-de Gennes (BdG) Hamiltonian

$$H_{\mathrm{BdG}} = \sum_{\boldsymbol{k}} \left(c^\dagger_{\boldsymbol{k}}, c_{-\boldsymbol{k}}\right) \begin{pmatrix} H_{\mathrm{kin}}(\boldsymbol{k}) & \Delta(\boldsymbol{k}) \\ \Delta^\dagger(\boldsymbol{k}) & -H^{\mathrm{T}}_{\mathrm{kin}}(-\boldsymbol{k}) \end{pmatrix} \begin{pmatrix} c_{\boldsymbol{k}} \\ c^\dagger_{-\boldsymbol{k}} \end{pmatrix} \tag{4.25}$$

where $H(\boldsymbol{k})$ contains the non-interacting terms in H_{kin} at a momentum $\boldsymbol{k}$ and $\Delta(\boldsymbol{k})$ is the superconducting order parameter. In the full multi-orbital model, the basis vectors in Nambu space are

$$\begin{aligned} \boldsymbol{c}_{\boldsymbol{k}} = (&c_{\boldsymbol{k},A,yz,\uparrow}, c_{\boldsymbol{k},A,yz,\downarrow}, c_{\boldsymbol{k},A,xz,\uparrow}, c_{\boldsymbol{k},A,xz,\downarrow}, c_{\boldsymbol{k},A,xy,\uparrow}, c_{\boldsymbol{k},A,xy,\downarrow}, \\ &c_{\boldsymbol{k},B,yz,\uparrow}, c_{\boldsymbol{k},B,yz,\downarrow}, c_{\boldsymbol{k},B,xz,\uparrow}, c_{\boldsymbol{k},B,xz,\downarrow}, c_{\boldsymbol{k},B,xy,\uparrow}, c_{\boldsymbol{k},B,xy,\downarrow}, \\ &c^\dagger_{-\boldsymbol{k},A,yz,\uparrow}, c^\dagger_{-\boldsymbol{k},A,yz,\downarrow}, c^\dagger_{-\boldsymbol{k},A,xz,\uparrow}, c^\dagger_{-\boldsymbol{k},A,xz,\downarrow}, c^\dagger_{-\boldsymbol{k},A,xy,\uparrow}, c^\dagger_{-\boldsymbol{k},A,xy,\downarrow}, \\ &c^\dagger_{-\boldsymbol{k},B,yz,\uparrow}, c^\dagger_{-\boldsymbol{k},B,yz,\downarrow}, c^\dagger_{-\boldsymbol{k},B,xz,\uparrow}, c^\dagger_{-\boldsymbol{k},B,xz,\downarrow}, c^\dagger_{-\boldsymbol{k},B,xy,\uparrow}, c^\dagger_{-\boldsymbol{k},B,xy,\downarrow})^{\mathrm{T}} \end{aligned} \tag{4.26}$$

If only a single orbital and sublattice is considered the eigenvalues are $E(\boldsymbol{k}) = \pm\sqrt{\xi^2_{\boldsymbol{k}} + |\Delta(\boldsymbol{k})|^2}$, where $\xi_{\boldsymbol{k}}$ are the eigenvalues of $H_{\mathrm{kin}}(\boldsymbol{k})$. In the single $j = 1/2$ band approximation, the most probable predicted superconducting order in Sr_2IrO_4 has been a $d_{x^2-y^2}$-wave order $\Delta(\boldsymbol{k}) = \Delta_{x^2-y^2}(\cos k_x - \cos k_y)$. For this order to be favorable it requires an effective attractive interaction between nearest neighbor sites. Understanding the processes that cause this effective attraction is one of the important questions in the study of unconventional superconductivity. What mediates superconductivity will have consequences for the shape of the effective interaction. In Bardeen-Cooper-Schrieffer theory the Cooper pairs are mediated by phonons. However, screening effects of the Coulomb interactions from other electrons can also results in attractive interactions. The interactions will be discussed further in Chapter 4.

An intra-orbital interaction in momentum space that connects the two sublattices has the form:

$$H_U = \frac{1}{N} \sum_{\boldsymbol{k}'} \sum_{\boldsymbol{k},\alpha} \sum_{\boldsymbol{\delta}=\pm\hat{x},\pm\hat{y}} V e^{i(\boldsymbol{k}-\boldsymbol{k}')\cdot\boldsymbol{\delta}} c^\dagger_{\boldsymbol{k}',A\alpha,\uparrow} c_{\boldsymbol{k},A\alpha,\uparrow} c^\dagger_{-\boldsymbol{k}',B\alpha,\downarrow} c_{-\boldsymbol{k},B\alpha,\downarrow} \tag{4.27}$$

A mean field decomposition gives us

$$\begin{aligned} H_U \approx & \sum_{\boldsymbol{k},\alpha} V \left[\Delta^{AB}_{\alpha,\uparrow\downarrow}(\boldsymbol{k}) e^{ik_x} c^\dagger_{\boldsymbol{k},B,\alpha,\downarrow} c^\dagger_{-\boldsymbol{k},A,\alpha,\uparrow} + \Delta^{\dagger,BA}_{\alpha,\downarrow\uparrow}(\boldsymbol{k}) e^{-ik_x} c_{\boldsymbol{k},A,\alpha,\uparrow} c_{-\boldsymbol{k},B,\alpha,\downarrow}\right] \\ & - \sum_{\boldsymbol{k},\alpha} V \Delta^{AB}_{\alpha,\uparrow\downarrow}(\boldsymbol{k}) \langle e^{ik_x} c^\dagger_{\boldsymbol{k},B,\alpha,\downarrow} c^\dagger_{-\boldsymbol{k},A,\alpha,\uparrow}\rangle \end{aligned} \tag{4.28}$$

with the order parameters defined as

$$\Delta^{AB}_{\alpha,\uparrow\downarrow}(\boldsymbol{k}) = \frac{1}{N} \sum_{\boldsymbol{k}'} \langle e^{-ik'_x} c_{\boldsymbol{k}',A,\alpha,\uparrow} c_{-\boldsymbol{k}',B,\alpha,\downarrow}\rangle \tag{4.29}$$

If the expectation value is calculated via the eigenstates as in Eq. (4.14), the values of the eigenstates of the BdG Hamiltonian gives us:

$$\begin{aligned} \Delta^{AB}_{\alpha,\uparrow\downarrow}(\boldsymbol{k}) &= -\frac{1}{N} \sum_{\boldsymbol{k}'} V \Delta^{AB}_{\alpha,\uparrow\downarrow}(\boldsymbol{k}') \frac{f(E(\boldsymbol{k}'),T) - f(-E(\boldsymbol{k}'),T)}{2E(\boldsymbol{k}')} \\ &= -\frac{1}{N} \sum_{\boldsymbol{k}'} V \frac{\Delta^{AB}_{\alpha,\uparrow\downarrow}(\boldsymbol{k}')}{2E(\boldsymbol{k}')} \tanh\left(\frac{E(\boldsymbol{k}')}{2k_{\mathrm{B}}T}\right) \end{aligned} \tag{4.30}$$

This is the BCS equation, which can have a solution $\Delta^{AB}_{\alpha,\uparrow\downarrow}(\boldsymbol{k}) \neq 0$ when $V < 0$. Values for an attractive nearest neighbor V that reproduce the superconducting region in cuprates have been previously approximated. However, such approximations depend both on the value of U and the hopping t. As the work in this thesis considers a varying strain, and therefore hopping parameters, we need to study closer how the effective interaction changes. In the following sections we will consider how the Coulomb interaction is treated to study spin-fluctuation mediated superconductivity.

4.3 Interaction vertices

To study our full model we combine the non-interacting Hamiltonian from section 3.2 with Eq. (4.2). In momentum space the Hamiltonian with the bare interactions is

$$H = H_{kin} + \sum_{a,b,c,d} \sum_{\boldsymbol{k}_1\boldsymbol{k}_2\boldsymbol{k}_3\boldsymbol{k}_4} V^{abcd}_{0,\boldsymbol{k}_1\boldsymbol{k}_2\boldsymbol{k}_3\boldsymbol{k}_4} c^\dagger_{\boldsymbol{k}_3 c} c_{\boldsymbol{k}_1 a} c^\dagger_{\boldsymbol{k}_4 d} c^\dagger_{\boldsymbol{k}_2 b} \tag{4.31}$$

where the translational invariance of the interactions requires that $\boldsymbol{k}_1 + \boldsymbol{k}_2 - \boldsymbol{k}_3 - \boldsymbol{k}_4$ is equal to 0 up to a reciprocal lattice vector $\boldsymbol{K}$. In the following section I will introduce how an interacting model is expanded, in perturbation theory, to get the parquet equations for an effective interaction and how to calculate self-energies. Approximations for solving the equations will be shown at both at the Hartree-Fock and random phase approximation (RPA) level. The connection between the order parameters in mean field, as discussed in the previous section, and self-energies in the Hartree-Fock calculation will be established.

4.3.1 Single-particle propagator

In the interacting system the particle-hole G and hole-particle $\bar{G}$ Green's functions for the full system are defined as

$$G_{ab}(k) = -\int_0^\beta d\tau e^{i\omega_n \tau} \langle T_\tau c_{\boldsymbol{k}a}(\tau) c^\dagger_{\boldsymbol{k}b}(0)\rangle \tag{4.32}$$

$$\bar{G}_{ab}(k) = -\int_0^\beta d\tau e^{i\omega_n \tau} \langle T_\tau c^\dagger_{-\boldsymbol{k}a}(\tau) c_{-\boldsymbol{k}b}(0)\rangle \tag{4.33}$$

where the momentum is $k = (\boldsymbol{k}, i\omega_n)$, with the fermionic Matsubara frequencies $\omega_n = (2n + 1)\pi/\beta$ and the inverse temperature $\beta = \hbar/(k_\mathrm{B}T)$. The anomalous Green's function F_{ab} can similarly be defined as

$$F_{ab}(k) = -\int_0^\beta d\tau e^{i\omega_n \tau} \langle T_\tau c_{\boldsymbol{k}a}(\tau) c_{-\boldsymbol{k}b}(0)\rangle \tag{4.34}$$

$$\bar{F}_{ab}(k) = -\int_0^\beta d\tau e^{i\omega_n \tau} \langle T_\tau c^\dagger_{-\boldsymbol{k}a}(\tau) c^\dagger_{\boldsymbol{k}b}(0)\rangle \tag{4.35}$$

The full Green's function $\boldsymbol{G}$ can be connected to the non-interaction Green's function $\boldsymbol{G}^{(0)}$, as introduced in Section 3.5, and the self-energy $\boldsymbol{\Sigma}$ via the Dyson-Gorkov equations:

$$\boldsymbol{G}(\boldsymbol{k}, i\omega_n) = \boldsymbol{G}^{(0)}(\boldsymbol{k}, i\omega_n) + \boldsymbol{G}^{(0)}(\boldsymbol{k}, i\omega_n)\boldsymbol{\Sigma}(\boldsymbol{k}, i\omega_n)\boldsymbol{G}(\boldsymbol{k}, i\omega_n) \tag{4.36}$$

The above equation can be represented diagrammatically as shown in Fig. 4.2. The particle-hole $G_{a\bar{b}}$ and particle-particle $\bar{F}_{\bar{a}\bar{b}}$ propagators, are elements in the matrix form of the full

single-particle propagator:

$$\boldsymbol{G} = \begin{bmatrix} G_{a\bar{b}} & F_{ab} \\ \bar{F}_{\bar{a}\bar{b}} & \bar{G}_{\bar{a}b} \end{bmatrix}, \qquad \boldsymbol{G}^{(0)} = \begin{bmatrix} G^{(0)}_{a\bar{b}} & 0 \\ 0 & \bar{G}^{(0)}_{\bar{a}b} \end{bmatrix}, \qquad \boldsymbol{\Sigma} = \begin{bmatrix} \Sigma_{a\bar{b}} & \Delta_{ab} \\ \bar{\Delta}_{\bar{a}\bar{b}} & \bar{\Sigma}_{\bar{a}b} \end{bmatrix} \tag{4.37}$$

The bar on propagators or indices $\bar{a}$ represents that is belongs to a hole rather than a particle. The particle-hole self-energy is $\Sigma_{a\bar{b}}$ and the particle-particle self-energy is Δ_{ab}. Writing Eq. (4.36) in terms of the components, the full set of coupled equations are

$$G_{a\bar{b}} = G^{(0)}_{a\bar{b}} + G^{(0)}_{a\bar{c}}\Sigma_{\bar{c}d}G_{d\bar{b}} + G^{(0)}_{a\bar{c}}\bar{\Delta}_{\bar{c}\bar{d}}F_{\bar{d}\bar{b}} \tag{4.38}$$

$$\bar{G}_{\bar{a}b} = \bar{G}^{(0)}_{\bar{a}b} + \bar{G}^{(0)}_{\bar{a}c}\bar{\Sigma}_{c\bar{d}}\bar{G}_{\bar{d}b} + \bar{G}^{(0)}_{\bar{a}c}\Delta_{cd}\bar{F}_{db} \tag{4.39}$$

$$F_{ab} = G^{(0)}_{a\bar{c}}\Sigma_{\bar{c}d}F_{db} + G^{(0)}_{a\bar{c}}\bar{\Delta}_{\bar{c}\bar{d}}\bar{G}_{\bar{d}b} \tag{4.40}$$

$$\bar{F}_{\bar{a}\bar{b}} = \bar{G}^{(0)}_{\bar{a}c}\bar{\Sigma}_{c\bar{d}}\bar{F}_{\bar{d}\bar{b}} + \bar{G}^{(0)}_{\bar{a}c}\Delta_{cd}G_{d\bar{b}} \tag{4.41}$$

Since the interacting Green's function appears on both sides of the equation, Eq. (4.36) can be expanded as

$$\boldsymbol{G} = \boldsymbol{G}^{(0)} + \boldsymbol{G}^{(0)}\boldsymbol{\Sigma}\boldsymbol{G} = \boldsymbol{G}^{(0)} + \boldsymbol{G}^{(0)}\boldsymbol{\Sigma}\boldsymbol{G}^{(0)} + \boldsymbol{G}^{(0)}\boldsymbol{\Sigma}\boldsymbol{G}^{(0)}\boldsymbol{\Sigma}\boldsymbol{G}^{(0)} + \boldsymbol{G}^{(0)}\boldsymbol{\Sigma}\boldsymbol{G}^{(0)}\boldsymbol{\Sigma}\boldsymbol{G}^{(0)}\boldsymbol{\Sigma}\boldsymbol{G}^{(0)} + \ldots \tag{4.42}$$

so that terms up to a certain order can be calculated. A general labeling of Green's functions can be used where $G(1,2)$ represent the propagation from 1 to 2. Each label represents both a point in space and time as well as label for the flavor of fermions $a = (s, \alpha, \sigma)$. The sublattice is s, orbital α, and spin σ.

4.3.2 Two-particle propagator

The two-particle particle-hole (ph) and particle-particle (pp) propagators can be written in terms of single particle propagators as $G^{ph}(12;34) = \beta G(13)G(42)$ and $G^{pp}(12;34) = -\frac{1}{2}\beta G(13)G(24)$. In this general notation an index $1, 2, 3, 4$ contains both time and space indices as well as the label for the fermion, in terms of spin, orbital, and sublatttice. The inverse temperature is $\beta = 1/(k_{\mathrm{B}}T)$ and the factor $1/2$ is included due to indistinguishability.

The two-particle propagators can be Fourier transformed into momentum space, and are then the particle-hole and particle-particle susceptibilities:

$$\chi^{ph}_{abcd}(q) = \frac{\beta}{N}\sum_k G_{ac}(k+q)\bar{G}_{bd}(-k) = -\frac{\beta}{N}\sum_k G_{ac}(k+q)G_{db}(k) \tag{4.43}$$

$$\chi^{pp}_{abcd}(q) = \frac{\beta}{N}\sum_k G_{ac}(k+q)G_{bd}(-k) \tag{4.44}$$

where N is the number of points in momentum space. Here translational invariance has been assumed and the Hamiltonian has the property $\bar{G}_{ab}(k) = -G_{ba}(k)$. The susceptibilities are in general defined for the full system as

$$\hat{\chi}^{ph}_{abcd}(q) = -\frac{1}{N_k^2}\int_0^\beta d\tau e^{i\omega_n\tau}\sum_{\boldsymbol{k}}\langle T_\tau c^\dagger_{a,\boldsymbol{k}}(\tau)c_{b,\boldsymbol{k}+\boldsymbol{q}}(\tau)c^\dagger_{d,-\boldsymbol{k}}(0)c_{c,-\boldsymbol{k}-\boldsymbol{q}}(0)\rangle_c \tag{4.45}$$

$$\hat{\chi}^{pp}_{abcd}(q) = \frac{1}{N_k^2}\int_0^\beta d\tau e^{i\omega_n\tau}\sum_{\boldsymbol{k}}\langle T_\tau c^\dagger_{a,\boldsymbol{k}}(\tau)c_{d,\boldsymbol{k}+\boldsymbol{q}}(\tau)c^\dagger_{b,-\boldsymbol{k}}(0)c_{c,-\boldsymbol{k}-\boldsymbol{q}}(0)\rangle_c \tag{4.46}$$

where $k = (\boldsymbol{k}, i\omega_n)$. The non-interacting susceptibilities are calculated via the non-interaction Green's functions:

$$\chi^{ph}_{0,abcd}(q) = -\frac{\beta}{N}\sum_k G^{(0)}_{ac}(k+q)G^{(0)}_{db}(k), \qquad \chi^{pp}_{0,abcd}(q) = \frac{\beta}{N}\sum_k G^{(0)}_{ac}(k+q)G^{(0)}_{bd}(-k) \tag{4.47}$$

Using the Green's functions in Eq. (4.37) the particle-hole susceptibility becomes the Lindhard function, by summing over all Matsubara frequencies:

$$\begin{aligned}\chi^{ph}_{0,abcd}(q) =& \frac{\beta}{N}\sum_{\boldsymbol{k},n,n'}[U_{\boldsymbol{k}+\boldsymbol{q}}]_{an}\left[U^\dagger_{\boldsymbol{k}+\boldsymbol{q}}\right]_{nc}[U_{\boldsymbol{k}}]_{dn'}\left[U^\dagger_{\boldsymbol{k}}\right]_{n'b}\sum_{\omega_n}\frac{1}{i\omega_n + i\omega_m - \xi_{\boldsymbol{k}+\boldsymbol{q},n}}\frac{1}{-i\omega_n + \xi_{\boldsymbol{k},n}} \\ =& \frac{1}{N}\sum_{\boldsymbol{k},n,n'}[U_{\boldsymbol{k}+\boldsymbol{q}}]_{an}\left[U^\dagger_{\boldsymbol{k}+\boldsymbol{q}}\right]_{nc}[U_{\boldsymbol{k}}]_{dn'}\left[U^\dagger_{\boldsymbol{k}}\right]_{n'b}\frac{f(\xi_{\boldsymbol{k}+\boldsymbol{q},n},T) - f(\xi_{\boldsymbol{k},n'},T)}{i\omega_m - (\xi_{\boldsymbol{k}+\boldsymbol{q},n} - \xi_{\boldsymbol{k},n'})}\end{aligned} \tag{4.48}$$

This means that for each band n the non-interacting susceptibilities have the form

$$\chi^{ph}_{0,n}(q) = -\frac{1}{N}\sum_{\boldsymbol{k}}\frac{f(\xi_{n,\boldsymbol{k}}) - f(\xi_{n,\boldsymbol{k}+\boldsymbol{q}})}{\xi_{n,\boldsymbol{k}} - \xi_{n,\boldsymbol{k}+\boldsymbol{q}} - i\omega_m}, \qquad \chi^{pp}_{0,n}(q) = \frac{1}{N}\sum_{\boldsymbol{k}}\frac{1 - f(\xi_{n,\boldsymbol{k}}) - f(\xi_{n,\boldsymbol{k}+\boldsymbol{q}})}{\xi_{n,\boldsymbol{k}} + \xi_{n,\boldsymbol{k}+\boldsymbol{q}} - i\omega_m} \tag{4.49}$$

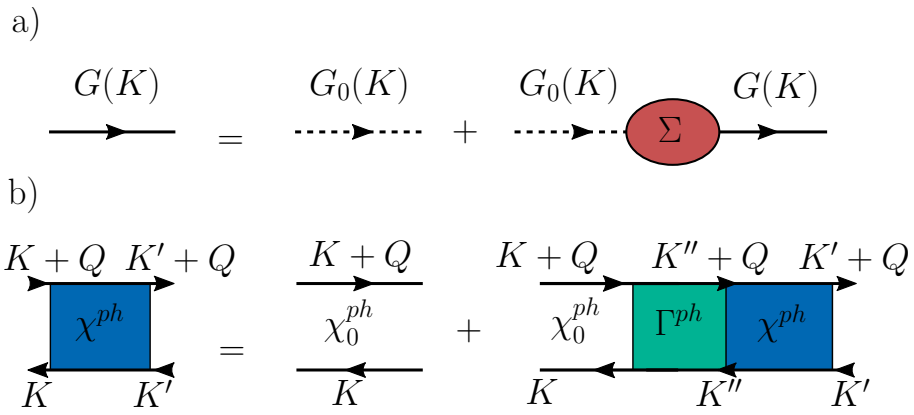

Figure 4.2: The Dyson equation is shown for the one-particle propagator and the Bethe-Salpeter equation for the susceptibility, the two-particle propagators.

where $f(\xi_{n,\boldsymbol{k}})$ is the Fermi-Dirac function, Eq. (4.15). The Bethe-Salpter equation is a similar equation to the Dyson equation and here results in the susceptibility being expanded as

$$\hat{\chi}^{\iota}(q) = \hat{\chi}_0^{\iota}(q) + \hat{\chi}_0^{\iota}(q)\hat{\Gamma}^{\iota}\hat{\chi}^{\iota}(q) = \hat{\chi}_0^{\iota}(q) + \hat{\chi}_0^{\iota}(q)\hat{\Gamma}^{\iota}\hat{\chi}_0^{\iota}(q) + \hat{\chi}_0^{\iota}(q)\hat{\Gamma}^{\iota}\hat{\chi}_0^{\iota}(q)\hat{\Gamma}^{\iota}\hat{\chi}_0^{\iota}(q) + \dots \quad (4.50)$$

where $\iota = ph, pp$. $\hat{\Gamma}^{\iota}$ are the interaction vertices and an approximation of their values gives us the effective interaction we need for our calculations. A diagrammatic version of Eq. (4.50) is shown in Fig. 4.2.

4.3.3 Parquet equations

It is possible to construct a partition function for the full interacting system by introducing the so-called Luttinger-Ward functional [3]. Equations for the self-energies can be constructed by taking functional derivatives of the functional with respect to the propagators [4, 5]. The irreducible vertex is similarly derived from the functional derivative

$$\Gamma^{ph}_{abcd}(33';44') = \frac{\delta\Sigma_{ab}(3;3')}{\delta G_{cd}(4;4')} \quad (4.51)$$

The vertex can also be obtained diagrammatically by removing one internal line from the skeleton self-energy in all possible ways [6]. Using the generalized labels of the propagators

introduced in section 4.3.1 the complete particle-hole vertex can be written as

$$\Gamma = \frac{1}{2}\sum_i \Gamma(12;34)\bar{c}(1)c(2)\bar{c}(4)c(3) \tag{4.52}$$

The $c, \bar{c}$ are Grassmann variables, that ensures the correct commutation relations for the term. This is equivalent to the interaction term in Eq. (4.31). Just by using commutation relations a particle-particle vertex can be defined as $\Gamma(12;34) = -\Gamma_P(14;32)$, such that

$$\Gamma_P = -\frac{1}{2}\sum_i \Gamma_P(12;34)\bar{c}(1)c(4)\bar{c}(2)c(3) \tag{4.53}$$

The complete vertices need to respect crossing symmetry, meaning that an exchange of labels must correspond to the correct expression when also taking into account fermion commutation relations in Eq. (4.52). The irreducible vertices then have the properties

$$\Lambda^{\text{irr}}(12;34) = -\Lambda^{\text{irr}}(42;31) = -\Lambda^{\text{irr}}_P(14;32) \tag{4.54}$$

These are irreducible in both particle-hole and particle-particle channels. In Chapter 6, the Hubbard-Kanamori interactions. Eq. (4.2), will be the bare interactions considered as the irreducible vertices. We can find the parquet equations [7, 8, 6] by rewriting the Bethe-Salpeter equations for the complete vertex such that the crossing symmetry is preserved to get equations for the irreducible vertices in each channel

$$\Gamma^{ph}(12;34) = \Lambda^{\text{irr}}(12;34) - \Gamma(42;56)G^{ph}(56;78)\Gamma^{ph}(78;31) + \Gamma_P(41;56)G^{pp}(56;78)\Gamma^{pp}(78;32) \tag{4.55}$$

$$\Gamma^{pp}(12;34) = -\Lambda^{\text{irr}}(14;32) + \Gamma(24;56)G^{ph}(56;78)\Gamma^{ph}(78;31) - \Gamma(14;56)G^{ph}(56;78)\Gamma^{ph}(78;32). \tag{4.56}$$

where repeated indices are summed over. The equations can be rewritten to not contain the full vertices $\Gamma, \Gamma_{\text{P}}$

$$\Gamma^{ph}(12;34) = \Lambda^{\text{irr}}(12;34) - \Phi(42;31) + \Psi(41;32) \tag{4.57}$$

$$\Gamma^{pp}(12;34) = -\Lambda^{\text{irr}}(14;32) + \Phi(24;31) - \Phi(14;32) \tag{4.58}$$

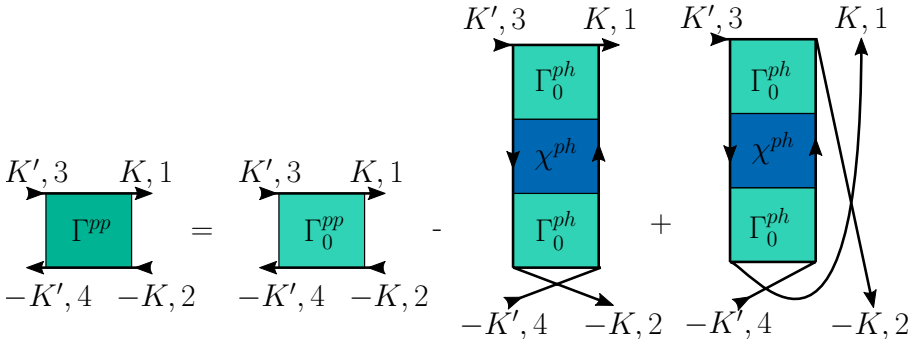

Figure 4.3: The parquet equation for the particle-particle vertex where no momentum is transferred in the pairing. The equation can be written as $\Gamma^{pp}_{K12;K'34}(0) = \Gamma^{pp}_{0,12;34} - \Phi_{24;31}(K - K') + \Phi_{14;32}(K + K')$, as for the pairing.

where we define

$$\begin{aligned} \Phi(12;34) &= [\Gamma^{ph}(1 - G^{ph}\Gamma^{ph})^{-1}G^{ph}\Gamma^{ph}](12;34) \\ \Psi(12;34) &= [\Gamma^{pp}(1 - G^{pp}\Gamma^{pp})^{-1}G^{pp}\Gamma^{pp}](12;34) \end{aligned} \tag{4.59}$$

An approximation of the terms in these equations gives us the effective particle-hole and particle-particle interactions which preserves the crossing symmetry. In Chapters 5 & 6, particle-hole and particle-particle interactions are not treated on equal basis. Parquet theory guarantees self-consistency of both one and two particle propagators. However, they do not always respect thermodynamic conservation laws. Methods aimed to self-consistently evaluate all self-energies and to ensure the preservation of the crossing symmetry of the full vertex, such as FLEX or solving the full parquet equations, are computationally heavy [8]. Therefore, more restricted approximations are used in this thesis to cover a larger parameter space of the phase diagrams.

4.3.4 Approximations

In the Hartree-Fock approximation the only terms that are kept renders the interaction local and instantaneous

$$\Gamma^{abcd}_{pp}(k - k') = -\Gamma^{adcb}_{0}\delta(k - k') \tag{4.60}$$

where again $k = (\boldsymbol{k}, \omega_n)$. In a one-orbital Hubbard model these are just $\Gamma_0^{\uparrow\uparrow\downarrow\downarrow} = U$. The random phase approximation (RPA) instead keeps terms which become a geometric sum:

$$\hat{\chi}^{\iota}(q) = \hat{\chi}_0^{\iota}(q) \left[1 - \hat{\Gamma}^{\iota}\hat{\chi}_0^{\iota}(q)\right]^{-1} \tag{4.61}$$

for $\iota = ph, pp$ and thus the effective pairing interaction, using Eq. (4.58) becomes

$$\Gamma_{pp}^{abcd}(k-k') = -\Gamma_0^{adcb}\delta(k-k') + \left[\Gamma_0\chi(k+k')\Gamma_0\right]^{bdca} - \left[\Gamma_0\chi(k-k')\Gamma_0\right]^{adcb} \tag{4.62}$$

with the $\hat{\chi}(q)$ being the RPA susceptibility. A diagrammatic version of the equation for Γ^{pp} is shown in Fig. 4.3, where the transferred momentum is $Q = 0$. When keeping the labels a general and with no transferred momentum being considered for the pairing, the equation simplifies further:

$$\Gamma_{pp}^{abcd}(k-k') = -\Gamma_0^{adcb}\delta(k-k') - 2\left[\Gamma_0\chi(k-k')\Gamma_0\right]^{adcb} \tag{4.63}$$

This can be seen in Fig. 4.3 by switching the labels $(K, 1)$ and $(-K, 2)$ in the last diagram. In the example below, we will see how the RPA can be used to get an effective interaction that can mediate superconductivity. However, first we can look at what the Hartree-Fock approximation means for instabilities. In general, an instability in the normal state, i.e. the formation of a particle-hole or particle-particle order, can be found via the Bethe-Salpeter equation. Like in the RPA the Bethe-Salpeter equation does in general contain terms that form a ladder sum such that [7]

$$\left[\hat{\Gamma}^{\iota} + \hat{\Gamma}^{\iota}\hat{G}_0^{\iota}\hat{\Gamma}^{\iota} + \dots\right]\hat{G}_0^{\iota}\phi = \left[1 - (\hat{\Gamma}^{\iota}\hat{G}_0^{\iota})\right]^{-1}(\hat{\Gamma}^{\iota}\hat{G}_0^{\iota})\phi \tag{4.64}$$

for $\iota = ph, pp$ and for some wavefunction ϕ. $\hat{G}^{\iota}$ is some two-particle propagator and $\hat{\Gamma}^{\iota}$ is the effective vertex in the channel considered. If this wavefunction is an eigenstate to the operator acting on it, one can analyze the properties of the eigenfunction

$$\lambda\phi = \left[1 - (\hat{\Gamma}^{\iota}\hat{G}_0^{\iota})\right]^{-1}(\hat{\Gamma}^{\iota}\hat{G}_0^{\iota})\phi \tag{4.65}$$

for an eigenvalue λ. As the denominator can be expanded, the same problem is solved by

$$\lambda\phi = (\hat{\Gamma}^{\iota}\hat{G}_0^{\iota})\phi. \tag{4.66}$$

Under the Hartree-Fock approximation, the interaction is instantaneous and local, and a solution to this equation also solves the scalar eigenvalue equation [7]

$$\lambda_q\phi_q = \hat{\chi}_0^{\iota}(q)\hat{\Gamma}^{\iota}_0\phi_q \tag{4.67}$$

with eigenvalue λ_q and a scalar eigenvector ϕ_q which does not depend on any internal momentum. At $\lambda_q = 1$ the normal state must have an instability as the Eq. (4.65) diverges. For a given momentum and frequency point $Q = (\boldsymbol{Q}, i\omega_n)$ if

$$1 = \mathrm{Max}\left[\mathrm{eig}\left[\hat{\chi}_0^{\iota}(Q)\hat{\Gamma}_0^{\iota}\right]\right] \tag{4.68}$$

there must be an instability of the normal state in the channel ι. This is called the Stoner criterion. It is often used to determine if Stoner magnetism is present, as a particle-hole self-energy must be present with a largest value at Q if it is fulfilled. We can also note that if this occurs at a point Q a consequence is that the RPA susceptibility diverges, as there is a point where $\left[1 - \hat{\Gamma}_0^{\iota}\hat{\chi}_0^{\iota}(Q)\right]^{-1} \to 0$.

4.3.5 Example: One-orbital RPA

To illustrate how the random phase approximation can be used to get an effective particle-particle interaction and why an approximation beyond Hartree-Fock is required to get pairing from that interaction, we look at a one-orbital model. For this model there are two degenerate bands of $\sigma = \uparrow, \downarrow$:

$$H_0 = \sum_{\boldsymbol{k},\sigma}(\epsilon_{\boldsymbol{k}} - \mu)c^{\dagger}_{\boldsymbol{k},\sigma}c_{\boldsymbol{k},\sigma} \tag{4.69}$$

The dispersion is set to $\epsilon_{\boldsymbol{k}} = -2t(\cos k_x + \cos k_y)$. The only non-vanishing non-interacting propagators are thus $G^{(0)}_{\uparrow\uparrow}(k) = G^{(0)}_{\downarrow\downarrow}(k) = G^{(0)}(k)$. The only non-vanishing non-interacting susceptibilities are then $\chi_0(q) = \chi^{ph}_{0,\sigma\sigma'\sigma\sigma'}(q)$. The interactions are the one-orbital Hubbard

interaction in Eq. (4.8) that has been Fourier transformed as

$$H_{\text{int}} = \frac{1}{2N} \sum_{\boldsymbol{k},\sigma,\sigma'} U c^\dagger_{\boldsymbol{k},\sigma} c_{-\boldsymbol{k},\sigma} c^\dagger_{-\boldsymbol{k},\sigma'} c_{\boldsymbol{k},\sigma'} \tag{4.70}$$

The susceptibility and interactions can be written on matrix form in the basis $(\uparrow\uparrow, \uparrow\downarrow, \downarrow\uparrow, \downarrow\downarrow)$. $\hat{\chi}_0(q)$ and the bare interactions $\hat{\Gamma}_0^{ph}$ are then the 4×4 matrices

$$\hat{\chi}_0(q) = \begin{pmatrix} \chi_0(q) & 0 & 0 & 0 \\ 0 & \chi_0(q) & 0 & 0 \\ 0 & 0 & \chi_0(q) & 0 \\ 0 & 0 & 0 & \chi_0(q) \end{pmatrix}, \qquad \hat{\Gamma}_0^{ph} = \begin{pmatrix} 0 & 0 & 0 & U \\ 0 & -U & 0 & 0 \\ 0 & 0 & -U & 0 \\ U & 0 & 0 & 0 \end{pmatrix} \tag{4.71}$$

such that $\Gamma^{ph}_{0,\uparrow\downarrow\uparrow\downarrow} = -U$ and $\Gamma^{ph}_{0,\uparrow\uparrow\downarrow\downarrow} = U$. There are only diagonal terms in the susceptibility matrix as the terms in Eq. (4.69) are diagonal in spin. With RPA this gives us, with spin components written out for clarity

$$\hat{\chi}(q) = \begin{pmatrix} \frac{\chi_0^{\uparrow\uparrow\uparrow\uparrow}}{1-\chi_0^{\uparrow\uparrow\uparrow\uparrow}\chi_0^{\downarrow\downarrow\downarrow\downarrow}U^2} & 0 & 0 & \frac{\chi_0^{\uparrow\uparrow\uparrow\uparrow}\chi_0^{\downarrow\downarrow\downarrow\downarrow}U}{\chi_0^{\uparrow\uparrow\uparrow\uparrow}\chi_0^{\downarrow\downarrow\downarrow\downarrow}U^2-1} \\ 0 & \frac{\chi_0^{\uparrow\downarrow\uparrow\downarrow}}{1-\chi_0^{\uparrow\downarrow\uparrow\downarrow}U} & 0 & 0 \\ 0 & 0 & \frac{\chi_0^{\downarrow\uparrow\downarrow\uparrow}}{1-\chi_0^{\downarrow\uparrow\downarrow\uparrow}U} & 0 \\ \frac{\chi_0^{\uparrow\uparrow\uparrow\uparrow}\chi_0^{\downarrow\downarrow\downarrow\downarrow}U}{\chi_0^{\uparrow\uparrow\uparrow\uparrow}\chi_0^{\downarrow\downarrow\downarrow\downarrow}U^2-1} & 0 & 0 & \frac{\chi_0^{\downarrow\downarrow\downarrow\downarrow}}{1-\chi_0^{\uparrow\uparrow\uparrow\uparrow}\chi_0^{\downarrow\downarrow\downarrow\downarrow}U^2} \end{pmatrix} \tag{4.72}$$

The effective pairing interaction is then

$$\hat{\Gamma}_{pp}(q) = \begin{pmatrix} \frac{\chi_0 U^2}{1-\chi_0^2 U^2} & 0 & 0 & 0 \\ 0 & \frac{U(\chi_0 U+1)}{2-2\chi_0 U} & -\frac{U(\chi_0^2 U^2+1)}{2-2\chi_0^2 U^2} & 0 \\ 0 & -\frac{U(\chi_0^2 U^2+1)}{2-2\chi_0^2 U^2} & \frac{U(\chi_0 U+1)}{2-2\chi_0 U} & 0 \\ 0 & 0 & 0 & \frac{\chi_0 U^2}{1-\chi_0^2 U^2} \end{pmatrix} \tag{4.73}$$

The effective pairing interaction can be spin-diagonalized and divided up into terms for spin-singlet and spin-triplet pairing

$$\Gamma_t^{s_z=+1} = \Gamma_t^{s_z=-1} = \Gamma_{P,\uparrow\uparrow\uparrow\uparrow} = \Gamma_{P,\downarrow\downarrow\downarrow\downarrow} \tag{4.74}$$

$$\Gamma_s = \Gamma_{pp,\uparrow\downarrow\uparrow\downarrow} - \Gamma_{pp,\uparrow\downarrow\downarrow\uparrow}, \qquad \Gamma_t^{s_z=0} = \Gamma_{P,\uparrow\downarrow\uparrow\downarrow} + \Gamma_{pp,\uparrow\downarrow\downarrow\uparrow} \tag{4.75}$$

So, for the one band case

$$\Gamma_s(q) = \frac{1}{1-\chi_0(q)U}\left(U\chi_0(q)U + \frac{U}{1+\chi_0(q)U}\right), \qquad \Gamma_t(q) = \frac{1}{1-\chi_0(q)U}\left(U - \frac{U}{1+\chi_0(q)U}\right) \tag{4.76}$$

where in the limit $\chi_0 = 0$ we get $\Gamma_s = U$ and $\Gamma_t = 0$. This limit is equivalent to the Hartree-Fock approximation. When $\chi_0 > 0$ and $U > 1$ the intraband singlet term is much larger than the triplet $\Gamma_s \gg \Gamma_t$. From here we can see that for the Hartree-Fock approximation in Eq. (4.67):

$$\lambda_q = \Gamma_{pp}(q)\chi_0^{pp}(q) = \frac{U}{N}\sum_{\boldsymbol{k}} \frac{1 - f(\xi_{n,\boldsymbol{k}}) - f(\xi_{n,\boldsymbol{k}+\boldsymbol{q}})}{\xi_{\boldsymbol{k}} + \xi_{\boldsymbol{k}+\boldsymbol{q}} - i\omega_m} \tag{4.77}$$

If we consider a static approximation $\omega_m \to 0$ and, for example, that $\boldsymbol{q} \approx (\pi, \pi)$ then it is only possible to have $\lambda_q < 1$. Thus, no particle-particle instability is found under this approximation. We must therefore use an effective interaction that has a momentum dependence to be able to get instabilities in the superconducting channels, like the one given by the RPA. For large peaks in the susceptibility, those spin-fluctuations can modify the effective interaction so that it also has large peaks at some momenta.

4.4 Eliashberg equation

Eliashberg theory describes superconductivity in a system with electrons and phonons. In a weak coupling limit where the vertex corrections are assumed to be small, a set of coupled self-consistency equations can be set up, following the same Green's function method as in the previous section. The self-energy can under these conditions be assumed to be on the matrix form

$$\boldsymbol{\Sigma}_\sigma(\boldsymbol{k}, i\omega_n) = i\omega_n\left[1 - Z(\boldsymbol{k}, i\omega_n)\right]\hat{\tau}_0 + \xi(\boldsymbol{k}, i\omega_n)\hat{\tau}_3 + \phi_\sigma(\boldsymbol{k}, i\omega_n)\hat{\tau}_1 \tag{4.78}$$

where $\hat{\tau}_i$, $i = 0, 1, 2, 3$ are Pauli matrices in particle and hole space. The parameters Z and ξ are formed from the particle-hole self-energy as the odd and even components with frequency: $i\omega_n\left[1 - Z(\boldsymbol{k}, i\omega_n)\right] \propto (\Sigma(\boldsymbol{k}, i\omega_n) - \Sigma(\boldsymbol{k}, -i\omega_n))$ and $\xi(\boldsymbol{k}, i\omega_n) \propto (\Sigma(\boldsymbol{k}, i\omega_n) + \Sigma(\boldsymbol{k}, -i\omega_n))$. A

general solution [9] to the Dyson equation Eq. (4.36) is

$$\boldsymbol{G}_\sigma(\boldsymbol{k}, i\omega_n) = \frac{i\omega_n Z(\boldsymbol{k}, i\omega_n)\hat{\tau}_0 + (\epsilon(\boldsymbol{k}) + \xi(\boldsymbol{k}, i\omega_n))\hat{\tau}_3 + \phi_\sigma(\boldsymbol{k}, i\omega_n)\hat{\tau}_1}{(i\omega_n Z(\boldsymbol{k}, i\omega_n))^2 - (\epsilon(\boldsymbol{k}) + \xi(\boldsymbol{k}, i\omega_n))^2 - (\phi_\sigma(\boldsymbol{k}, i\omega_n))^2} \tag{4.79}$$

where the poles of the Green's function occur at

$$E_{\boldsymbol{k}} = \pm\sqrt{\left(\frac{\epsilon(\boldsymbol{k}) + \xi(\boldsymbol{k}, i\omega_n))}{Z(\boldsymbol{k}, i\omega_n)}\right)^2 + \frac{(\phi_\sigma(\boldsymbol{k}, i\omega_n))^2}{(Z(\boldsymbol{k}, i\omega_n))^2}} \tag{4.80}$$

In the band basis n, the solution for the self-energies becomes the following set of self-consistent equations

$$Z_n(\boldsymbol{k}, i\omega_m) = 1 + \frac{T}{\omega_m}\sum_{\boldsymbol{k}', m', n'} V^{(+)}_{nn'}(\boldsymbol{q}, iq_{m-m'})\frac{\omega_{m'} Z_{n'}(\boldsymbol{k}', i\omega_{m'})}{\Theta_{n'}(\boldsymbol{k}', i\omega_{m'})} \tag{4.81}$$

$$\xi_n(\boldsymbol{k}, i\omega_m) = -T\sum_{\boldsymbol{k}', m', n'} V^{(+)}_{nn'}(\boldsymbol{q}, iq_{m-m'})\frac{\epsilon_{\boldsymbol{k}'n'} + \xi_{n'}(\boldsymbol{k}', i\omega_{m'})}{\Theta_{n'}(\boldsymbol{k}', i\omega_{m'})} \tag{4.82}$$

$$\phi_n(\boldsymbol{k}, i\omega_m) = -T\sum_{\boldsymbol{k}', m', n'} V^{(-)}_{nn'}(\boldsymbol{q}, iq_{m-m'})\frac{\phi_{n'}(\boldsymbol{k}', i\omega_{m'})}{\Theta_{n'}(\boldsymbol{k}', i\omega_{m'})} \tag{4.83}$$

$$\Theta_n(\boldsymbol{k}, i\omega_m) = \omega_m^2 Z_n^2(\boldsymbol{k}, i\omega_m) + [\epsilon_{\boldsymbol{k}n} + \xi_n(\boldsymbol{k}, i\omega_m)]^2 + \phi_n^2(\boldsymbol{k}, i\omega_m) \tag{4.84}$$

and the gap function is $\Delta_n(\boldsymbol{k}, i\omega_m) = \phi_n(\boldsymbol{k}, i\omega_m)/Z_n(\boldsymbol{k}, i\omega_m)$. Here the effective interactions are given the different notation $V^{(\pm)}_{nn'}(\boldsymbol{q}, iq_{m-m'})$ with $+$ for particle-hole and $-$ for particle-particle. In Eliashberg theory these are not just electron-electron interactions and depends on phonon coupling. These equations should also be supplemented by the electron number equation to determine the chemical potential μ:

$$n_e = 1 - \frac{2}{N\beta}\sum_{\boldsymbol{k}', m', n'} \frac{\epsilon_{\boldsymbol{k}'n'} + \xi_{n'}(\boldsymbol{k}', i\omega_{m'})}{\Theta_{n'}(\boldsymbol{k}', i\omega_{m'})}. \tag{4.85}$$

4.4.1 Connection to BCS

In the BCS limit one sets $Z(\boldsymbol{k}, i\omega_n) = 1$, so that $\phi_n(\boldsymbol{k}, i\omega_m) = \Delta_n(\boldsymbol{k}, i\omega_m)$, and $\xi(\boldsymbol{k}, i\omega_n) = 0$ since we are only considering superconductivity. The poles of the Green's function then

occur at

$$E_{\boldsymbol{k}} = \sqrt{\epsilon(\boldsymbol{k})^2 + (\Delta_n(\boldsymbol{k}, i\omega_m))^2} \tag{4.86}$$

and the self-consistency equation for the pairing order parameter $\phi_n(\boldsymbol{k}, i\omega_m)$ becomes

$$\begin{aligned}\Delta_n(\boldsymbol{k}, i\omega_m) = -T \sum_{\boldsymbol{k}',m',n'} V^{(-)}_{nn'}(\boldsymbol{q}, iq_{m-m'}) \frac{\Delta_{n'}(\boldsymbol{k}', i\omega_{m'})}{(i\omega_{m'}) - \sqrt{(\epsilon(\boldsymbol{k}))^2 + (\Delta_{n-}(\boldsymbol{k}, i\omega_{m'}))^2}} \\ \times \frac{1}{(i\omega_{m'}) + \sqrt{(\epsilon(\boldsymbol{k}))^2 + (\Delta_{n'}(\boldsymbol{k}, i\omega_{m'}))^2}}\end{aligned} \tag{4.87}$$

A static approximation of the pairing and the interactions gets rid of the frequency dependence as $V^{(-)}_{nn'}(\boldsymbol{q}, iq_{m-m'}) \to V^{(-)}_{nn'}(\boldsymbol{q})$ and $\Delta_n(\boldsymbol{k}, i\omega_m) \to \Delta_n(\boldsymbol{k})$. For one band the gap equation becomes

$$\begin{aligned}\Delta(\boldsymbol{k}, i\delta \to 0) = -T \sum_{\boldsymbol{k}'} V^{(-)}(\boldsymbol{q}) \sum_{\omega_{m'}} \frac{\Delta(\boldsymbol{k}')}{(i\omega_{m'} + i\delta) - \sqrt{(\epsilon(\boldsymbol{k}))^2 + (\Delta(\boldsymbol{k}))^2}} \\ \times \frac{1}{(i\omega_{m'}) + \sqrt{(\epsilon(\boldsymbol{k}))^2 + (\Delta(\boldsymbol{k}))^2}}\end{aligned} \tag{4.88}$$

$$\Delta(\boldsymbol{k}, i\delta \to 0) = -T \sum_{\boldsymbol{k}'} V^{(-)}(\boldsymbol{q}) \sum_{\omega_{m'}} \frac{\Delta_(\boldsymbol{k}')}{(i\omega_{m'} + i\delta) - E(\boldsymbol{k})} \frac{1}{(i\omega_{m'}) + E(\boldsymbol{k})} \tag{4.89}$$

$$\Delta(\boldsymbol{k}) = -\sum_{\boldsymbol{k}'} V^{(-)}(\boldsymbol{q}) \Delta(\boldsymbol{k}') \frac{f(E(\boldsymbol{k}')) - f(-E(\boldsymbol{k}'))}{i\delta - 2E(\boldsymbol{k}')} \tag{4.90}$$

Using that the Fermi-Dirac function can be written as $f(E_{n'}(\boldsymbol{k}')) - f(-E_{n'}(\boldsymbol{k}')) = \tanh\left(\frac{E_{n'}(\boldsymbol{k}')}{2Tk_{\mathrm{B}}}\right)$:

$$\Delta(\boldsymbol{k}) = -\sum_{\boldsymbol{k}'} V^{(-)}(\boldsymbol{k} - \boldsymbol{k}') \frac{\Delta(\boldsymbol{k}')}{2E(\boldsymbol{k}')} \tanh\left(\frac{E(\boldsymbol{k}')}{2Tk_{\mathrm{B}}}\right) \tag{4.91}$$

We can identify this as the BCS equation Eq. (4.30). The connection to the mean field calculation can also be seen here as with the Hartree-Fock approximation $V^{(+)} = U$. With the same other approximations the particle-hole self-energy in Eq. (4.82) becomes a mean field self-consistency equation.

We can now go back to the one-orbital model in section 4.3.5. From here we can observe that if the effective interaction is the RPA singlet interaction in Eq. (4.76), where we take

the static approximation $V^{(-)}(\boldsymbol{k}-\boldsymbol{k}') = \Gamma_s(\boldsymbol{q}, \omega_n \to 0)/N$ with $\boldsymbol{q} = \boldsymbol{k}-\boldsymbol{k}'$:

$$\Delta(\boldsymbol{k}) = -\frac{1}{N}\sum_{\boldsymbol{k}'} \frac{1}{1-\chi_0(\boldsymbol{q})U}\left(U\chi_0(\boldsymbol{q})U + \frac{U}{1+\chi_0(\boldsymbol{q})U}\right)\frac{\Delta(\boldsymbol{k}')}{2E(\boldsymbol{k}')}\tanh\left(\frac{E(\boldsymbol{k}')}{2Tk_{\mathrm{B}}}\right). \tag{4.92}$$

We can see that this equation can allow for some momentum dependent pairings. For example if the effective interaction peaks around the specific point $\Gamma_s(\boldsymbol{q}) \propto \delta(\boldsymbol{q} = (\pi,\pi))$ and the pairing has a d-wave symmetry $\Delta(\boldsymbol{k}) = \Delta(\cos k_x - \cos k_y)$, then Eq. (4.92) becomes:

$$\begin{aligned}\Delta(\cos k_x - \cos k_y) \propto & -\frac{\Delta(\cos(k_x+\pi) - \cos(k_y+\pi))}{2E(\boldsymbol{k}+(\pi,\pi))}\tanh\left(\frac{E(\boldsymbol{k}+(\pi,\pi))}{2Tk_{\mathrm{B}}}\right)\\ =&\frac{\Delta(\cos k_x - \cos k_y)}{2E(\boldsymbol{k})}\tanh\left(\frac{E(\boldsymbol{k})}{2Tk_{\mathrm{B}}}\right)\end{aligned} \tag{4.93}$$

and since the positive $E_{\boldsymbol{k}} > 0$ is included in this calculation, we can fulfill the self-consistency equation $\Delta(\cos k_x - \cos k_y) \propto \Delta(\cos k_x - \cos k_y)$.

4.4.2 Multi-orbital case

If we only consider superconductivity, without any magnetic order, we can see how we get the Eliashberg equation as the self-consistency from the Dyson equation. One can linearize the matrix version of the Dyson-Gorkov equation, Eq. (6.9), by first rewriting the anomalous Green's function F by substituting in the expression for $\bar{G}$ as follows:

$$\begin{aligned}F = \left(G_0^{-1} - \Sigma\right)^{-1}\Delta\bar{G}, \qquad \bar{G} = \left(\bar{G}_0^{-1} - \Sigma\right)^{-1} + \Delta\bar{F}\\ F = \left(G_0^{-1} - \Sigma\right)^{-1}\Delta\left(\bar{G}_0^{-1} - \bar{\Sigma}\right)^{-1} + \mathcal{O}(\Delta^2)\end{aligned} \tag{4.94}$$

If only the terms linear in Δ are kept, we can also see that $\bar{\Delta}F \propto \mathcal{O}(\Delta^2)$, and we explicitly write the generalized coordinates Eq. (4.37) becomes

$$G(k)(12) = \left(G_0^{-1} - \Sigma\right)^{-1}(1,2), \qquad F(k)(12) = G(k)(13)\Delta(k)(34)\bar{G}(k)(42) \tag{4.95}$$

The solution to the particle-particle self-energy is can, similarly to the definition of the vertex, be derived for the Luttinger-Ward functional as [4, 5]:

$$\Delta(k)(12) = \sum_{k'} \Gamma_{pp}(k-k')(12,34)F(k')(34) \tag{4.96}$$

with the interaction $\Gamma_{pp}^{abcd}(\boldsymbol{k})$ as given in Eq. (4.58). If $Z(\boldsymbol{k}, i\omega_n) = 1$, this is equivalent to a linearized Eq. (4.83):

$$\Delta_{ab}(\boldsymbol{k}, i\omega_m) = \frac{1}{\beta N} \sum_{\boldsymbol{k}', \omega_{m'}} \sum_{a'b', \mu\nu} \Gamma_{pp,aa'b'b}(\boldsymbol{k}-\boldsymbol{k}', i\omega_{m'}) G_{a'\mu}(\boldsymbol{k}', i\omega_{m'}) \bar{G}_{\nu b'}(\boldsymbol{k}', i\omega_{m'}) \Delta_{\mu\nu}(\boldsymbol{k}', i\omega_{m'}) \tag{4.97}$$

As the effective interaction is a rank 4 tensor it scales with the number of species of fermions as $\sim N_f^4$. It also scales with the total number of lattice points $N = N_k^2$. Any numerical computation of the self-consistency equations therefore quickly becomes intensive, even for smaller lattice sizes in multi-orbital systems. One approximation that reduces the complexity of the computation is to calculate the gap equation in the normal state. This is accomplished by making the approximation of setting the Green's function as the non-interacting value $G_{ab}(k) \approx G_{ab}^{(0)}(k)$.

$$\Delta_{ab}(k) = \frac{1}{\beta N} \sum_{\boldsymbol{k}', \omega_{m'}} \sum_{a'b', \mu\nu} \Gamma_{pp,aa'b'b}(k-k') G_{a'\mu}^{(0)}(k') \bar{G}_{\nu b'}^{(0)}(k') \Delta_{\mu\nu}(k') \tag{4.98}$$

The equation can be solved as an eigenvalue problem and solved by finding the eigenvalue λ_e of the linearized gap equation:

$$\lambda_e \Delta_{ab}(k) = \frac{1}{\beta N} \sum_{\boldsymbol{k}', \omega_{m'}} \sum_{a'b', \mu\nu} \Gamma_{pp,aa'b'b}(k-k') G_{a'\mu}^{(0)}(k') \bar{G}_{\nu b'}^{(0)}(k') \Delta_{\mu\nu}(k') \tag{4.99}$$

At a given temperature T, finding $\lambda_e \geq 1$, means that $\Delta_{ab}(\boldsymbol{k}, i\omega_m) \neq 0$ and superconductivity is present. The critical temperature is found as when $\lambda_e(T_c) = 1$ and the size of the eigenvalue therefor carries information about how far a found eigenstate is from the transition. In Chapter 6 the linearized gap equation will be considered in both the static limit and in the normal state. It should be noted that in this limit the lack of frequency dependence or

phonon contributions means that the equation does not capture Eliashberg physics. Rather the equation is a multi-band BCS-like equation.

4.4.3 Multigap superconductivity

Generally, there aren't multiple gaps in conventional superconductors, since the large coherence length leads to averaging due to the interband scattering [10]. However, if there are multiple pockets at the Fermi surface in an unconventional superconductor there can be multiple gaps. The size of the gaps on two FS depends on intraband coupling $\lambda_{11}, \lambda_{22}$ and interband coupling $\lambda_{12}, \lambda_{21}$ [10, 11]. The two gaps have the same critical temperature T_c and their coexistence can raise it. In BCS the effective coupling determines the critical temperature as:

$$T_c = 1.14\tilde{\Omega}e^{-1/\tilde{\lambda}}, \qquad \tilde{\lambda} = \frac{1}{2}\left[\lambda_{11} + \lambda_{22} + \sqrt{(\lambda_{22} - \lambda_{11})^2 + 4\lambda_{12}\lambda_{21}}\right] \tag{4.100}$$

From here it can be shown that one of the gaps always exceeds the BCS value, while the other is smaller than it. Since the usual BCS relation between T_c and the $T = 0$ gap is derived only for a single pairing function, the usual BCS relation for the size of the gap does not hold. In the special case $\lambda_{22} = 0$ superconductivity is still induced in the second band from interband transitions [12] since then $\tilde{\lambda} = \frac{1}{2}[\lambda_1 + 2\lambda_{12}]$. It is thus expected that in a superconducting phase all pockets have some superconducting gap function. The interband coupling is often mediated by phonons [10]. Other studies however show that the induced gap is inversely proportional to the mass enhancement on a FS [13]. The most direct probe of a multigap state is local density of states measurements, where it is possible for two gaps to have different symmetries [14, 15].

4.4.4 Temperature and lattice size

Any numerical solution to the self-consistency equations requires a finite size of the momentum grid and a finite temperature. The temperature dependence enters in the regular way via the Green's functions, as they are given for a specific Matsubara frequency $\omega_n = (1 + 2n)\pi/\beta$. The resolution is thus determined by the sampling of frequencies, where

a lower temperature requires a higher number. Other studies of multi-orbital compounds study the frequency dependence and are therefore performed at higher temperatures [16, 17, 18]. In this thesis a static approximation, $\omega_n \to 0$, is ultimately considered for the linearized gap equation. We also don't include phonon mediated interactions $g(\omega)$, only electron-electron interactions. All frequency, and consequently temperature, dependence is therefore confined to calculations of the two-particle propagators. As a result, setting the number of Matsubara frequencies to infinity and using the identity in the Lindhard function, Eq. (4.48), is possible. The limit to temperature and lattice size considered with these approximations will depend on the features in momentum space. In a grid of $\boldsymbol{k}$-points, the distance between points must be smaller than the thermal broadening of peaks in the susceptibility. In a multi-orbital model the susceptibility is a large tensor of size $N_s^2 \times N_o^2 \times N_\sigma^2 \times N_k^2$. The lattice size and temperatures must be chosen such that they ensure convergence with increasing lattice size of positions and height of peaks, for all susceptibility channels.

4.4.5 Structure factors

The magnetic susceptibilities, in Eq. 4.45, will depend on the self-energies of the system. The fluctuation-dissipation theorem [19], relates the scattering intensity to the dynamical magnetic susceptibility $\hat{\chi}(\boldsymbol{q}, i\omega_m)$ as:

$$S_{ab}(\boldsymbol{q}, \omega_m) = 2\hbar(1 + f_{\mathrm{B}}(\omega))\mathrm{Im}\left[\chi_{ab}(\boldsymbol{q}, i\omega_m)\right] \tag{4.101}$$

where the factor 1 comes from the quantum part and the thermal part is the Bose-Einstein distribution $f_{\mathrm{B}}(\omega)$ [20]. The dynamical structure factor is a useful quantity since it can be directly compared to neutron scattering data. The static structure factor is in general

$$S^x(\boldsymbol{q}) = \int_{-\infty}^{\infty} d\omega S^x(q, \omega) \tag{4.102}$$

where $x = z, \pm, c$ is the channel. So it can be written as [21]:

$$S^x(\boldsymbol{q}) = \int_{-\infty}^{\infty} \frac{d\omega}{\pi} \frac{\mathrm{Im}\left[\chi^x(q,\omega)\right]}{1 - e^{-\omega\hbar\beta}} \tag{4.103}$$

The static susceptibility can the other way around be given as

$$\int_0^{\infty} d\omega S^x_{ab}(\boldsymbol{q},\omega) = 3k_{\mathrm{B}}T\chi^x_{ab}(\boldsymbol{q},T) \tag{4.104}$$

in the high temperature limit [22]. Then the static structure factor and susceptibility are proportional $S_{ab}(\boldsymbol{q}) \propto \chi_{ab}(\boldsymbol{q})$. If spin-fluctuation mediated superconductivity is possible in system, there will be large peaks in the dynamical and static susceptibility at given momenta $\boldsymbol{Q}$. It is directly the effective pairing interaction which determines in which channels and at what momenta connection points at the Fermi surface that pairing is favored. However, as the structure factors can provide direct information about susceptibility peaks it is useful to connect superconducting orders to which type of spin-fluctuations that can mediate them. This information can provide experimental signatures for when a compound in the normal state is close to a superconducting instability. In Chapter 6 spin-fluctuation mediated superconductivity is studied and the evolution of peaks in the static spin susceptibility is calculated. There the information given by the susceptibility calculations is discussed further.

Bibliography

[1] J. Kanamori, "Electron correlation and ferromagnetism of transition metals," *Progress of Theoretical Physics*, vol. 30, pp. 275–289, sep 1963.

[2] A. Georges, L. de' Medici, and J. Mravlje, "Strong Correlations from Hund's Coupling," *Annual Review of Condensed Matter Physics*, vol. 4, pp. 137–178, apr 2013.

[3] J. M. Luttinger and J. C. Ward, "Ground-State Energy of a Many-Fermion System. II," *Phys. Rev.*, vol. 118, pp. 1417–1427, Jun 1960.

[4] G. Baym and L. P. Kadanoff, "Conservation Laws and Correlation Functions," *Physical Review*, vol. 124, pp. 287–299, oct 1961.

[5] G. Baym, "Self-Consistent Approximations in Many-Body Systems," *Physical Review*, vol. 127, pp. 1391–1401, aug 1962.

[6] N. E. Bickers, *Self-Consistent Many-Body Theory for Condensed Matter Systems*, pp. 237–296. New York, NY: Springer New York, 2004.

[7] N. E. Bickers and D. J. Scalapino, "Conserving approximations for strongly fluctuating electron systems. I. Formalism and calculational approach," *Annals of Physics*, vol. 193, no. 1, pp. 206–251, 1989.

[8] N. E. Bickers and S. R. White, "Conserving approximations for strongly fluctuating electron systems. II. Numerical results and parquet extension," *Physical Review B*, vol. 43, no. 10, pp. 8044–8064, 1991.

[9] F. Marsiglio, "Eliashberg theory: A short review," *Annals of Physics*, vol. 417, p. 168102, 2020. Eliashberg theory at 60: Strong-coupling superconductivity and beyond.

[10] V. Z. Kresin, H. Morawitz, and S. A. Wolf, "Multigap superconductivity," in *Superconducting State*, pp. 103–113, Oxford University Press, dec 2013.

[11] R. M. Fernandes, J. T. Haraldsen, P. Wölfle, and A. V. Balatsky, "Two-band superconductivity in doped $SrTiO_3$ films and interfaces," *Phys. Rev. B*, vol. 87, p. 014510, Jan 2013.

[12] M. E. Zhitomirsky and T. M. Rice, "Interband Proximity Effect and Nodes of Superconducting Gap in Sr_2RuO_4," *Phys. Rev. Lett.*, vol. 87, p. 057001, Jul 2001.

[13] L. P. Gor'kov, "Quantum oscillations in the vortex state of underdoped $YBa_2Cu_3O_{6.5}$ and other multiband superconductors," *Phys. Rev. B*, vol. 86, p. 060501, Aug 2012.

[14] K. Cho, A. Fente, S. Teknowijoyo, M. A. Tanatar, K. R. Joshi, N. M. Nusran, T. Kong, W. R. Meier, U. Kaluarachchi, I. Guillamón, H. Suderow, S. L. Bud'Ko, P. C. Canfield, and R. Prozorov, "Nodeless multiband superconductivity in stoichiometric single-crystalline $CaKFe_4As_4$," *Physical Review B*, vol. 95, no. 10, pp. 1–5, 2017.

[15] F. K. K. Kirschner, D. T. Adroja, Z.-C. Wang, F. Lang, M. Smidman, P. J. Baker, G.-H. Cao, and S. J. Blundell, "Two-gap superconductivity with line nodes in $\mathbf{CsCa_2Fe_4As_4F_2}$," *Phys. Rev. B*, vol. 97, p. 060506, Feb 2018.

[16] X. Wang, H. Li, Y. Huang, Z. Dong, C. Zhong, and J. Liu, "Tuning tetrahedral structure and electronic properties of FeSe films through strain engineering," *Journal of Physics and Chemistry of Solids*, vol. 145, no. May, p. 109541, 2020.

[17] F. Schrodi, A. Aperis, and P. M. Oppeneer, "Eliashberg theory for spin-fluctuations mediated superconductivity - Application to bulk and monolayer FeSe," *Physical Review B*, vol. 102, apr 2020.

[18] S. Käser, H. U. Strand, N. Wentzell, A. Georges, O. Parcollet, and P. Hansmann, "Interorbital singlet pairing in Sr_2RuO_4: A Hund's superconductor," *Physical Review B*, vol. 105, no. 15, 2022.

[19] R. Kubo, "The fluctuation-dissipation theorem," *Reports on Progress in Physics*, vol. 29, pp. 255–284, jan 1966.

[20] P. Coleman, *Fluctuation–dissipation theorem and linear response theory*, p. 292–331. Cambridge University Press, 2015.

[21] K. Sturm, "Dynamic Structure Factor: An Introduction," *Zeitschrift für Naturforschung A*, vol. 48, pp. 233–242, feb 1993.

[22] J. Staunton, B. L. Gyorffy, G. M. Stocks, and J. Wadsworth, "The static, paramagnetic, spin susceptibility of metals at finite temperatures," *Journal of Physics F: Metal Physics*, vol. 16, no. 11, pp. 1761–1788, 1986.

Preface to Chapter 5

There are two motivations for modeling Sr_2IrO_4 under epitaxial strain. Firstly, the experiments introduced in section 2.3 found the compound to have a magnetic order which is exceptionally sensitive to the strain. Secondly, the multi-orbital model of Sr_2IrO_4 is affected by strain in such a way that the properties of the orbitals change in different amounts, as introduced in section 3.2. Undoped and unstrained Sr_2IrO_4 is a spin-orbit coupled antiferromagnetic insulator. To understand a transition out of this order, and potentially into a superconducting one, changes to the order can be studied for both strain and doping. In the following publication, chapter 5, undoped Sr_2IrO_4 is modeled under compressive epitaxial strain and with an external magnetic field.

To better understand the order in the multiple spin-orbit coupled orbitals and how it changes, the mean field model introduced in section 4.2 is used to study all on-site order parameters. In total 42 complex order parameters are considered, which include both staggered and uniform orders. Of particular interest is how well the $j = 1/2$ states describe the magnetic order, if the contributions originating from each of the d_{yz}, d_{xz}, d_{xy} orbitals changes, and what states are present at the Fermi surface once there is one. An effective model for the $j = 1/2$ can capture much of the physics determining the magnetic order for undoped Sr_2IrO_4 and such a model predicts superconductivity. Understanding the validity of that model as strain is increased is thus crucial for determining how the strained compound should be modeled. Studying the magnetic order of the undoped compound is a first step towards determining if there is any regime where superconductivity can be favored. For the overarching goal of modeling superconductivity in the system we need to determine when the bandstructure can be favorable for superconductivity and when it can be favorable for a magnetic order. A model with many parameters would be required to

fully capture the effects of the competition between magnetism and superconductivity. The approach here is therefore to determine which parameters are needed to describe the strained system, so that appropriate approximations can be made when calculating a full phase diagram.

The magnetic field considered in this chapter gives us the opportunity to probe possible signatures of the multi-orbital physics. As the undoped compound under compressive epitaxial strain has been studied experimentally, such signatures give us information about the validity of how the strain is modeled and how the interactions are treated.

Chapter 5

Modeling multiorbital effects in Sr_2IrO_4 under strain and a Zeeman field

Lena Engström, T. Pereg-Barnea, and William Witczak-Krempa

Reprinted article with permission from L. Engström, T. Pereg-Barnea, and W. Witczak-Krempa Phys. Rev. B 103, 155147 (2021). A preprint is available as arXiv:2012.08583.

Abstract

We present a comprehensive study of a three-orbital lattice model suitable for the layered iridate Sr_2IrO_4. Our analysis includes various on-site interactions (including Hubbard and Hund's) as well as compressive strain, and a Zeeman magnetic field. We use a self-consistent mean field approach with multiple order parameters to characterize the resulting phases. While in some parameter regimes the compound is well described by an effective $J = 1/2$ model, in other regimes the full multiorbital description is needed. As a function of the compressive strain, we uncover two quantum phase transitions: first a continuous metal-insulator transition, and subsequently a first order magnetic melting of the antiferromagnetic order. Crucially, bands of both $J = 1/2$ and $J = 3/2$ nature play important roles in these transitions. Our results qualitatively agree with experiments of Sr_2IrO_4 under strain induced by a substrate, and motivate the study of higher strains.

5.1 Introduction

The combination of strong correlations, spin-orbit coupling (SOC), and multiple relevant orbitals has proven to lead to many interesting states including spin- and orbital- orders, topological states and unconventional superconductivity [1, 2, 3, 4, 5, 6]. The iridate family of compounds displays a very rich phenomenology due to a combination of all of these factors [1, 7, 8]. The five d-orbitals are usually split by crystal fields into two groups, e_g and t_{2g}, with two-fold and three-fold degeneracy respectively. On the other hand, strong spin-orbit coupling may lead to further energy splitting which in turn may reduce the number of relevant bands. Early works on the iridates noted that the spin-orbit coupling affects the system to such an extent that the local total angular momentum states, referred to here as J-eigenstates, do not mix. Moreover, the strong SOC allows one to project onto the $J = 1/2$ subspace and arrive at a simplified effective one-orbital model. In this work we go beyond this effective $J_{\text{eff}} = 1/2$ model and examine regimes where considering a larger subspace, with multiple orbitals, is deemed necessary.

Sr_2IrO_4 is the single-layer compound in the Ruddlesden-Popper series of perovskite iridates and is a spin-orbit coupled Mott insulator with a canted antiferromagnetic order,

as seen in Fig. 5.1. In each layer the iridium atoms are arranged in a square lattice. Each iridium site is surrounded by an oxygen octahedron which is rotated with respect to the crystallographic axes, by a staggered angle $\phi \approx \pm 12^\circ$ [9]. The magnetic moment roughly follows the rotation of each octahedron, resulting in the canted order. In this state the system's properties are dominated by the $J = 1/2$ bands, which are separated from the $J = 3/2$ bands [10, 11, 12]. A projected effective model therefore seems appropriate. This view is further supported by the x-ray absorption spectra that indicate scattering paths corresponding to an order formed by $J = 1/2$ pseudospins [13].

The appropriate effective one-orbital model is surprisingly similar to the one used successfully to describe many of the features of the cuprate high-T_c superconductors. A three-orbital model can take into account both the $J = 1/2$ and $J = 3/2$ subspaces. Previous studies of this multiorbital model of Sr_2IrO_4 predict that superconductivity could occur in this compound as well. However, d-wave superconductivity seems only possible for interorbital interaction parameters in the lower end of the predicted range [14, 15, 16]. These predictions indicate that the effective one-orbital model, $J_{\text{eff}} = 1/2$, might only be valid in some regimes. The system enters other regimes when effects, such as of doping, are no longer small compared to the energy scale of the spin-orbit coupling.

In this paper we take the approach that the three-orbital model is necessary. Including the six bands of the three t_{2g} orbitals, allows us to study several regimes where the effective one-orbital model may be insufficient. We consider the effects of an epitaxial strain and an external magnetic field on *undoped* Sr_2IrO_4. Strain and a Zeeman field are both orbital dependent effects: the strain deforms the lattice and changes the inter-orbital overlaps; the Zeeman field couples to the magnetic moment which depends on the orbital as well as the spin angular momentum.

When considering strain, we should note that Sr_2IrO_4 is sensitive to changes in lattice geometry via a strong Jahn-Teller effect [17]. Epitaxial strain affects the lattice constants as well as the rotation angle ϕ. Strain is introduced by growing Sr_2IrO_4 on a substrate with a mismatch in lattice parameters [18, 19, 20, 21]. In Sr_2IrO_4, an epitaxial strain which changes the lattice parameters by 0.5% is not only easily achievable but also enough to reduce the Néel temperature by 30K [18, 19]. Epitaxial strain is thus a suitable handle for

tuning interactions and lattice deformations. *Ab initio* calculations have previously identified contributions from different J-states to the experimentally observed magnetic order, as well as excitations between the states for some strain values [22, 23]. Compressive epitaxial strain mainly modifies the lattice structure by increasing the rotation angle of the octahedra surrounding the iridium sites, see Fig. 5.1b.

The same effect can be achieved by other means. Two recent promising methods to modify the rotation angle, are electrical current [24] and "field altering" via growth in a magnetic field [25]. In particular, the method of "field altering" in combination with doping has recently been proposed to provide a more favorable environment for observing superconductivity in Sr_2IrO_4 [25]. These experiments motivate us to study trends for a range of strain values and a range of interaction parameters.

Another regime where it might be important to include all three orbitals is reached when a Zeeman field is applied. The field couples to the total magnetic moment which is a combination of the orbital and spin angular momentum, and therefore mixes the local J-states. This mixing has been largely neglected in previous literature as the Zeeman field effects were studied in the context of the effective $J = 1/2$ model [12, 26, 27, 28, 29]. Previously, both experiments and modelling of the Sr_2IrO_4 compound have observed a metamagnetic transition at small fields [13, 30, 31, 32, 33]. This transition aligns the canting of the antiferromagnetic order between layers in the compound, at a field around 0.3T [17, 34]. In this work we consider higher fields as we expect to be able to see effects originating from in-plane interaction within each layer after the metamagnetic transition has taken place.

Some recent work with orbital resolved measurements in a magnetic field has, in addition, shown unequal contributions from each of the t_{2g} orbitals to the magnetic moment [35]. For the simpler $J_{\text{eff}} = 1/2$ projected model, contributions from each orbital are assumed to be equal. This motivates our choice to study the three-orbital model in a Zeeman field.

In this work we aim to give further insight into how quantum phase transitions can arise in Sr_2IrO_4 under a compressive epitaxial strain, with the addition of a Zeeman field. In section II we introduce a three-orbital Hubbard-Kanamori model with on-site interactions. The interactions are treated with a self-consistent mean field approximation.

The mean field decoupling includes all possible uniform and staggered order parameters, except superconductivity. We include a Zeeman field which is applied in different directions and couples to the full magnetic moment $\boldsymbol{\mu} = -\mu_B(\boldsymbol{L} + g\boldsymbol{S})$, where μ_B is the Bohr magneton. The compressive epitaxial strain is modelled as a linear change in hopping parameters. This allows us to reach higher compressive epitaxial strain than previously modeled. We are considering a 2-atom unit cell in the canted lattice, as in Fig. 5.1, where the mean field order parameters are calculated without assuming any relation between the two sublattices. A set of 42 independent order parameters is therefore used. These parameters describe order in the orbital and spin angular momentum and can be expressed in the J-state basis or the orbital basis. By considering the full set of order parameters the contributions to the order from each J-state as well as contributions from order parameters mixing J-states, are considered. Section III presents the results where our model predicts phase transitions from an insulating antiferromagnet into metallic states at high strains. In section III.A details are given for the transitions which are induced by a compressive strain. The Fermi surfaces for the metallic orders are predicted to include several J-states, highlighting the necessity of the multiorbital model. In section III.B the contributions to the magnetic moment from our set of order parameters are considered when a field is applied. Changes to the contributions of order parameters from different J-states are predicted as a function of strain and field. Finally, in section IV we relate our results to experimental findings and discuss implications of entering regimes where the $J_{\text{eff}} = 1/2$ model is insufficient.

5.2 Model

In Sr_2IrO_4, the octahedral crystal fields around the iridium splits its d-levels into t_{2g} and e_g orbitals. Without doping, the three t_{2g} orbitals, d_{yz}, d_{xz}, and d_{xy}, are filled with five electrons while the e_g orbitals are unoccupied at higher energy. Besides the intra- and inter-orbital hopping, these atomic states are also subject to a large on-site spin-orbit coupling and interactions. While the Hubbard interaction strength U is rather moderate, around $1-2$eV, the spin-orbit coupling (SOC) is strong, $\lambda \approx 0.4$eV. The strong SOC splits the six t_{2g} bands

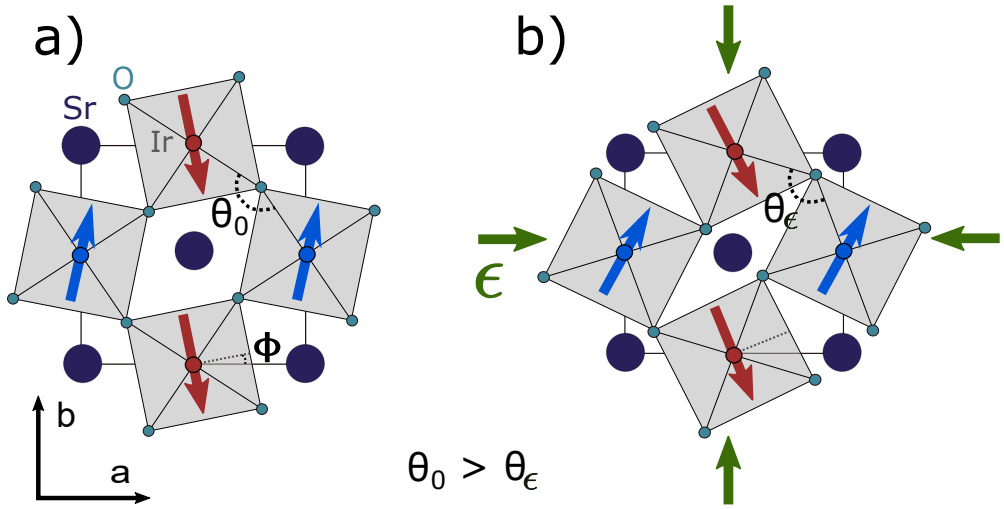

Figure 5.1: a) The structure of a single layer of Sr_2IrO_4 without strain, $\epsilon = 0$. The IrO_6 octahedra are rotated in-plane by an angle of $\phi \approx \pm 12°$ with the sign opposite on neighboring octahedra. This yields an angle $\theta_0 \approx 156°$. The arrows represent the total magnetic moments in the ground state, $\boldsymbol{\mu} = -\mu_B (\boldsymbol{L} + g\boldsymbol{S})$, which are arranged in a canted antiferromagnetic fashion with a small net moment along the a-axis. b) When compressive strain, ϵ, is applied to the layer, the angle θ_ϵ decreases as the rigid octahedra are rotated closer together. A tensile strain has the opposite effect, resulting in a larger angle θ_ϵ.

roughly in two groups: four bands of mainly $J = 3/2$ character and two bands of mainly $J = 1/2$ character. In the undoped compound the Fermi level is placed in such a way that the $J = 3/2$ bands are filled and $J = 1/2$ bands are half-filled. The interaction strength is therefore enough to form an AFM state dominated by the $J = 1/2$ pseudospins [13]. This state is depicted in Fig. 5.1. The anisotropy of the system causes the interactions to be significantly stronger in the plane than out-of-plane. A combination of the anisotropy and the in-plane staggered rotations of the iridium sites causes the magnetic order to form in the plane along the crystallographic b-axis with a canting angle of the magnetic moment along the a-axis in each plane. In this work, given the large anisotropy, we model the system as a single layer.

5.2.1 Hubbard-Kanamori Model

Before we introduce the strain and Zeeman field, we recall the Hamiltonian of the system:

$$H = H_{\text{kin}} + H_{\text{SOC}} + H_{\text{I}} \tag{5.1}$$

where H_{kin} is the kinetic part, H_{SOC} is the spin-orbit coupling, and H_{I} contains the on-site interactions, as defined below. The kinetic part includes hopping between nearest and next nearest neighbouring sites for each of the d-orbitals $\alpha = yz, xz, xy$, with inter- and intra-orbital hopping. In order to study uniform and staggered orders we consider a unit cell with two sites, with sublattices $s = A, B$. The sublattices include the staggered rotation $\phi_s = \pm\phi$, with opposite signs for sublattice A and B. For both sublattices defined in the same global basis $\boldsymbol{c} = (c_{A,yz,\uparrow}, c_{A,yz,\downarrow}, c_{A,xz,\uparrow}, c_{A,xz,\downarrow}, c_{A,xy,\uparrow}, c_{A,xy,\downarrow}, c_{B,yz,\uparrow}, c_{B,yz,\downarrow}, c_{B,xz,\uparrow}, c_{B,xz,\downarrow}, c_{B,xy,\uparrow}, c_{B,xy,\downarrow})$, the labelling of orbital and spin directions are along the crystallographic a- and b-axes. The rotation of each site can be taken into account in the kinetic Hamiltonian which therefore includes non-zero hoppings between the d_{yz} and d_{xz} orbitals. Our Hamiltonian follows the form of Ref. [[36]], which uses a Slater-Koster approach [37]. For each spin

$\sigma = \uparrow, \downarrow$ the kinetic terms take the form (in momentum space):

$$H_{\text{kin}} = \begin{pmatrix} H_{AA} & H_{AB} \\ H_{AB}^{\dagger} & H_{BB} \end{pmatrix} \tag{5.2}$$

$$H_{AA} = \begin{pmatrix} \epsilon_d & \epsilon_{1d} & 0 \\ \epsilon_{1d} & \epsilon_d & 0 \\ 0 & 0 & \epsilon_d^{xy} \end{pmatrix}, H_{AB} = \begin{pmatrix} \epsilon_{yz} & -\epsilon_{rot} & 0 \\ \epsilon_{rot} & \epsilon_{xz} & 0 \\ 0 & 0 & \epsilon_{xy} \end{pmatrix} \tag{5.3}$$

where

$$\begin{aligned} \epsilon_{xy} &= 2t\left(\cos k_x + \cos k_y\right) \\ \epsilon_{yz} &= 2\left(t_\delta \cos k_x + t_1 \cos k_y\right) \\ \epsilon_{xz} &= 2\left(t_1 \cos k_x + t_\delta \cos k_y\right) \\ \epsilon_{rot} &= 2t'\left(\cos k_x + \cos k_y\right) \\ \epsilon_d^{xy} &= 4t_n \cos k_x \cos k_y + \mu_{xy} \\ \epsilon_{1d} &= 4t_{1d} \sin k_x \sin k_y \\ \epsilon_d &= 4t_{nd} \cos k_x \cos k_y. \end{aligned} \tag{5.4}$$

The nearest-neighbor hopping for d_{yz}- and d_{xz}-orbitals is nearly one dimensional in-plane, with t_1 along the direction in which they are orientated and a smaller t_δ along the other direction. The d_{yz}-d_{xz} inter-orbital hopping, t', and the nearest-neighbor hopping between d_{xy}-orbitals, t, are equal in both directions. For the next-nearest-neighbors, along the diagonal of the square lattice, the hopping is t_n for d_{xy} and t_{nd} for the d_{yz}- and d_{xz}-orbitals. The d_{yz}-d_{xz} inter-orbital hopping is t_{1d} along the diagonal. In the absence of strain we use the following values: $(t, t_1, t_\delta, t', t_n, t_{1d}, t_{nd}) =$
(-0.211, -0.186, -0.055, -0.042, -0.118, -0.004, 0.021)eV. These values are extrapolated from those calculated for compressive epitaxial strain by the lineraziation given in detail below in section 5.2.3. The hopping amplitudes have been calculated by Seo *et al.* [23] through *ab initio* for varying strain. The corresponding rotation angle of the sites is $\phi_s = \pm 12.3°$ and $\mu_{xy} = 0.7t$ [38, 8] takes the tetragonal splitting into account, with the value of t being fixed to that of $\epsilon = 0$. In general, the tetragonal splitting is expected to change under

compression as the tetragonal elongation of the oxygen octahedra increases [34]. Works considering a superexchange Hamiltonian predict that for an increased elongation, either an order along the c-axis can be favoured or the canting moment can be suppressed [39, 40]. An additional small staggering of the distortion has been observed to stabilize the canted magnetic moment [41]. However, we chose to study the strain-induced hopping modifications separately as there are conflicting predictions on how the energy splitting depends on strain. *Ab initio* calculations predicted a μ_{xy} where the absolute value decreases until μ_{xy} changes sign [42, 22], while recent RIXS data observed a linearly increasing absolute value of μ_{xy} [43]. Section 5.4 expands on how strain-dependent distortions could affect our results.

The atomic spin-orbit interaction, with the coupling λ, is defined at each site from spin and orbital angular momentum along the same axes as:

$$H_{\mathrm{SOC}} = \frac{\lambda}{2} \sum_{\boldsymbol{j},i} \sum_{\alpha\beta,\sigma\sigma'} L^i_{\alpha\beta} \sigma^i_{\sigma\sigma'} c^\dagger_{\boldsymbol{j}\alpha\sigma} c_{\boldsymbol{j}\beta\sigma'} \tag{5.5}$$

where $i = x, y, z$, $\boldsymbol{\sigma} = (\sigma^x, \sigma^y, \sigma^z)$ are the Pauli matrices in the spin basis $\sigma = \uparrow, \downarrow$, and the matrices

$$\boldsymbol{L} = \left(\begin{bmatrix} 0 & 0 & 0 \\ 0 & 0 & -i \\ 0 & i & 0 \end{bmatrix}, \begin{bmatrix} 0 & 0 & i \\ 0 & 0 & 0 \\ -i & 0 & 0 \end{bmatrix}, \begin{bmatrix} 0 & -i & 0 \\ i & 0 & 0 \\ 0 & 0 & 0 \end{bmatrix} \right) \tag{5.6}$$

are the orbital angular momentum operators, projected onto the t_{2g} subspace and written in the orbital basis $\alpha = yz, xz, xy$. The interactions in the multiband model on each site take the form of the Kanamori-Hubbard interactions [44]

$$\begin{aligned} H_{\mathrm{I}} = \; & U \textstyle\sum_{\boldsymbol{j},\alpha} n_{\boldsymbol{j}\alpha\uparrow} n_{\boldsymbol{j}\alpha\downarrow} \\ & + \textstyle\sum_{\boldsymbol{j},\alpha\neq\beta} J_{\mathrm{H}} \left[c^\dagger_{\boldsymbol{j}\alpha\uparrow} c^\dagger_{\boldsymbol{j}\beta\downarrow} c_{\boldsymbol{j}\alpha\downarrow} c_{\boldsymbol{j}\beta\uparrow} + c^\dagger_{\boldsymbol{j}\alpha\uparrow} c^\dagger_{\boldsymbol{j}\alpha\downarrow} c_{\boldsymbol{j}\beta\downarrow} c_{\boldsymbol{j}\beta\uparrow} \right] \\ & + \textstyle\sum_{\boldsymbol{j},\alpha<\beta,\sigma} \left[U' n_{\boldsymbol{j}\alpha\sigma} n_{\boldsymbol{j}\beta\bar{\sigma}} + (U' - J_{\mathrm{H}}) n_{\boldsymbol{j}\alpha\sigma} n_{\boldsymbol{j}\beta\sigma} \right] \end{aligned} \tag{5.7}$$

with the intraorbital interactions U, the Hund's coupling J_{H}, and the interorbital repulsion U'. For simplicity the spherically symmetric value $U' = U - 2J_{\mathrm{H}}$ is taken. For Sr_2IrO_4 the Hund's coupling is approximated to be in the range $0.05U - 0.2U$ [14, 15, 16, 45].

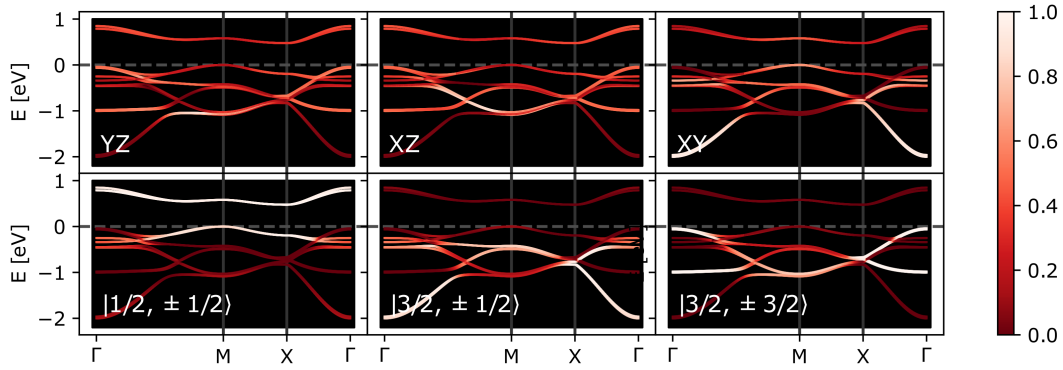

Figure 5.2: The band structure is shown for the antiferromagnetic insulating state in Sr_2IrO_4, calculated for $\lambda = 0.38$eV, $U = 0.9$eV, and $J_H/U = 0.1$, with no applied strain or field. As there are 6 states per site, the band structure consists of 12 bands forming a staggered order. In the top row, the weight from each orbital d_{yz}, d_{xz}, and d_{xy} is projected onto the eigenstates at each k-point in the Brillouin zone as in Eq. (5.17). The large spin-orbit coupling mixes the orbitals, so the bands closest to the Fermi level have contributions from all three orbitals. The second row shows the eigenstates projected onto the $J = 1/2$ and $J = 3/2$ states as in Eq. (5.18). The $J = 1/2$ bands dominate near the Fermi level except near Γ, where $J = 3/2$ takes over.

5.2.2 Zeeman Coupling

We consider the effect of an external magnetic field $\boldsymbol{H}$ through the Zeeman field. The field couples to the full magnetic moment $\boldsymbol{\mu} = \mu_B (\boldsymbol{L} + g\boldsymbol{S})$, with $g \approx 2$ being the gyromagnetic ratio. The additional term in the Hamiltonian is

$$H_Z = \mu_B \sum_{\boldsymbol{j},s} \sum_{\alpha,\sigma} \left[\sum_\beta \boldsymbol{H} \cdot \boldsymbol{L}_{\alpha\beta} c^\dagger_{s,\boldsymbol{j}\alpha\sigma} c_{s,\boldsymbol{j}\beta\sigma} + \frac{1}{2} \sum_{\sigma'} g\boldsymbol{H} \cdot \boldsymbol{\sigma}_{\sigma\sigma'} c^\dagger_{s,\boldsymbol{j}\alpha\sigma} c_{s,\boldsymbol{j}\alpha\sigma'} \right]. \tag{5.8}$$

For realistic magnetic fields, the Zeeman energy is significantly smaller than the spin-orbit coupling $\lambda \approx 0.4$eV, and the gap ≈ 0.5eV. For example, a field of $H \approx 10$T corresponds to an energy of the order of $g\mu_B H = 1.2$meV.

5.2.3 Epitaxial Strain

We model the effect of a compressive strain on the system by modifying the hopping parameters linearly with the strain. We use a linearization of the set of values for the hopping parameters calculated by Seo *et al.* [23]. In Ref. [[23]], the compound is grown on three different substrates which have lattice constants that are smaller than that of Sr_2IrO_4: $(LaAlO_3)_{0.3}(Sr_2TaAlO_6)_{0.7}$, $NdGaO_3$, and $LaAlO_3$. The resulting misfit strain modifies the lattice constants in the Sr_2IrO_4 thin film. X-ray diffraction measurements find these modified lengths and *ab initio* calculations are performed for those structures. The calculations therefore provide three data points for the hopping parameters at given values of the compressive strain. In this work we use those three data points to fit a linear dependence of the hopping with the strain. Our linearization results in the proportional changes, ρ, which modify our hopping amplitudes as

$$\begin{aligned} t(\epsilon) &= t\,(1+\rho\epsilon) \\ t_1(\epsilon) &= t_1\,(1+\rho_1\epsilon) \\ t'(\epsilon) &= t'\,(1+\rho'\epsilon) \\ t_n(\epsilon) &= t_n\,(1+\rho_n\epsilon) \\ t_\delta(\epsilon) &= t_\delta\,(1+\rho_\delta\epsilon) \\ t_{1d}(\epsilon) &= t_{1d}\,(1+\rho_{1d}\epsilon) \\ t_{nd}(\epsilon) &= t_{nd}\,(1+\rho_{nd}\epsilon) \\ \phi(\epsilon) &= \phi\,(1+\rho_\phi\epsilon)\,. \end{aligned} \tag{5.9}$$

For a compressive strain ($\epsilon < 0$) the resulting values are $(\rho, \rho_1, \rho', \rho_n, \rho_\delta, \rho_{1d}, \rho_{nd}, \rho_\phi) =$ (0.014,-0.251, -0.309, -0.048, 0, 0,-0.02,-0.085). The values used for $\epsilon = 0$ are those given by this linearisation. As illustrated in Fig. 5.1, the effect of compressive strain is mainly to increase the relative rotation angle between adjacent octahedra. However, by using these values we are not restricted to consider only rotation effects. The rotations change the overlap integrals between orbitals on different sites. The nearest neighbor inter-orbital d_{yz}-d_{xz} hopping, as well as the next nearest neighbor intra-orbital d_{xy} hopping are increased under strain. On the other hand, the nearest neighbor d_{xy} hopping is decreased.

Our linearized strain model allows us to predict what orders can arise when we reach strain values beyond the experimentally achieved $\epsilon = -1.9\%$ [23].

5.2.4 Mean Field Approximation

In mean field theory one approximates the Hamiltonian by a quadratic one, so that the quartic interaction terms are decomposed by introducing a variety of order parameters. This yields an auxiliary Hamiltonian for which the spectrum can be found by diagonalizing a single-particle Hamiltonian. The resulting eigenstates are then used as variational states to calculate the expectation value of the original *interacting* Hamiltonian for a given electron density. The energy is minimized with respect to the order parameters, thus determining their values. With two atoms per unit cell, three orbitals and two spin states, each unit cell has 12 creation/annihilation operators. A mean field order parameter is the expectation value of a bilinear operator $\langle c^\dagger_\alpha c_\beta \rangle$. Our mean field decomposition is done by choosing to include the full set of on-site order parameters under the condition of a hermitian auxiliary/mean-field Hamiltonian. For each of the sites in the unit cell we form a 6×6 hermitian matrix of order parameters, meaning that we calculate a total of $2 \cdot 21 = 42$ independent complex-valued order parameters. The set of order parameters is therefore $\langle c^\dagger_{\gamma_1} c_{\gamma_2} \rangle_s$, where γ_i is a label combining the spin label σ and the orbital label α in each sublattice $s = A, B$. The order parameters are calculated in iterative steps through the coupled set of self-consistency equations, as given in Appendix A. The calculated order parameters are used as input into the Hamiltonian in order to repeat the process in iterative steps until the input and output, of the form presented in table 5.1, differ by less than the total tolerance of 10^{-5}. The calculations were performed on a 200×200 grid of momentum k-points. A range of initial conditions are considered to ensure that the global minimum of the energy functional is found.

Our analysis assumes no relations between the order parameters on the different sites. Uniform orders are considered by calculating the net value of the order parameters from both sites, $(A + B)/2$, and staggered orders are the difference in order parameters between sites, $(A - B)/2$. Such staggered orders include commensurate charge density waves (CDW), spin density waves (SDW), orbital density waves (ODW), and spin-orbit density waves (SODW).

It is convenient to rewrite the order parameters in order to directly describe the spin and orbital angular momentum. The order parameters n_{yz}, n_{xz}, and n_{xy} are the filling of each orbital. The spin S^i and the orbital angular momentum L^i are calculated in each direction $i = x, y, z$. Order parameters that couple spin and orbital degrees of freedoms, like the bare SOC, Λ^i are included as well. Suppressing the sublattice label, these order parameters are given by:

$$S^i_\alpha = \frac{1}{2}\sum_{\sigma,\sigma'} \sigma^i_{\sigma\sigma'} \langle c^\dagger_{\alpha\sigma} c_{\alpha\sigma'}\rangle \tag{5.10}$$

$$L^i_\sigma = \sum_{\alpha,\beta} L^i_{\alpha\beta} \langle c^\dagger_{\alpha\sigma} c_{\beta\sigma}\rangle \tag{5.11}$$

$$\Lambda^i = \frac{1}{2}\sum_{\alpha,\beta}\sum_{\sigma,\sigma'} L^i_{\alpha\beta}\sigma^i_{\sigma\sigma'} \langle c^\dagger_{\alpha\sigma} c_{\beta\sigma'}\rangle. \tag{5.12}$$

Once a set of self-consistent order parameters has been found in the orbital and spin basis, they can also be expressed in the J-basis. This basis represents the eigenstates of the non-interacting model in the $\lambda \to \infty$ limit, in which the hopping can be neglected. Order parameters expressed in this basis represent contributions of each J-state as well as a measure of the mixing between states. The transformation $\tilde{c}_{m,\tau} = \sum_{\alpha,\sigma} U^{\alpha,\sigma}_{m,\tau} c_{\alpha,\sigma}$, generates the basis $\tilde{c}_{m,\tau}$ at each site where $m = |j, j^z\rangle : 1 = |1/2, \pm 1/2\rangle, 2 = |3/2, \pm 1/2\rangle, 3 = |3/2, \pm 3/2\rangle$ are the pseudospins and $\tau = +, -$. The same transformation is applied for both sublattices, which defines the J-states in the global basis. It is important to note that J-states that are defined for *local* rotated orbitals are different states and such a definition may slightly shift the resulting contributions of each state. In the J-basis, order parameters are constructed as a linear combination of the ones discussed above in Eqs. (5.10),(5.11),(5.12). These order parameters are given by $\langle \tilde{c}^\dagger_{m,\tau} \tilde{c}_{n,\tau'}\rangle$ and are transformed from the orbital basis as:

$$\langle \tilde{c}^\dagger_{m\tau} \tilde{c}_{n\tau'}\rangle = \sum_{\alpha,\beta,\sigma,\sigma'} (U^{\alpha\sigma}_{m\tau})^* U^{\beta\sigma'}_{n\tau'} \langle c^\dagger_{\alpha\sigma} c_{\beta\sigma'}\rangle \tag{5.13}$$

with the matrix U given in Appendix B. In this basis we consider the order parameters:

$$J^i_m = \frac{1}{2}\sum_{\tau,\tau'} \sigma^i_{\tau\tau'} \langle \tilde{c}^\dagger_{m\tau} \tilde{c}_{m\tau'}\rangle \tag{5.14}$$

	n_{yz}	n_{xz}	n_{xy}	L	S_{yz}	S_{xz}	S_{xy}	Λ_x	Λ_y	Λ_z
staggered	0	0	0	-0.47	0.13	-0.15	0.11	0	0	0
net	1.66	1.63	1.71	0.15	0.040	-0.042	-0.037	0.32	0.30	0.35
	n_1	n_2	n_3	J_1	J_2	J_3	J_{12}	J_{13}	J_{23}	
staggered	0	0	0	-0.29	-0.0047	0.0040	-0.023	0.011	0.0005	
net	1.02	1.99	1.99	0.12	0.0018	0.0012	0.0035	-0.0010	-0.0002	

Table 5.1: The order parameters are given in the three-orbital basis, as in Eqs. (5.10), (5.11), (5.12), as well as in the basis of J-states, as in Eqs. (5.14), (5.15). The calculation is performed at $\lambda = 0.38$eV, $U = 0.9$eV, and $J_H/U = 0.1$, with no strain or field, meaning that the state is the canted antiferromagnet in Fig. 5.1a. The differences between order parameters in the two sublattices are given as the staggered value. The net values of the order parameters are defined as the average for the two-site unit cell. For the L and $S_{yz,xz,xy}$ order parameters, the staggered values are along the b-axis, while the net values are along the a-axis. The order parameters Λ renormalize the spin-orbit coupling strength.

$$J^i_{mn} = \frac{1}{2}\sum_{\tau,\tau'} \sigma^i_{\tau\tau'} \langle \tilde{c}^\dagger_{m\tau} \tilde{c}_{n\tau'} \rangle \tag{5.15}$$

for the J-states $m, n = 1, 2, 3$, and the pseudospins $\tau, \tau' = +, -$. In addition, the filing of each J-state is given by

$$n_m = \sum_\tau \langle \tilde{c}^\dagger_{m\tau} \tilde{c}_{m\tau} \rangle. \tag{5.16}$$

This transformation extends the analysis of Mohapatra and Singh in Ref. [[38]], who studied the contributions J_m, without strain and a Zeeman field. In this work we include the additional mixing J_{mn}, which includes effects beyond those that can be projected onto the individual subspaces of the J-states. The amount of mixing J_{mn} allows us to see whether strain and Zeeman fields require us to go beyond the effective $J_{\text{eff}} = 1/2$ model.

5.3 Results

First, our mean field solution in the absence of Zeeman field and strain is in agreement with previous studies [38, 14, 15, 16, 45, 10, 46, 12]. In Fig. 5.2 we present the band structure for $\lambda = 0.38$eV, $U = 0.9$eV, and $J_H/U = 0.1$. Under these conditions, both this work and other studies, find a band gap close to the experimentally observed value [1]. The resulting state

is an antiferromagnet along the b-axis with a small staggered canting angle of $\phi_\mu \approx \pm 14°$ along the a-axis. This angle is larger than the rotation of the underlying lattice and slightly larger than what is observed in experiments [9]. The magnetic order canting angle does not precisely match the lattice rotation angle due to the tetragonal distortion and a non-zero Hund's coupling. An angle difference is captured by our model and even by the projected $J = 1/2$ model [11]. The resulting eigenstates are expressed in the two bases, the orbital and the J-basis, and the contributions of each state can be calculated at all k-points for each band. For orbitals defined in the *global* basis the eigenstates $|n(\boldsymbol{k})\rangle$ can be expressed in the components $|n(\boldsymbol{k})\rangle = \sum_{\alpha,\sigma,s} \eta_{\alpha,\sigma,s,n}(\boldsymbol{k})|\alpha,\sigma,s\rangle$. The transformation onto the J-basis is done for each site individually in the global basis with the matrix U given in (5.20) in Appendix B, $|n(\boldsymbol{k})\rangle = \sum_{m,\tau,s} \eta'_{m,\tau,s,n}(\boldsymbol{k})|m,\tau,s\rangle = \sum_{m,\tau,s}\sum_{\alpha,\sigma} \eta'_{m,\tau,s,n}(\boldsymbol{k})\,(U^{\alpha\sigma}_{m\tau})^*\,|\alpha,\sigma,s\rangle$. The weight of an orbital in an eigenstate at a given k-point is calculated as

$$P_{n,\alpha}(\boldsymbol{k}) = \sum_{s=A,B}\sum_{\sigma=\uparrow,\downarrow} |\eta_{\alpha,\sigma,s,n}(\boldsymbol{k})|^2, \tag{5.17}$$

in the original three-orbital basis and:

$$P_{n,m}(\boldsymbol{k}) = \sum_{s=A,B}\sum_{\tau=+,-} |\eta'_{m,\tau,s,n}(\boldsymbol{k})|^2, \tag{5.18}$$

in the J-state basis. The values are displayed for the full bandstructure in Fig. 5.2 and the figure is complemented by the values of the order parameters in Table 5.1. The magnetic order receives the largest contribution from the $J = 1/2$ states, as given by Eq. (5.14). Similarly, as can be seen in the lower panels of Fig. 5.2, the $J = 1/2$ states are dominant in the two bands closest to the Fermi level, except near the Γ-point. Expressed in the orbital basis, the same bands are a mixture of all three orbitals, with the contribution of d_{xy} being slightly smaller. Additional bands that appear close to the Fermi level, at the Γ-point, are bands of $|3/2,\pm 3/2\rangle$ character. However, Table 5.1 shows that these states offer only a small contribution to the AFM order. Similarly, the order parameters which mix the $|1/2,\pm 1/2\rangle$ and the $|3/2,\pm 1/2\rangle$ states have a contribution of about 5-10% of the one of $J = 1/2$, which is not negligible. A similar discrepancy in the magnetic order has been

identified previously [10] by observing a larger ratio of orbital angular momentum, compared to spin angular momentum, than expected from a pure $J = 1/2$ order.

5.3.1 Strain-Driven Phase Transitions

In this subsection we discuss the effects of strain. The magnetic moment for both the staggered AFM order and the net moment is shown in Fig. 5.3. As the compressive strain is increased the antiferromagnetic order decreases and two phase transitions occur. At lower strain values the staggered magnetic moment in the insulating (AFM-I) order continuously decreases until the gap closes, in a continuous Lifshitz transition into an antiferromagnetic metal (AFM-M). The strain dependence of the band gap is plotted in Fig. 5.7 in Appendix C. As the strain increases further, the antiferromagnetic order continues to decrease until a strain value where a first order transition into a paramagnetic metal (PM-M) occurs. The transitions are driven by the increasing bandwidth of the $J = 1/2$ bands and an increase in the energy of the $J = 3/2$ bands. We will describe several multiorbital aspects of the strain-driven phase transitions: (i) the changes in multiorbital contributions close to critical strain, (ii) the additional bands contributing to the Fermi surface in the metallic state, and (iii) the dependence of the critical strain on model parameters.

Approaching the first transition by increasing the strain, we see a decrease in the staggered magnetic moment. The decrease is mostly felt in the $J = 1/2$ subspace, and therefore the relative contribution of the $J = 3/2$ states to the magnetic order is increased. As the underlying rotations of the lattice increase, so does the canting angle of the antiferromagnetic state. The changes in orbital contributions are discussed further in III.B. At higher strains in the metallic state, several bands cross the Fermi level. The resulting Fermi surfaces are shown in Fig. 5.4 for several strain values. Different parts of the Fermi surface have a different character, as shown in Fig. 5.5. In this figure both possible bases are projected onto the Brillouin zone. Pockets around the M- and X-points are clearly dominated by the $J = 1/2$ states. However, another pocket near the Γ-point originates from a band with a high $|3/2, \pm 3/2\rangle$ contribution. In the orbital basis, the pockets can be described as alternating sections of d_{yz} and d_{xz} orbitals, where the sections dominated by each orbital are related by a rotation of $\pi/2$, see Fig. 5.5.

The two phase transitions, as indicated in Fig. 5.3, are determined to occur at $\epsilon = -3.47\%$, the point at which the indirect gap closes, and at $\epsilon = -4.9\%$, where the order parameters for the staggered magnetic moment become lower than $2 \cdot 10^{-2}$. The Fermi surfaces appearing at lower strain values have small pockets of $J = 1/2$ and $J = 3/2$ character which gradually increase in size as the strain increases. In the AFM phase, the canting angle of the AFM order is larger than the rotation angle of the underlying lattice. As a result, a small band splitting can be observed close to the Γ-point for the pockets of $J = 3/2$ character. As the size of the pocket increases at higher strain values and the AFM order decreases, this splitting is decreased. In the paramagnetic phase an additional pocket of $J = 1/2$ character appears at the M-point.

The value of the critical compressive strain that we obtain as the transition point between metallic and insulating magnetically ordered states depends on our model parameters. Fig. 5.7 in Appendix C shows a range of critical compressive strains for other possible values of the interaction U. In our model, the critical strain value mainly depends on the size of the initial gap. Therefore, the critical strain increases with spin-orbit coupling and with the interaction U, and decreases with the Hund's coupling J_{H}. The agreement between experimental work and our predictions for the decreasing AFM order as a function of strain, as well as possible values for a realistic critical strain are discussed below.

When a Zeeman field is applied only minimal changes to the critical strain are observed. This is shown in the phase diagrams in Fig. 5.9 in Appendix D. Additional effects to orbital contribution from a magnetic field are discussed in the following section.

5.3.2 Orbital contributions

At the strain-driven phase transitions depicted in Fig. 5.3, contributions from the J-states, J_m, and the mixing between those states, J_{mn}, change by different amounts. The contributions from the spin angular momentum and the J-states to the net moment are shown in Fig. 5.6, both without an applied field and for a Zeeman field in-plane along the a-axis (H_x). The figure shows how the strain and the Zeeman field affect the magnetic order. As the insulating AFM order decreases under strain, the order in $J = 1/2$ decreases

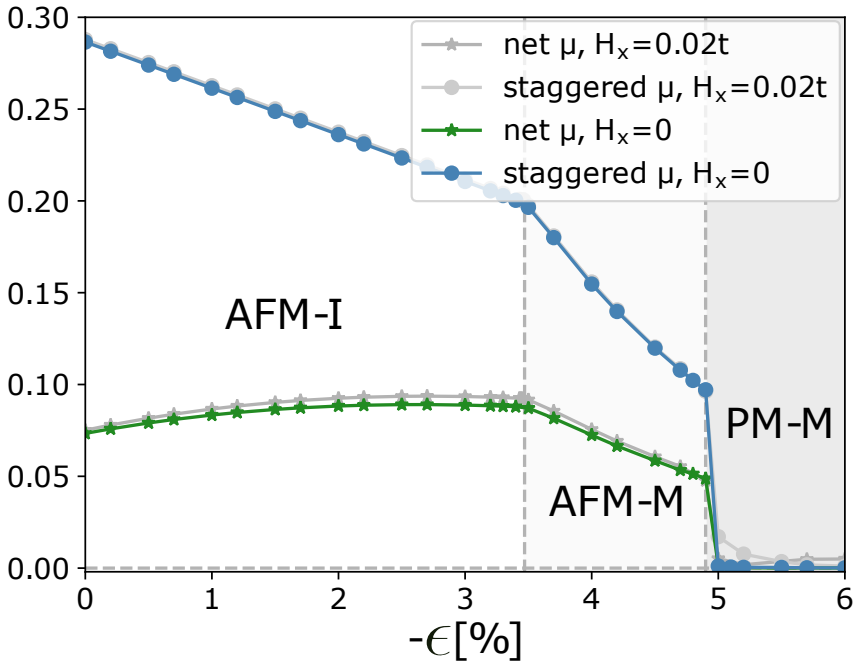

Figure 5.3: The total magnetic moment is plotted for increasing compressive strain. The staggered moment is the difference between the two sublattices and the net moment results from the canting of the moments at both sites. The strain-driven transitions take place both under zero field as well as under a large Zeeman field $H_x = 0.02t$, along the a-direction. The critical strain values, at which the gap closes and the system first goes into a metallic AFM (AFM-M) and subsequently into a paramagnetic (PM-M) state, are marked for zero field by vertical dashed lines. As shown in Fig. 5.9, these transitions are only slightly shifted by the field. When a field is applied there is a small remaining AFM moment, below $2 \cdot 10^{-2}$, that appears right after the transition into the PM-M state. The evolution of the bandgap with strain is shown in Fig. 5.7.

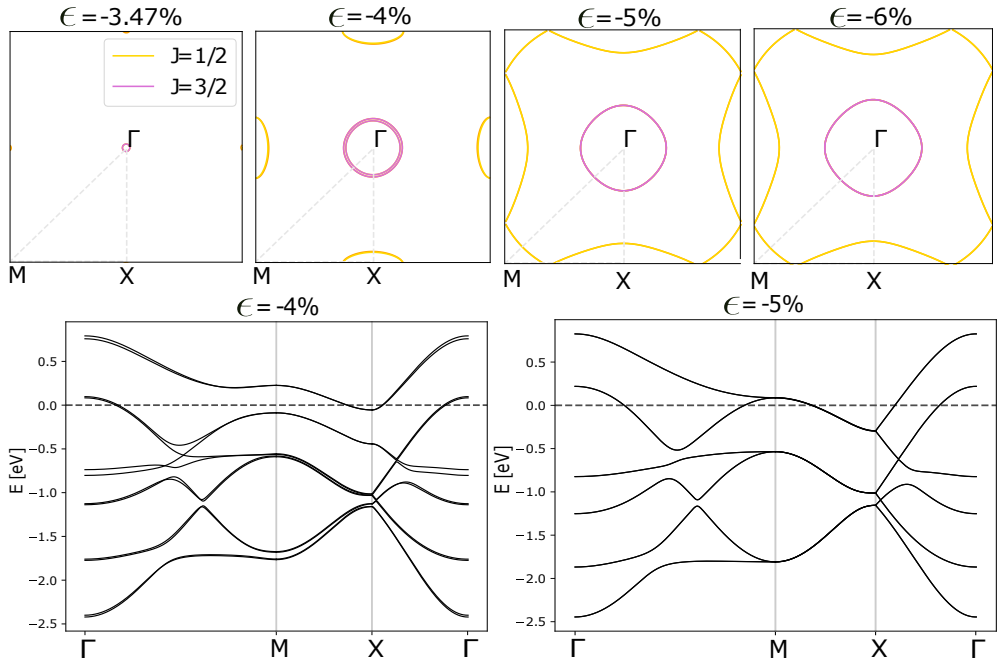

Figure 5.4: Fermi surfaces ($E = 0$) for the strain-driven transitions at zero field. The dominant bands are identified as being of mainly $|j, j^z\rangle = |1/2, \pm 1/2\rangle$ and of $|j, j^z\rangle = |3/2, \pm 3/2\rangle$ character, by the same method as in Fig 5.5. As the strain is increased the indirect gap in the AFM order decreases and eventually closes at $\epsilon = -3.47\%$. For Fermi surfaces in the metallic AFM (AFM-M) phase, such as at $\epsilon = -4\%$, some band splitting can be observed. The splitting occurs at these points as the resulting FM component corresponds to a larger canting angle than the underlying rotation of the lattice. At $\epsilon = -5\%$, the system becomes a paramagnetic metal and an additional $J = 1/2$ surface appears around the M-point.

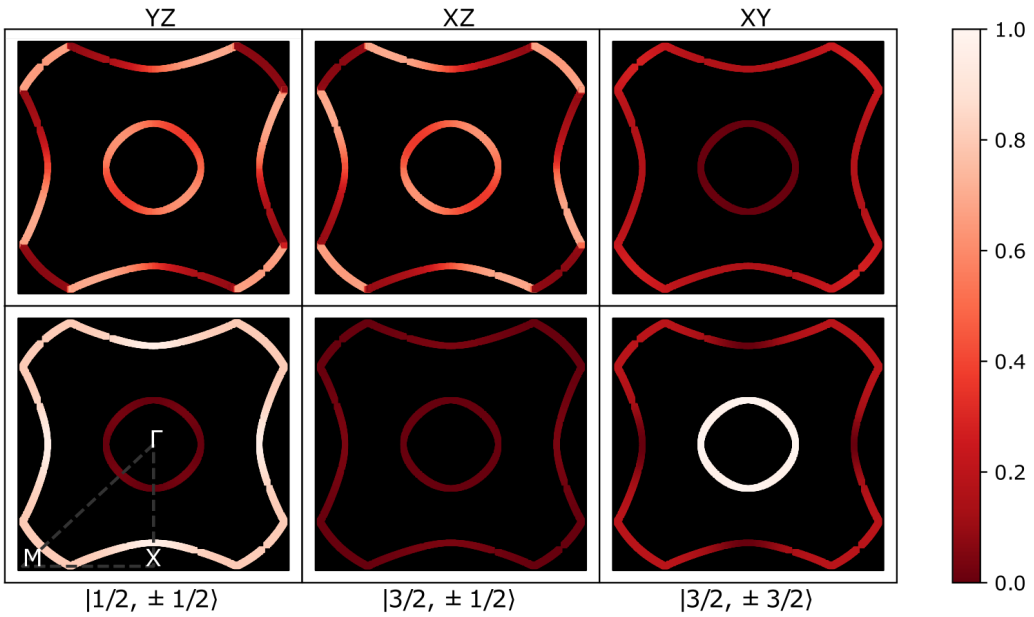

Figure 5.5: The Fermi surface at zero field and a compressive strain $\epsilon = -5\%$ is shown with the calculated contributions from each orbital, in the upper row, and from each J-state, in the lower row. As in Fig. 5.2, orbital weights for each state are calculated for eigenstates at each k-point in the Brillouin zone, according to Eqs. (5.17), (5.18). As shown in Fig. 5.4 the bands can be described mainly by the $|j, j^z\rangle = |1/2, \pm 1/2\rangle$ states around the M- and X-points, and by the $|j, j^z\rangle = |3/2, \pm 3/2\rangle$ states around the Γ-point.

while the order in other states remain roughly constant. While strain increases the staggered rotation angle of the AFM state and therefore all J-states, the Zeeman field tends to affect orbitals depending on their relative orientation to the field.

The changes in contributions to the net moment under strain are minor. The net moment increases as the staggered AFM order follows the increased underlying staggered rotation of the octahedra surrounding the Ir sites. In the metallic AFM order the contribution from the $J = 1/2$ states to the net moment mainly decreases while the others remain constant. When a high in-plane field is applied there are additional distinguishing effects between the AFM and the PM. In the insulating AFM state there is some increased mixing contributions to the net moment, as the field does not couple purely to the J-states. The $J = 1/2$ states however still clearly dominate in the antiferromagnetic phase.

For the orbital angular momentum basis, the spin order S_α, in each orbital, α, is also plotted in Fig. 5.6. For zero field the orbitals start out with close to equal spin order and as the strain is increased the S_{xy} order decreases. When the in-plane field is applied, the AFM-I state has a larger contribution from the S_{yz} order while this dominance does not remain in the paramagnetic state. For an out-of-plane field (H_z) this results in a larger contribution from the d_{xy}-orbital, which corresponds to an increased mixing between $|1/2, \pm 1/2\rangle$ and $|3/2, \pm 1/2\rangle$ in the J-state basis. An in-plane field (H_x) increases contributions from the d_{yz}-orbital, or a mixing between the states $|1/2, \pm 1/2\rangle$ and $|3/2, \pm 3/2\rangle$.

In addition, in Fig. 5.8 in Appendix C the parameters λ and J_{H} take on a range of possible values. At different values the amount of mixing between J-states (at zero strain) changes. The mixed J order parameters, J_{mn}, in Eq. (5.15) are useful as they indicate whether a projected $J = 1/2$ model is appropriate. Regimes with larger J_{mn} values can therefore be identified as promising starting points for future studies of possible interband fluctuations and orders.

5.4 Discussion

In this work, we have presented a mean field, zero temperature, analysis of the six-band Hubbard-Kanamori model for *undoped* Sr_2IrO_4. A self-consistent mean field treatment

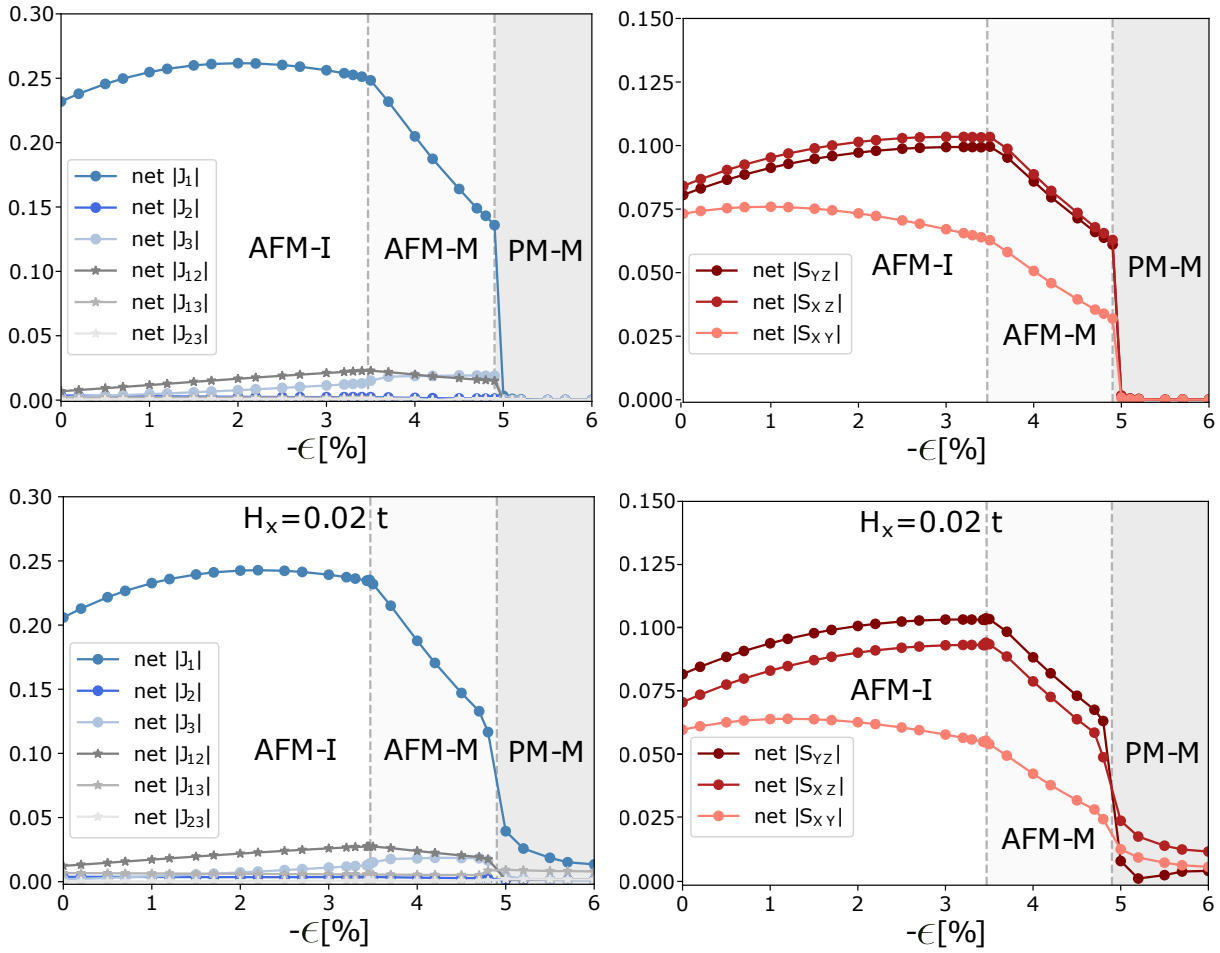

Figure 5.6: Order parameters for the net magnetization are plotted for an increasing compressive strain, both in the J-basis and as spin contributions from each orbital. These plots display the strain-driven transitions into metallic states shown in Fig. 5.3. In the J-basis, order parameters J_m for each state and order parameters J_{mn} mixing J-states, as in Eqs. (5.14) and (5.15), are shown. There are minor changes in the contributions from each order parameter with strain, before the transition out of the insulating antiferromagnetic (AFM-I) state. However, once a field is applied there is a clear difference in contributions to the net moment between AFM and PM orders.

considers a 2-atom unit cell and all 42 possible local order parameters. We study the undoped compound in the presence of both strain and a Zeeman field. In the absence of strain and field our model predicts an insulating canted antiferromagnetic state, in agreement with previous studies [38, 14, 15, 16, 45, 10, 46, 12] and experimental evidence [47, 48, 49, 50]. Upon applying a compressive strain our model predicts two transitions: a Lifshitz transition into an antiferromagnetic metallic state and, at higher strain, a first order transition into a metallic paramagnet. These transitions exist for a range of plausible interaction strengths. The inclusion of multiple bands is crucial to model these transitions. A decreased $J = 1/2$ AFM order can in principle be described by projecting the effects of the strain onto the effective one-orbital $J_{\text{eff}} = 1/2$ model. However, the strain causes the appearance of additional bands at the Fermi level that are missed by a $J_{\text{eff}} = 1/2$ model.

Our predictions for the strain effects agree with trends from previous theoretical and experimental studies. For example, in Ref. [[19]] the strain is shown to cause a decrease in the AFM order manifested in a lowered Néel temperature. As found in our model, the increased importance, due to strain, of the $J = 3/2$ states also agrees with the observed intensity increase in optical transitions between $J = 3/2$ and $1/2$ states found in other studies [42, 51, 43]. In addition, transport measurements observe a steady decrease in resistivity as the compressive epitaxial strain is increased [52]. Such a trend can be expected from our calculations, as they predict a decreasing gap. At the highest measured strain value for epitaxial strain, $\epsilon = -1.9\%$, the behavior is determined to still be insulating [52]. Therefore, a transition has not been reached at that point. Our model predicts the same behavior. It is however important to note that generally mean field theory overestimates ordering. Fluctuations not taken into account here may shift the phase boundaries. Moreover, the interaction and spin-orbit coupling strength aren't directly measurable and we therefore choose parameters that match the previously found band structure [38, 45, 10, 46, 12]. To get a range of possible strain values which will be relevant for future studies, a relation between possible initial gaps and the critical strain is given in Appendix C.

Our results also include effects of various parameters on the mixing between different total angular momentum sectors. When the mixing between J-states is small, the $J_{\text{eff}} = 1/2$

model can describe the ordered state well. However, for a larger mixing the full six-band model is necessary. We find that a larger strain, larger Hund's coupling, and lower spin-orbit coupling all increase the mixing. The Zeeman field also results in increased mixing, which depends on the direction of the field. It is worth noting that the mixing can be traced by studying the orbital content of each band. The orbital dependence of the magnetic state was recently determined, by Jeong *et al.* in Ref. [[35]], from the symmetry of occupied orbitals as measured by polarized neutron diffraction experiments. A similar experiment could potentially observe the strain-induced changes in orbital contributions found here.

The comparisons of our results to experiments with pressure are limited due to our one-layer model. For epitaxial strain/hydrostatic pressure, the distance between layers in the perovskite structure increases/decreases. Under pressure, the resulting increased interlayer interactions affect the magnetic order [53]. Additionally, our model may not be capturing all aspects of the strain-driven phase transitions. At high hydrostatic pressures, experiments are possibly pointing towards frustration from enhanced nearest- and next-nearest-neighbor interactions in an insulating quantum paramagnet [53]. Similarly as transport measurements not displaying any anomaly at the Néel temperature [7], studies considering hydrostatic pressure found a separation in the behaviour between magnetic order and insulating properties [34], which is beyond the scope of our mean field theory. As can be seen in Fig. 5.4, we predict that several of the bands are located close to the Fermi surface during the strain-driven transitions. This regime could therefore potentially host strongly correlated interband effects.

The model considered in our work only describes compressive strain. There have however been several studies showing interesting effects at tensile strain or for other methods decreasing the rotation angle of the octahedra in Sr_2IrO_4, such as "field altering" or applying an electrical current [24, 25]. Experiments have shown both decreasing resistivity for tensile strain values [52] and a lower Néel temperature for samples with a tensile strain of $\epsilon = 0.4\%$ than for those with a compressive strain of $\epsilon = -0.7\%$ [23]. However, *ab initio* calculations at tensile strain [51] pointed towards an increased charge gap which agrees with that observed in RIXS spectra [43]. Accurately modelling the tensile regime might require the inclusion of additional effects. In future work, the strain value for

which the pocket at the Γ-point appears in the Fermi surface could be adjusted by studying how the tetragonal splitting evolves with strain. Currently, calculations in Ref. [[22]] suggest a lowering of the $J = 3/2$-band at this point, while the measurements in Ref. [[43]] indicate the opposite.

Works modelling greater tetragonal elongation in a superexchange model, such as Ref. [[39]], have explored regimes our work did not. In those regimes the canting angle is supressed by the distortions. Ref. [[41]] found that the angles of the octahedral rotation and of the canting moment followed each other more closely with an additional staggered splitting between sublattices. Since we did not consider tetragonal splitting as a function of strain, the effects of an increased or staggered splitting is beyond the scope of this work.

Another interesting aspect expected to be affected by strain and an external field is the tendency to develop superconductivity. The mixing of J-states and the appearance of additional bands at the Fermim level might indicate that a $J = 1/2$ d-wave superconducting state is less likely to develop. It is possible, however, that while the d-wave order parameter is less likely, another pairing function which involves multiple bands will become favorable. This is beyond the scope of the current manuscript and will be studied elsewhere.

Acknowledgments

The authors would like to thank Zi Yang Meng for useful discussions. We acknowledge financial support from NSERC, RQMP, FRQNT, a grant from Fondation Courtois, a Canada Research Chair, and an Alexander McFee Fellowship from McGill University. Computations were made on the supercomputers Beluga from École de technologie supérieure, and Cedar from Simon Fraser University, managed by Calcul Québec and Compute Canada. The operation of these supercomputers is funded by the Canada Foundation for Innovation (CFI), the ministère de l'économie, de la science et de l'innovation du Québec (MESI) and the Fonds de recherche du Québec - Nature et technologies (FRQ-NT).

5.A Self-Consistency Equations

In the mean field analysis, the order parameters are defined as the expectation values of bilinear operators calculated for the mean field eigenstates $|n(\boldsymbol{k})\rangle$. Each order parameter is given by $\langle c^\dagger_{\gamma_1} c_{\gamma_2}\rangle_s$, where γ_i is the label of one of the 6 local creation/annihilation operators given by $\alpha = yz, xz, xy$, and $\sigma = \uparrow, \downarrow$, for each of the sublattices $s = A, B$. The self-consistent solution for all possible order parameters is found iteratively and simultaneously by solving the set of coupled self-consistency equations:

$$\begin{aligned}\langle c^\dagger_{\gamma_1} c_{\gamma_2}\rangle_s &= \frac{1}{N}\sum_{\boldsymbol{k}}^{N}\sum_{n}^{12}\langle n(\boldsymbol{k})|\gamma_1, s\rangle\langle\gamma_2, s|n(\boldsymbol{k})\rangle n_{\mathrm{F}}\left[E_n(\boldsymbol{k})\right] \\ &= \frac{1}{N}\sum_{\boldsymbol{k}}^{N}\sum_{n}^{12}\eta^*_{\gamma_1,s,n}(\boldsymbol{k})\eta_{\gamma_2,s,n}(\boldsymbol{k}) n_{\mathrm{F}}\left[E_n(\boldsymbol{k})\right]\end{aligned} \tag{5.19}$$

where n_{F} is the Fermi-Dirac distribution and the eigenvalues are given, for each $\boldsymbol{k}$ value, in the three-orbital basis, $|\gamma, s\rangle$, as $|n(\boldsymbol{k})\rangle = \sum_{\gamma,s}\eta_{\gamma,s,n}(\boldsymbol{k})|\gamma, s\rangle$.

5.B Transformation into the J-basis

The order parameters are expressed in two alternative bases. The spin and orbital angular momenta are expressed in the basis of the three t_{2g} orbitals. The other basis considered is the total angular momentum J-basis, which is the eigenstates in the large λ limit. The transformation from the orbital and spin basis to the total angular momentum basis which is used in Eq. (5.13), i.e., $\tilde{c}_{m,\tau} = \sum_{\alpha,\sigma} U^{\alpha,\sigma}_{m,\tau} c_{\alpha,\sigma}$, is given by

$$U = \begin{pmatrix} 0 & \frac{1}{\sqrt{3}} & 0 & -\frac{i}{\sqrt{3}} & \frac{1}{\sqrt{3}} & 0 \\ \frac{1}{\sqrt{3}} & 0 & \frac{i}{\sqrt{3}} & 0 & 0 & -\frac{1}{\sqrt{3}} \\ 0 & \frac{1}{\sqrt{6}} & 0 & -\frac{i}{\sqrt{6}} & -\sqrt{\frac{2}{3}} & 0 \\ \frac{1}{\sqrt{6}} & 0 & \frac{i}{\sqrt{6}} & 0 & 0 & \sqrt{\frac{2}{3}} \\ 0 & \frac{1}{\sqrt{2}} & 0 & \frac{i}{\sqrt{2}} & 0 & 0 \\ \frac{1}{\sqrt{2}} & 0 & -\frac{i}{\sqrt{2}} & 0 & 0 & 0 \end{pmatrix} \tag{5.20}$$

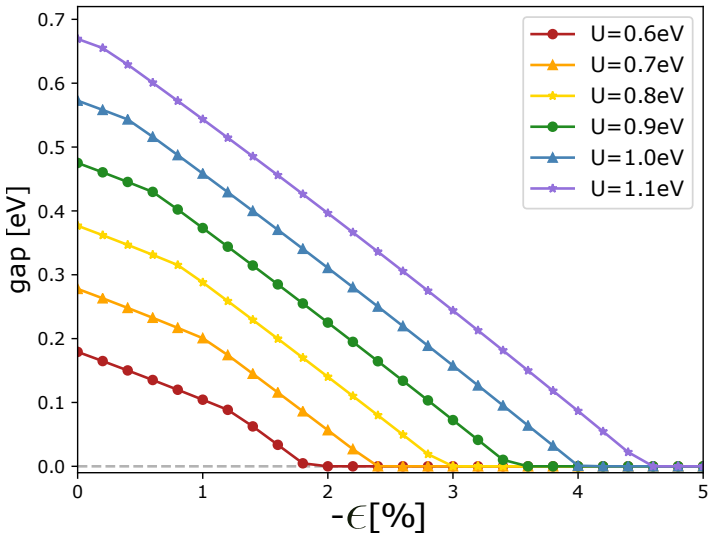

Figure 5.7: An increasing compressive strain, $\epsilon < 0$, decreases the initial insulating antiferromagnetic order. The critical strain, the value at which the gap closes, will be determined by the value of the gap at zero strain. The gap is plotted for different values of the interaction parameter U, with a Hund's coupling set to $J_H/U = 0.1$. As the mean field approximation overestimates the order at zero strain, several vales of U within the expected range are considered to get a possible range of values for the critical strain. Similarly as for the gap, the AFM order remains present at higher strains as U is increased.

where $\boldsymbol{c} = (c_{yz,\uparrow}, c_{yz,\downarrow}, c_{xz,\uparrow}, c_{xz,\downarrow}, c_{xy,\uparrow}, c_{xy,\downarrow})$ and $\tilde{\boldsymbol{c}} = (\tilde{c}_{1,+}, \tilde{c}_{1,-}, \tilde{c}_{2,+}, \tilde{c}_{2,-}, \tilde{c}_{3,+}, \tilde{c}_{3,-})$. The new basis is $\tilde{c}_{m,\tau}$ where $m : 1 = |1/2, \pm 1/2\rangle, 2 = |3/2, \pm 1/2\rangle, 3 = |3/2, \pm 3/2\rangle$ and the pseudospin projections are labelled by $\tau = \pm$.

5.C Critical strain values

The parameter choice of $U = 0.9$eV, $J_H/U = 0.1$, and $\lambda = 0.38$eV, is used for the calculation in Fig. 5.3. The values are close to the middle of the possible range for the Hund's coupling, $J_H/U = 0.05 - 0.2$, and the spin-orbit coupling, $\lambda = 0.3 - 0.7$eV, and has a value U, as well as chosen to have a gap at zero strain close to that found in experiments $\Delta_c = 0.350.65$eV [45, 46, 54, 10, 13, 55]. The critical strains, the values at which the strain-driven phase transitions occur for compressive strain, are directly dependent on the size of the initial gap. The initial gap depends on the strength of the various interaction terms, the SOC λ,

the Hund's coupling J_{H}, and the Zeeman field. Therefore the critical strain values increase with λ and U, and decrease with J_{H}.

In Fig. 5.7 we present results for calculations of the gap when the compressive strain is increased, for a range of possible values of the interaction U. The values for U are those which have replicated the zero strain band structure using other methods. As a mean field analysis tends to overestimate the antiferromagnetic order we find a gap corresponding to experimental values at zero strain for a smaller U than other methods do [15, 14, 56]. The experimental compressive strain values [23] reach up to $\epsilon = -1.9\%$, so a quantitative prediction of the transition into a metallic state should be found at higher compressive strain values. Stronger interactions U predict higher critical strain values while going through the same phase transitions. Within the limits of the mean field approximation, a prediction of a realistic band structure at zero strain and the value for critical strain will be a trade-off, and therefore a range of possible values are given here.

In Fig. 5.8 the contributions to the staggered moment are considered, with no strain, for some additional values of the spin-orbit coupling λ and the Hund's coupling J_{H}. For a higher SOC the $J = 1/2$ states, J_1 as defined in Eq. (5.14), become clearly more dominant as the J_1 net moment increases in magnitude while the other contributions decrease. This is to be expected as the SOC separates the remaining bands from those of mainly $J = 1/2$ character. A higher Hund's coupling the $J = 1/2$ states instead become less dominant as the contribution remains constant while the mixing between J-states increases.

5.D Phase diagrams with Zeeman field

A Zeeman field only has minor effects on the gap closing and the transition from the metallic AFM order to the paramagnetic state. The main effect of a Zeeman field on the strain-induced transitions is to lower the critical strain value, by reducing the indirect gap. The orbital and spin content of each band vary around some points of the Brillouin zone, which is shown in Fig. 5.2. Therefore, a Zeeman field allows for the manipulation of the band structure with possible gap closures at various points in momentum space. An in-plane field (H_x) increases the band splitting around the M-point of the Brillouin zone and an out-

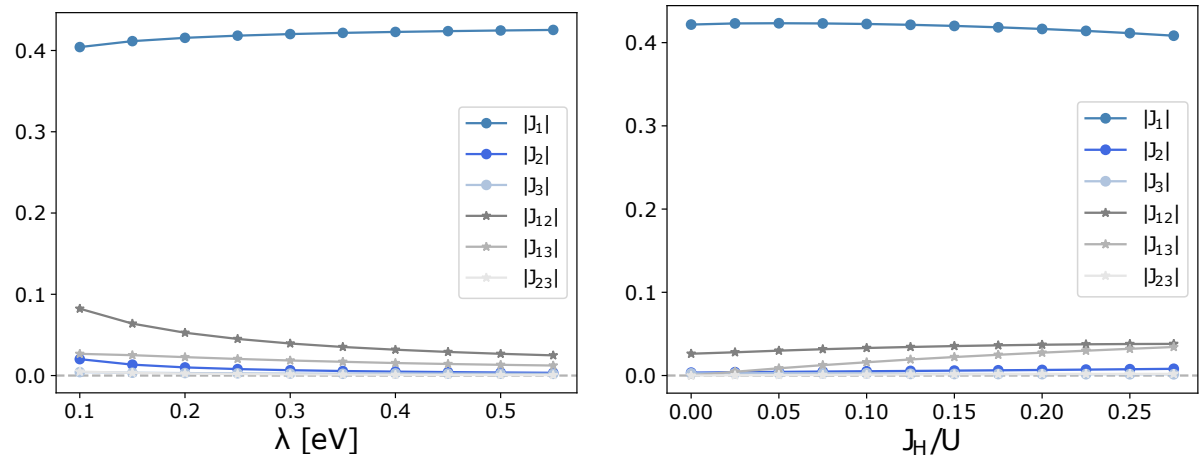

Figure 5.8: The three-orbital model used in this work allows us to consider how the contributions from each orbital changes for different sets of interaction strengths. The contributions to the staggered AFM order are shown at varying spin-orbit coupling λ at $U = 0.9$eV and $J_H/U = 0.1$ as well as for varying Hund's coupling J_H at $U = 0.9$eV and $\lambda = 0.38$. A higher λ separates out the $J = 1/2$ bands from the rest, resulting in a larger dominance of the J_1 contribution, as defined in Eq. (5.14). A larger Hund's coupling J_H increases interorbital contributions and results in a larger mixing between J-sectors, as given in Eq. (5.15).

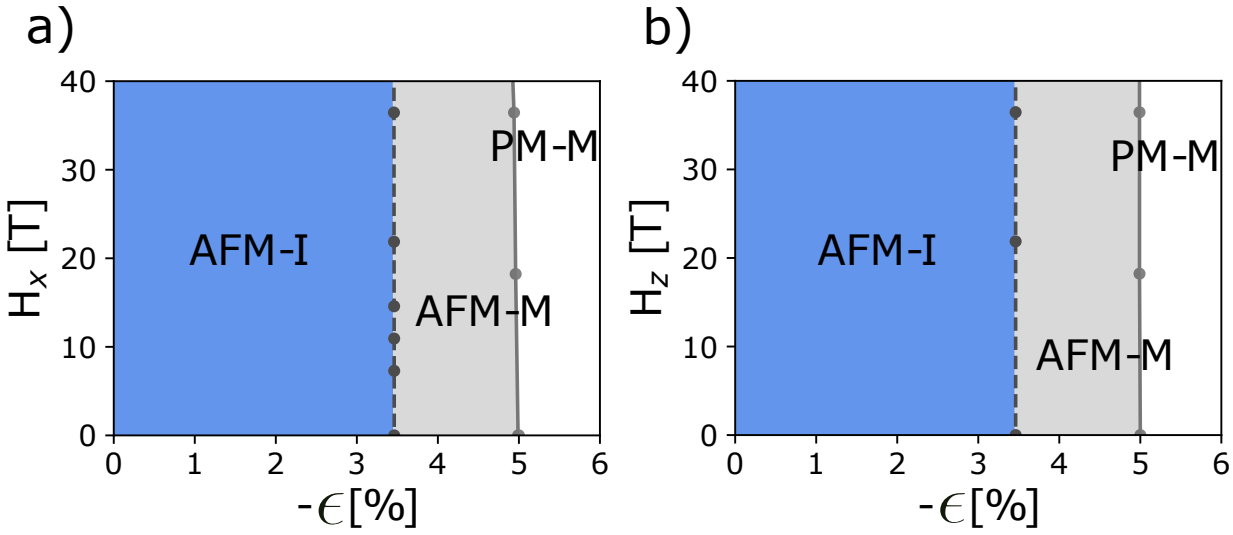

Figure 5.9: Phase transitions from the insulating AFM (AFM-I) state into metallic states occurs under compressive epitaxial strain $\epsilon < 0$. Phase diagrams are presented for a) an in-plane field along the a-direction (H_x), and b) the field is in the out-of-plane z-direction. As in Fig. 5.3 the AFM order decreases under an increasing strain until the indirect gap closes into a metallic order (AFM-M) and eventually goes through a first-order transition into a paramagnetic state (PM-M). The Zeeman field offers a minimal shift of the phase boundaries.

of-plane field (H_z) results in an increased splitting at the Γ-point. In the phase diagrams in Fig. 5.9, where compressive strain and a Zeeman field has been applied, it is however apparent that even a large field can only modify the critical strain by an amount around 0.01%. The second transition, from the antiferromagnetic metallic (AFM-M) order into the paramagnetic metal (PM-M), occurs when the antiferromagnetic order parameters have reached a low enough value. An out-of-plane field results only in a small modification of the antiferromagnetic order and the second transition remains largely unchanged. An in-plane field has a slightly larger effect due to its effect on the canting angle and can shift the transition point further, yet still to a minimal amount. Although any shifts of transition points are difficult to achieve in Sr_2IrO_4, due to the large fields required, their effects might be of interest in other systems with similar characteristics.

Bibliography

[1] W. Witczak-Krempa, G. Chen, Y. B. Kim, and L. Balents, "Correlated Quantum Phenomena in the Strong Spin-Orbit Regime," *Annual Review of Condensed Matter Physics*, vol. 5, no. 1, pp. 57–82, 2014.

[2] T. Sato, T. Shirakawa, and S. Yunoki, "Spin-orbit-induced exotic insulators in a three-orbital Hubbard model with $(t_{2g})^5$ electrons," *Phys. Rev. B*, vol. 91, p. 125122, Mar 2015.

[3] M. Kargarian, J. Wen, and G. A. Fiete, "Competing exotic topological insulator phases in transition-metal oxides on the pyrochlore lattice with distortion," *Phys. Rev. B*, vol. 83, p. 165112, Apr 2011.

[4] A. Georges, L. de' Medici, and J. Mravlje, "Strong Correlations from Hund's Coupling," *Annual Review of Condensed Matter Physics*, vol. 4, no. 1, pp. 137–178, 2013.

[5] J. G. Rau, E. K. Lee, and H. Kee, "Spin-Orbit Physics Giving Rise to Novel Phases in Correlated Systems: Iridates and Related Materials," *Annual Review of Condensed Matter Physics*, vol. 7, no. 1, pp. 195–221, 2016.

[6] G. Chen, "Dilemma in strongly correlated materials: Hund's metal vs relativistic Mott insulator," 2020.

[7] G. Cao and P. Schlottmann, "The challenge of spin–orbit-tuned ground states in iridates: a key issues review," *Reports on Progress in Physics*, vol. 81, p. 042502, feb 2018.

[8] J. Bertinshaw, Y. Kim, G. Khaliullin, and B. Kim, "Square Lattice Iridates," *Annual Review of Condensed Matter Physics*, vol. 10, pp. 315–336, mar 2019.

[9] S. Boseggia, H. C. Walker, J. Vale, R. Springell, Z. Feng, R. S. Perry, M. M. Sala, H. M. Rønnow, S. P. Collins, and D. F. McMorrow, "Locking of iridium magnetic moments to the

correlated rotation of oxygen octahedra in Sr_2IrO_4 revealed by x-ray resonant scattering," *Journal of Physics: Condensed Matter*, vol. 25, p. 422202, sep 2013.

[10] B. J. Kim, H. Jin, S. J. Moon, J.-Y. Kim, B.-G. Park, C. S. Leem, J. Yu, T. W. Noh, C. Kim, S.-J. Oh, J.-H. Park, V. Durairaj, G. Cao, and E. Rotenberg, "Novel $J_{\text{eff}} = 1/2$ Mott State Induced by Relativistic Spin-Orbit Coupling in Sr_2IrO_4," *Phys. Rev. Lett.*, vol. 101, p. 076402, Aug 2008.

[11] G. Jackeli and G. Khaliullin, "Mott Insulators in the Strong Spin-Orbit Coupling Limit: From Heisenberg to a Quantum Compass and Kitaev Models," *Phys. Rev. Lett.*, vol. 102, p. 017205, Jan 2009.

[12] F. Wang and T. Senthil, "Twisted Hubbard Model for Sr_2IrO_4: Magnetism and Possible High Temperature Superconductivity," *Phys. Rev. Lett.*, vol. 106, p. 136402, Mar 2011.

[13] B. J. Kim, H. Ohsumi, T. Komesu, S. Sakai, T. Morita, H. Takagi, and T. Arima, "Phase-Sensitive Observation of a Spin-Orbital Mott State in Sr_2IrO_4," *Science*, vol. 323, pp. 1329–1332, mar 2009.

[14] Z. Y. Meng, Y. B. Kim, and H.-Y. Kee, "Odd-Parity Triplet Superconducting Phase in Multiorbital Materials with a Strong Spin-Orbit Coupling: Application to Doped Sr_2IrO_4," *Phys. Rev. Lett.*, vol. 113, p. 177003, Oct 2014.

[15] K. Nishiguchi, T. Shirakawa, H. Watanabe, R. Arita, and S. Yunoki, "Possible Superconductivity Induced by a Large Spin–Orbit Coupling in Carrier Doped Iridium Oxide Insulators: A Weak Coupling Approach," *Journal of the Physical Society of Japan*, vol. 88, no. 9, p. 094701, 2019.

[16] Y. Yang, W.-S. Wang, J.-G. Liu, H. Chen, J.-H. Dai, and Q.-H. Wang, "Superconductivity in doped sr_2iro_4: A functional renormalization group study," *Phys. Rev. B*, vol. 89, p. 094518, Mar 2014.

[17] H. Liu and G. Khaliullin, "Pseudo-Jahn-Teller Effect and Magnetoelastic Coupling in Spin-Orbit Mott Insulators," *Phys. Rev. Lett.*, vol. 122, p. 057203, Feb 2019.

[18] A. Lupascu, J. P. Clancy, H. Gretarsson, Z. Nie, J. Nichols, J. Terzic, G. Cao, S. S. A. Seo, Z. Islam, M. H. Upton, J. Kim, D. Casa, T. Gog, A. H. Said, V. M. Katukuri, H. Stoll, L. Hozoi, J. van den Brink, and Y.-J. Kim, "Tuning Magnetic Coupling in Sr_2IrO_4 Thin Films with Epitaxial Strain," *Phys. Rev. Lett.*, vol. 112, p. 147201, Apr 2014.

[19] L. Hao, D. Meyers, M. Dean, and J. Liu, "Novel spin-orbit coupling driven emergent states in iridate-based heterostructures," *Journal of Physics and Chemistry of Solids*, vol. 128, pp. 39 – 53, 2019. Spin-Orbit Coupled Materials.

[20] L. Miao, H. Xu, and Z. Q. Mao, "Epitaxial strain effect on the Jeff $= 1/2$ moment orientation in Sr_2IrO_4 thin films," *Phys. Rev. B*, vol. 89, p. 035109, Jan 2014.

[21] S. Geprägs, B. E. Skovdal, M. Scheufele, M. Opel, D. Wermeille, P. Thompson, A. Bombardi, V. Simonet, S. Grenier, P. Lejay, G. A. Chahine, D. Q. Castro, R. Gross, and D. Mannix, "Precise control of $J_{\text{eff}} = 1/2$ magnetic properties in Sr_2IrO_4 epitaxial thin films by variation of strain and thin film thickness," 2020.

[22] C. Bhandari, Z. S. Popović, and S. Satpathy, "Electronic structure and optical properties of Sr_2IrO_4 under epitaxial strain," *New Journal of Physics*, vol. 21, p. 013036, jan 2019.

[23] A. Seo, P. P. Stavropoulos, H.-H. Kim, K. Fürsich, M. Souri, J. G. Connell, H. Gretarsson, M. Minola, H. Y. Kee, and B. Keimer, "Compressive strain induced enhancement of exchange interaction and short-range magnetic order in Sr_2IrO_4 investigated by Raman spectroscopy," *Phys. Rev. B*, vol. 100, p. 165106, Oct 2019.

[24] G. Cao, "Towards electrical-current control of quantum states in spin-orbit-coupled matter," *Journal of Physics: Condensed Matter*, vol. 32, p. 423001, jul 2020.

[25] G. Cao, H. Zhao, B. Hu, N. Pellatz, D. Reznik, P. Schlottmann, and I. Kimchi, "Quest for quantum states via field-altering technology," *npj Quantum Materials*, vol. 5, p. 83, dec 2020.

[26] J.-M. Carter, V. V. Shankar, M. A. Zeb, and H.-Y. Kee, "Semimetal and Topological Insulator in Perovskite Iridates," *Phys. Rev. B*, vol. 85, p. 115105, Mar 2012.

[27] T. Takayama, A. Matsumoto, G. Jackeli, and H. Takagi, "Model analysis of magnetic susceptibility of Sr_2IrO_4: A two-dimensional $J_{\text{eff}} = \frac{1}{2}$ Heisenberg system with competing interlayer couplings," *Phys. Rev. B*, vol. 94, p. 224420, Dec 2016.

[28] U. F. P. Seifert and L. Balents, "Optical excitation of magnons in an easy-plane antiferromagnet: Application to Sr_2IrO_4," *Phys. Rev. B*, vol. 100, p. 125161, Sep 2019.

[29] J. Porras, J. Bertinshaw, H. Liu, G. Khaliullin, N. H. Sung, J.-W. Kim, S. Francoual, P. Steffens, G. Deng, M. M. Sala, A. Efimenko, A. Said, D. Casa, X. Huang, T. Gog, J. Kim, B. Keimer, and B. J. Kim, "Pseudospin-lattice coupling in the spin-orbit Mott insulator Sr_2IrO_4," *Phys. Rev. B*, vol. 99, p. 085125, Feb 2019.

[30] G. Cao, J. Bolivar, S. McCall, J. E. Crow, and R. P. Guertin, "Weak ferromagnetism, metal-to-nonmetal transition, and negative differential resistivity in single-crystal Sr_2IrO_4," *Phys. Rev. B*, vol. 57, pp. R11039–R11042, May 1998.

[31] M. Nauman, Y. Hong, T. Hussain, M. S. Seo, S. Y. Park, N. Lee, Y. J. Choi, W. Kang, and Y. Jo, "In-plane magnetic anisotropy in strontium iridate Sr_2IrO_4," *Phys. Rev. B*, vol. 96, p. 155102, Oct 2017.

[32] A. Rathi, P. Rout, S. Perween, R. Singh, P. Babu, A. Gupta, R. Pant, and G. Basheed, "Signature of a Griffiths phase in layered canted antiferromagnet Sr_2IrO_4," *Journal of Magnetism and Magnetic Materials*, vol. 468, pp. 230 – 234, 2018.

[33] S. T. Rodan, S. Yoon, S. Lee, K.-Y. Choi, G. Kim, J.-S. Rhyee, A. Koda, W.-T. Chen, and F. Chou, "Quantum critical nature of the short-range magnetic order in $Sr_{2-x}La_xIrO_4$," *Phys. Rev. B*, vol. 98, p. 214412, Dec 2018.

[34] D. Haskel, G. Fabbris, M. Zhernenkov, P. P. Kong, C. Q. Jin, G. Cao, and M. van Veenendaal, "Pressure Tuning of the Spin-Orbit Coupled Ground State in Sr_2IrO_4," *Phys. Rev. Lett.*, vol. 109, p. 027204, Jul 2012.

[35] J. Jeong, B. Lenz, A. Gukasov, X. Fabrèges, A. Sazonov, V. Hutanu, A. Louat, D. Bounoua, C. Martins, S. Biermann, V. Brouet, Y. Sidis, and P. Bourges, "Magnetization Density Distribution of Sr_2IrO_4: Deviation from a Local $j_{\text{eff}} = 1/2$ Picture," *Phys. Rev. Lett.*, vol. 125, p. 097202, Aug 2020.

[36] J.-M. Carter, V. Shankar V., and H.-Y. Kee, "Theory of metal-insulator transition in the family of perovskite iridium oxides," *Phys. Rev. B*, vol. 88, p. 035111, Jul 2013.

[37] J. C. Slater and G. F. Koster, "Simplified LCAO Method for the Periodic Potential Problem," *Phys. Rev.*, vol. 94, pp. 1498–1524, Jun 1954.

[38] S. Mohapatra and A. Singh, "Correlated motion of particle-hole excitations across the renormalized spin-orbit gap in Sr_2IrO_4," *Journal of Magnetism and Magnetic Materials*, vol. 512, p. 166997, 2020.

[39] N. B. Perkins, Y. Sizyuk, and P. Wölfle, "Interplay of many-body and single-particle interactions in iridates and rhodates," *Phys. Rev. B*, vol. 89, p. 035143, Jan 2014.

[40] P. Liu, S. Khmelevskyi, B. Kim, M. Marsman, D. Li, X.-Q. Chen, D. D. Sarma, G. Kresse, and C. Franchini, "Anisotropic magnetic couplings and structure-driven canted to collinear transitions in Sr_2IrO_4 by magnetically constrained noncollinear DFT," *Phys. Rev. B*, vol. 92, p. 054428, Aug 2015.

[41] D. H. Torchinsky, H. Chu, L. Zhao, N. B. Perkins, Y. Sizyuk, T. Qi, G. Cao, and D. Hsieh, "Structural Distortion-Induced Magnetoelastic Locking in Sr_2IrO_4 Revealed through Nonlinear Optical Harmonic Generation," *Phys. Rev. Lett.*, vol. 114, p. 096404, Mar 2015.

[42] H. Zhang, K. Haule, and D. Vanderbilt, "Effective J=1/2 Insulating State in Ruddlesden-Popper Iridates: An LDA+DMFT Study," *Phys. Rev. Lett.*, vol. 111, p. 246402, Dec 2013.

[43] E. Paris, Y. Tseng, E. M. Pärschke, W. Zhang, M. H. Upton, A. Efimenko, K. Rolfs, D. E. McNally, L. Maurel, M. Naamneh, M. Caputo, V. N. Strocov, Z. Wang, D. Casa, C. W. Schneider, E. Pomjakushina, K. Wohlfeld, M. Radovic, and T. Schmitt, "Strain engineering of the charge and spin-orbital interactions in Sr_2IrO_4," *Proceedings of the National Academy of Sciences*, vol. 117, no. 40, pp. 24764–24770, 2020.

[44] J. Kanamori, "Electron Correlation and Ferromagnetism of Transition Metals," *Progress of Theoretical Physics*, vol. 30, pp. 275–289, sep 1963.

[45] S. Zhou, K. Jiang, H. Chen, and Z. Wang, "Correlation Effects and Hidden Spin-Orbit Entangled Electronic Order in Parent and Electron-Doped Iridates Sr_2IrO_4," *Phys. Rev. X*, vol. 7, p. 041018, Oct 2017.

[46] H. Watanabe, T. Shirakawa, and S. Yunoki, "Microscopic Study of a Spin-Orbit-Induced Mott Insulator in Ir Oxides," *Physical Review Letters*, vol. 105, p. 216410, nov 2010.

[47] S. Chikara, O. Korneta, W. P. Crummett, L. E. DeLong, P. Schlottmann, and G. Cao, "Giant magnetoelectric effect in the $J_{\text{eff}} = \frac{1}{2}$ Mott insulator Sr_2IrO_4," *Phys. Rev. B*, vol. 80, p. 140407(R), Oct 2009.

[48] S. Fujiyama, H. Ohsumi, T. Komesu, J. Matsuno, B. J. Kim, M. Takata, T. Arima, and H. Takagi, "Two-Dimensional Heisenberg Behavior of J_{eff}=1/2 Isospins in the Paramagnetic State of the Spin-Orbital Mott Insulator Sr_2IrO_4," *Phys. Rev. Lett.*, vol. 108, p. 247212, Jun 2012.

[49] J. Dai, E. Calleja, G. Cao, and K. McElroy, "Local density of states study of a spin-orbit-coupling induced Mott insulator Sr_2IrO_4," *Phys. Rev. B*, vol. 90, p. 041102(R), Jul 2014.

[50] F. Ye, S. Chi, B. C. Chakoumakos, J. A. Fernandez-Baca, T. Qi, and G. Cao, "Magnetic and crystal structures of Sr_2IrO_4: A neutron diffraction study," *Phys. Rev. B*, vol. 87, p. 140406(R), Apr 2013.

[51] B. Kim, B. H. Kim, K. Kim, and B. I. Min, "Substrate-tuning of correlated spin-orbit oxides revealed by optical conductivity calculations," *Scientific Reports*, vol. 6, p. 27095, jun 2016.

[52] M. Souri, J. G. Connell, J. Nichols, J. Terzic, G. Cao, and A. Seo, "Crossover between Mott and Efros-Shklovskii variable-range hopping in Sr_2IrO_4 epitaxial thin films by misfit strain and isovalent doping," *Journal of Applied Physics*, vol. 126, no. 18, p. 185101, 2019.

[53] D. Haskel, G. Fabbris, J. H. Kim, L. S. I. Veiga, J. R. L. Mardegan, C. A. Escanhoela, S. Chikara, V. Struzhkin, T. Senthil, B. J. Kim, G. Cao, and J.-W. Kim, "Possible Quantum Paramagnetism in Compressed Sr_2IrO_4," *Phys. Rev. Lett.*, vol. 124, p. 067201, Feb 2020.

[54] J. C. Wang, S. Aswartham, F. Ye, J. Terzic, H. Zheng, D. Haskel, S. Chikara, Y. Choi, P. Schlottmann, R. Custelcean, S. J. Yuan, and G. Cao, "Decoupling of the antiferromagnetic and insulating states in Tb-doped Sr_2IrO_4," *Phys. Rev. B*, vol. 92, p. 214411, Dec 2015.

[55] B. H. Kim, G. Khaliullin, and B. I. Min, "Magnetic Couplings, Optical Spectra, and Spin-Orbit Exciton in $5d$ Electron Mott Insulator Sr_2IrO_4," *Phys. Rev. Lett.*, vol. 109, p. 167205, Oct 2012.

[56] B. Lenz, C. Martins, and S. Biermann, "Spectral functions of Sr_2IrO_4: theory versus experiment," *Journal of Physics: Condensed Matter*, vol. 31, p. 293001, may 2019.

Preface to Chapter 6

The goal of this chapter is to model superconductivity in Sr_2IrO_4 under a combination of doping and compressive strain. Strain-enhanced or strain-induced superconductivity is a phenomenon observed in several known superconductors. In the cuprates YBCO and LSCO compressive strain leads to an increased T_c [1]. In organic superconductors compressive strain can instead induce a superconductivity/insulator phase transition [2]. A similar result has been predicted theoretically in Sr_2RuO_4 [3]. Depending on the active orbitals in the compound a compressive strain can either increase or decrease the overall bandwidth. As a rough estimate the change to hopping parameters is linear with strain. On-site interactions remain largely unaffected while longer range interactions can increase/decrease roughly proportional to the strain [4]. As such, compressive strain decreases the hopping in cuprates [1]. On the other hand, the strain increases the hopping in some organic superconductors [2]. The study of magnetism in undoped Sr_2IrO_4 under compressive strain, in the previous chapter, concludes that the increased bandwidth is sufficient to induce a phase transition. As superconductivity has previously been predicted under doping, the next step is to consider the combination of strain and doping to see if a strain-induced superconducting region is possible.

In Chapter 5 only one set of values were considered for the interaction parameters U, J_H and for the spin-orbit coupling. They were chosen to be realistic for undoped Sr_2IrO_4. The previously predicted $j = 1/2$ d-wave is expected to be possible for those values and electron doping, just by considering an effective one-orbital model. In the second publication of this thesis, Chapter 6, superconductivity is modeled in Sr_2IrO_4 under doping and compressive strain with an effective pairing interaction calculated via the random phase approximation, as in section 4.3. In this Chapter we aim to answer the questions: Can superconductivity

be induced by compressive strain? Are the $j = 1/2$ bands sufficient to model such a superconductivity?

The reason for this approach is two-fold. Firstly, the Fermi surfaces found in Chapter 5 at compressive strain have bands of $j = 1/2$ character and $j = 3/2$ character, and not just $j = 1/2$ as for the unstrained case. The effective interaction is highly dependent on screening from states close to the Fermi surface. A significant change to the interaction is therefore expected as the compressive strain increases. Secondly, there are additional effects to chemical doping that can result in changes to the values of the spin-orbit and Hund's coupling. As previous studies have found, see section 2.2, multiple superconducting symmetries can be possible when changing the interaction parameters in doped Sr_2IrO_4. Strain allows us additional manipulation of which orbitals are close to the Fermi surface, as well as manipulation of the Fermi surface topology. The possibility for superconductivity should therefore be modeled for an effective interaction that depends on the multi-orbital interaction and hopping parameters.

The manuscript in Chapter 6 is the first work to study both a multi-orbital model and the staggered rotations in the structure of Sr_2IrO_4. As it expands upon the model used in [5] the hopping parameters in the non-interacting model are given an overall scaling $t = 0.211\text{eV} \rightarrow t = 0.36\text{eV}$, to be comparable. The calculations are performed at a finite temperature, $T \approx 11\text{K}$, compared to the previous chapter where $T = 0\text{K}$. A phase diagram for both electron and hole doping with compressive strain is considered for the most realistic parameters to get results that can be of interest to future experiments. These parameters are informed by the calculations in Chapter 5, as the renormalization of the SOC in the interacting system has been accounted for. Further comparison of the inclusion of this effect is included in Appendix B. Chapter 6 also includes a wider phase diagram showing how the combination of SOC, Hund's coupling, and Hubbard interactions of comparable size results in several new magnetic and superconducting orders. Even though the phase diagrams are less realistic for Sr_2IrO_4, they are of wider theoretical interest, as other multi-orbital superconductors have a non-negligible spin-orbit coupling.

Bibliography

[1] R. Hühne, D. Okai, K. Dörr, S. Trommler, A. Herklotz, B. Holzapfel, and L. Schultz, "Dynamic investigations on the influence of epitaxial strain on the superconducting transition in $YBa_2Cu_3O_{7-x}$," *Superconductor Science and Technology*, vol. 21, no. 7, 2008.

[2] Y. Kawasugi, H. M. Yamamoto, M. Hosoda, N. Tajima, T. Fukunaga, K. Tsukagoshi, and R. Kato, "Strain-induced superconductor/insulator transition and field effect in a thin single crystal of molecular conductor," *Applied Physics Letters*, vol. 92, no. 24, pp. 24–26, 2008.

[3] Y. C. Liu, W. S. Wang, F. C. Zhang, and Q. H. Wang, "Superconductivity in Sr_2RuO_4 thin films under biaxial strain," *Physical Review B*, vol. 97, no. 22, pp. 1–10, 2018.

[4] X. Wang, H. Li, Y. Huang, Z. Dong, C. Zhong, and J. Liu, "Tuning tetrahedral structure and electronic properties of FeSe films through strain engineering," *Journal of Physics and Chemistry of Solids*, vol. 145, no. May, p. 109541, 2020.

[5] K. Nishiguchi, T. Shirakawa, H. Watanabe, R. Arita, and S. Yunoki, "Possible Superconductivity Induced by a Large Spin–Orbit Coupling in Carrier Doped Iridium Oxide Insulators: A Weak Coupling Approach," *Journal of the Physical Society of Japan*, vol. 88, p. 094701, sep 2019.

Chapter 6

Strain-induced superconductivity in Sr_2IrO_4

Lena Engström, Chia-Chuan Liu, William Witczak-Krempa, and T. Pereg-Barnea

Reprinted article with permission from L. Engström, C.-C. Liu, W. Witczak-Krempa, and T. Pereg-Barnea. A preprint is available as arXiv:2212.07596.

Abstract

Multi-orbital quantum materials with strong interactions can host a variety of novel phases. In this work we study the possibility of interaction-driven superconductivity in the iridate compound Sr_2IrO_4 under strain and doping. We find numerous regimes of strain-induced superconductivity in which the pairing structure depends on model parameters. Spin-fluctuation mediated superconductivity is modeled by a Hubbard-Kanamori model with an effective particle-particle interaction, calculated via the random phase approximation. Magnetic orders are found using the Stoner criterion. The most likely superconducting order we find has d-wave pairing, predominantly in the total angular momentum, $J = 1/2$ states. Moreover, an $s_{\pm}$-order which mixes different bands is found at high Hund's coupling, and at high strain anisotropic s- and d-wave orders emerge. Finally, we show that in a fine-tuned region of parameters a spin-triplet p-wave order exists. The combination of strong spin-orbit coupling, interactions, and a sensitivity of the band structure to strain proves a fruitful avenue for engineering new quantum phases.

6.1 Introduction

The iridates display a rich phase diagram due to an interplay between strong correlations, spin-orbit coupling, and crystal field effects, all acting on multiple d-orbitals which in some cases lead to multiple Fermi surfaces. Various iridates show novel phenomena such as Kitaev and Weyl physics [1, 2, 3]. The first compound in the family of Ruddlesden-Popper perovskite strontium iridates, Sr_2IrO_4, consists of stacked quasi-2d layers. In each layer, the iridium atoms form a square lattice, and are surrounded by octahedra of oxygen atoms. As shown in Fig. 6.1, every other IrO_6 octahedron is rotated by an angle of $\phi = \pm\phi_{\epsilon=0} \approx \pm 12^\circ$ relative to the iridate lattice and we therefore use a two-site basis [4]. In Sr_2IrO_4 the three t_{2g} orbitals are located close to the Fermi surface. However, due to a strong spin-orbit coupling the resulting band structure is better characterized by the on-site total angular momentum J eigenstates, with $J = 1/2$ states having $J_z = \pm 1/2$ and $J = 3/2$ having the projections along the z-axis $J_z = \pm 1/2, \pm 3/2$. We refer to this basis as the j-states. For the undoped compound the electron filling is $n = 5$, out of the 6 t_{2g} bands per site, and an antiferromagnetic insulator

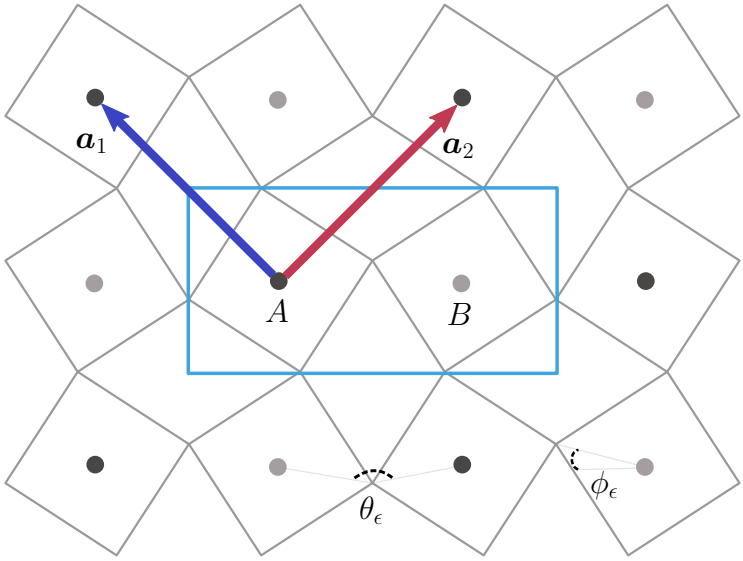

Figure 6.1: Single plane of Sr_2IrO_4 where the iridium atoms (gray) form a square lattice, and are surrounded by oxygen octahedra. There are two sites in the unit cell $s = A, B$ with staggered rotations ϕ_ϵ of the octahedra, resulting in a bond angle $\theta_\epsilon = 180° - 2\phi_\epsilon$. The staggered rotation angle increases with compressive strain $\phi_\epsilon > \phi_{\epsilon=0}$, with $\phi_{\epsilon=0} \approx 12°$.

is found up to $T_N = 240$ K [5]. For this state, the two bands of mainly $j = 1/2$ character are half-filled and located close to the Fermi surface while additional bands of $j = 3/2$ character are further from the Fermi level [6].

Experimentally, Sr_2IrO_4 shows Fermi arcs and a pseudogap under electron doping [7, 8] as well as non-Fermi liquid behavior under hole doping [8]. Superconductivity has been predicted for both types of charge doping of Sr_2IrO_4 in multiple theoretical works [9, 10, 11, 12, 13, 14]. At a first approximation the band structure and the interactions suggest a direct parallel to known high T_c superconductors, the cuprates. Indeed, projecting the Hamiltonian on the $j = 1/2$ states results in a model similar to those used to describe the cuprates [15] and a simplified one-band model therefore predicts d-wave superconductivity for electron doped Sr_2IrO_4 [9]. However, theoretical studies of Sr_2IrO_4 found that d-wave superconductivity is likely to arise only in a limited range of interaction parameters. At hole doping, additional pockets of $j = 3/2$ character appear at the Fermi level. In this region of the phase diagram, previous studies have predicted Sr_2IrO_4 to have either multi-band $s_\pm$-wave or a p-wave pairing. However, as of yet no superconducting order has been experimentally

confirmed for Sr_2IrO_4 when chemical doping is the only tuneable parameter [16, 17, 18, 19]. The question then remains whether there could be a tuning parameter that would make superconductivity more favorable.

The local staggered rotations of iridium sites introduce an in-plane translation symmetry breaking accompanied by additional hybridization of orbitals. These effects have been previously ignored in multi-orbital models of iridate superconductivity [20]. The rotations increase under compression and as a result the hopping between orbitals at neighboring sites is modified to reflect the new geometry [21, 4, 22, 23, 24]. Moreover, the orbitals are modified by different amounts such that the bands belonging to the $j = 3/2$ subspace move closer to the Fermi surface [25]. Naturally, the number of Fermi pockets and their orbital composition are important factors for superconductivity. As the undoped Sr_2IrO_4 is an antiferromagnetic insulator, a prerequisite for any superconducting order is that it must exist in a regime where the system is no longer magnetic. Several experimental studies have shown that by growing Sr_2IrO_4 on a substrate with mismatched lattice parameters, the induced compressive epitaxial strain significantly suppresses the magnetic order [26, 27, 28, 29, 30, 31]. In a variety of known superconductors biaxial, either compressive or tensile, strain has proven to increase the critical temperature [32, 33, 34, 35, 36] or to induce a superconductivity/insulator phase transition [37, 38]. In the current work compressive strain is suggested to induce the same type of phase transition and could thus expand the region of doping where superconductivity can be observed. The purpose of our study is therefore to determine if superconductivity is more likely when strain is applied. More precisely, we aim to answer the following two questions. First, are there regimes of applied strain where a superconducting order is possible? Second, does the in-plane symmetry breaking due to the rotations result in different superconducting orders?

Experiments in undoped Sr_2IrO_4 under high hydrostatic pressure have been performed in recent years [39, 40, 41]. While both hydrostatic pressure and epitaxial strain change the interatomic distances, they do so in different ways. The experiments approximate the pressure to strain conversion to be $(\Delta a/a)/\Delta P = -0.146\%/\text{GPa}$ [39]. A transition into a non-magnetic insulating state occurs under a compression of 17GPa. At sufficient pressure

beyond that the resistivity shows a rapid increase accompanied by a pressure-induced structural phase transition [39, 40]. However, it is important to remember that while the effect on in-plane distances is similar, hydrostatic pressure decreases the inter-layer distance while epitaxial strain increases it [31]. In the hydrostatic pressure, the c-axis compression increases interactions between perovskite layers while the epitaxial strain does not. A persistent insulating state is thus not expected in the realistic regimes of our phase diagrams. In addition, our region of interest is for charge doping, where the insulating nature of the compound is weaker.

Spin-fluctuations are believed to be able to mediate superconductivity in the iridates [12, 14]. Multi-orbital superconductivity has successfully been modeled with spin-fluctuations in other families of materials such as ruthenates [42, 43, 44] and iron-based superconductors [45, 46]. In this work, a linearized superconducting gap equation (in the static limit) is solved to find regimes where superconductivity is possible. We consider a multi-orbital Hubbard-Kanamori model of Sr_2IrO_4 in a rotated two-site basis. The spin susceptibility is calculated via the random phase approximation (RPA). The spin fluctuations are thus dependent on the staggered sublattice rotations. As the rotations increase with an increasing strain and the RPA susceptibility is used to derive the effective particle-particle interaction, the interaction is dependent on the strain. This in turn results in a strain-dependent linearized gap equation for the superconducting order. Magnetic orders can be identified via the RPA susceptibility. We find a large region of strain-induced superconductivity, as well as several possible magnetic orders. The different types of superconducting order are either mediated by spin or pseudospin fluctuations. We find that as the compressive strain is increased the fluctuations become more spin-like in character. Although several types of fluctuations compete in parts of the calculated phase diagrams, the most prevalent type is antiferromagnetic fluctuations in the $j = 1/2$ state. These pseudospin fluctuations can mediate a d-wave order. Longer range fluctuations in the spin basis instead mediate the $s_{\pm}$-wave superconductivity. For high compressive strain, intraorbital spin fluctuations can become large enough to mediate anisotropic superconducting orders. All superconductivity in the calculated phase diagrams are mediated by fluctuations of spins oriented in-plane. However, there exists regions where

ferromagnetic out-of-plane fluctuations are of equal size. The ferromagnetic fluctuations are found to mediate an odd parity p-wave order.

The paper is structured as follows. In section 6.2, we introduce the underlying tight-binding Hamiltonian of Sr_2IrO_4 and how the compressive strain is modeled. In subsection 6.2.2, the model for superconductivity mediated by spin-fluctuations is introduced. The resulting phase diagram is presented in section 6.3, for realistic values of model parameters. Additional phase diagrams are shown for a wider variety of possible values for the Hund's and spin-orbit coupling. We then analyze the nature of the magnetic fluctuations in section 6.4. The types of superconducting orders, and the fluctuations believed to mediate them, are detailed in section 6.5. Finally, in section 5.4 we discuss the experimental possibilities of strain-induced superconductivity, and signatures of the found orders.

6.2 Model and methods

6.2.1 Kinetic Hamiltonian with rotations

The band structure of Sr_2IrO_4 can be modeled by a spin-orbit coupled tight-binding Hamiltonian:

$$H = H_{\text{kin}} + H_{\text{SOC}} \tag{6.1}$$

We consider a 2-site orbital-spin basis: $\boldsymbol{c} = (c_{\boldsymbol{k},A,yz,\uparrow},\ c_{\boldsymbol{k},A,yz,\downarrow},\ c_{\boldsymbol{k},A,xz,\uparrow},\ c_{\boldsymbol{k},A,xz,\downarrow},\ c_{\boldsymbol{k},A,xy,\uparrow},\ c_{\boldsymbol{k},A,xy,\downarrow},\ c_{\boldsymbol{k},B,yz,\uparrow},\ c_{\boldsymbol{k},B,yz,\downarrow},\ c_{\boldsymbol{k},B,xz,\uparrow},\ c_{\boldsymbol{k},B,xz,\downarrow},\ c_{\boldsymbol{k},B,xy,\uparrow},\ c_{\boldsymbol{k},B,xy,\downarrow})$. For each spin $\sigma =\uparrow,\downarrow$ the kinetic terms have intra- and inter-sublattice hopping:

$$H_{\text{kin}} = \begin{pmatrix} H_{AA} & e^{ik_x} H_{AB} \\ e^{-ik_x} H_{AB}^{\dagger} & H_{BB} \end{pmatrix} \tag{6.2}$$

$$H_{AA} = \begin{pmatrix} \epsilon_d & \epsilon_{1d} & 0 \\ \epsilon_{1d} & \epsilon_d & 0 \\ 0 & 0 & \epsilon_d^{xy} \end{pmatrix}, H_{AB} = \begin{pmatrix} \epsilon_{yz} & -\epsilon_{rot} & 0 \\ \epsilon_{rot} & \epsilon_{xz} & 0 \\ 0 & 0 & \epsilon_{xy} \end{pmatrix} \tag{6.3}$$

and $H_{BB} = H_{AA}$. The factor e^{ik_x} arises from the choice of unit cell, where the two sublattice sites are chosen as in Fig. 6.1 and the lattice spacing, a, is set to 1. The hopping terms are

$$\begin{aligned}
\epsilon_{xy} &= 2t\,(\cos k_x + \cos k_y) \\
\epsilon_{yz} &= 2\,(t_\delta \cos k_x + t_1 \cos k_y) \\
\epsilon_{xz} &= 2\,(t_1 \cos k_x + t_\delta \cos k_y) \\
\epsilon_{rot} &= 2t'\,(\cos k_x + \cos k_y) \\
\epsilon_d^{xy} &= 4t_n \cos k_x \cos k_y + \mu_{xy} \\
\epsilon_{1d} &= 4t_{1d} \sin k_x \sin k_y \\
\epsilon_d &= 4t_{nd} \cos k_x \cos k_y.
\end{aligned} \tag{6.4}$$

The hopping values are $(t, t_1, t_\delta, t',\ t_n, t_{1d}, t_{nd}, \mu_{xy}) = -0.36(1, 0.882, 0.260, 0.199, 0.559, 0.019, -0.010, 0.7)$eV, when no strain is applied. The staggered rotations result in the non-zero inter-orbital hopping, ϵ_{rot} and ϵ_{1d}, between the yz- and xz-orbitals. When the compressive strain, $\epsilon < 0$, is increased the hopping parameters change. We use a linear strain dependence as in Ref. [25], following data by Ref. [31]:

$$\begin{aligned}
t(\epsilon) &= t\,(1 + \rho\epsilon) \\
t_1(\epsilon) &= t_1\,(1 + \rho_1\epsilon) \\
t'(\epsilon) &= t'\,(1 + \rho'\epsilon) \\
t_n(\epsilon) &= t_n\,(1 + \rho_n\epsilon) \\
t_\delta(\epsilon) &= t_\delta\,(1 + \rho_\delta\epsilon) \\
t_{1d}(\epsilon) &= t_{1d}\,(1 + \rho_{1d}\epsilon) \\
t_{nd}(\epsilon) &= t_{nd}\,(1 + \rho_{nd}\epsilon) \\
\phi_\epsilon &= \phi_{\epsilon=0}\,(1 + \rho_\phi\epsilon)
\end{aligned} \tag{6.5}$$

with $(\rho, \rho_1, \rho', \rho_n, \rho_\delta, \rho_{1d}, \rho_{nd}, \rho_\phi) = (0.014, -0.251,\ -0.309,\ -0.048,\ 0,\ 0, -0.02, -0.085)$. ϕ_ϵ is angle of the staggered rotations. The approximation considers not only rigid rotations of the oxygen octahedra but also changes in bond lengths, as was recently proposed to be a more accurate description of the strain effect in Ref. [47]. The strain, and the associated

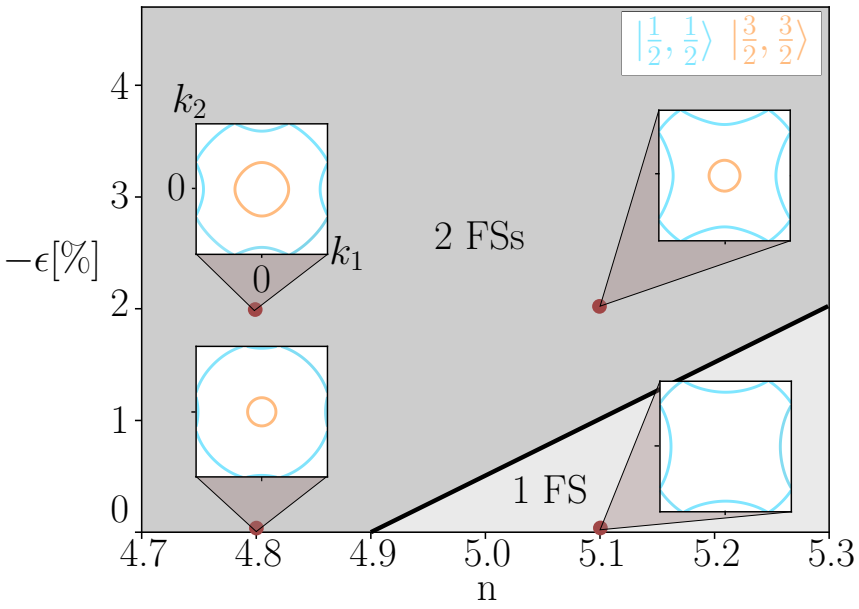

Figure 6.2: The Fermi surface (FS) or surfaces are shown as a function of strain and doping. There are one or two types of pockets whose spin and orbital character is indicated by color. These are found by diagonalizing the non-interacting model in Eq. (6.1). The number of pockets and a few examples of the Fermi surface are shown for $\lambda = 0.6$eV. The pocket of $j = 3/2$ character is only present at hole doping $n \leq 4.9$ at $\epsilon = 0$. For increasing compressive strain two types of pockets are present for all doping.

rotations of the octahedra, increase the inter-orbital t' and intra-orbital t_1. On the other hand hopping within the xy-orbital decreases. The effect of strain on the tetragonal splitting μ_{xy} is not discussed here and is deferred to Appendix 6.C. It has been well-established that the spin-orbit coupling in Sr_2IrO_4 is large enough for each band to have a clear character of either total angular momenta $j = 1/2$ or $j = 3/2$. The atomic SOC is

$$H_{\text{SOC}} = \frac{\lambda}{2} \sum_{\alpha\beta,\sigma\sigma'} \sum_{s=A,B} \boldsymbol{L}_{\alpha\beta} \cdot \boldsymbol{\sigma}_{\sigma\sigma'} c^{\dagger}_{\boldsymbol{k}s\alpha\sigma} c_{\boldsymbol{k}s\beta\sigma'} \tag{6.6}$$

where $\boldsymbol{\sigma} = (\sigma^x, \sigma^y, \sigma^z)$ are the Pauli matrices in the spin basis $\sigma = \uparrow, \downarrow$ with respect to the z-direction, and

$$\boldsymbol{L} = \left(\begin{bmatrix} 0 & 0 & 0 \\ 0 & 0 & -i \\ 0 & i & 0 \end{bmatrix}, \begin{bmatrix} 0 & 0 & i \\ 0 & 0 & 0 \\ -i & 0 & 0 \end{bmatrix}, \begin{bmatrix} 0 & -i & 0 \\ i & 0 & 0 \\ 0 & 0 & 0 \end{bmatrix} \right). \tag{6.7}$$

The eigenstates of H_{SOC} are the j-states, with associated annihilation operators: $\boldsymbol{a}_{m,\tau} = \sum_{\alpha,\sigma} M_{(m,\tau),(\alpha,\sigma)} \boldsymbol{c}_{\alpha,\sigma}$. Where

$$M = \begin{pmatrix} 0 & \frac{1}{\sqrt{3}} & 0 & -\frac{i}{\sqrt{3}} & \frac{1}{\sqrt{3}} & 0 \\ \frac{1}{\sqrt{3}} & 0 & \frac{i}{\sqrt{3}} & 0 & 0 & -\frac{1}{\sqrt{3}} \\ 0 & \frac{1}{\sqrt{6}} & 0 & -\frac{i}{\sqrt{6}} & -\sqrt{\frac{2}{3}} & 0 \\ -\frac{1}{\sqrt{6}} & 0 & -\frac{i}{\sqrt{6}} & 0 & 0 & -\sqrt{\frac{2}{3}} \\ 0 & -\frac{1}{\sqrt{2}} & 0 & -\frac{i}{\sqrt{2}} & 0 & 0 \\ \frac{1}{\sqrt{2}} & 0 & -\frac{i}{\sqrt{2}} & 0 & 0 & 0 \end{pmatrix} \tag{6.8}$$

with $\boldsymbol{c}_{\alpha,\sigma} = (c_{yz,\uparrow}, c_{yz,\downarrow}, c_{xz,\uparrow}, c_{xz,\downarrow}, c_{xy,\uparrow}, c_{xy,\downarrow})$ and $\boldsymbol{a}_{m,\tau} = (a_{1,+}, a_{1,-}, a_{2,+}, a_{2,-}, a_{3,+}, a_{3,-})$. In this basis each site has the states $a_{m,\tau}$, where m denotes the total angular momentum and its z-axis projection (j, j_z) such that $1 = \left(\frac{1}{2}, \pm\frac{1}{2}\right), 2 = \left(\frac{3}{2}, \pm\frac{1}{2}\right), 3 = \left(\frac{3}{2}, \pm\frac{3}{2}\right)$ and the projections along the z-axis are labeled by $\tau = \pm$. The projections τ can be treated as pseudospins, here not mixing sublattice and spin degrees of freedom but orbital and spin [48]. The total of 12 bands $b_{\boldsymbol{k},n}$ have eigenvalues $\xi_{\boldsymbol{k},n}$ and are connected to the orbital basis via $c_{\boldsymbol{k},j} = \sum_n U_{\boldsymbol{k},jn} b_{\boldsymbol{k},n}$. The only spin-mixing in the Hamiltonian comes from the atomic spin-orbit coupling and all hopping terms are pseudospin-conserving. The non-interacting Hamiltonian is therefore separable into pseudospin $\tau = +, -$ sectors, containing the states $\{(yz,\downarrow), (xz,\downarrow), (xy,\uparrow)\}$ and $\{(yz,\uparrow), (xz,\uparrow), (xy,\downarrow)\}$ respectively. Therefore the 12 bands can be described by 6 bands in each pseudospin-sector n_τ.

As the strain modifies the hopping parameters, both the shape and the number of pockets at the Fermi surface changes. Therefore the Fermi surface is different at every point in the phase diagrams. As can be seen in Figs. 6.2, there are pockets belonging to the bands of $(j, j_z) = \left(\frac{1}{2}, \pm\frac{1}{2}\right)$ present at every point in the phase diagram. For fillings corresponding to hole doping, $n < 5$, another pocket with $(j, j_z) = \left(\frac{3}{2}, \pm\frac{3}{2}\right)$ appears around $(k_1, k_2) = (0, 0)$.

The strain increases the bandwidth and cause the $(\frac{3}{2}, \pm\frac{3}{2})$ pocket to appear for all doping values. As shown further in Appendix 6.B the size of the $j = 1/2$ electron pocket increases with strain.

6.2.2 Spin-fluctuation mediated superconductivity

To analyze the possibility of spin fluctuation mediated superconductivity, we solve a linearized gap equation in the static limit and normal state. A similar calculation has been performed previously for Sr_2IrO_4 in Ref. [14], for a model without staggered rotations or strain. In general, the particle-hole and particle-particle self-energies are defined by the Dyson-Gorkov equation:

$$\boldsymbol{G}(k) = \boldsymbol{G}^{(0)}(k) + \boldsymbol{G}^{(0)}(k)\boldsymbol{\Sigma}(k)\boldsymbol{G}(k) \tag{6.9}$$

with

$$\boldsymbol{G}(k) = \begin{bmatrix} G(k) & F(k) \\ \bar{F}(k) & \bar{G}(k) \end{bmatrix}, \qquad \boldsymbol{\Sigma}(k) = \begin{bmatrix} \Sigma(k) & \Delta(k) \\ \bar{\Delta}(k) & \bar{\Sigma}(k) \end{bmatrix} \tag{6.10}$$

$$\boldsymbol{G}^{(0)}(k) = \begin{bmatrix} G^{(0)}(k) & 0 \\ 0 & \bar{G}^{(0)}(k) \end{bmatrix} \tag{6.11}$$

where $G(k)$ is the particle-hole and $\bar{G}(k)$ the hole-particle Green's functions

$$G_{ab}(k) = -\int_0^\beta d\tau e^{i\omega_n\tau}\langle T_\tau c_{\boldsymbol{k}a}(\tau)c^\dagger_{\boldsymbol{k}b}(0)\rangle \tag{6.12}$$

$$\bar{G}_{ab}(k) = -\int_0^\beta d\tau e^{i\omega_n\tau}\langle T_\tau c^\dagger_{-\boldsymbol{k}a}(\tau)c_{-\boldsymbol{k}b}(0)\rangle \tag{6.13}$$

for crystal momentum $\boldsymbol{k}$ and fermionic Matsubara frequencies $\omega_n = (2n+1)\pi/\beta$, with $\beta = \hbar/(k_\mathrm{B}T)$. In the orbital-spin-sublattice basis $a = (\alpha, \sigma, s)$ with orbital α, spin σ, and sublattice s. The non-interacting Green's functions are calculated with the operators $c_{\boldsymbol{k}a}$ for the Hamiltonian in Eq. (6.1). In the band (n) and orbital-spin-sublattice basis respectively:

$$G^{(0)}_n(\boldsymbol{k}, i\omega_n) = [i\omega_n - \xi_{\boldsymbol{k},n}]^{-1} \tag{6.14}$$

$$G^{(0)}_{ab}(k) = \sum_n U_{\boldsymbol{k},an} G^{(0)}_n(k) U^\dagger_{\boldsymbol{k},nb}. \tag{6.15}$$

For the non-interacting model $G^{(0)}_{ab}(k) = -\bar{G}^{(0)}_{ba}(-k)$. Under the approximations of this work, only the particle-particle self-energy is calculated. In a multi-orbital system, the non-interacting particle-hole susceptibility $\hat{\chi}_0(k) = \hat{\chi}^{ph}_0(k)$ is a tensor calculated from the non-interacting Green's functions in the $N_k \times N_k$-lattice we are considering:

$$\chi^{ph}_{0,abcd}(q) = \frac{1}{N_k^2 \beta} \sum_k G^{(0)}_{ac}(q+k) \bar{G}^{(0)}_{bd}(-k) \tag{6.16}$$

Using the well-known summation for the Lindhard function over all fermionic Matsubara frequencies ω_n and the analytic continuation:

$$\begin{aligned} &\chi_{0,abcd}(\boldsymbol{q}, i\omega_n \to i\delta) = \\ &\frac{1}{N_k^2} \sum_{\boldsymbol{k},n,n'} [U_{\boldsymbol{k}+\boldsymbol{q}}]_{an} \left[U^\dagger_{\boldsymbol{k}+\boldsymbol{q}}\right]_{nc} [U_{\boldsymbol{k}}]_{dn'} \left[U^\dagger_{\boldsymbol{k}}\right]_{n'b} \\ &\times \frac{f(\xi_{\boldsymbol{k}+\boldsymbol{q},n}, T) - f(\xi_{\boldsymbol{k},n'}, T)}{i\delta - (\xi_{\boldsymbol{k}+\boldsymbol{q},n} - \xi_{\boldsymbol{k},n'})} \end{aligned} \tag{6.17}$$

where δ is a small number, here set to 10^{-4}eV. $f(\xi_{\boldsymbol{k},n}, T)$ is the Fermi-Dirac distribution at temperature T. The tensor $\hat{\chi}_0(q)$ can be written as a rank 4 tensor. The number of spins $N_\sigma = 2$, orbitals $N_o = 3$, and sublattices $N_s = 2$, results in a tensor of dimension $12 \times 12 \times 12 \times 12$. However, to separate the spin degrees of freedom we can reshape the tensor to have the dimension $N_\sigma^2 \times N_\sigma^2 \times (N_o N_s)^2 \times (N_o N_s)^2$. In terms of spin and orbital indices, the basis for the tensor on this form is given as all combinations of two indices $(\sigma\sigma') \times (\alpha_s \beta_{s'})$. The spin combinations are $(\sigma\sigma') = \{(\uparrow\uparrow), (\uparrow\downarrow), (\downarrow\uparrow), (\downarrow\downarrow)\}$, and $(\alpha_s \beta_{s'})$ are the 36 combinations of orbitals $\alpha = yz, xz, xy$ and sublattices $s = A, B$.

Interactions are treated by calculating the irreducible particle-particle vertex, which is modified by spin-fluctuations from the random phase approximation (RPA). The irreducible vertex is given by the parquet equations [49], where here the bare vertex is $\hat{\Gamma}_0 = \hat{V}$. The

bare vertex is the Hubbard-Kanamori interaction [50], which is defined in real space as

$$\begin{aligned} H_{\mathrm{I}} =& U \sum_{\boldsymbol{j},\alpha} n_{\boldsymbol{j}\alpha\uparrow} n_{\boldsymbol{j}\alpha\downarrow} \\ &+ \sum_{\boldsymbol{j},\alpha\neq\beta} J_{\mathrm{H}} \left[c^{\dagger}_{\boldsymbol{j}\alpha\uparrow} c^{\dagger}_{\boldsymbol{j}\beta\downarrow} c_{\boldsymbol{j}\alpha\downarrow} c_{\boldsymbol{j}\beta\uparrow} + c^{\dagger}_{\boldsymbol{j}\alpha\uparrow} c^{\dagger}_{\boldsymbol{j}\alpha\downarrow} c_{\boldsymbol{j}\beta\downarrow} c_{\boldsymbol{j}\beta\uparrow} \right] \\ &+ \sum_{\boldsymbol{j},\alpha<\beta,\sigma} \left[U' n_{\boldsymbol{j}\alpha\sigma} n_{\boldsymbol{j}\beta\bar{\sigma}} + (U' - J_{\mathrm{H}})\, n_{\boldsymbol{j}\alpha\sigma} n_{\boldsymbol{j}\beta\sigma} \right] \end{aligned} \tag{6.18}$$

with the intraorbital Hubbard interaction U, the Hund's coupling J_{H}, and the interorbital repulsion $U' = U - 2J_{\mathrm{H}}$. Following the notation of Ref. [14], we define the bare vertex $\hat{V}$ as:

$$H_{\mathrm{I}} = \frac{1}{N_k^2} \sum_{\boldsymbol{k},\boldsymbol{q}} \sum_{a,b,c,d} V_{abcd}(\boldsymbol{q}) c^{\dagger}_{\boldsymbol{k},a} c^{\dagger}_{-\boldsymbol{k},c} c_{-(\boldsymbol{k}-\boldsymbol{q}),b} c_{\boldsymbol{k}-\boldsymbol{q},d} \tag{6.19}$$

for all orbit-spin-sublattice indices $a = (\alpha, \sigma, s)$. On the same rank 4 tensor structure form as the susceptibility, the tensor $\hat{V}$ can be divided into spin sectors

$$\hat{V} = \begin{pmatrix} \hat{V}^{\uparrow\uparrow\uparrow\uparrow} & 0 & 0 & \hat{V}^{\uparrow\uparrow\downarrow\downarrow} \\ 0 & \hat{V}^{\uparrow\downarrow\uparrow\downarrow} & 0 & 0 \\ 0 & 0 & \hat{V}^{\downarrow\uparrow\downarrow\uparrow} & 0 \\ \hat{V}^{\downarrow\downarrow\uparrow\uparrow} & 0 & 0 & \hat{V}^{\downarrow\downarrow\downarrow\downarrow} \end{pmatrix} \tag{6.20}$$

with only on-site terms $s = s'$. Each matrix $\hat{V}^{\sigma_1\sigma_2\sigma_3\sigma_4}$ in the orbit-sublattice basis is defined as

$$V^{\uparrow\uparrow\uparrow\uparrow}_{\alpha_s\beta_s\gamma_s\delta_s} = V^{\downarrow\downarrow\downarrow\downarrow}_{\alpha_s\beta_s\gamma_s\delta_s} = \begin{cases} U' - J_{\mathrm{H}} & (\alpha = \gamma \neq \beta = \delta) \\ -U' + J_{\mathrm{H}} & (\alpha = \beta \neq \gamma = \delta) \\ 0 & (\text{otherwise}) \end{cases} \tag{6.21}$$

$$V^{\uparrow\uparrow\downarrow\downarrow}_{\alpha_s\beta_s\gamma_s\delta_s} = V^{\downarrow\downarrow\uparrow\uparrow}_{\alpha_s\beta_s\gamma_s\delta_s} = \begin{cases} -U & (\alpha=\beta=\gamma=\delta) \\ -J_{\mathrm{H}} & (\alpha=\gamma\neq\beta=\delta) \\ -U' & (\alpha=\beta\neq\gamma=\delta) \\ -J_{\mathrm{H}} & (\alpha=\delta\neq\beta=\gamma) \\ 0 & (\text{otherwise}) \end{cases} \tag{6.22}$$

$$V^{\uparrow\downarrow\uparrow\downarrow}_{\alpha_s\beta_s\gamma_s\delta_s} = V^{\downarrow\uparrow\downarrow\uparrow}_{\alpha_s\beta_s\gamma_s\delta_s} = \begin{cases} U & (\alpha=\beta=\gamma=\delta) \\ U' & (\alpha=\gamma\neq\beta=\delta) \\ J_{\mathrm{H}} & (\alpha=\beta\neq\gamma=\delta) \\ J_{\mathrm{H}} & (\alpha=\delta\neq\beta=\gamma) \\ 0 & (\text{otherwise}) \end{cases} \tag{6.23}$$

for each sublattice $s = A, B$ and for orbital indices $\alpha, \beta, \gamma, \delta$. The effective particle-particle vertex [49] is:

$$\hat{\Gamma}^{pp}(q = K - K') = -\frac{1}{2}\hat{V} - \hat{V}\hat{\chi}(K - K')\hat{V} \tag{6.24}$$

The susceptibility $\hat{\chi}(q)$ is approximated as the RPA susceptibility:

$$\hat{\chi}(q) = \left(1 - \hat{\chi}_0(q)\hat{V}\right)^{-1}\hat{\chi}_0(q) \tag{6.25}$$

which uses the same bare vertex $\hat{V}$ and has the same tensor structure as $\hat{\chi}_0(q)$. The tensor multiplication is defined as a matrix multiplication in the spin and orbital-sublattice combinations

$$\left[\hat{A}\hat{B}\right]^{(\sigma\sigma')_1(\sigma\sigma')_2}_{(\alpha_s\beta_{s'})_1(\alpha_s\beta_{s'})_2} = \sum_{\tilde{\alpha},\tilde{\beta},\tilde{\sigma},\tilde{\sigma}'} A^{(\sigma\sigma')_1(\tilde{\sigma}\tilde{\sigma}')}_{(\alpha_s\beta_{s'})_1(\tilde{\alpha}\tilde{\beta})} B^{(\tilde{\sigma}\tilde{\sigma}')(\sigma\sigma')_2}_{(\tilde{\alpha}\tilde{\beta})(\alpha_s\beta_{s'})_2} \tag{6.26}$$

The effective vertex is not further spin-diagonalized into spin-singlet and spin-triplet vertices as our regime of intermediate to strong spin-orbit coupling inherently mixes the two sectors. The linearized gap equation can be obtained from the Luttinger-Ward functional [51, 52], where the linearization of the anomalous Green's function is given by the Dyson-Gorkov

equations Eq. (6.9).

$$\Delta_{ab}(k) = \frac{1}{N\beta}\sum_{k'}\sum_{a'b'}\Gamma^{pp}_{aa'b'b}(k-k')F_{a'b'}(k') \tag{6.27}$$

$$F_{a'b'}(k') = \sum_{\mu\nu} G_{a'\mu}(k')\bar{G}_{\nu b'}(k')\Delta_{\mu\nu}(k') \tag{6.28}$$

where β is the inverse temperature and $N = N_k^2$. Each index here runs over all orbit-spin-sublattice combinations $a = (\alpha, \sigma, s)$. Further, we apply both the static ($\omega_n \to \delta = 10^{-4}$eV, $\hat{\Delta}(k) \to \hat{\Delta}(\boldsymbol{k})$, $\Gamma^{pp}(q) \to \Gamma^{pp}(\boldsymbol{q})$) and normal state ($\hat{G}(k') \to \hat{G}^{(0)}(k')$) approximations. The linearized gap equation can be solved as an eigenvalue problem, as a version of the Eliashberg equation:

$$\lambda_e\Delta_{ab}(\boldsymbol{k}) = \frac{1}{N}\sum_{\boldsymbol{k}',a'b',\mu\nu}\Gamma^{pp}_{aa'b'b}(\boldsymbol{k}-\boldsymbol{k}')\phi^{\boldsymbol{k}'}_{a'b'\mu\nu}\Delta_{\mu\nu}(\boldsymbol{k}') \tag{6.29}$$

with

$$\phi^{\boldsymbol{k}'}_{a'b'\mu\nu} = -\frac{1}{\beta}\sum_{\omega_n} G^{(0)}_{a'\mu}(k')\bar{G}^{(0)}_{\nu b'}(k') \tag{6.30}$$

A largest eigenvalue of unity or higher $\lambda_e \geq 1$ indicates a possible superconducting order. A non-explicit summation over Matsubara frequencies is performed, like in Eq. (6.17), and the equation depends only on momentum $\boldsymbol{k}$.

While this system is strongly interacting one might expect a multitude of order parameters including magnetic orders. We use the Stoner criterion to identify phases in the particle-hole channel. Methods attempting to treat particle-hole and particle-particle self-energies on equal footing are beyond the scope of this work [53, 54]. The RPA susceptibility, Eq. (6.25), will pass a critical point and diverge, when the Hartree-Fock term in the particle-hole channel has an eigenvalue above unity at any k-point which we name Q [53, 54]:

$$\max \text{ eig}\left[\hat{\chi}_0(Q)\hat{V}\right] = 1 \tag{6.31}$$

The particle-hole instability is given by the eigenvector to the tensor $\hat{\chi}_0(Q)\hat{V}$, which can be unfolded into a matrix. A rank 4 tensor C_{ijkl} of dimension $N_1 \times N_2 \times N_1 \times N_2$ can be mapped

onto a matrix $C_{\mu\nu}$ of dimension $N_1N_2 \times N_1N_2$ via

$$\begin{aligned} \mu &= i + N_1(j-1), \qquad && \mu \in [1, \ldots, N_1N_2] \\ i &= 1 + \mathrm{mod}(\mu - 1, N_1), && i \in [1, \ldots, N_1] \\ j &= 1 + \mathrm{div}(\mu - 1, N_1), && j \in [1, \ldots, N_2] \end{aligned} \tag{6.32}$$

where "mod" is the modulus operation and "div" is integer division. The given mapping preserves the defined tensor multiplication, in Eq. (6.26), as matrix multiplication in the unfolded matrix. The type of instability can also be classified by the magnetic channel it occurs in. The susceptibility can be spin block-diagonalized by rewriting it in the basis of magnetic operators $m^z_{\tilde{\alpha}\tilde{\beta}} = \frac{1}{\sqrt{2}}(c^\dagger_{\tilde{\alpha}\uparrow}c_{\tilde{\beta}\uparrow} - c^\dagger_{\tilde{\alpha}\downarrow}c_{\tilde{\beta}\downarrow})$:

$$\hat{\chi}^z_{\tilde{\alpha}\tilde{\beta}\tilde{\gamma}\tilde{\delta}}(q) = \frac{1}{N_k^2}\int_0^\beta d\tau e^{i\omega_n\tau}\langle T_\tau m^z_{\tilde{\alpha}\tilde{\beta},\boldsymbol{q}}(\tau)m^z_{\tilde{\gamma}\tilde{\delta},-\boldsymbol{q}}(0)\rangle_c \tag{6.33}$$

with the indices $\tilde{\alpha} = \alpha_s$ running over all orbital $\alpha = yz, xz, xy$ and sublattice $s = A, B$ combinations. The magnetic channels are

$$\hat{\chi}^z(q) = \frac{1}{2}\left(\hat{\chi}^{\uparrow\uparrow\uparrow\uparrow}(q) - \hat{\chi}^{\uparrow\uparrow\downarrow\downarrow}(q)\right) \tag{6.34}$$

$$\hat{\chi}^+(q) = \hat{\chi}^{\uparrow\downarrow\uparrow\downarrow}(q), \qquad \hat{\chi}^-(q) = \hat{\chi}^{\downarrow\uparrow\downarrow\uparrow}(q) \tag{6.35}$$

with the out-of-plane spin $\hat{\chi}^z(q)$ and in-plane spin $\hat{\chi}^\pm(q)$ channels [1]. As the j-state basis describes the bands better than the orbital-spin basis, the $\chi(q)$-terms can be transformed, via Eq. (6.8), as

$$\chi_{J,ijkl}(q) = \sum_{\alpha\beta\gamma\delta} M_{i\alpha}M^\dagger_{\gamma k}M_{l\delta}M^\dagger_{\beta j}\chi_{\alpha\beta\gamma\delta}(q) \tag{6.36}$$

where M is the transformation from spin and orbit to the total angular momentum basis. In this basis, the susceptibility is similarly divided into different pseudospin channels $\hat{\chi}^z_J(q)$ and $\hat{\chi}^\pm_J(q)$.

[1] The spin block-diagonalization introduces an additional density channel $\hat{\chi}^d(q)$. No density-channel instability is found in this work and the peaks are significantly smaller than in the magnetic channels. This remains true for $\hat{\chi}^d_J(q)$ in the j-state basis.

6.2.3 Computational details

All RPA calculations, for the susceptibility Eq. (6.25) and superconductivity Eq. (6.29) were performed on a $N_k \times N_k = 46 \times 46$ momentum lattice. The finite momentum resolution limits the lowest accessible temperature. Peaks in the susceptibility cannot be narrower than the lattice spacing and we thus require some thermal broadening to get reliable results. In this work we use $k_B T = 0.001$eV ($T \approx 11$K). The temperature was chosen such that less than a 10% change in largest eigenvalue was found when going from a lattice of size $N_k = 32$ to $N_k = 46$, at most points. In the data of Figs. 6.7b & 6.11 a larger change is observed, therefore calculations for these figures where done at $N_k = 64$. The specific temperature is of interest for a potential d-wave superconducting order in the electron doped compound. The 2016 experiment in Ref. [16] observed an order with this symmetry below $T \approx 30$K, with a maximum at $T \approx 10$K. The largest value of the linearized gap equation is found via the Arnoldi method, with a convergence criterion of 10^{-7}.

6.3 Phase diagram: strain and doping

In the following sections we discuss the phase diagrams obtained by varying the charge doping and applying an increasing compressive strain. For the most realistic parameter range one obtains Fig. 6.3. To explore additional effects from chemical doping and to illustrate the richness of similar compounds, additional phase diagrams are shown in Fig. 6.4. All phase diagrams show strain-induced superconductivity for a broad range of parameters. In addition, three main features can be observed. First, the two types of superconductivity found in earlier works [11, 14], a pseudospin $j = 1/2$ d-wave and an orbital $s_\pm$-wave, are found. In addition, both types can be found when varying only the doping, for a select set of parameters. Second, at high enough strain an orbital selective pairing which favors one of the in-plane directions can be found. This type of order has a larger component originating from the xz orbital than from yz, spontaneously breaking the in-plane symmetry. And third, under compressive strain the susceptibility goes from having the largest peaks in the pseudospin states to peaks instead originating from the spin states. This shift affects both the magnetic order and the possible pairing symmetries.

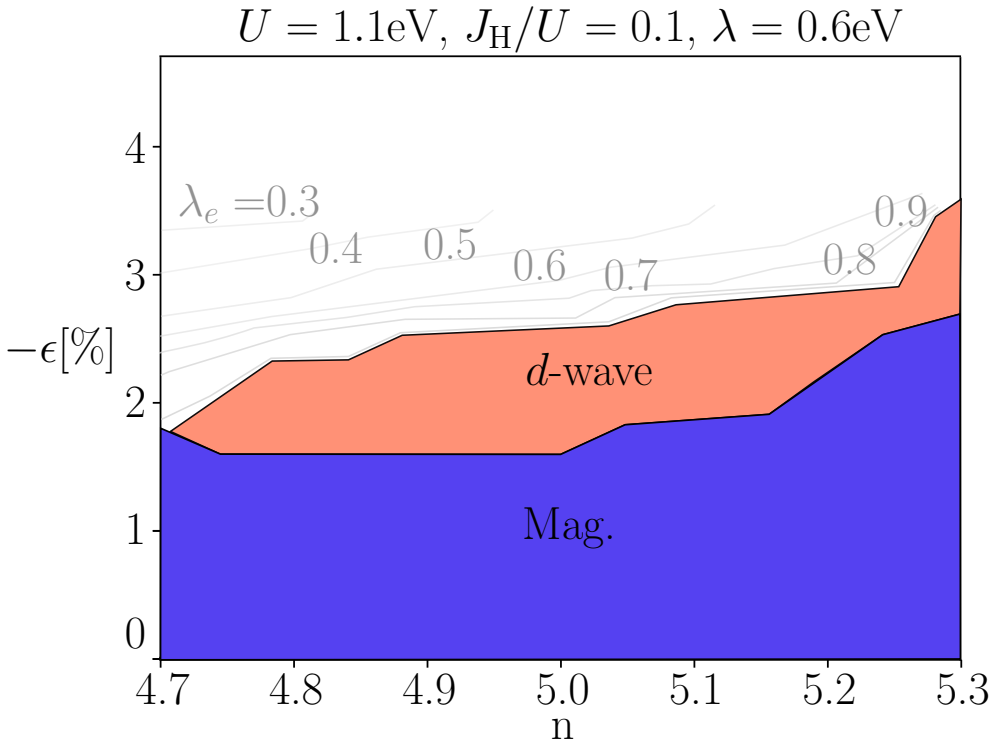

Figure 6.3: The phase diagram for charge doping and compressive strain are shown at $U = 1.1\text{eV} \approx 3|t|$ for realistic values of the spin orbit λ and Hund's couplings J_H. Two types of regions are found in the RPA calculations: the magnetic region where the Stoner criterion has been met and a superconducting order with d-wave symmetry. The nature of the magnetic transition is characterized in Fig. 6.6. In the normal state the largest eigenvalue $\lambda_e < 1$, and the contours of the values are shown up to $\epsilon = -3.5\%$. The phase diagram extends to the higher strain values as to be comparable to Fig. 6.4, in this regime no superconducting order is possible.

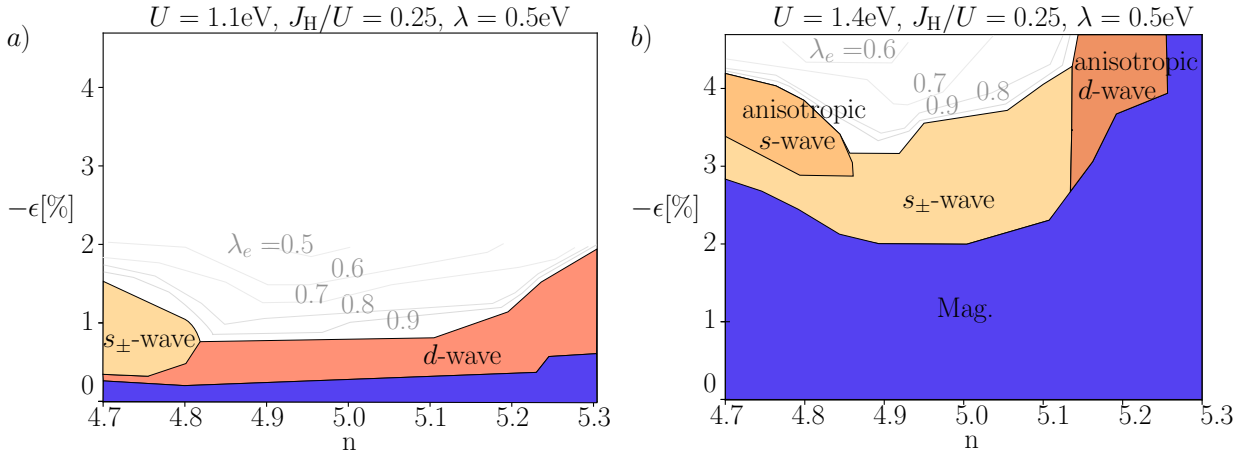

Figure 6.4: The phase diagrams for for a lower SOC and a higher Hund's, at a) $U = 1.1\text{eV} \approx 3|t|$ and b) $U = 1.4\text{eV} \approx 4|t|$. In a) there are two types of superconducting orders: the d-wave and another with $s_\pm$-wave symmetry. In b) there are two additional anisotropic types of superconducting orders, an s-wave and a d-wave. The magnetic phase transitions are here of multiple types and are characterized in Figs. 6.6 & 6.7. The eigenvalues are only calculated up until to a strain value where superconductivity is no longer possible.

Choosing a realistic regime for the phase diagram, there are two criteria for the chosen interaction parameters. The first criterion is that sufficient doping, either hole or electron, should in accordance to experiment, result in a transition out of the magnetic order. The second criterion is that in undoped Sr_2IrO_4 the magnetic order persists up to a strain value of $\epsilon \approx -2\%$ [31, 39]. For the most realistic values of the Hund's and spin-orbit coupling, $J_H = 0.1U$ and $\lambda = 0.6$eV, the first criterion is satisfied for $U \approx 2|t|$, shown in Appendix 6.A. The realistic phase diagram is presented for $U = 1.1\text{eV} \approx 3|t|$. Since the model overestimates the orders this choice only satisfies the second criterion. In Appendix 6.A the phase diagram for $U = 1.4\text{eV} \approx 4|t|$ results in the same phase transitions at higher strain values. Complementary mean field calculations, containing magnetic, superconducting as well as other order parameters, yields a qualitatively similar phase diagram, with differences explained in Appendix 6.B.

In Fig. 6.4, we also consider a higher Hund's coupling of $J_H = 0.25U$, with a lower spin orbit coupling of $\lambda = 0.5$eV for the following reason. Hole doping via the substitution of iridium atoms for rhodium or ruthenium atoms could modify the effective interaction

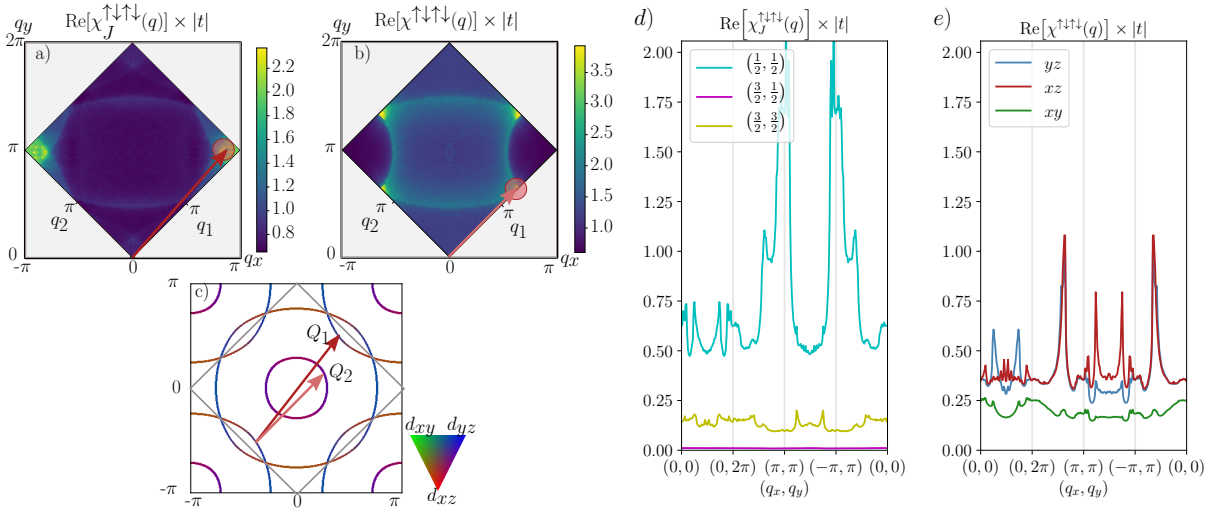

Figure 6.5: The in-plane a) pseudospin $\chi_J^{\uparrow\downarrow\uparrow\downarrow}(\boldsymbol{q})$ and b) spin susceptibility $\chi^{\uparrow\downarrow\uparrow\downarrow}(\boldsymbol{q})$, Eqs. (6.37), (6.38), for $U = 1.1\text{eV}$, $J_\text{H} = 0.25U$, $\lambda = 0.5\text{eV}$, $n = 4.8$, $\epsilon = -1\%$. The largest peaks are around $\boldsymbol{Q}_1 \approx (\pi, \pi)$ and $\boldsymbol{Q}_2 \approx (\frac{\pi}{2}, \frac{\pi}{2})$, respectively. c) Shown for the FS in the extended BZ, $\boldsymbol{Q}_1$ connects FS_1 to itself while $\boldsymbol{Q}_2$ connects FS_1 and FS_2. On the FS the orbital contributions are given as $|\langle\alpha|\text{FS}_n|\alpha\rangle|$, for $\alpha = yz, xz, xy$. In d) & e), the pseudospin susceptibility is split into each j-state contribution and the spin susceptibility into that of each orbital. Even though the $j = 1/2$ states have the individually largest peaks, the total susceptibility originating from the yz- and xz-orbitals is larger. Peaks of the type $\boldsymbol{Q}_{1d} \approx (\frac{\pi}{2}, \pi)$ are present in the spin susceptibility as peaks belonging entirely to one of the orbitals yz or xz.

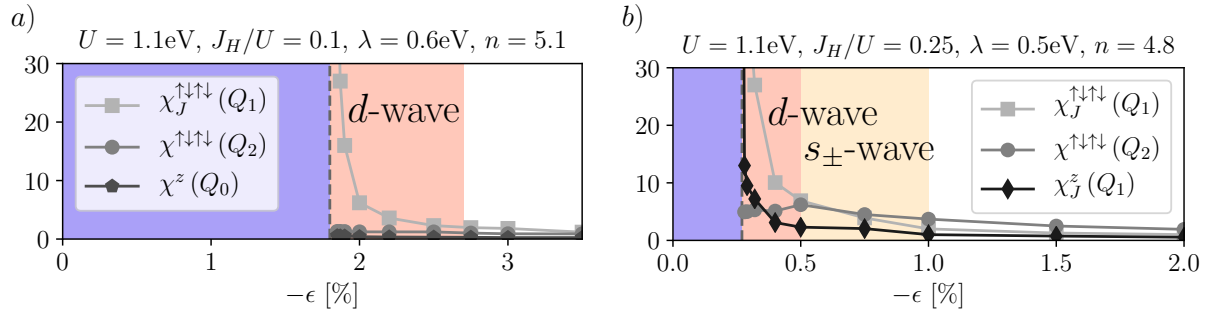

Figure 6.6: Two out of the five types of magnetic instabilities found at the Stoner criterion and the components for the largest susceptibility peaks $\mathrm{Re}[\chi(\boldsymbol{Q})] \times |t|$, are shown along constant doping lines in a) Fig. 6.3 & b) Fig. 6.4a. The most prevalent instability occurs in the $j = 1/2$ state, in-plane, and with the nesting vector $\boldsymbol{Q}_1 \approx (\pi, \pi)$: $\chi^{\uparrow\downarrow\uparrow\downarrow}_{J,(\frac{1}{2},\pm\frac{1}{2})}(\boldsymbol{Q}_1)$. b) At $J_\mathrm{H} = 0.25U$ and hole doping, the $j = 1/2$ $\boldsymbol{Q}_1$-nesting instability has both in- and out-of-plane components. Close to these instabilities the $\boldsymbol{Q}_1$-peaks are the largest. As the strain increases the total in-plane spin susceptibility, Eq. (6.37), decreases at a slower rate and eventually dominates instead

parameters and spin-orbit coupling. Some works estimate the spin orbit coupling of iridium, rhodium and ruthenium as $\lambda^\mathrm{Ir} \approx 0.45$eV, $\lambda^\mathrm{Rh} = \lambda^\mathrm{Ru} \approx 0.19$eV respectively [55, 56, 57]. Moreover, ruthenium atoms have a higher Hund's coupling of $J_\mathrm{H} \approx 0.15U - 0.2U$ [58]. The full set of phase diagrams are presented in Figs. 6.3 & 6.4, with identified superconducting and magnetic phases.

6.4 Magnetic order

In the RPA calculation, the particle-hole order is found using the Stoner criterion, Eq. (6.31). An order can be characterized by two features of $\hat{\chi}(\boldsymbol{q})$. First is the nesting vector $\boldsymbol{Q} = (q_x, q_y)$, given in the extended BZ, at which the Stoner criterion is met. The instabilities in the phase diagrams all appear at the four points, $\boldsymbol{Q}_1 \approx (\pi, \pi)$, $\boldsymbol{Q}_2 \approx (\frac{\pi}{2}, \frac{\pi}{2})$, $\boldsymbol{Q}_0 \approx (0, 0)$, and $\boldsymbol{Q}_{1d} \approx (\frac{\pi}{2}, \pi)$. The exact location of the instabilities is shifted a small distance from the ideal values, which depends on doping as well as strain. Examples of the dominant peaks are shown in Fig. 6.5. The most relevant components of the susceptibility are shown in Figs. 6.6 & 6.7, along a few cuts in the phase diagrams. For the lower Hund's coupling in

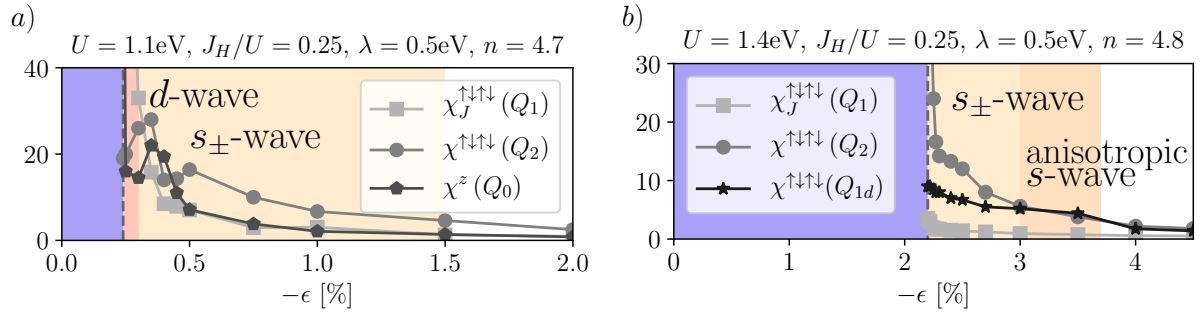

Figure 6.7: Additional magnetic instabilities are found for $J_{\mathrm{H}} = 0.25U$. In a small region around $n = 4.7$, in Fig. 6.4a, an out-of-plane ferromagnetic instability $\chi^z(\boldsymbol{Q}_0)$ accompanies the in-plane order. Note that the competing sizes of different channels here could be an effect of the momentum resolution. In Fig. 6.4b, a spin instability with $\boldsymbol{Q}_2 \approx (\frac{\pi}{2}, \frac{\pi}{2})$, is present for all hole doping. The superconducting $s_\pm$-wave is found close to the instability, while the anisotropic s-wave appears when the $\boldsymbol{Q}_{1d}$-peak, in the xz-orbital, becomes equal in size.

Fig. 6.3 the only instability is at $\boldsymbol{Q}_1$. An order described in real space by a two site unit cell in a square lattice will have a reduced Brillouin zone with a unit vector $\boldsymbol{Q} = (\pi, \pi)$. As antiferromagnetism is a two site order expected in this compound, the $\boldsymbol{Q}_1$ susceptibility peaks are expected to be antiferromagnetic. In Fig. 6.4 the $\boldsymbol{Q}_2$-instability occurs at most doping values. A real space order corresponding to $\boldsymbol{Q} = (\frac{\pi}{2}, \frac{\pi}{2})$, will have a unit cell containing 4 sites. However, it should be noted that the peak $\boldsymbol{Q}_2 \approx (\frac{\pi}{2}, \frac{\pi}{2})$ is doping dependent and never occurs exactly at this value. It is an incommensurate order closer to $(0.6\pi, 0.6\pi)$ for hole doping and $(0.4\pi, 0.4\pi)$ for electron doping. In Fig. 6.5 there is an additional copy of these peaks that connects different copies of pockets in the extended BZ. Another instability, at $\boldsymbol{Q}_{1d}$, only occurs at the highest strains and electron dopings considered. This nesting vector connects segments on the FS with either a clear xz-character to other segments belonging to the same orbital. The quasi-1d dispersion of the xz orbital, with $t_1 \gg t_\delta$ in Eq. (6.4), leads to the susceptibility in the intra-xz channel having peaks connecting point in momentum space mainly along the x-direction. Finally, a ferromagnetic instability at $\boldsymbol{Q}_0$ is possible in Fig. 6.4a at $n = 4.7$.

The second feature that characterizes a magnetic instability is the channel in which the instability occurs. In Eqs. 6.34 & 6.35, the spin susceptibility $\hat{\chi}(\boldsymbol{q})$, as well as the pseudospin susceptibility $\hat{\chi}_J(\boldsymbol{q})$, are divided into magnetic channels. Most instabilities found in Figs. 6.3

& 6.4 are of the type $\chi^{\uparrow\downarrow\uparrow\downarrow}_{J,\left(\frac{1}{2},\pm\frac{1}{2}\right)}(\boldsymbol{Q}_1)$, an in-plane magnetic instability with mainly $j = 1/2$ contributions. This can be interpreted as the canted in-plane antiferromagnetic order (x-cAFM) observed in each layer experimentally. As denoted in Fig. 6.6b, the higher Hund's coupling, $J_{\mathrm{H}} = 0.25U$ and $U = 1.1$eV, results in an additional out-of-plane component accompanying the in-plane order, with $\chi^{z}_{J,\left(\frac{1}{2},\pm\frac{1}{2}\right)}(\boldsymbol{Q}_1)$.

At any point where the $\boldsymbol{Q}_2$ instability is present, it occurs in channels of the spin susceptibility, rather than pseudospin. The instability is in-plane and has contributions mainly from the yz and xz orbitals: $\chi^{\uparrow\downarrow\uparrow\downarrow}_{yz}(\boldsymbol{Q}_2)$ & $\chi^{\uparrow\downarrow\uparrow\downarrow}_{xz}(\boldsymbol{Q}_2)$. Even though this instability is only present at $U = 1.4$eV and $J_{\mathrm{H}} = 0.25U$, these susceptibility peaks remain large in the entire Fig. 6.4a phase diagram. At high hole doping in Fig. 6.4a a purely out-of-plane ferromagnetic instability $\chi^{z}(\boldsymbol{Q}_0)$ occurs for spins in each of the orbitals yz, xz, and xy.

As the strain increases the peaks in the susceptibility at different channels decrease at different rates. Moreover, we will see below that superconductivity found directly adjacent to a magnetic order is mediated by those magnetic fluctuations while superconducting orders which are mediated by other fluctuations can become more favorable as strain is increased further. In Fig. 6.6b, at $J_{\mathrm{H}} = 0.25U$, the spin susceptibility peaks decrease significantly slower than those of the antiferromagnetic pseudospin order. At strain $\epsilon = -0.5\%$, and beyond, the peaks in spin susceptibility become dominant. The effective particle-particle vertex, Eq. (6.24), develops peaks at the same $\boldsymbol{Q}$-points as for the spin (or pseudospin) susceptibility. To track which magnetic fluctuation mediates the superconducting orders, the strengths of spin and pseudospin fluctuations are compared. The total susceptibilities in the two bases are

$$\chi^{\sigma\sigma'\sigma\sigma'}(\boldsymbol{q}) = \frac{1}{2}\sum_{s,s'}\sum_{\alpha,\beta} e^{iq_x(\Theta_s-\Theta_{s'})}\chi^{(\alpha\sigma)(\alpha\sigma')(\beta\sigma)(\beta\sigma')}_{sss's'}(\boldsymbol{q}) \tag{6.37}$$

$$\chi^{\tau\tau'\tau\tau'}_{J}(\boldsymbol{q}) = \frac{1}{2}\sum_{s,s'}\sum_{m,n} e^{iq_x(\Theta_s-\Theta_{s'})}\chi^{(m\tau)(m\tau')(n\tau)(n\tau')}_{J,sss's'}(\boldsymbol{q}) \tag{6.38}$$

where Θ_s, with $s = A, B$, chooses the sublattice such that $\Theta_A = 0$ and $\Theta_B = 1$.

It should be noted, that the pseudospin susceptibility nesting vector $\boldsymbol{Q}_1$ can be related to the hidden spin density wave (hSDW) orders found in other models for multi-band

Symmetry $\eta_R^\mu(\boldsymbol{k})$	$R=0$	$R=1$	$R=2$	$R=3$
A_{1g}, s	1	$\cos k_x + \cos k_y$	$2\cos k_x \cos k_y$	$\cos 2k_x + \cos 2k_y$
B_{1g}, $d_{x^2-y^2}$	-	$\cos k_x - \cos k_y$	-	$\cos 2k_x - \cos 2k_y$
B_{2g}, d_{xy}	-	-	$2\sin k_x \sin k_y$	-
E_u, p	-	$\sin k_x, \sin k_y$	$\sin(k_x + k_y)$, $\sin(k_x - k_y)$	$\sin 2k_x, \sin 2k_y$

Table 6.1: The lattice harmonics for each relevant symmetry on the square lattice is given for different radii R, describing what distance neighbors the symmetry is found on. $R = 0$ is on-site, $R = 1$ is nearest neighbors, and so on.

superconductors [59, 60]. The j-state basis mixes spin and orbital degrees of freedom and therefore the peaks found correspond to a linear combination of channels that favors both SDW and hSDW orders.

6.5 Superconductivity

6.5.1 Symmetries

In single-orbital models, it is of highest importance to determine whether the superconductivity is a spin-singlet or a spin-triplet order. Topological superconductivity and Majorana modes arise from superconductivity with p-wave pairing, which requires spin-triplet pairing in those systems. Efforts to induce superconductivity through the proximity effect are thus often focused on finding spin-triplet orders. However, once multiple orbitals and spin-orbit coupling are considered the connection between spin-triplets and p-wave symmetry is no longer a strict requirement. Multi-orbital models allow for a large set of possible pairing symmetries. The pairing matrix $\hat{\Delta}(\boldsymbol{k})$ must be antisymmetric under the full $\mathcal{SPOT}$-exchange [48, 61]. Therefore, any pairing can be classified as being either even or odd under spin exchange ($\mathcal{S}$), relative coordinate reflection ($\mathcal{P}$), orbital exchange ($\mathcal{O}$), and relative time exchange ($\mathcal{T}$) as defined in Appendix 6.D. As only the static case is considered in this work the order parameter is constant, and therefore even, under $\mathcal{T}$. Note that the operators $\mathcal{P}$ and $\mathcal{T}$ only exchange relative parameters, and are thus different from the reflection and time reversal operators.

For example, classifying symmetries for strong spin-orbit coupling in the predicted $j = 1/2$ d-wave, will inherently result in both spin-singlet and spin-triplet contributions. The pairing is more accurately described by the total angular momentum of the pair, which can take the values $J = 0, 1, 2, 3$ [62, 63]. Only within the $j_1 \otimes j_2 = \frac{1}{2} \otimes \frac{1}{2}$ sector do we still only get pairs that are either a $J = 0$ singlet or triplets $J = 1$ with $M = -1, 0, +1$. In Appendix 6.D the symmetry operations in the orbital basis are shown for the two types of pairing found in Fig. 6.3.

The spatial symmetry can be considered for the non-interacting bands n_τ by projecting the intraband pairing onto the Fermi surface (FS). The FS may contain three types of pockets belonging to two types of bands. The larger pockets, consisting mainly of $(j, j_z) = (\frac{1}{2}, \pm\frac{1}{2})$ states, are located around the points $(k_1, k_2) = (\pi, \pi), (\pi, 0)$ and have superconducting gaps that can be described by the same spatial symmetry. We therefore only look at one of these pockets, denoted FS_1. The smaller FS_2, with mainly $(j, j_z) = (\frac{3}{2}, \pm\frac{3}{2})$ is centered around $(k_1, k_2) = (0, 0)$. The spatial symmetry is thus studied for four intraband parameters: pseudospin-singlets $\Delta^s_{\mathrm{FS}_1}(\boldsymbol{k})$, $\Delta^s_{\mathrm{FS}_2}(\boldsymbol{k})$ and pseudospin-triplets $\Delta^t_{\mathrm{FS}_1}(\boldsymbol{k})$, $\Delta^t_{\mathrm{FS}_2}(\boldsymbol{k})$. $\Delta^{s/t}_{\mathrm{FS}_n}(\boldsymbol{k})$ is the order parameter Eq. (6.29) projected onto the band at the Fermi surface FS_n. The number of points belonging to a pocket is N_{FS_n}. For example the pseudospin-singlet is

$$\begin{aligned}\Delta^s_{\mathrm{FS}_n}(\boldsymbol{k}) = &\sum_{\boldsymbol{k}\in\mathrm{FS}_n}\sum_{\alpha\beta}\sum_{mm'}\left[U^\dagger_{\boldsymbol{k}}\right]_{n\alpha}\left[U^\dagger_{-\boldsymbol{k}}\right]_{n\beta}\\ &\times\frac{1}{\sqrt{2}}\Big(M^\dagger_{\alpha(m+)}M^\dagger_{\beta(m'-)}\Delta_{(m+)(m'-)}(\boldsymbol{k})\\ &-M^\dagger_{\alpha(m-)}M^\dagger_{\beta(m'+)}\Delta_{(m-)(m'+)}(\boldsymbol{k})\Big)\end{aligned} \tag{6.39}$$

where M is the matrix in Eq. (6.8) and the matrix $U_{\boldsymbol{k},\alpha n}$ transforms the band basis into the orbital basis. In the numerical calculations, there are small but non-zero interband contributions that will not be considered further. The spatial symmetries can be quantified via the projection coefficients $P^{\mu,R}_{s/t,\mathrm{FS}_n}$ onto the basis functions for each parity irreducible representation, $\eta^\mu_R(\boldsymbol{k})$, as given in Table 6.1

$$\Delta^{s/t}_{\mathrm{FS}_n}(\boldsymbol{k}) = \sum_{\mu,R} P^{\mu,R}_{s/t,\mathrm{FS}_n}\eta^\mu_R(\boldsymbol{k}). \tag{6.40}$$

The projection coefficient for each irreducible representation is thus found via

$$P^{\mu,R}_{s/t,\mathrm{FS}_n} = \frac{1}{N_{\mathrm{FS}_n}} \sum_{\boldsymbol{k}\in \mathrm{FS}_n} \eta^{\mu}_{R}(\boldsymbol{k}) \Delta^{s/t}_{\mathrm{FS}_n}(\boldsymbol{k}). \tag{6.41}$$

Examples of the two leading types of pairings are shown in Fig. 6.8. The most prominent d-wave is a $j = 1/2$ pseudospin singlet with a $\eta^{B_{1g}}_{R=1}$ pairing. The found $s_{\pm}$-wave order has contributions from both $\eta^{A_{1g}}_{R=0}(\boldsymbol{k})$ and $\eta^{A_{1g}}_{R=2}(\boldsymbol{k})$, with opposite sign for the two pockets. The main j-states components are from $(\frac{1}{2}, \pm\frac{1}{2})$ and $(\frac{3}{2}, \pm\frac{3}{2})$. However, components mixing j-states is stronger than for the d-wave. The symmetry in terms of orbital origin is specified further in Appendix 6.D.

6.5.2 Realistic strain-induced order

At low Hund's coupling and high SOC, a d-wave is found for a wide range of doping values once there is no longer a magnetic order present. The mean field calculations in Appendix 6.B corroborate the prediction of this order. The magnetic region extends up to $\epsilon = -1.5\%$ at the undoped $n = 5$, while it persists at higher strains on the electron doped side. Because of the required compressive strain, two bands are present at the FS at all points where superconductivity is found. As seen in Fig. 6.8, the gap on FS_1 is significantly larger than on FS_2. The d-wave originates from the $j = 1/2$ states, which are the states the band at FS_1 also belongs to. Strain has increased the size of the $j = 1/2$ electron pocket, FS_1, in the entire region where superconductivity is found. Even for hole doping at $\epsilon = -2\%$ the pocket FS_1 is comparable in size to FS_1 at $\epsilon = 0$ and electron doping, as further explained in Appendix 6.B.

6.5.3 Varying Hund's coupling

There are several important factors that determine which pairing symmetry is favored. Doping and strain change the shape of the Fermi surface, and thus the nesting vectors $\boldsymbol{Q}$, as well as the orbital contributions in each pocket. Both compressive strain and hole doping increase the presence of yz and xz orbitals. However, the type of fluctuations which dominate the RPA interaction vertex depends on the interaction parameters. In Fig. 6.8

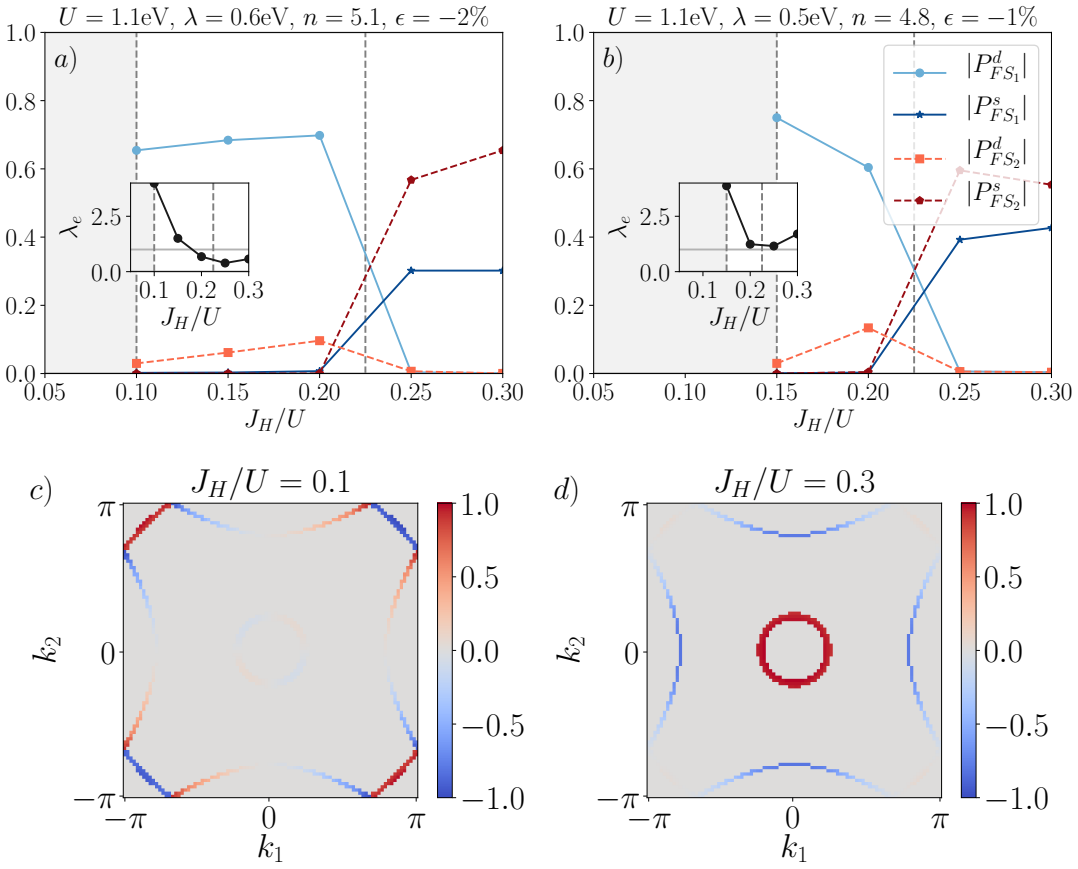

Figure 6.8: Both the dominant symmetry and the relative weight on the pockets change as the Hund's coupling is varied. In a) and b) the spin-orbit coupling λ is fixed and the spin-singlet order for each pocket at the Fermi surface is projected onto each spatial symmetry, as in Eq. (6.41). The inserts show the largest eigenvalue λ_e of the linearized gap equation Eq. (6.29). c) and d) show $\Delta^{s/t}_{\mathrm{FS}_n}(\boldsymbol{k})$ for two values of J_H for the FS belonging to a). In the d-wave state, the weight on the FS_1 is largest. For the s-wave state, the opposite is true and pockets have opposite signs, identifying it as an $s_\pm$-wave.

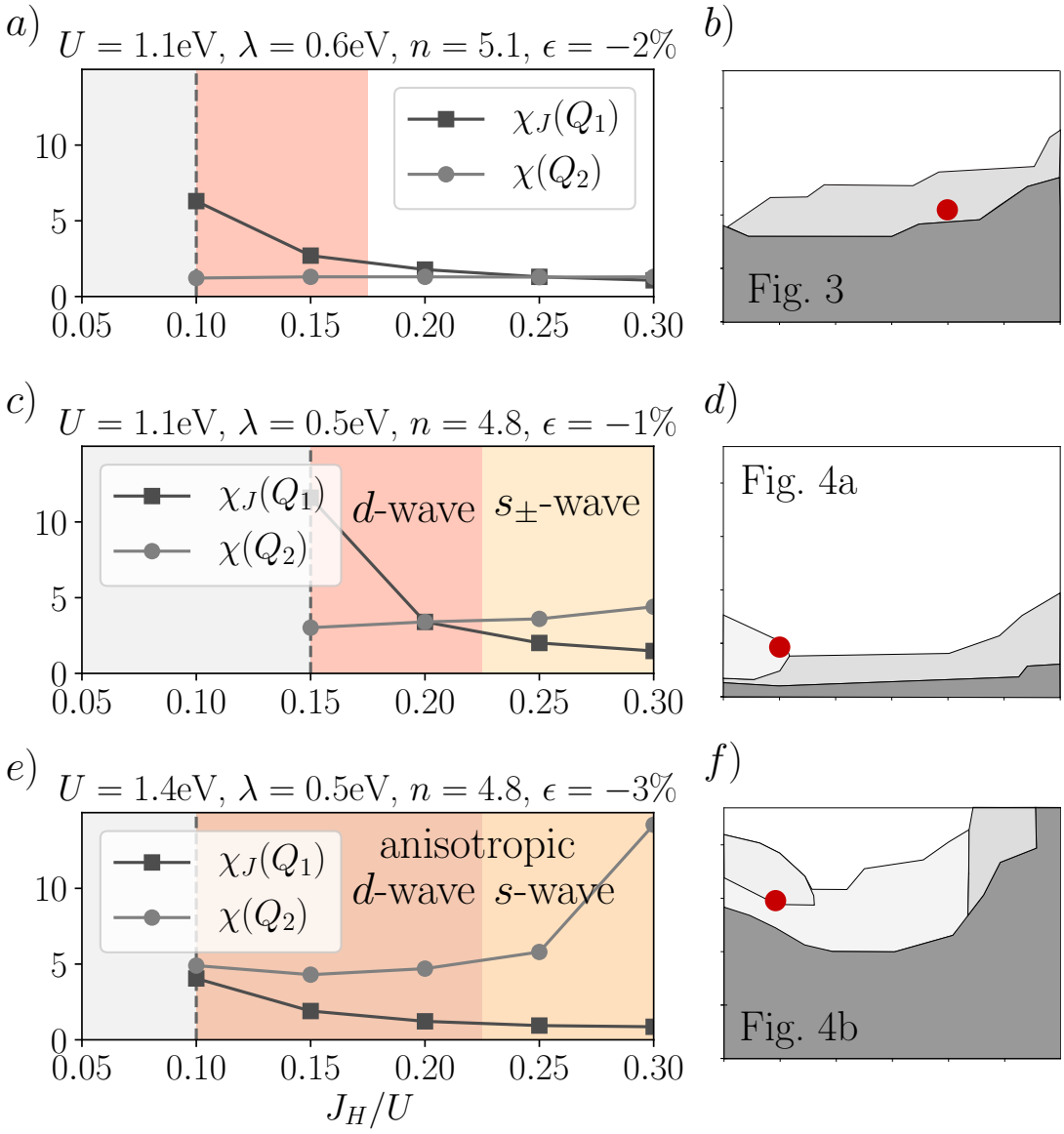

Figure 6.9: Maximum peaks in the spin and pseudospin susceptibility, Eqs. (6.37) & (6.38), for the same calculation as in Fig. 6.8 and for $U = 1.4$eV. Each value is the in-plane $\mathrm{Re}\left[\chi^{\uparrow\downarrow\uparrow\downarrow}(\boldsymbol{Q})\right] \times |t|$. For a Hund's coupling where a pseudospin d-wave is favored $\chi_J(\boldsymbol{Q}_1) > \chi(\boldsymbol{Q}_2)$. The location in the phase diagrams for the points chosen in each plot is shown in the lower row.

the largest eigenvalue of Eq. (6.29), and the symmetry of the pairing, are shown as the Hund's coupling varies. We observe a general trend in which the $s_\pm$-order becomes more favorable than d-wave superconductivity at $J_\mathrm{H} \geq 0.25U$. For the lower SOC, $\lambda = 0.5$eV, the largest eigenvalue is above unity for all values of Hund's coupling considered. The $s_\pm$-wave is only possible for low SOC and hole doping, since that places the Fermi level deeper in the band of $(j, j_z) = (\frac{3}{2}, \pm\frac{3}{2})$ character. By contrast, the d-wave order is present for a wider range of parameters.

At all points there are two main types of competing fluctuations; pseudospin fluctuations around $\boldsymbol{Q}_1 \approx (\pi, \pi)$ and spin fluctuations around $\boldsymbol{Q}_2 \approx (\frac{\pi}{2}, \frac{\pi}{2})$. By studying the maximum peak values in Fig. 6.9 one can determine which one of these fluctuations best describes the system. As can be seen in Figs. 6.6 & 6.7, dominating spin fluctuations promote an $s_\pm$-wave order. However, if both types of fluctuations are of roughly equal size the $j = 1/2$ d-wave is favored.

6.5.4 Multi-band orders

For a higher Hund's coupling superconducting orders are favored which open large gaps on multiple pockets at the Fermi surface. In Fig. 6.4a, there are two distinct superconducting orders at $U = 1.1$eV. The magnetic order disappears for small strains and superconductivity is only possible up to $\epsilon = -2\%$. Moreover, the symmetry of the superconducting order is dependent on doping. At high hole doping and some strain the pairing is an $s_\pm$-wave, while remaining a d-wave for all other doping values. When we set the Hubbard U to a higher value of $U \approx 4|t|$, as seen in Fig. 6.4, and turn on a high compressive strain the band structure changes. This can lead to new pairing functions which were not seen earlier. A drastic change occurs in Fig. 6.4b where some regions have an anisotropic s- or d-wave pairing. For all values of J_H considered in Fig. 6.10, the anisotropic order, which is a mix of s- and d- wave pairing, is found. The s-wave contribution increases with Hund's. The orbital components, as well as a simple model for this state, are described in Appendix 6.E. This superconducting order is an orbital-selective state with a stronger spin-singlet in the xz-orbital. One notable reason for this new type of pairing is the increased spin nature of the fluctuations as compressive strain is increased. As already discussed, all regions with

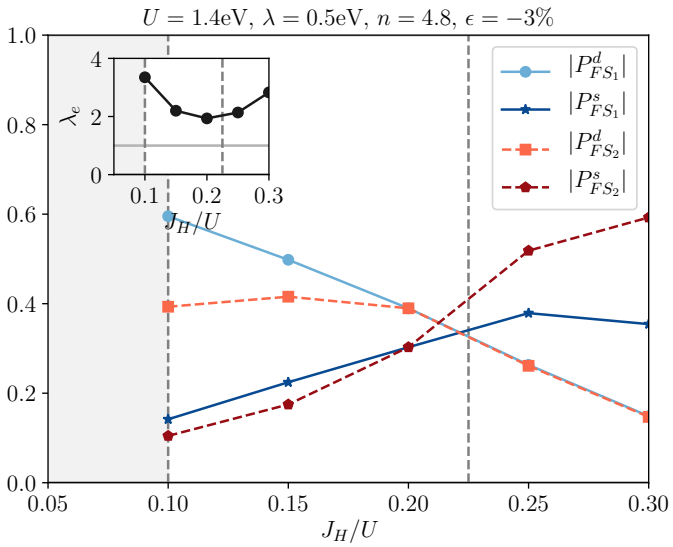

Figure 6.10: For a higher $U = 1.4$eV and high compressive strain $\epsilon = -3\%$ two new anisotropic orders are found. In Appendix 6.E the origin is identified as a higher contribution to the pairing from one of the orbitals (xz). For the pairing at the Fermi surface this manifests as both orders being a mix of s- and d-wave symmetries. As the Hund's coupling is increased the order goes from being predominantly a d-wave order, with nodes, to a node-less order with stronger s-wave components. The insert shows the largest eigenvalue λ_e.

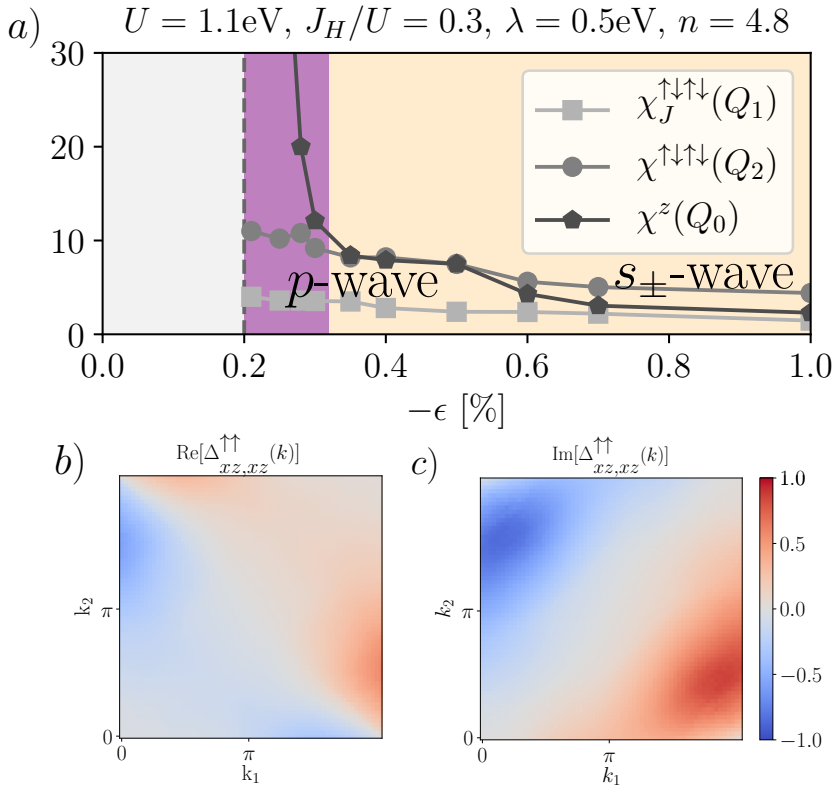

Figure 6.11: a) The total in- and out-of-plane susceptibility, Eqs. (6.37) & (6.38), are shown for a higher $J_{\mathrm{H}} = 0.3U$, where $\chi^z(\boldsymbol{Q}_0)$ is the largest component. Only for a small region close to the magnetic instability is an odd parity p-wave pairing favored. b) & c) $\Delta^{\uparrow\uparrow}_{xz,xz}(\boldsymbol{k})$ of the p-wave pairing is shown, revealing a dominating $p + ip$ structure. The equally large orbital component is $\Delta^{\uparrow\uparrow}_{yz,yz}(\boldsymbol{k}) = -\Delta^{\uparrow\uparrow}_{xz,xz}(\boldsymbol{k})$.

anisotropic pairing are mediated by a large spin susceptibility peak in $\chi^{\uparrow\downarrow\uparrow\downarrow}_{xz}(\boldsymbol{Q}_{1d})$. In Fig. 6.9, the larger spin to pseudospin susceptibility ratio can be compared for the increased strain, at all J_{H} values.

6.5.5 Odd parity

In general, the out-of-plane $\chi^z(\boldsymbol{Q}_0)$ susceptibility peaks remain smaller than either the in-plane spin $\chi^{\uparrow\downarrow\uparrow\downarrow}(\boldsymbol{Q})$ or pseudospin $\chi_J^{\uparrow\downarrow\uparrow\downarrow}(\boldsymbol{Q})$ peaks. This is the case for all values calculated so far, except for the one small region in Fig. 6.7 with large hole doping, high Hund's coupling, and low compressive strain. A high enough Hubbard interaction $U \geq 1.1$eV is also required. As several of these factors also increase the in-plane spin susceptibility, the out-of-

plane susceptibility only dominates in a very small parameter range. In Fig. 6.11 one such small patch can be found for a very high Hund's coupling, $J_{\mathrm{H}} = 0.3U$. Accompanying these fluctuations is an odd parity p-wave superconductivity. The main contribution, described by the symmetry representation detailed in Appendix 6.D, is

$$\Delta_p(\boldsymbol{k}) \approx (h_x \otimes \sigma^z + i h_y \otimes \mathbb{I}) \otimes \lambda_3. \tag{6.42}$$

where λ_j is the j^{th} Gell-Mann matrix [64] acting in the three-orbitals space. The p-wave pairing has several leading terms, which are $h_x = -\sin k_x + \sin k_x \cos k_y + \sin(2k_x)$ and $h_y = -\sin k_y + \sin k_y \cos k_x + \sin(2k_y)$. Some smaller terms are proportional to $(h_x \otimes \sigma^z + i h_y \otimes \mathbb{I}) \otimes \lambda_1$ and $\Delta^{\downarrow\downarrow}_{xy,xy}(\boldsymbol{k}) \propto \Delta^{\uparrow\uparrow}_{yz,yz}(\boldsymbol{k})$. Up- and down-spin pairing have the opposite chirality. This helical p-wave thus preserves time-reversal symmetry (TRS), since $\Delta^{\downarrow\downarrow}_{\alpha\beta}(\boldsymbol{k}) = \left(\Delta^{\uparrow\uparrow}_{\alpha\beta}\right)^* (-\boldsymbol{k})$. The helical nature is preserved for both Fermi surfaces, FS_1 and FS_2, with a larger gap on FS_2. A $\mathbb{Z}_2$ topological invariant can therefore be determined. We can consider a Chern number for each pseudospin sector, as outlined in Appendix 6.F. The defining features of the pairing are

- The helical p-wave preserves time reversal symmetry, such that the total Chern number vanishes, $\mathcal{C}_{\mathrm{tot}} = 0$.
- The pseudospin Chern number, $\nu = (\mathcal{C}_+ - \mathcal{C}_-)/2$, also vanishes such that in each pseudospin sector $\mathcal{C}_\tau = 0$.
- In each pseudospin sector we define the pocket Chern number $\mathcal{C}_{n,\tau}$ for the band n. We find $\mathcal{C}_{n,\tau} = \pm 1$ such that for each band the pseudospin Chern number is $\nu_n = \pm 1$. The pocket contributions cancel such that $\nu = \sum_n \nu_n = 0$, as the pocket of $j = 3/2$-character has the opposite chirality to the $j = 1/2$ pocket.
- Therefore no topologically protected edge/vortex modes are expected.

Even for chiral TRS-breaking superconductors the Fermi surface topology can result in a topologically trivial state, when multiple pockets are present [65, 66]. The possible Chern numbers in multiband superconductors depend on the pairing function, and the location in the Brillouin zone of the resulting topological charges [67, 68, 69].

It might be possible to expand the p-wave regime by tuning parameters such that ferromagnetism is favored. In our model, increasing the Hubbard coupling, U, accomplishes this. However, with a higher U, a higher strain required to reach the superconducting regime but a higher U also increases the in-plane fluctuations, as in Fig. 6.7. This is caused by the other fluctuations being favored when the pocket with $j = 3/2$ states becomes large. Only for a smaller pocket and a large U would the p-wave be favored. The odd parity order is thus a fine-tuned case which is found beyond realistic parameters.

6.6 Discussion

While strong interactions, spin-orbit coupling, and the proximity of multiple d-bands to the Fermi level all point to the possibility of unconventional superconductivity, experimental observation of superconductivity is still missing. In this work we suggest that compressive strain may be a possible knob that, together with doping, can turn the system from magnetic to superconducting. We model the system using the extended Hubbard-Kanamori Hamiltonian and map out its phase diagram. Magnetic orders are found using the Stoner criterion while superconductivity is studied using the RPA linearized Eliashberg equation. For the range of parameters considered in this work, we find prominent regions of strain-induced superconductivity, among them a large fraction exhibits d-wave pairing.

The d- and $s_\pm$-wave orders found are the same as in previous studies of the unstrained compound. For the values considered here the $s_\pm$-wave can arise adjacent to the AFM order, for a high enough Hund's coupling. For high strains and Hund's coupling, new orbital-selective, anisotropic s- or d-wave orders are found. In addition, we find an out-of-plane ferromagnetic order. In a very fine-tuned region, the out-of-plane susceptibility mediates an odd parity p-wave order. We note that the work of Ref. [12] finds a p-wave order in hole doped Sr_2IrO_4, albeit at an extremely large Hubbard coupling, $U = 12t$, and a lower Hund's coupling of $J_H = 0.15U$. The odd parity order we find is favored by a high Hubbard coupling, U, in the unstrained compound and could be the dominant order at those values. At higher strains the ferromagnetic fluctuations vanish. The p-wave order is found to be helical and topologically trivial, as determined via the $\mathbb{Z}_2$ invariant. However, other values of the

Hund's coupling and different Fermi surface geometry could potentially break time reversal symmetry and result in a chiral p-wave [70]. As in the case of Sr_2RuO_4, the topological nature of such a state in the iridates is highly dependent on the Fermi surface geometry and orbital composition.

It should be mentioned that the type of possible magnetic instabilities is not altered by the compressive strain for the realistic value of the Hund's coupling, $J_H = 0.1U$. However, with increasing compression the pseudospin $j = 1/2$ susceptibility decreases faster than the spin susceptibility, bringing the two leading fluctuation peaks to comparable sizes. At high Hund's coupling and lower SOC we find an antiferromagnetic order that can have a mixed in- and out-of-plane structure. Moreover, at higher strains a spin-like incommensurate magnetic order is possible. Further calculations of the particle-hole self-energy are required to characterize this magnetic order. The competition between two types of susceptibility peaks mediating the d- and s-wave orders, shares many similarities with work done on iron-pnictide superconductors [71, 72]. In iron pnictides a different nesting vector $\boldsymbol{Q} = (\pi, 0)$ connects pockets and mediates the $s_{\pm}$-wave. Ref. [71] predicts nearly degenerate multi-band s- and d-wave orders where a small change in the interaction parameters determines the favorable order. However, in contrast to our work their model does not contain spin-orbit coupling. In our work, the strong SOC and the consequent pseudospin degrees of freedom are partially responsible for the dominance of the d-wave order in the realistic regime phase diagram.

The strain-induced superconducting regimes we find all occur when the Fermi surface has multiple pockets. All superconducting orders are thus multigap orders [73, 74]. However, for a higher SOC or lower U that would not necessarily be the case. The size of the second pocket FS_2 and the value of the Hund's coupling determine the relative sizes of the gap for the two pockets. In Fig. 6.8, the relative gaps are shown projected onto the FS at low Hund's coupling, and we find that pocket 1 dominates: $\mathrm{Max}[\Delta_{FS_1}(\boldsymbol{k})] \gg \mathrm{Max}[\Delta_{FS_2}(\boldsymbol{k})]$. The smaller gap is expected to have a smaller effect on the (shared) critical temperature. Methods to determine the relative size and pairing structures of two gap superconductors have been explored in multiple compounds such as MgB_2 [75] and $SrTiO_3$ [76]. Further proposals have been made to detect any offset phases between pairing functions. Especially for the $s_{\pm}$-wave

order where signatures of the phase difference between the two pockets could be detected via Josephson tunneling [77, 78, 79].

Our results indicate that the doped and strained regime is of interest for potential iridate superconductivity. Understanding changes to magnetic fluctuations for any experiment combining strain and doping would provide great insight to the interplay of interactions and spin-orbit coupling in transition metal oxides. An observation of the susceptibility peaks that we identify as mediating superconductivity could hint at a possible superconducting phase nearby. Further understanding the signatures of the possible superconductivity, such as the Knight shift in the magnetic susceptibility [42] could be a direction for future work.

Acknowledgments

We acknowledge financial support from NSERC, RQMP, FRQNT, an Alexander McFee Fellowship from McGill University (LE), a Team Research Project from FRQNT, a grant from Fondation Courtois, and a Canada Research Chair. Computations were made on the supercomputers managed by Calcul Québec and Compute Canada. The operation of these supercomputers is funded by the Canada Foundation for Innovation (CFI), the ministère de l'économie, de la science et de l'innovation du Québec (MESI) and the Fonds de recherche du Québec - Nature et technologies (FRQ-NT).

6.A Phase diagrams at other U

In the model used in this paper there is a trade-off between doping- and strain- dependent behavior for a given strength of the Hubbard interaction U, as motivated in section 6.3. The value for the calculated the phase diagram, $U \approx 3|t|$, finds a magnetic phase transition for an expected range of strain values. In Fig. 6.12 phase diagrams are calculated at a lower $U = 0.78\text{eV} \approx 2.2|t|$. For the most realistic choice of Hund's ($J_\text{H} = 0.1U$) and spin-orbit ($\lambda = 0.6\text{eV}$), the magnetic region at $\epsilon = 0$ only extends up to $n = 4.85$ on the hole doped side. We note that for the chosen temperature and interaction parameters, a magnetic region

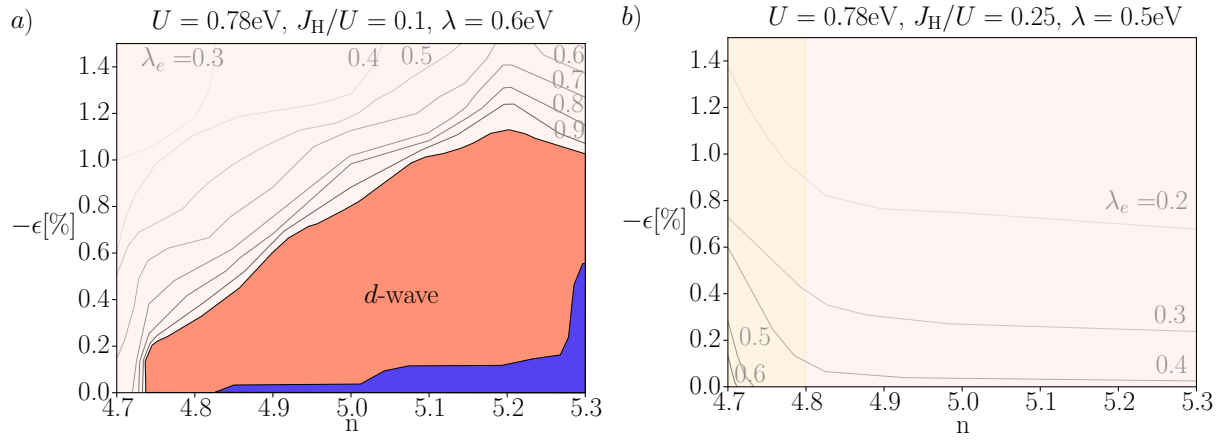

Figure 6.12: For a choice of $U = 0.78\text{ev} \approx 2.2|t|$ the Stoner criterion is met only for some doping values, for the realistic interaction parameters in a). The superconducting region has a stronger doping-dependence than in Figs. 6.3 & 6.4. However, the strain values here are lower. In b), the largest eigenvalue is $\lambda_e < 1$ for the higher Hund's coupling $J_H = 0.25U$ and lower SOC $\lambda = 0.5$eV. The pairing associated with the highest eigenvalue is an $s_{\pm}$-wave for $n < 4.8$ and a d-wave for all higher doping values.

extends beyond $n = 5.3$. Mean field studies for the lattice with staggered rotations, such as in Appendix 6.B, reveal a possible canted ferromagnetic order for this doping. The high electron doping region is therefore likely to be a canted ferromagnet, as it has nesting vector $\boldsymbol{Q} = (\pi, \pi)$. The phase diagram has a clear doping-dependence of the superconducting region, with a dome centered at the electron doped regime. However, the considered strain values only extend up to $\epsilon = -1.5\%$.

For the choice $J_H = 0.25U$ and $\lambda = 0.5$eV, neither a magnetic nor superconducting region is found for the temperature $T \approx 11$K. Similarly to the result at $U \approx 3|t|$, the leading eigenvector corresponds to two different types of pairing, depending on the considered doping regime. To explore the robustness of the strain-induces d-wave superconductivity, an additional phase diagram at $U \approx 4|t|$ is shown in Fig. 6.13. Even though the magnetic order persists up to higher values of the strain, the order is still a d-wave with mainly $j = 1/2$ contributions. At higher strains, the pocket FS_2 is larger than in Fig. 6.8 and the ratio $\text{Max}[\Delta_{FS_2}(\boldsymbol{k})]\,/\text{Max}[\Delta_{FS_1}(\boldsymbol{k})]$ is increased.

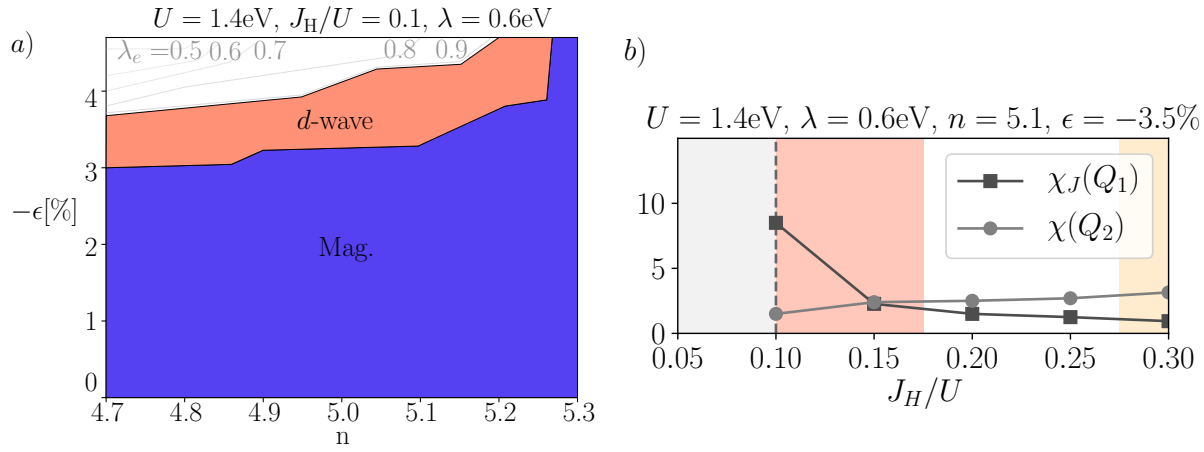

Figure 6.13: a) Phase diagram at $U = 1.4$eV and additional parameters the same as in Fig. 6.3. The mainly $j = 1/2$ d-wave order is present for a significant region in the higher strain regime. b) As in Fig. 6.9 the maximum values of pseudospin $\chi_J^{\uparrow\downarrow\uparrow\downarrow}(Q)$ and spin $\chi^{\uparrow\downarrow\uparrow\downarrow}(Q)$ susceptibility peaks are compared as the Hund's coupling is increased for one point in the phase diagram in a).

6.B Mean field calculation

The phase diagrams presented in this work are limited in the determination of competition between orders. Even though all superconducting orders are treated equally, they are calculated in the normal state. Therefore any influence of particle-hole self-energies are ignored. To compare phase boundaries for the regions of interest a self-consistent mean-field calculation was performed. We have chosen to only compare the RPA calculation for the most realistic phase diagram in Fig. 3. For the $j = 1/2$ superconducting order we can make an approximation of the effectively attractive interaction between sites. However, the anisotropic s- and d-wave orders, as well as for the p-wave, require approximations of the effective attractive interactions between both nearest and next-nearest neighbor sites. As these multi-orbital pairing functions affect more than one j-state, one must also approximate the strength of the interaction in each of these channels. The mean field calculation was chosen to include all possible on-site magnetic order parameters, in a two-site unit cell, as well as for a d-wave superconducting order

parameter in the $j = 1/2$ state. The on-site order parameters, at sublattice $s = A, B$, are

$$\begin{aligned}&\langle c^\dagger_{s,a} c_{s,b}\rangle_{\mathrm{MF},T} = \\ &\frac{1}{N_k^2}\sum_{n,\boldsymbol{k}} f(\xi_{\boldsymbol{k},n}, T)\left[U_{\mathrm{MF},\boldsymbol{k}}\right]_{(s,a)n}\left[U^\dagger_{\mathrm{MF},\boldsymbol{k}}\right]_{n(s,b)}\end{aligned} \tag{6.43}$$

with the orbit-spin label $a = (\alpha, \sigma)$, were calculated from a mean-field decoupling of the bare interactions in Eq. (6.20), as described in Ref. [25].

The superconducting order parameter is introduced by mean field decoupling of the Bogoliubov-de Genne (BdG) Hamiltonian. $\Delta_{j=1/2}$ is set to be a $j = 1/2$ d-wave singlet between the sublattices as

$$\begin{aligned}H_{\mathrm{MF,SC}} = \sum_{\boldsymbol{k}} &V(\epsilon)\Delta_{j=1/2} e^{ik_x}\left(\cos k_x - \cos k_y\right) \\ &\times \Big[a_{\boldsymbol{k},A,(\frac{1}{2},+\frac{1}{2})} a_{-\boldsymbol{k},B,(\frac{1}{2},-\frac{1}{2})} \\ &- a_{\boldsymbol{k},A,(\frac{1}{2},-\frac{1}{2})} a_{-\boldsymbol{k},B,(\frac{1}{2},+\frac{1}{2})} + \mathrm{h.c.}\Big]\end{aligned} \tag{6.44}$$

where the operators a are in the j-state basis, as in section 6.2, and $V(\epsilon) = -\frac{3}{4}J_{\mathrm{eff}}(\epsilon)$ is the effective interaction [80, 81]. Due to the structure of the hopping terms we approximate $J_{\mathrm{eff}}(\epsilon)$ in the $j = 1/2$ subspace as $J_{\mathrm{eff}}(\epsilon) = \sqrt{J_1^2 + D^2}$ [31], where

$$J_1 = \frac{4\left(t_{\mathrm{eff}}(\epsilon) - t_{\mathrm{eff},z}(\epsilon)\right)^2}{U_{\mathrm{eff}}}, \qquad D = \frac{8 t_{\mathrm{eff}}(\epsilon) t_{\mathrm{eff},z}(\epsilon)}{U_{\mathrm{eff}}} \tag{6.45}$$

Here the effective hopping parameters are $t_{\mathrm{eff}}(\epsilon) = \frac{1}{3}\left(t_1 + t_4 + t_5\right)$ and $t_{\mathrm{eff},z}(\epsilon) = t_{rot}$. The order parameter is calculated via the self-consistency equation

$$\begin{aligned}\Delta_{j=1/2} = \frac{1}{N_k^2}\sum_{n,\boldsymbol{k}}\sum_{\alpha,\beta} &e^{-ik_x} M_{\left(A,(\frac{1}{2},+\frac{1}{2})\right),\alpha} M_{\left(B,(\frac{1}{2},-\frac{1}{2})\right),\beta} \\ &\times \left[U_{\mathrm{MF},\boldsymbol{k}}\right]_{\alpha n}\left[U_{\mathrm{MF},\boldsymbol{k}}\right]_{\beta n} f(\xi_{\boldsymbol{k},n}, T)\end{aligned} \tag{6.46}$$

where the matrix M is Eq. (6.8). This and Eq. (6.43) are solved simultaneously via iterations as a set of coupled equations. Here we are treating only the interaction within the $j = 1/2$ as if it was a one-band model, where the interaction projected onto that subspace is $H_{\mathrm{eff}} = \left(U - \frac{4}{3}J_{\mathrm{H}}\right) n_{i,(\frac{1}{2},+\frac{1}{2})} n_{i,(\frac{1}{2},-\frac{1}{2})} = U_{\mathrm{eff}} n_{i,(\frac{1}{2},+\frac{1}{2})} n_{i,(\frac{1}{2},-\frac{1}{2})}$, so for the calculations $U_{\mathrm{eff}} = \frac{13}{15}U$. An

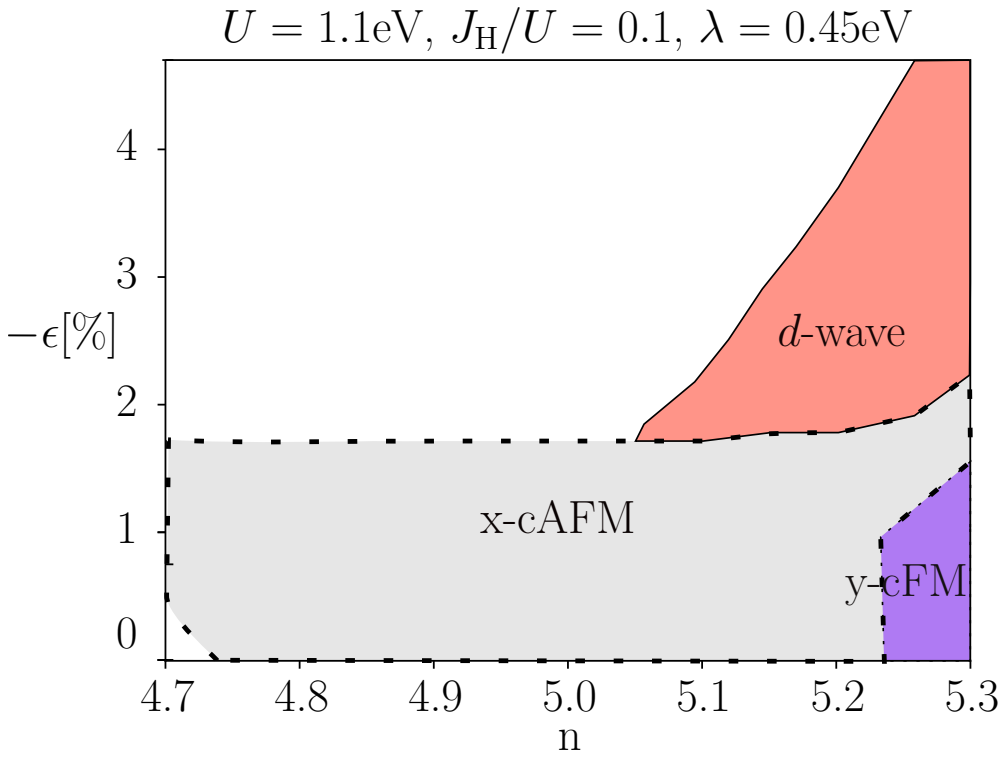

Figure 6.14: The mean field calculation for magnetic and superconducting order parameters, for the same model parameters as in Fig. 6.3 except $\lambda = 0.45$eV. Here $V = -0.25U \approx -\frac{3}{4}J_{\text{eff}}(-2.5\%)$. As the SOC is renormalized the resulting bandstructure is the same as for the phase diagram in the main text.

inclusion of d-wave pairing within the $(j, j_z) = (\frac{3}{2}, \pm\frac{3}{2})$ sate or between the $j = 3/2$ and $j = 1/2$ does not extend the superconducting phase in the calculation. The interaction used here is $U \approx t_{\text{eff}}$, and not close to the strong coupling limit. However, to compare the competition between the d-wave and magnetic orders for for the RPA calculations results in an order of roughly equal size.

Calculations were performed on a $N_k \times N_k$ lattice in momentum space, with $N_k = 100$, and self-consistent solutions were found iteratively with a convergence criterion of 10^{-7}. Due to the full set of order parameters containing terms that renormalize the spin-orbit coupling, the self-consistent mean field calculation predicts effects not included in the RPA calculation. However, the included mean field orders can only have nesting vectors $\boldsymbol{Q} = (0, 0)$ or $\boldsymbol{Q} = (\pi, \pi)$ as the two sites allow us to study either net $(\langle c^\dagger_{A,a} c_{A,b}\rangle_{\text{MF},T} + \langle c^\dagger_{B,a} c_{B,b}\rangle_{\text{MF},T})/2$ or staggered $(\langle c^\dagger_{A,a} c_{A,b}\rangle_{\text{MF},T} - \langle c^\dagger_{B,a} c_{B,b}\rangle_{\text{MF},T})/2$ values of the order parameters.

In Fig. 6.14 there are two magnetic mean field orders. The most common order is the canted in-plane antiferromagnet (x-cAFM), with a staggered magnetic moment along the x-direction and a net magnetic moment along the y-direction. Similarly to previous works, the canting angle follows the rotations of the octahedra in the lattice. When a compressive strain increases the rotations, the magnetic canting angle thus increases as well. For a high enough U the magnetic order remains up to high electron number ($n > 5.2$) the in-plane ferromagnetic component becomes dominant. A small AFM component remains, identifying this order as y-cFM. The canted orders consist mainly of $j = 1/2$ pseudospins. However, as the SOC is lowered the AFM order in the hole doped region has small $(j, j_z) = (\frac{3}{2}, \pm\frac{3}{2})$ contributions. The order parameters which renormalize the SOC depend on strain and doping. However, if $\lambda = 0.45$eV is chosen the effective spin orbit coupling $\lambda_{\text{eff}} \approx 0.6$eV.

A superconducting region is present in Fig. 6.14 and the competition between superconductivity and magnetism therefore does not affect its existence. However, in contrast to Fig. 6.3 superconductivity is only present for electron doping $n > 5.05$. For the non-interacting band structure, used for the RPA calculations in this paper, the $j = 3/2$ pocket is present in the full charge doping region around $\epsilon = -2.2\%$. As the $j = 3/2$ hole pocket increases in size for a given charge doping, the $j = 1/2$ electron pocket grows as well. The superconductivity in Fig. 6.3 is therefore present for a region where the $j = 1/2$ electron pocket is significantly larger than for $\epsilon = 0$. There the d-wave is present for all considered n.

The discrepancy between the RPA and the mean field result is due to several factors. Since these two approaches make different approximations it is not possible to determine which phase diagram is more realistic. Instead, we can gain confidence in our results in parts of the phase diagram where the two approaches agree. Each approach has its strength and weaknesses. In mean field we must pre-determine the possible channels of superconductivity and the effective attractive interaction which does not change with strain and doping. On the other hand, the self-consistency equation Eq. (6.46) is not linearized like the RPA gap equation in Eq. (6.27) and therefore the mean field is better suited for determining the relative strength of the order parameters considered. The comparison between RPA and mean field theory therefore suggest that the electron doped region is more likely to host a

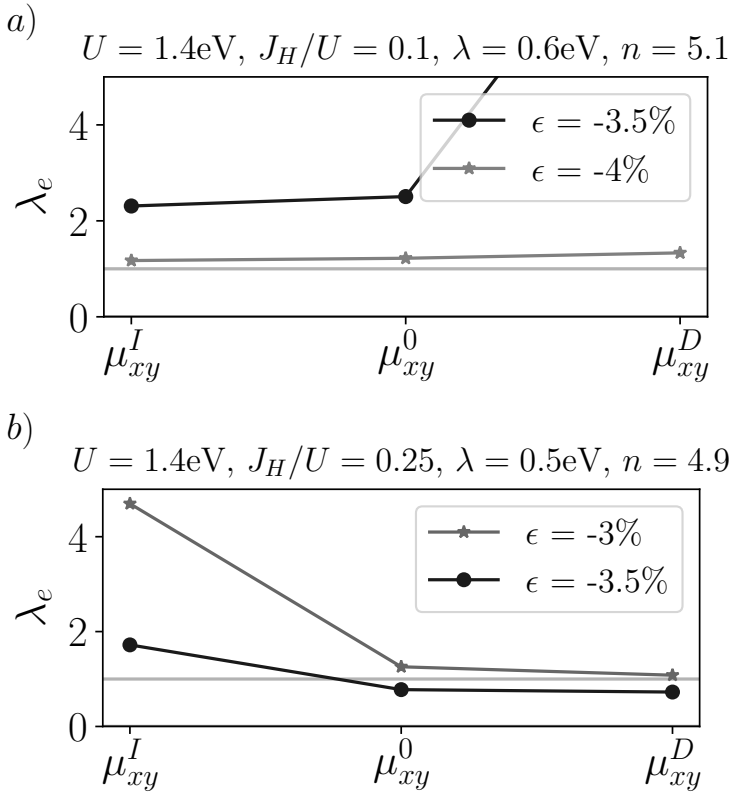

Figure 6.15: The largest eigenvalue λ_e is compared for the three options for the strain-dependence of $\mu_{xy}(\epsilon)$, as given by Eqs. (6.47) & (6.48). For $J_{\rm H} = 0.1U$ and SOC $\lambda = 0.6$eV we note the increasing eigenvalue, for a d-wave order, as the absolute value of μ_{xy} decreases. For a lower $|\mu_{xy}|$, the bands of $(3/2, \pm 3/2)$-character are pushed further down and a larger fraction of bands at the Fermi surface has $j = 1/2$ character. For $J_{\rm H} = 0.25U$ and lower SOC, the opposite trend is observed and the order is the $s_\pm$-wave.

d-wave superconducting order.

6.C Tetragonal splitting

Compression has an additional effect relevant to the iridates: an increased tetragonal distortion. The tetragonal distortion of the oxygen octahedra encompassing the iridium atoms has been measured to increase with compression - becoming more elongated when the in-plane compression increases. For unstrained Sr_2IrO_4 a small elongation is observed, which theoretically should result in a tetragonal splitting $\mu_{xy} > 0$. However, early *ab initio*

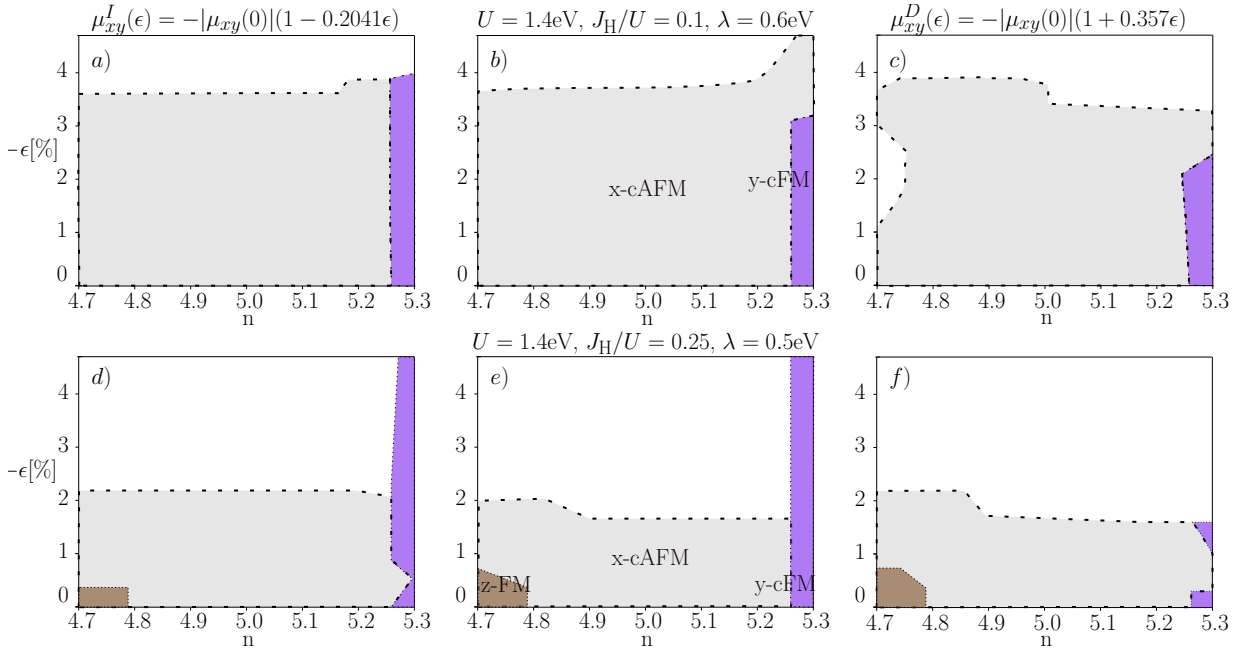

Figure 6.16: The magnetic mean field phase diagrams, Eq. (6.43), for three different options for $\mu_{xy}(\epsilon)$: μ^I_{xy} (absolute value increasing, Eq. (6.47)), μ^0_{xy} (constant), μ^D_{xy} (absolute value decreasing, Eq. (6.48)). No significant shift of the amount of strain required for a phase transition is observed. A larger absolute value of the splitting favors a magnetic order for electron doping. At the strain values required for the transition, μ^D_{xy} has changed sign, $\mu^D_{xy} > 0$, and the order instead favors hole doping. For $J_H = 0.25U$ a lower splitting favors the z-FM order while it suppresses the y-cFM order.

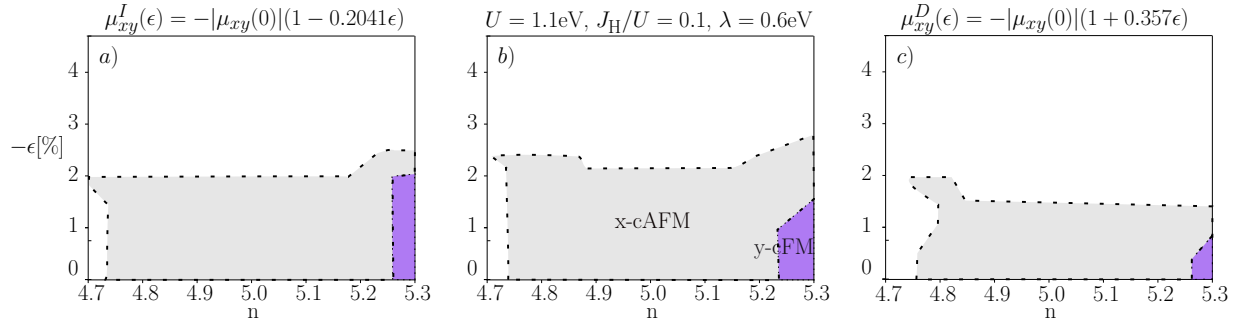

Figure 6.17: The magnetic mean field phase diagrams at a lower $U = 1.1$eV. Since the magnetic order does not remain up to as high strains, the tetragonal splitting effects are less prominent. Only $J_H = 0.1U$ is shown here as the magnetic regions for $J_H = 0.25U$ are too small to see any difference between the three models.

calculations found that the band structure is best described by a shift $\mu_{xy} < 0$ [6, 82]. Later works have proposed that the sign could arise from hybridization with ligand oxygen orbitals [83, 84]. Due to this sign difference, previous works modeling the tetragonal splitting's dependence on strain come to contradictory results, where $|\mu_{xy}|$ either increases or decreases [21, 82, 30]. A fitting of the change in energy splitting to RIXS measurements, in Ref. [28], found an increasing $|\mu_{xy}|$ for low compressive strain. A linearization of these results gives:

$$\mu^I_{xy}(\epsilon) = -|\mu_{xy}(0)|(1 - 0.2041\epsilon). \tag{6.47}$$

where ϵ is given in units of %. In Fig. 6.15 the largest eigenvalue for the linearized gap equation is compared for an approximation of $\mu_{xy}(\epsilon)$ as given by either Ref. [28] or Ref. [30]. The second approximation is based on theoretical calculations and the linearization is instead

$$\mu^D_{xy}(\epsilon) = -|\mu_{xy}(0)|(1 + 0.357\epsilon) \tag{6.48}$$

which results in a decreasing $|\mu_{xy}|$ under strain. We can note that even though the experimentally approximated values are only based on data points up to $\epsilon = -0.7\%$, the theoretical approximation $\mu^D_{xy}(\epsilon)$ is not compatible with the found trend. The experimentally motivated $\mu^I_{xy}(\epsilon)$ results in a slightly lower eigenvalue than the constant μ_{xy} for the d-wave order, at $\lambda = 0.6$eV and $J_{\mathrm{H}} = 0.1U$. Any change to the tetragonal splitting is thus expected to have a small impact on the strain-induced superconducting regions with d-wave symmetry.

As a check of the magnetic phase boundaries, for different values of the tetragonal splitting, the mean field calculation in Appendix 6.A was performed, for only the magnetic order parameters, at $N_k = 200$. In Fig. 6.16, an additional out-of-plane ferromagnetic order (z-FM) appears at the lower SOC and higher Hund's coupling. This order is only favored at high enough U and has a clear spin character, $\langle L_z\rangle/\langle S_z\rangle \approx 0.16$. Contributions from each orbital are of approximately equal strength. In terms of j-states the contributions are thus mainly from the $(j, j_z) = (\frac{1}{2}, \pm\frac{1}{2})$ and $(j, j_z) = (\frac{3}{2}, \pm\frac{3}{2})$ states.

As seen in Figs. 6.16 & 6.17, a larger absolute value of the splitting, $\mu^I_{xy}(\epsilon)$, does not result in major changes to the magnetic phase boundaries. For the other option, $\mu^D_{xy}(\epsilon)$, the

behavior with doping changes as $\mu_{xy}^{D}(\epsilon \approx -2.8\%) = 0$. The x-cAFM order remains up to higher strains for hole instead of electron doping once the sign of μ_{xy} changes.

6.D Symmetry classification

In section 6.5.1 the $\mathcal{SPOT}$-formalism [48, 61] of classifying the symmetry of the superconducting pairing is introduced. The pairing must be antisymmetric under the product of operators

$$\mathcal{SPOT}\Delta_{ab}(k) = \Delta_{ba}(-k) \tag{6.49}$$

where each exchange operator is defined as

$$\begin{aligned}
\mathcal{S}\Delta_{(s,\alpha,\sigma)(s',\alpha',\sigma')}(\boldsymbol{k},\omega) =& \Delta_{(s,\alpha,\sigma')(s',\alpha',\sigma)}(\boldsymbol{k},\omega) \\
\mathcal{P}\Delta_{(s,\alpha,\sigma)(s',\alpha',\sigma')}(\boldsymbol{k},\omega) =& \Delta_{(s,\alpha,\sigma)(s',\alpha',\sigma')}(-\boldsymbol{k},\omega) \\
\mathcal{O}\Delta_{(s,\alpha,\sigma)(s',\alpha',\sigma')}(\boldsymbol{k},\omega) =& \Delta_{(s,\alpha',\sigma)(s',\alpha,\sigma')}(\boldsymbol{k},\omega) \\
\mathcal{T}\Delta_{(s,\alpha,\sigma)(s',\alpha',\sigma')}(\boldsymbol{k},\omega) =& \Delta_{(s,\alpha,\sigma)(s',\alpha',\sigma')}(\boldsymbol{k},-\omega)
\end{aligned} \tag{6.50}$$

In Fig. 6.18 the symmetries of a found $j = 1/2$ d-wave pairing is shown. The maxima of each component of Δ are separated under the present spin-singlet and spin-triplet operations. An ideal pseudospin singlet will have both spin-singlet and spin-triplet components of comparable size, in the orbital-spin basis. As the transformation between bases is independent of momentum, the spatial parity of the state is unchanged. The spin-triplet components are therefore orbital-singlets $\mathcal{S}^{+}\mathcal{P}^{+}\mathcal{O}^{-}\mathcal{T}^{+}$. The found d-wave in Fig. 6.18 has additional small components from other j-states. The compressive strain decreases the contributions from the xy-orbital at the Fermi surface as well as increases the interorbital xz-yz hopping. There are therefore more contributions from spin-singlet and $m_z = 0$ spin-triplet components, than from $m_z = 1$ triplets. In Fig. 6.19 the symmetries of an $s_{\pm}$-wave is shown. The $s_{\pm}$-wave has strong components from several j-states. As this order is found to be mediated by spin-like fluctuations mainly in the yz- and xz-orbitals, between bands of $j = 1/2$ and $j = 3/2$ character, we can consider the main components of the pairing to come from pairing within and between those orbitals.

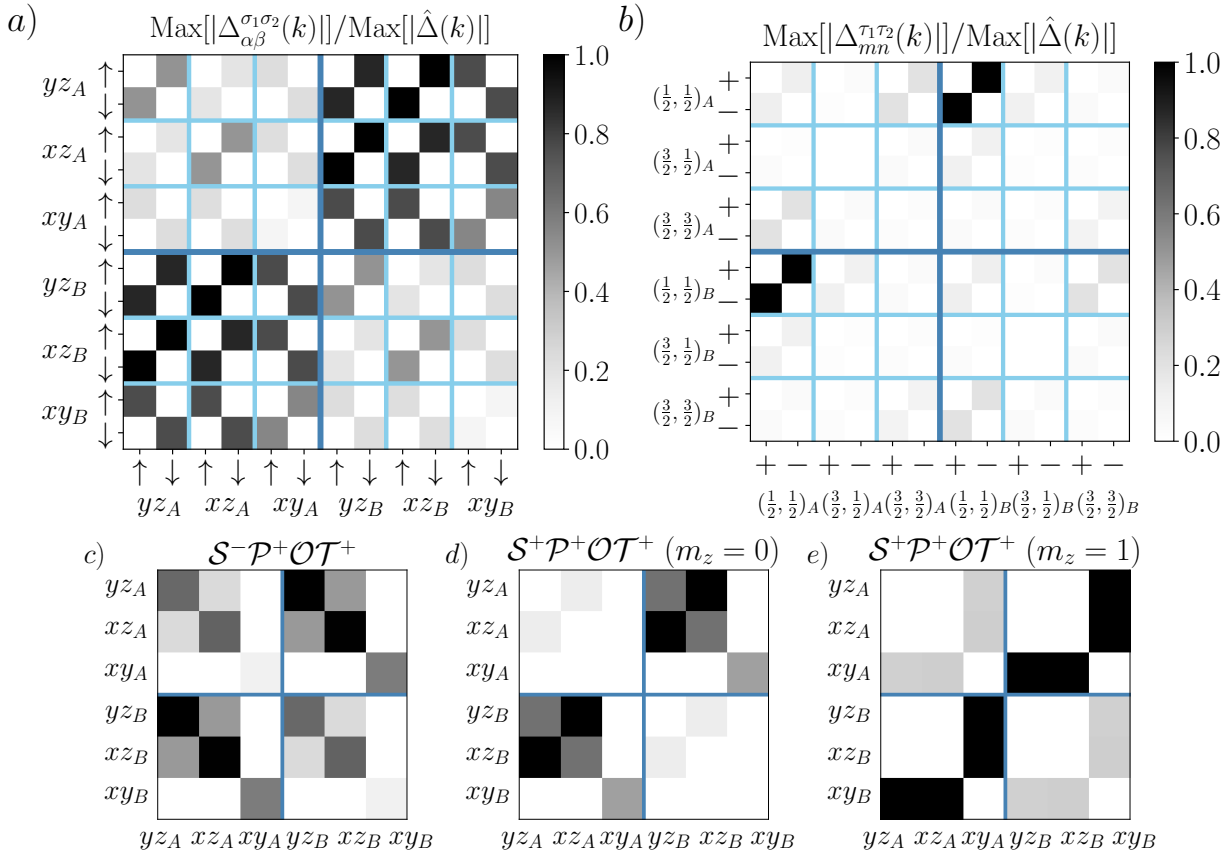

Figure 6.18: The calculated even parity d-wave pairing (found eigenstate to the largest eigenvalue at the point $U = 1.1$eV, $J_{\mathrm{H}} = 0.1U$, $\lambda = 0.6$eV, $n = 5.1$, $\epsilon = -2\%$), where the maximum value of each component is shown both in a) the orbital $\Delta^{\sigma_1\sigma_2}_{\alpha\beta}$ and in the b) j-state bases $\Delta^{\tau_1\tau_2}_{mn}$. The largest value of the order parameter is normalized to $\mathrm{Max}|\hat{\Delta}(k)| = 1$. In the orbital basis, the pairing has many inter-sublattice components of equal size. As shown in c),d),e), considering the pairing with even or odd spin symmetries results in both large spin-singlet and spin-triplet components. In j-state components the pairing is clearly dominated by a $j = 1/2$ pseudospin singlet.

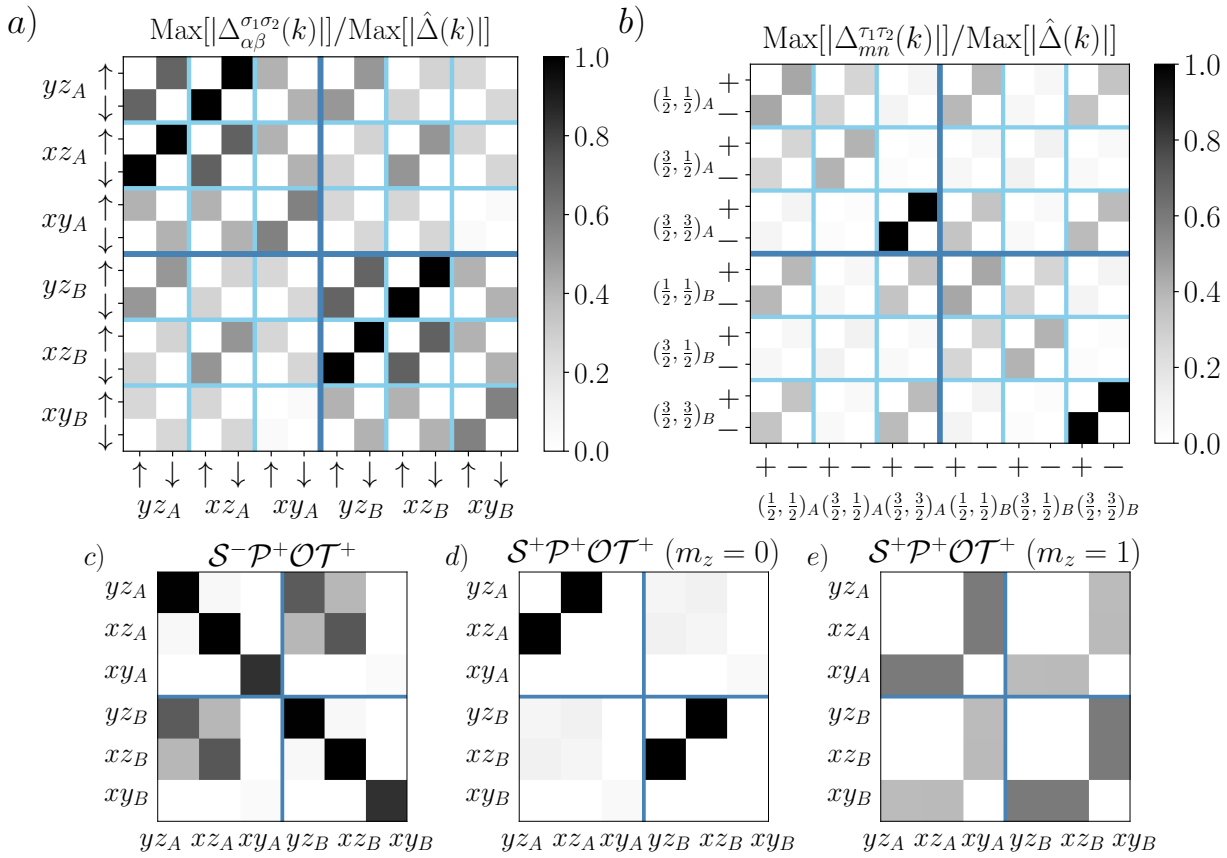

Figure 6.19: The calculated even parity $s_{\pm}$-wave pairing (at $U = 1.1$eV, $J_{\mathrm{H}} = 0.3U$, $\lambda = 0.5$eV, $n = 4.8$, $\epsilon = -1\%$). This order is a combination of several components both in a) the orbital and b) j-state bases, which are normalized by the largest value of the order parameter $\mathrm{Max}|\hat{\Delta}(k)|$. The pairing consists mainly of intra-sublattice pseudospin-singlets. The strongest components at this point in the phase diagram in the $(j, j_z) = (\frac{3}{2}, \pm\frac{3}{2})$-state, with a $(j, j_z) = (\frac{1}{2}, \pm\frac{1}{2})$ pseudospin singlet following in size.

The superconducting order can be expressed exactly via its full symmetry representation. We consider the pairing for a spin and orbital combination:

$$\Delta^{\alpha\beta}_{\sigma\sigma'}(\boldsymbol{k}) = \frac{1}{2}\sum_{s,s'} e^{ik_x(\Theta_s - \Theta_{s'})}\Delta^{(\alpha,s)(\beta,s')}_{\sigma\sigma'}(\boldsymbol{k}) \tag{6.51}$$

where Θ_s is the same function as in Eq. (6.38) and gives us the combined contribution from both sublattice sites. The symmetry representation for the spatial symmetry $\eta^\mu(\boldsymbol{k})$ is specified in Table 6.1. The pairing can be decomposed into symmetry representations for the spin and orbital structure. If $\mathcal{C}_{\mu\nu\rho}$ is the projection constant for a chosen representation, then any superconducting order can be written as:

$$\Delta^{\alpha\beta}_{\sigma\sigma'}(\boldsymbol{k}) = \sum_{\mu,\nu,\rho} \mathcal{C}_{\mu\nu\rho}\eta^\mu(\boldsymbol{k})S^\nu_{\sigma\sigma'}O^\rho_{\alpha\beta} \tag{6.52}$$

For the spin degree of freedom, $S^\nu_{\sigma\sigma'}$ are the generators for the SU(2) algebra, the Pauli matrices σ^i with $i = 0, x, y, z$. For the orbital degree of freedom, $O^\rho_{\alpha\beta}$ are the generators for the SU(3) algebra, the Gell-Mann matrices [64] λ_i with $i = 0, 1, \ldots, 8$. The Pauli matrices act in spin $(\uparrow, \downarrow)$ space and can form spin-triplets $(\sigma^0, \sigma^x, \sigma^z)$ and spin-singlets (σ^y). The Gell-Mann matrices act in orbital (d_{yz}, d_{xz}, d_{xy}) space and can form intraorbital pairings $(\lambda_0, \lambda_3, \lambda_8)$, and interorbital pairings that can be either even $(\lambda_1, \lambda_4, \lambda_6)$ or odd $(\lambda_2, \lambda_5, \lambda_7)$ under orbital exchange.

The found d-wave is a pseudospin singlet, which within the $j = 1/2$ subspace is

$$\Delta_d(\boldsymbol{k}) \approx \eta^{B_{1g}}_{R=1}(\boldsymbol{k}) \otimes (i\tilde{\sigma}^y) \tag{6.53}$$

where $\tilde{\sigma}^y$ acts on the pseudospins $\tau = +, -$. The $s_\pm$-wave can be expressed approximately as intraorbital spin-singlets and interorbital spin-triplets in the yz- and xz-orbitals:

$$\begin{aligned}\Delta_{s_\pm}(\boldsymbol{k}) \approx \Big(\mathcal{C}^{A_{1g}}_{R=0}\eta^{A_{1g}}_{R=0}(\boldsymbol{k}) + \eta^{A_{1g}}_{R=2}(\boldsymbol{k})\Big) \otimes \\ [(i\sigma^y) \otimes (\lambda_{11} + \lambda_{22}) - i\sigma^x \otimes (i\lambda_2)]\end{aligned} \tag{6.54}$$

with $\lambda_{11} = \left(\frac{1}{3}\lambda_0 + \frac{1}{2}\lambda_3 + \frac{1}{2\sqrt{3}}\lambda_8\right)$ and $\lambda_{22} = \left(\frac{1}{3}\lambda_0 - \frac{1}{2}\lambda_3 + \frac{1}{2\sqrt{3}}\lambda_8\right)$ representing intraorbital

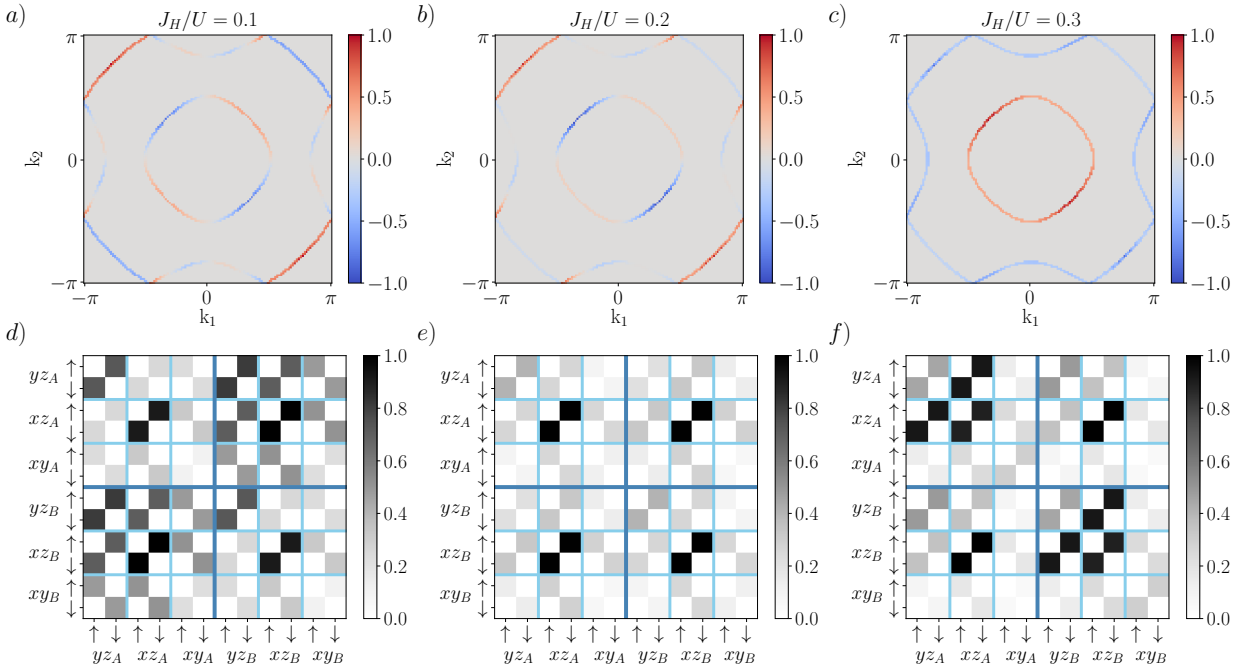

Figure 6.20: a),b),c): The intraband pairing for the anisotropic superconducting orders is shown on the FS as the Hund's coupling J_{H} is increased, for the same values as in Fig. 6.10. All orders are a mix of s- and d-wave symmetries, with only the one at $J_{\mathrm{H}} = 0.3U$ being node-less. d), e),f): The maximum of pairing components in the orbital basis for the same Hund's coupling as the plot above, shown as $\mathrm{Max}\left[|\Delta^{\sigma\sigma'}_{\alpha\beta}(\boldsymbol{k})|\right]/\mathrm{Max}\left[|\hat{\Delta}(\boldsymbol{k})|\right]$. For all values the order exists mainly in the yz- and xz-orbitals, with barely any contributions from xy. However, the order is stronger in xz. At $J_{\mathrm{H}} = 0.2U$ the pairing originates almost entirely from the xz-orbital.

pairing. The A_{1g} spatial symmetry has two contributions with a relative weight specified by $\mathcal{C}^{A_{1g}}_{R=0} \approx 0.7$. This pairing has additional smaller contributions involving the xy-orbital: $\propto (i\sigma^y) \otimes \lambda_{33} = (i\sigma^y) \otimes \left(\lambda_0 - \sqrt{3}\lambda_8\right)$, $\propto (-i)\sigma^0 \otimes (i\lambda_5)$, and $\propto (-i)\sigma^z \otimes (i\lambda_7)$.

6.E Anisotropic pairing

The anisotropic orders found at high compressive strain, in section 6.5.3, appear when fluctuations with $\boldsymbol{Q}$-vectors which connect states of the same orbitals become large enough. In Fig. 6.20 the found anisotropic orders, for three values of the Hund's coupling, are characterized by projecting the pairing on the Fermi surface as well as the maximal value

of each orbital-spin component of the pairing. At the Fermi surface the weight is stronger along the x-direction, on all pockets. The xz orbital has the largest contribution. The other notable difference, from the d- and $s_{\pm}$-wave orders, is that the anisotropic orders have equal size intra- and inter-sublattice components of the xz-orbital.

The anisotropic orders and $s_{\pm}$-order are mediated mainly by spin fluctuations. However, the pockets at the Fermi surface have a strong character of the $(j, j_z) = (\frac{1}{2}, \pm\frac{1}{2})$ or $(j, j_z) = (\frac{3}{2}, \pm\frac{3}{2})$ state. The orders originate mostly from the yz- and xz-orbitals, and the pairing can be transformed into the j-states, via Eq. (6.8), as

$$\begin{aligned}\Delta^{\tau\tau'}_{mn}(k) &= \sum_{\alpha\beta\sigma\sigma'} c^{(\tau\tau')(\sigma\sigma')}_{(mn)(\alpha\beta)} \Delta^{\sigma\sigma'}_{\alpha\beta}(k) \\ &= \sum_{\alpha\beta\sigma\sigma'} M_{(m,\tau),(\alpha,\sigma)} M_{(n,\tau'),(\beta,\sigma')} \Delta^{\sigma\sigma'}_{\alpha\beta}(k)\end{aligned} \tag{6.55}$$

where $m = \left(\frac{1}{2}, \pm\frac{1}{2}\right), \left(\frac{3}{2}, \pm\frac{1}{2}\right), \left(\frac{3}{2}, \pm\frac{3}{2}\right)$, $\tau = +, -$, $\alpha = yz, xz, xy$, and $\sigma = \uparrow, \downarrow$. We can identify $c^{(+-)(\uparrow\downarrow)}_{(\frac{3}{2},\pm\frac{3}{2})(yz,yz)} = c^{(+-)(\uparrow\downarrow)}_{(\frac{3}{2},\pm\frac{3}{2})(xz,xz)} = -\frac{1}{2}$ and $c^{(+-)(\uparrow\downarrow)}_{(\frac{1}{2},\pm\frac{1}{2})(yz,yz)} = c^{(+-)(\uparrow\downarrow)}_{(\frac{1}{2},\pm\frac{1}{2})(xz,xz)} = \frac{1}{3}$. As can be seen in Fig. 6.5, sections of the hole doped Fermi surface are mainly of either yz- or xz-character. This is a result of the quasi-1d dispersion in each of these orbitals in Eq. (6.4). A simplified model for the two Fermi surfaces is to introduce orbitals with a spatial dependence along the parameter θ around a circular FS:

$$\begin{aligned}|yz\rangle_\theta &= |\cos\theta||yz\rangle \\ |xz\rangle_\theta &= |\sin\theta||xz\rangle \\ |xy\rangle_\theta &= (|\cos\theta| + |\sin\theta|)\,|xy\rangle\end{aligned} \tag{6.56}$$

Here only one site and the full Brillouin zone (BZ) are considered for simplicity. So in a BZ where FS_1 is purely $(\frac{1}{2}, \pm\frac{1}{2})$ and FS_2 is $(\frac{3}{2}, \pm\frac{3}{2})$ (with an energy shift ξ of the xy-orbital):

$$\begin{aligned}|\mathrm{FS}_1, \uparrow\rangle_\theta &= |\frac{1}{2}, +\frac{1}{2}\rangle_\theta - \xi|xy, \uparrow\rangle_\theta \\ &= \frac{1}{\mathcal{N}_1}\left(|yz, \downarrow\rangle_\theta - i|xz, \downarrow\rangle_\theta + (1 - \sqrt{3}\xi)|xy, \uparrow\rangle_\theta\right)\end{aligned} \tag{6.57}$$

and

$$|\mathrm{FS}_2,\uparrow\rangle_\theta = |\frac{3}{2},+\frac{3}{2}\rangle_\theta = \frac{1}{\mathcal{N}_2}\left(-|yz,\downarrow\rangle_\theta - i|xz,\downarrow\rangle_\theta\right) \tag{6.58}$$

where $\mathcal{N}_1, \mathcal{N}_2$ are normalization factors. For a simplified constant order only within each orbital, $\Delta^{\uparrow\downarrow}_{yz,yz}(k) = \Delta$ the pairing on each FS becomes

$$\Delta^{\downarrow\uparrow}_{\mathrm{FS}_1} = \frac{\cos^2\theta}{\mathcal{N}_1^2}\Delta, \qquad \Delta^{\downarrow\uparrow}_{\mathrm{FS}_2} = -\frac{\cos^2\theta}{\mathcal{N}_2^2}\Delta \tag{6.59}$$

If instead $\Delta^{\uparrow\downarrow}_{xz,xz} = \Delta$

$$\Delta^{\downarrow\uparrow}_{\mathrm{FS}_1} = \frac{\sin^2\theta}{\mathcal{N}_1^2}\Delta, \qquad \Delta^{\downarrow\uparrow}_{\mathrm{FS}_2} = -\frac{\sin^2\theta}{\mathcal{N}_2^2}\Delta \tag{6.60}$$

Each orbital thus results in a quasi-1d pairing on both Fermi surfaces. If one of the orbitals dominate $\Delta^{\uparrow\downarrow}_{xz,xz} > \Delta^{\uparrow\downarrow}_{yz,yz}$ the order is an anisotropic s-wave, with some d-wave components.

To study the full $s_\pm$-wave, it can be modeled as equal parts from both orbitals, $\Delta^{\uparrow\downarrow}_{yz,yz} = \Delta^{\uparrow\downarrow}_{xz,xz} = \Delta$:

$$\begin{aligned}\Delta^{\downarrow\uparrow}_{\mathrm{FS}_1} &= \frac{\cos^2\theta + \sin^2\theta}{\mathcal{N}_1^2}\Delta &&= \frac{1}{\mathcal{N}_1^2}\Delta \\ \Delta^{\downarrow\uparrow}_{\mathrm{FS}_2} &= -\frac{\cos^2\theta + \sin^2\theta}{\mathcal{N}_2^2}\Delta &&= -\frac{1}{\mathcal{N}_2^2}\Delta\end{aligned} \tag{6.61}$$

where in the ideal j-state case $\mathcal{N}_1^2 = 3$ and $\mathcal{N}_2^2 = 2$. This is one of the primary reasons for the s-wave symmetry resulting in an $s_\pm$-wave with a larger weight on FS_2. However, the found $s_\pm$-wave does not have purely $\mathcal{S}^-\mathcal{P}^+\mathcal{O}^+\mathcal{T}^+$ intraorbital components but also interorbital $\mathcal{S}^+\mathcal{P}^+\mathcal{O}^-\mathcal{T}^+$-terms, see Fig. 6.19. As these terms all have the same magnitude $\Delta^{\uparrow\downarrow}_{yz,xz} = -\Delta^{\uparrow\downarrow}_{xz,yz} = i\Delta$. Projected onto the Fermi surface

$$\Delta^{\downarrow\uparrow}_{\mathrm{FS}_1} = \frac{2|\cos\theta||\sin\theta|}{\mathcal{N}_1^2}\Delta, \qquad \Delta^{\downarrow\uparrow}_{\mathrm{FS}_2} = \frac{2|\cos\theta||\sin\theta|}{\mathcal{N}_2^2}\Delta. \tag{6.62}$$

They contribute to both bands with the same sign and to the same sections. The pairing used for these examples so far has been a uniform s-wave, $\Delta(\boldsymbol{k}) = \Delta$. In Eq. (6.54) we can note that the found $s_\pm$-wave has a dependence on momentum, with a large contribution from the $\eta^{A_{1g}}_{R=2}(\boldsymbol{k}) = 2\cos k_x \cos k_y$ symmetry. The placement of FS_1 and FS_2 in the BZ therefore affects the sign of the gaps. As a result, both intra- and inter-orbital terms play a role in the origin of the $s_\pm$-wave pairing.

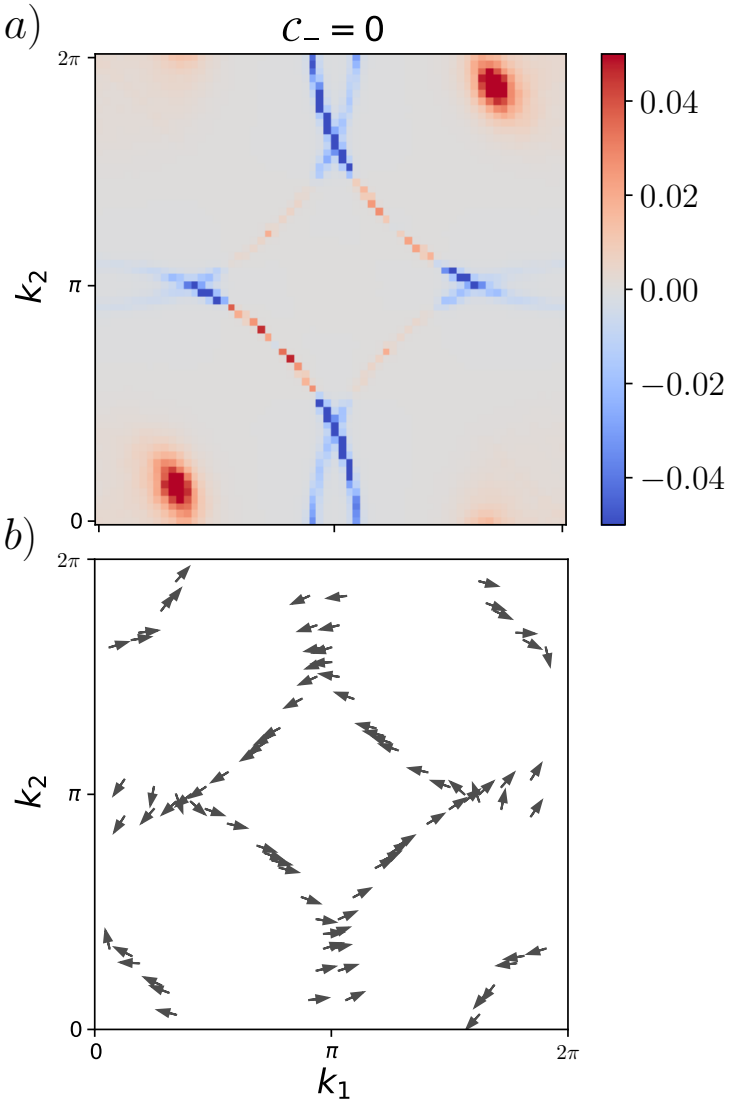

Figure 6.21: The a) Berry curvature and b) intraband phase winding are calculated for bands in the pseudospin down sector, for the pairing in Fig. 6.11. For the folded BZ we can consider 4 pockets, centered around $(k_1, k_2) = (0,0), (0,\pi), (\pi,0), (\pi,\pi)$. Each pocket has $\mathcal{C}_{n,-} = \pm 1$, such that the total Chern number cancels out to $\mathcal{C}_- = 0$. For each pocket the phase $\phi_{\boldsymbol{k}}$ can be seen to wind in opposite directions for the different pockets.

6.F Topological invariant

To determine the topological properties of the found odd parity order we consider the pairing in the Bogoliubov-de Gennes (BdG) Hamiltonian

$$H_{\mathrm{BdG}} = \sum_{\boldsymbol{k}} \left(c^\dagger_{\boldsymbol{k}}, c_{-\boldsymbol{k}}\right) \begin{pmatrix} H(\boldsymbol{k}) & \Delta(\boldsymbol{k}) \\ \Delta^\dagger(\boldsymbol{k}) & -H^{\mathrm{T}}(-\boldsymbol{k}) \end{pmatrix} \begin{pmatrix} c_{\boldsymbol{k}} \\ c^\dagger_{-\boldsymbol{k}} \end{pmatrix} \tag{6.63}$$

with the non-interacting Hamiltonian $H(\boldsymbol{k})$ from Eq. (6.1). $\Delta(\boldsymbol{k})$ is the eigenstate of the largest eigenvalue for Eq. (6.29), scaled to set the minimal gap at the Fermi surface to 0.02eV. As the specific odd parity pairing found in section 6.5.5 is block diagonal in pseudospin up and down, the full Hamiltonian can be rearranged into a block-diagonal form

$$H_{\mathrm{BdG}} = \sum_{\boldsymbol{k}} \boldsymbol{\Psi}^\dagger_{\boldsymbol{k}} \begin{pmatrix} H^+_{\mathrm{BdG}}(\boldsymbol{k}) & 0 \\ 0 & H^-_{\mathrm{BdG}}(\boldsymbol{k}) \end{pmatrix} \boldsymbol{\Psi}_{\boldsymbol{k}} \tag{6.64}$$

where $\boldsymbol{\Psi}_{\boldsymbol{k}} = (\Psi_{+,\boldsymbol{k}}, \Psi_{-,\boldsymbol{k}})^{\mathrm{T}}$ is divided into the pseudospin sectors $\{(yz,\downarrow),(xz,\downarrow),(xy,\uparrow)\}$ and $\{(yz,\uparrow),(xz,\uparrow),(xy,\downarrow)\}$. The eigenstates and eigenvalues are given as $H_{\mathrm{BdG}}|n\rangle = E_n|n\rangle$ and for each pseudospin sector $H^\tau_{\mathrm{BdG}}|n\rangle = E_{n,\tau}|n,\tau\rangle$. We calculate the Berry curvature for all filled bands via [85]

$$\begin{aligned} \Omega^{(n)}_z(\boldsymbol{k}) = &- \mathrm{Im} \sum_{n'\neq n} f(E_n) f(1-E_{n'}) \\ &\times \frac{\langle n|\partial_x H_{\mathrm{BdG}}|n'\rangle\langle n'|\partial_y H_{\mathrm{BdG}}|n\rangle - \langle n|\partial_y H_{\mathrm{BdG}}|n'\rangle\langle n'|\partial_x H_{\mathrm{BdG}}|n\rangle}{(E_n - E_{n'})^2} \end{aligned} \tag{6.65}$$

$$\begin{aligned} \Omega^{(n)}_z(\boldsymbol{k}) = &- \mathrm{Im} \sum_{n'\neq n} \sum_{a,b,c,d} \sum_{i,j\in\{x,y\}} f(E_n) f(1-E_{n'}) \left[U^\dagger_{\boldsymbol{k}}\right]_{na} [U_{\boldsymbol{k}}]_{bn'} \left[U^\dagger_{\boldsymbol{k}}\right]_{n'c} [U_{\boldsymbol{k}}]_{dn} \\ &\times \epsilon_{ij} \frac{\langle a|\partial_i H_{\mathrm{BdG}}|b\rangle\langle c|\partial_j H_{\mathrm{BdG}}|d\rangle}{(E_n - E_{n'})^2} \end{aligned} \tag{6.66}$$

where $\epsilon_{xy} = -\epsilon_{yx} = 1$ and $\epsilon_{ii} = 0$. $|a\rangle$ is the spin-orbital basis $a = (\alpha, \sigma, s)$ with orbital α, spin σ, and sublattice s. However, since all $\langle a,+|\partial_i H_{\mathrm{BdG}}|b,-\rangle = 0$ the Berry curvature can

be calculated separately for each pseudospin sector

$$\Omega_z^{(n)}(\boldsymbol{k}) = \Omega_z^{(n,+)}(\boldsymbol{k}) + \Omega_z^{(n,-)}(\boldsymbol{k}) \tag{6.67}$$

and the Chern number per pseudospin is

$$\mathcal{C}_\tau = \frac{1}{2\pi} \int_{\mathrm{BZ}} \sum_n \Omega^{(n,\tau)}(\boldsymbol{k}) dk_x dk_y \tag{6.68}$$

In Fig. 6.21 the Berry curvature for all filled bands is shown for the pseudospin down sector. In addition, the phase $\phi_{\boldsymbol{k}}$ of the intraband pairing, where $\Delta^{\downarrow\downarrow}_{\mathrm{FS}_n}(\boldsymbol{k}) = |\Delta^{\downarrow\downarrow}_{\mathrm{FS}_n}(\boldsymbol{k})| e^{i\phi_{\boldsymbol{k}}}$, is plotted along the Fermi surface. The winding of the phase can be seen to be opposite for the bands. If the pockets are fully separated the Chern number for each pocket can also be given by the winding of the phase [86]

$$\mathcal{C}_n = \frac{1}{2\pi} \oint_{\mathrm{FS}_n} \nabla \phi_{\boldsymbol{k}} \cdot d\boldsymbol{k}. \tag{6.69}$$

Bibliography

[1] W. Witczak-Krempa, G. Chen, Y. B. Kim, and L. Balents, "Correlated Quantum Phenomena in the Strong Spin-Orbit Regime," *Annual Review of Condensed Matter Physics*, vol. 5, pp. 57–82, mar 2014.

[2] G. Cao and P. Schlottmann, "The challenge of spin–orbit-tuned ground states in iridates: a key issues review," *Reports on Progress in Physics*, vol. 81, p. 042502, apr 2018.

[3] J. Bertinshaw, Y. Kim, G. Khaliullin, and B. Kim, "Square Lattice Iridates," *Annual Review of Condensed Matter Physics*, vol. 10, pp. 315–336, mar 2019.

[4] S. Boseggia, H. C. Walker, J. Vale, R. Springell, Z. Feng, R. S. Perry, M. Moretti Sala, H. M. Rønnow, S. P. Collins, and D. F. McMorrow, "Locking of iridium magnetic moments to the correlated rotation of oxygen octahedra in Sr_2IrO_4 revealed by x-ray resonant scattering," *Journal of Physics: Condensed Matter*, vol. 25, p. 422202, oct 2013.

[5] M. K. Crawford, M. A. Subramanian, R. L. Harlow, J. A. Fernandez-Baca, Z. R. Wang, and D. C. Johnston, "Structural and magnetic studies of Sr_2IrO_4," *Phys. Rev. B*, vol. 49, pp. 9198–9201, Apr 1994.

[6] B. J. Kim, H. Jin, S. J. Moon, J.-Y. Kim, B.-G. Park, C. S. Leem, J. Yu, T. W. Noh, C. Kim, S.-J. Oh, J.-H. Park, V. Durairaj, G. Cao, and E. Rotenberg, "Novel $J_{\mathrm{eff}} = 1/2$ Mott State Induced by Relativistic Spin-Orbit Coupling in Sr_2IrO_4," *Physical Review Letters*, vol. 101, p. 076402, aug 2008.

[7] Y. K. Kim, O. Krupin, J. D. Denlinger, A. Bostwick, E. Rotenberg, Q. Zhao, J. F. Mitchell, J. W. Allen, and B. J. Kim, "Fermi arcs in a doped pseudospin-1/2 Heisenberg antiferromagnet," *Science*, vol. 345, pp. 187–190, jul 2014.

[8] Y. Cao, Q. Wang, J. A. Waugh, T. J. Reber, H. Li, X. Zhou, S. Parham, S. R. Park, N. C. Plumb, E. Rotenberg, A. Bostwick, J. D. Denlinger, T. Qi, M. A. Hermele, G. Cao, and D. S. Dessau, "Hallmarks of the Mott-metal crossover in the hole-doped pseudospin-1/2 Mott insulator Sr_2IrO_4," *Nature Communications*, vol. 7, pp. 1–7, 2016.

[9] F. Wang and T. Senthil, "Twisted Hubbard Model for Sr_2IrO_4 : Magnetism and Possible High Temperature Superconductivity," *Physical Review Letters*, vol. 106, p. 136402, mar 2011.

[10] H. Watanabe, T. Shirakawa, and S. Yunoki, "Monte Carlo Study of an Unconventional Superconducting Phase in Iridium Oxide $J_{\mathrm{eff}} = 1/2$ Mott Insulators Induced by Carrier Doping," *Physical Review Letters*, vol. 110, p. 027002, jan 2013.

[11] Y. Yang, W.-S. Wang, J.-g. Liu, H. Chen, J.-h. Dai, and Q.-h. Wang, "Superconductivity in doped Sr_2IrO_4: A functional renormalization group study," *Physical Review B*, vol. 89, p. 094518, mar 2014.

[12] Z. Y. Meng, Y. B. Kim, and H.-Y. Kee, "Odd-Parity Triplet Superconducting Phase in Multiorbital Materials with a Strong Spin-Orbit Coupling: Application to Doped Sr_2IrO_4," *Phys. Rev. Lett.*, vol. 113, p. 177003, Oct 2014.

[13] Y. Gao, T. Zhou, H. Huang, and Q. H. Wang, "Possible superconductivity in Sr_2IrO_4 probed by quasiparticle interference," *Scientific Reports*, vol. 5, pp. 1–7, 2015.

[14] K. Nishiguchi, T. Shirakawa, H. Watanabe, R. Arita, and S. Yunoki, "Possible Superconductivity Induced by a Large Spin–Orbit Coupling in Carrier Doped Iridium Oxide Insulators: A Weak Coupling Approach," *Journal of the Physical Society of Japan*, vol. 88, p. 094701, sep 2019.

[15] J. Kim, D. Casa, M. H. Upton, T. Gog, Y.-J. Kim, J. F. Mitchell, M. van Veenendaal, M. Daghofer, J. van den Brink, G. Khaliullin, and B. J. Kim, "Magnetic Excitation Spectra of Sr_2IrO_4 Probed by Resonant Inelastic X-Ray Scattering: Establishing Links to Cuprate Superconductors," *Phys. Rev. Lett.*, vol. 108, p. 177003, Apr 2012.

[16] Y. K. Kim, N. H. Sung, J. D. Denlinger, and B. J. Kim, "Observation of a d-wave gap in electron-doped Sr_2IrO_4," *Nature Physics*, vol. 12, no. 1, pp. 37–41, 2016.

[17] X. Chen, T. Hogan, D. Walkup, W. Zhou, M. Pokharel, M. Yao, W. Tian, T. Z. Ward, Y. Zhao, D. Parshall, C. Opeil, J. W. Lynn, V. Madhavan, and S. D. Wilson, "Influence of electron doping on the ground state of $(Sr_{1-x}La_x)_2IrO_4$," *Phys. Rev. B*, vol. 92, p. 075125, Aug 2015.

[18] I. Battisti, K. M. Bastiaans, V. Fedoseev, A. de la Torre, N. Iliopoulos, A. Tamai, E. C. Hunter, R. S. Perry, J. Zaanen, F. Baumberger, and M. P. Allan, "Universality of pseudogap and emergent order in lightly doped Mott insulators," *Nature Physics*, vol. 13, pp. 21–25, jan 2017.

[19] X. Chen, J. L. Schmehr, Z. Islam, Z. Porter, E. Zoghlin, K. Finkelstein, J. P. Ruff, and S. D. Wilson, "Unidirectional spin density wave state in metallic $(Sr_{1-x}La_x)_2IrO_4$," *Nature Communications*, vol. 9, no. 1, p. 103, 2018.

[20] A. W. Lindquist and H.-Y. Kee, "Odd-parity superconductivity driven by octahedra rotations in iridium oxides," *Physical Review B*, vol. 100, p. 054512, aug 2019.

[21] G. Jackeli and G. Khaliullin, "Mott Insulators in the Strong Spin-Orbit Coupling Limit: From Heisenberg to a Quantum Compass and Kitaev Models," *Phys. Rev. Lett.*, vol. 102, p. 017205, Jan 2009.

[22] N. B. Perkins, Y. Sizyuk, and P. Wölfle, "Interplay of many-body and single-particle interactions in iridates and rhodates," *Physical Review B*, vol. 89, p. 035143, jan 2014.

[23] P. Liu, S. Khmelevskyi, B. Kim, M. Marsman, D. Li, X.-Q. Chen, D. D. Sarma, G. Kresse, and C. Franchini, "Anisotropic magnetic couplings and structure-driven canted to collinear transitions in Sr_2IrO_4 by magnetically constrained noncollinear DFT," *Phys. Rev. B*, vol. 92, p. 054428, Aug 2015.

[24] D. H. Torchinsky, H. Chu, L. Zhao, N. B. Perkins, Y. Sizyuk, T. Qi, G. Cao, and D. Hsieh, "Structural Distortion-Induced Magnetoelastic Locking in Sr_2IrO_4 Revealed through Nonlinear Optical Harmonic Generation," *Physical Review Letters*, vol. 114, p. 096404, mar 2015.

[25] L. Engström, T. Pereg-Barnea, and W. Witczak-Krempa, "Modeling multiorbital effects in Sr_2IrO_4 under strain and a Zeeman field," *Physical Review B*, vol. 103, p. 155147, apr 2021.

[26] A. Lupascu, J. P. Clancy, H. Gretarsson, Z. Nie, J. Nichols, J. Terzic, G. Cao, S. S. A. Seo, Z. Islam, M. H. Upton, J. Kim, D. Casa, T. Gog, A. H. Said, V. M. Katukuri, H. Stoll, L. Hozoi, J. van den Brink, and Y.-J. Kim, "Tuning Magnetic Coupling in Sr_2IrO_4 Thin Films with Epitaxial Strain," *Physical Review Letters*, vol. 112, p. 147201, apr 2014.

[27] L. Hao, D. Meyers, M. Dean, and J. Liu, "Novel spin-orbit coupling driven emergent states in iridate-based heterostructures," *Journal of Physics and Chemistry of Solids*, vol. 128, pp. 39–53, may 2019.

[28] E. Paris, Y. Tseng, E. M. Pärschke, W. Zhang, M. H. Upton, A. Efimenko, K. Rolfs, D. E. McNally, L. Maurel, M. Naamneh, M. Caputo, V. N. Strocov, Z. Wang, D. Casa, C. W. Schneider, E. Pomjakushina, K. Wohlfeld, M. Radovic, and T. Schmitt, "Strain engineering of the charge and spin-orbital interactions in Sr_2IrO_4," *Proceedings of the National Academy of Sciences*, vol. 117, pp. 24764–24770, oct 2020.

[29] K. Samanta, F. M. Ardito, N. M. Souza-Neto, and E. Granado, "First-order structural transition and pressure-induced lattice/phonon anomalies in Sr_2IrO_4," *Physical Review B*, vol. 98, p. 094101, sep 2018.

[30] C. Bhandari, Z. S. Popović, and S. Satpathy, "Electronic structure and optical properties of Sr_2IrO_4 under epitaxial strain," *New Journal of Physics*, vol. 21, no. 1, 2019.

[31] A. Seo, P. P. Stavropoulos, H.-H. Kim, K. Fürsich, M. Souri, J. G. Connell, H. Gretarsson, M. Minola, H. Y. Kee, and B. Keimer, "Compressive strain induced enhancement of exchange interaction and short-range magnetic order in Sr_2IrO_4 investigated by Raman spectroscopy," *Phys. Rev. B*, vol. 100, p. 165106, Oct 2019.

[32] S. Trommler, R. Hühne, K. Iida, P. Pahlke, S. Haindl, L. Schultz, and B. Holzapfel, "Reversible shift in the superconducting transition for $La_{1.85}Sr_{0.15}CuO_4$ and $BaFe_{1.8}Co_{0.2}As_2$ using piezoelectric substrates," *New Journal of Physics*, vol. 12, pp. 0–6, 2010.

[33] R. Hühne, D. Okai, K. Dörr, S. Trommler, A. Herklotz, B. Holzapfel, and L. Schultz, "Dynamic investigations on the influence of epitaxial strain on the superconducting transition in $YBa_2Cu_3O_{7-x}$," *Superconductor Science and Technology*, vol. 21, no. 7, p. 075020, 2008.

[34] G. N. Phan, K. Nakayama, K. Sugawara, T. Sato, T. Urata, Y. Tanabe, K. Tanigaki, F. Nabeshima, Y. Imai, A. Maeda, and T. Takahashi, "Effects of strain on the electronic structure, superconductivity, and nematicity in FeSe studied by angle-resolved photoemission spectroscopy," *Physical Review B*, vol. 95, p. 224507, jun 2017.

[35] K. Ahadi, L. Galletti, Y. Li, S. Salmani-Rezaie, W. Wu, and S. Stemmer, "Enhancing superconductivity in $SrTiO_3$ films with strain," *Science Advances*, vol. 5, no. 4, pp. 1–6, 2019.

[36] J. Zhang, H. Wu, G. Zhao, L. Han, and J. Zhang, "A review on strain study of cuprate superconductors," *Nanomaterials*, vol. 12, no. 19, 2022.

[37] Y. Kawasugi, H. M. Yamamoto, M. Hosoda, N. Tajima, T. Fukunaga, K. Tsukagoshi, and R. Kato, "Strain-induced superconductor/insulator transition and field effect in a thin single crystal of molecular conductor," *Applied Physics Letters*, vol. 92, no. 24, pp. 24–26, 2008.

[38] Y.-C. Liu, W.-S. Wang, F.-C. Zhang, and Q.-H. Wang, "Superconductivity in Sr_2RuO_4 thin films under biaxial strain," *Phys. Rev. B*, vol. 97, p. 224522, Jun 2018.

[39] D. Haskel, G. Fabbris, J. H. Kim, L. S. I. Veiga, J. R. L. Mardegan, C. A. Escanhoela, S. Chikara, V. Struzhkin, T. Senthil, B. J. Kim, G. Cao, and J.-W. Kim, "Possible Quantum Paramagnetism in Compressed Sr_2IrO_4," *Physical Review Letters*, vol. 124, p. 067201, feb 2020.

[40] C. Chen, Y. Zhou, X. Chen, T. Han, C. An, Y. Zhou, Y. Yuan, B. Zhang, S. Wang, R. Zhang, L. Zhang, C. Zhang, Z. Yang, L. E. DeLong, and G. Cao, "Persistent insulating state at megabar pressures in strongly spin-orbit coupled Sr_2IrO_4," *Physical Review B*, vol. 101, p. 144102, apr 2020.

[41] X. Li, S. E. Cooper, A. Krishnadas, A. de la Torre, R. S. Perry, F. Baumberger, D. M. Silevitch, D. Hsieh, T. F. Rosenbaum, and Y. Feng, "Magnetic order, disorder, and excitations under pressure in the Mott insulator Sr_2IrO_4," *Phys. Rev. B*, vol. 104, p. L201111, Nov 2021.

[42] A. T. Rømer, D. D. Scherer, I. M. Eremin, P. J. Hirschfeld, and B. M. Andersen, "Knight Shift and Leading Superconducting Instability from Spin Fluctuations in Sr_2RuO_4," *Physical Review Letters*, vol. 123, no. 24, p. 247001, 2019.

[43] S. Käser, H. U. R. Strand, N. Wentzell, A. Georges, O. Parcollet, and P. Hansmann, "Interorbital singlet pairing in Sr_2RuO_4: A Hund's superconductor," *Phys. Rev. B*, vol. 105, p. 155101, Apr 2022.

[44] O. Gingras, N. Allaglo, R. Nourafkan, M. Côté, and A. M. S. Tremblay, "Superconductivity in correlated multiorbital systems with spin-orbit coupling: Coexistence of even- and odd-frequency pairing, and the case of Sr_2RuO_4," *Phys. Rev. B*, vol. 106, p. 064513, Aug 2022.

[45] H. Ikeda, R. Arita, and J. Kuneš, "Phase diagram and gap anisotropy in iron-pnictide superconductors," *Phys. Rev. B*, vol. 81, p. 054502, Feb 2010.

[46] F. Schrodi, A. Aperis, and P. M. Oppeneer, "Eliashberg theory for spin fluctuation mediated superconductivity: Application to bulk and monolayer FeSe," *Phys. Rev. B*, vol. 102, p. 014502, Jul 2020.

[47] E. M. Pärschke, W.-C. Chen, R. Ray, and C.-C. Chen, "Evolution of electronic and magnetic properties of Sr_2IrO_4 under strain," *npj Quantum Materials*, vol. 7, p. 90, sep 2022.

[48] M. Sigrist and K. Ueda, "Phenomenological theory of unconventional superconductivity," *Reviews of Modern Physics*, vol. 63, pp. 239–311, apr 1991.

[49] N. E. Bickers, *Self-Consistent Many-Body Theory for Condensed Matter Systems*, pp. 237–296. New York, NY: Springer New York, 2004.

[50] J. Kanamori, "Electron correlation and ferromagnetism of transition metals," *Progress of Theoretical Physics*, vol. 30, pp. 275–289, sep 1963.

[51] G. Baym and L. P. Kadanoff, "Conservation Laws and Correlation Functions," *Physical Review*, vol. 124, pp. 287–299, oct 1961.

[52] G. Baym, "Self-Consistent Approximations in Many-Body Systems," *Physical Review*, vol. 127, pp. 1391–1401, aug 1962.

[53] N. E. Bickers and D. J. Scalapino, "Conserving approximations for strongly fluctuating electron systems. I. Formalism and calculational approach," *Annals of Physics*, vol. 193, no. 1, pp. 206–251, 1989.

[54] N. E. Bickers and S. R. White, "Conserving approximations for strongly fluctuating electron systems. II. Numerical results and parquet extension," *Physical Review B*, vol. 43, no. 10, pp. 8044–8064, 1991.

[55] S. Lee, Y.-S. Seo, E. Jung, S. Roh, M. Lee, H. Y. Choi, J. H. Kim, N. Lee, Y. J. Choi, and J. Hwang, "Evolution of the electronic structure of Ru-doped single-crystal iridates $Sr_2Ir_{1-x}Ru_xO_4$," *Physical Review B*, vol. 104, p. 165106, oct 2021.

[56] B. Zwartsenberg, R. P. Day, E. Razzoli, M. Michiardi, N. Xu, M. Shi, J. D. Denlinger, G. Cao, S. Calder, K. Ueda, J. Bertinshaw, H. Takagi, B. J. Kim, I. S. Elfimov, and A. Damascelli, "Spin-orbit-controlled metal–insulator transition in Sr_2IrO_4," *Nature Physics*, vol. 16, pp. 290–294, mar 2020.

[57] V. Brouet, P. Foulquier, A. Louat, F. Bertran, P. Le Fèvre, J. E. Rault, and D. Colson, "Origin of the different electronic structure of Rh- and Ru-doped Sr_2IrO_4," *Physical Review B*, vol. 104, p. L121104, sep 2021.

[58] A. Georges, L. de' Medici, and J. Mravlje, "Strong Correlations from Hund's Coupling," *Annual Review of Condensed Matter Physics*, vol. 4, pp. 137–178, apr 2013.

[59] E. Berg, M. A. Metlitski, and S. Sachdev, "Sign-Problem–Free Quantum Monte Carlo of the Onset of Antiferromagnetism in Metals," *Science*, vol. 338, pp. 1606–1609, dec 2012.

[60] J. P. Rodriguez, "Spin resonances in iron selenide high-T_c superconductors by proximity to a hidden spin density wave," *Phys. Rev. B*, vol. 102, p. 024521, Jul 2020.

[61] J. Linder and A. V. Balatsky, "Odd-frequency superconductivity," *Reviews of Modern Physics*, vol. 91, p. 045005, dec 2019.

[62] P. Dutta, F. Parhizgar, and A. M. Black-Schaffer, "Superconductivity in spin-3/2 systems: Symmetry classification, odd-frequency pairs, and Bogoliubov Fermi surfaces," *Phys. Rev. Research*, vol. 3, p. 033255, Sep 2021.

[63] A. S. Patri and Y. B. Kim, "Unconventional Superconductivity arising from Multipolar Kondo Interactions," *SciPost Phys.*, vol. 12, p. 057, 2022.

[64] M. Gell-Mann, "The eightfold way: A theory of strong interaction symmetry," technical report, California Inst. of Tech., Pasadena. Synchrotron Lab., 3 1961.

[65] M. Sato, "Topological properties of spin-triplet superconductors and fermi surface topology in the normal state," *Phys. Rev. B*, vol. 79, p. 214526, Jun 2009.

[66] A. Farrell and T. Pereg-Barnea, "Topological superconductivity without proximity effect," *Phys. Rev. B*, vol. 87, p. 214517, Jun 2013.

[67] S. Raghu, A. Kapitulnik, and S. A. Kivelson, "Hidden Quasi-One-Dimensional Superconductivity in Sr_2RuO_4," *Phys. Rev. Lett.*, vol. 105, p. 136401, Sep 2010.

[68] Y. Imai, K. Wakabayashi, and M. Sigrist, "Properties of edge states in a spin-triplet two-band superconductor," *Phys. Rev. B*, vol. 85, p. 174532, May 2012.

[69] T. Scaffidi and S. H. Simon, "Large Chern Number and Edge Currents in Sr_2RuO_4," *Phys. Rev. Lett.*, vol. 115, p. 087003, Aug 2015.

[70] T. Scaffidi, J. C. Romers, and S. H. Simon, "Pairing symmetry and dominant band in Sr_2RuO_4," *Phys. Rev. B*, vol. 89, p. 220510(R), Jun 2014.

[71] S. Graser, T. A. Maier, P. J. Hirschfeld, and D. J. Scalapino, "Near-degeneracy of several pairing channels in multiorbital models for the Fe pnictides," *New Journal of Physics*, vol. 11, 2009.

[72] T. A. Maier, S. Graser, P. J. Hirschfeld, and D. J. Scalapino, "d-wave pairing from spin fluctuations in the $K_xFe_{2-y}Se_2$ superconductors," *Phys. Rev. B*, vol. 83, p. 100515(R), Mar 2011.

[73] V. Z. Kresin, H. Morawitz, and S. A. Wolf, "Multigap superconductivity," in *Superconducting State*, pp. 103–113, Oxford University Press, dec 2013.

[74] M. E. Zhitomirsky and T. M. Rice, "Interband Proximity Effect and Nodes of Superconducting Gap in Sr_2RuO_4," *Phys. Rev. Lett.*, vol. 87, p. 057001, Jul 2001.

[75] S. Souma, Y. Machida, T. Sato, T. Takahashi, H. Matsui, S.-C. Wang, H. Ding, A. Kaminski, J. C. Campuzano, S. Sasaki, and K. Kadowaki, "The origin of multiple superconducting gaps in MgB_2," *Nature*, vol. 423, pp. 65–67, may 2003.

[76] R. M. Fernandes, J. T. Haraldsen, P. Wölfle, and A. V. Balatsky, "Two-band superconductivity in doped $SrTiO_3$ films and interfaces," *Phys. Rev. B*, vol. 87, p. 014510, Jan 2013.

[77] C.-T. Chen, C. C. Tsuei, M. B. Ketchen, Z.-A. Ren, and Z. X. Zhao, "Integer and half-integer flux-quantum transitions in a niobium–iron pnictide loop," *Nature Physics*, vol. 6, pp. 260–264, apr 2010.

[78] E. Berg, N. H. Lindner, and T. Pereg-Barnea, "Metastable π junction between an $s_{\pm}$-wave and an s-wave superconductor," *Phys. Rev. Lett.*, vol. 106, p. 147003, Apr 2011.

[79] R. Rodríguez-Mota, E. Berg, and T. Pereg-Barnea, "Effects of order parameter self-consistency in a $s_{\pm} - s$ junction," *Phys. Rev. B*, vol. 93, p. 214507, Jun 2016.

[80] R. B. Laughlin, "Hartree-Fock computation of the high-T_c cuprate phase diagram," *Physical Review B*, vol. 89, p. 035134, jan 2014.

[81] A. Farrell and T. Pereg-Barnea, "Strong coupling expansion of the extended Hubbard model with spin-orbit coupling," *Physical Review B*, vol. 89, p. 035112, jan 2014.

[82] H. Zhang, K. Haule, and D. Vanderbilt, "Effective J=1/2 Insulating State in Ruddlesden-Popper Iridates: An LDA+DMFT Study," *Phys. Rev. Lett.*, vol. 111, p. 246402, Dec 2013.

[83] S. Agrestini, C.-Y. Kuo, M. Moretti Sala, Z. Hu, D. Kasinathan, K.-T. Ko, P. Glatzel, M. Rossi, J.-D. Cafun, K. O. Kvashnina, A. Matsumoto, T. Takayama, H. Takagi, L. H. Tjeng, and M. W. Haverkort, "Long-range interactions in the effective low-energy Hamiltonian of Sr_2IrO_4: A core-to-core resonant inelastic x-ray scattering study," *Phys. Rev. B*, vol. 95, p. 205123, May 2017.

[84] C. Lane, Y. Zhang, J. W. Furness, R. S. Markiewicz, B. Barbiellini, J. Sun, and A. Bansil, "First-principles calculation of spin and orbital contributions to magnetically ordered moments in Sr_2IrO_4," *Phys. Rev. B*, vol. 101, p. 155110, Apr 2020.

[85] M. V. Berry, "Quantal phase factors accompanying adiabatic changes," *Proceedings of the Royal Society of London. A. Mathematical and Physical Sciences*, vol. 392, pp. 45–57, mar 1984.

[86] M. Cheng, K. Sun, V. Galitski, and S. Das Sarma, "Stable topological superconductivity in a family of two-dimensional fermion models," *Phys. Rev. B*, vol. 81, p. 024504, Jan 2010.

Chapter 7

Discussion

The studies, in Chapters 5 and 6, of interacting Sr_2IrO_4 under doping and compressive strain have presented several ideas concerning spin-orbit coupled magnetism and superconductivity. The methods for tuning the multi-orbital bandstructure and for calculating effective interactions, as outlined in the introductory chapters, have been used to treat magnetic and superconducting orders. The orders have been considered separately as well as in competition with one another. The key ideas that can be taken away from the two manuscripts, about the iridate system in particular, are:

- Compressive epitaxial strain can suppress the insulating magnetic order and induce an insulator/superconductivity phase transition.
- Strain changes the topology of the Fermi surface, even when interactions are present.
- A lower SOC and a higher Hund's coupling result in a competition between a rich variety of magnetic and superconducting orders. In this regime neither solely spin nor pseudospin degrees of freedom describe the system well.
- The shift between spin-orbit dominated physics or not, is mainly determined by the interactions rather than the strength of the spin-orbit coupling in the non-interacting bands.

The arguments in support of the thesis statement that can be distilled from these conclusions are made as the following:

Both manuscripts start from a high spin-orbit coupling and observe that the bands from which the magnetic order parameters originate remain robust under strain and doping. In terms of total angular momentum states, the description of the two possible bands at the Fermi surface remains largely unchanged compared to the undoped and unstrained bandstructure. However, in a multi-orbital model with a unique dispersion for each orbital there are effectively no longer just two types of interactions U, J_{H}. Instead, each of the SOC, Hund's, and hopping terms couples different spin and orbital degrees of freedom, and the number of interaction terms becomes large. From the RPA treatment we can directly identify the importance of each orbital's contribution to the correlated state, from which channel the susceptibility peaks occur in. We observe that by modifying the hopping parameters differently in each orbital their susceptibility peaks also change. The SOC couples orbitals in a number of susceptibility channels. The Hund's coupling introduces interaction terms that couple the same orbitals in different channels. When Hund's coupling becomes large, susceptibility peaks in new dominating channels therefore become important. Thus, a multi-orbital interacting model, from the direction of high SOC, can be tuned between a rich variety of competing phases by modifying the non-interacting model for each orbital via strain. This is of particular relevance in potentially superconducting iridates, as even with their large spin-orbit coupling a simplified model is possible only in parts of the phase diagram.

The wider significance of these results can be separated into two aspects. Let us first discuss these results in relation to unconventional superconductivity in similar compounds. Then we will move on to consider future prospects for the iridates. Included there are identified open questions for which further research can benefit from the conclusion of this thesis.

7.1 Connection to similar materials

Based on the orders found in this thesis, perovskite iridates could be considered as a family of compounds in-between cuprates and iron pnictides. In some regimes they even display

ruthenate-like orders. This unique behavior originates from the fact that the iridate physics close to the Fermi surface is both multi-orbital and that bands well-described by states in a different basis.

The similarities and relevance of the results to cuprate physics, is based on the effective $j = 1/2$ model. As noted both in Chapters 5 and 6 the bands at the Fermi surface and the largest pseudospin susceptibility peaks are well-described in the j-state basis, even at large compressive strain for both hole and electron doping. The d-wave superconductivity found in Chapter 6 originates mainly from the $j = 1/2$ states if the Hund's coupling is low, even at high compressive strain. Seemingly, as cuprate-like physics is dominating the system it would be sufficient to use a one-orbital model. However, for a compressive strain the filling of states in the $j = 1/2$ band must match that found in the full bandstructure, as detailed in Appendix B. To further understand the most likely region of superconductivity in the iridates one could study in detail an effective $j = 1/2$ model with compression, taking into account the additional effects identified in this thesis.

One additional aspect of hole doped cuprates, not considered in this work, is the role of hybridization with the oxygen p-orbitals. In cuprates, hole doping leads to Zhang-Rice singlets which are states with a large oxygen contribution. Electrons introduced into Sr_2IrO_4 via doped have a much smaller hybridization with the adjacent oxygen orbitals. The consequences of this to potential superconductivity is yet to be included in any iridate model.

The regimes with multi-pocket Fermi surfaces and potential multi-band superconducting orders places the iridates closer to iron pnictide-physics. In FeSe the iron orbitals have a $3d$ character and the SOC is significantly lower than for Ir with $\lambda_{\text{FeSe}} \approx 0.2\text{eV}$ [1]. In Chapter 6 we find an iron pnictide-like $s_{\pm}$-wave, even close to a $\boldsymbol{Q} = (\pi, \pi)$ AFM instability. As mentioned in the manuscript this is similar to the SDW fluctuations close to the same type of superconductivity in iron based superconductors [2]. However, in the iridates the SOC plays the additional role of favoring the AFM, even though there is a clear orbital texture of the Fermi surface that determines which superconducting order is favored. Similar effects could be present in systems with a lower SOC and it would be of interest to understand the role that it plays for the pairing mechanism in these known superconducting systems.

Similar studies of superconductivity with competing Hubbard, Hund's, and SOC, have previously been approached from the limit of a small SOC. For works in ruthenates this small modification to the Hamiltonian, has the effect of favoring some additional components with pairing symmetries previously not favored [3]. The ruthenates are commonly modeled with a three-orbital t_{2g} model in a square lattice. However, compared to the model used in this thesis, the ruthenates have a lower filling of 4 electrons/site in Ru, a lower SOC, and the opposite sign of tetragonal splitting. In Chapter 6 we find that the found pseudospin pairing, when decomposed into spin components, has contributions to the order parameters with the same symmetry as the additional components found in ruthenates with SOC. For example, these components can be additional $s_z = 0$ spin-triplet components.

Some studies propose Sr_2RuO_4 to have a topologically non-trivial chiral p-wave order. The helical time-reversal preserving p-wave order found in Chapter 6 is similar to those found in some calculations for Sr_2RuO_4. There, an underlying pairing in the yz- and xz-orbitals also cancels out the Berry curvature contributions from different bands at the Fermi surface [4, 5]. However, like in ruthenates, higher Chern numbers could be possible for odd pairing functions with poles placed at different positions in the Brillouin zone [6]. The similarities of the ruthenates and iridates in the regime where the p-wave is found, in Chapter 6, indicate that there is an increased sensitivity to the approximations and self-energies included when calculating a potential odd parity order. Just like some calculations first found the proposed ruthenate p-wave to be topologically trivial while later calculations have found it to be non-trivial, a different calculation of superconductivity in the iridates could potentially find a non-trivial order. Even though the odd parity order in Chapter 6 is found for such a high Hund's coupling that it is non-realistic for the iridates, a deeper understanding of why and when it is favored could bring insight into the potential role of spin-orbit coupling in both the iridates and the ruthenates.

7.2 General prospects for iridates

The results from considering magnetism and superconductivity under doping and compressive strain show these parameters to be promising for inducing new orders. As

magnetism in iridates is so sensitive to lattice configuration, the strain is an effective and experimentally available knob for tuning the system. As the coupling of magnetic order to the lattice is dependent on the SOC strength, the spin-orbit coupling becomes another effective tuning parameter for the system. Ru or Rh doping could achieve this [7, 8], even though additional effects are also expected for such chemical substitution.

There are additional ways that the iridates could be used to engineer novel physics, based on the interacting regimes found in this thesis. The j-states in the three orbital models have both spin 1/2 and 3/2 states. When it comes to interacting states, the pairing found in Chapter 6 can mix the two subsectors. The pairing in the orbital basis has only spin-1/2 states and can thus be described in spin-singlet ($s_1 + s_2 = 0$) and spin-triplet components ($s_1 + s_2 = 1$). For the total angular momentum there are pairing states of higher total angular momentum $J = 0, 1, 2, 3$, as $j_i = 1/2, 3/2$ for the two particles $i = 1, 2$. For example, the found $s_{\pm}$-wave can be described with a large spin-quintet component, as shown in Appendix C. As noted in Ref. [9] the $\mathcal{SPOT}$-analysis of the symmetry can no longer be used and higher angular momentum pairing can have unexpected properties [10, 11]. Sr_2IrO_4 has the potential to form novel pairing symmetries due to the large region of both $j = 1/2$ and $j = 3/2$ bands at the Fermi surface. However, the properties of such states have not been explored.

In general, our understanding of the many parameters that determine the order in Sr_2IrO_4 remains limited. Having for example a superconducting pairing in a system which couples so many degrees of freedom: SOC, Hund's, between sites or additional inter-orbital coupling from the hopping, is expected to have consequences both to the likelihood of experimentally achieving the state as well as to the experimental signatures. In this thesis the robustness of the states or how they couple to other systems has not been treated. Those aspects of iridate physics are largely unexplored. Specifically for doped and strained Sr_2IrO_4 there are several open questions in which future theoretical research could give new insight into the underlying physics. Related to this thesis are the following:

- To expand the analysis of the possible strain-induced superconductivity a calculation including the frequency dependence could be a first step in determining the robustness of the region. The static approximation used in Chapter 6 does in general overestimate

the orders. An inclusion of sufficient number of frequencies is however a significantly heavier computational problem and could potentially have to be performed at higher temperatures.

- To better understand the competition between magnetism and the d-wave order close to where the one-orbital model is valid, methods such as renormalization group calculations or Eliashberg theory, to include phonon effects, could be utilized. As many parameters are included in the model it is crucial that the interplay between orders are taken into account properly. We also expect that the effect from phonons is affected by the change in lattice geometry.

- Expected effects that are present with doping, and that could increase with compressive strain, are impurities and lattice distortions. As the magnetism is sensitive to the lattice geometry it is important to understand how each degree of freedom couples to impurities. Differences between how a spin- or pseudospin-singlet order couples to different types of impurities could offer great insight into why the existence of predicted superconducting order has eluded confirmation.

- Only compressive strain is considered in this thesis. However, tensile strain has been shown to decrease the amount of lattice distortions, by decreasing the staggered rotations of the oxygen octahedra [12]. Tensile strain also decreases the Néel temperature even further than the equivalent amount of compressive strain does [13]. A model for tensile strain and doping could therefore be another promising direction for favoring superconductivity. If tensile strain decreases the bandwidth of the system the critical temperature of a potential superconducting order could increase.

- Interlayer effects and additional effects from tetragonal distortion under compression play a role for the magnetic order. Even though the interlayer coupling is much smaller than the intralayer effects, they may play an increased role for undoped Sr_2IrO_4 under hydrostatic pressure. A better understanding of the contributing factors to the insulating order found under high pressure would help identify other regions where such an order could compete with superconductivity.

As for insight that can be gained from future experimental studies, any study combining epitaxial strain and charge doping is crucial for the understanding of how these knobs tune the system in practice. Of further interest to the theoretical studies of multi-orbital physics are attempts to determine the contributions from each orbital to the correlated states and the correlation between them [35].

Bibliography

[1] R. P. Day, G. Levy, M. Michiardi, B. Zwartsenberg, M. Zonno, F. Ji, E. Razzoli, F. Boschini, S. Chi, R. Liang, P. K. Das, I. Vobornik, J. Fujii, W. N. Hardy, D. A. Bonn, I. S. Elfimov, and A. Damascelli, "Influence of spin-orbit coupling in iron-based superconductors," *Phys. Rev. Lett.*, vol. 121, p. 076401, Aug 2018.

[2] R. M. Fernandes and A. V. Chubukov, "Low-energy microscopic models for iron-based superconductors: A review," *Reports on Progress in Physics*, vol. 80, no. 1, 2017.

[3] J. Clepkens, A. W. Lindquist, and H.-Y. Kee, "Shadowed triplet pairings in Hund's metals with spin-orbit coupling," *Phys. Rev. Res.*, vol. 3, p. 013001, Jan 2021.

[4] S. Raghu, A. Kapitulnik, and S. A. Kivelson, "Hidden Quasi-One-Dimensional Superconductivity in Sr_2RuO_4," *Phys. Rev. Lett.*, vol. 105, p. 136401, Sep 2010.

[5] Y. Imai, K. Wakabayashi, and M. Sigrist, "Properties of edge states in a spin-triplet two-band superconductor," *Phys. Rev. B*, vol. 85, p. 174532, May 2012.

[6] T. Scaffidi and S. H. Simon, "Large Chern Number and Edge Currents in Sr_2RuO_4," *Phys. Rev. Lett.*, vol. 115, p. 087003, Aug 2015.

[7] B. Zwartsenberg, R. P. Day, E. Razzoli, M. Michiardi, N. Xu, M. Shi, J. D. Denlinger, G. Cao, S. Calder, K. Ueda, J. Bertinshaw, H. Takagi, B. J. Kim, I. S. Elfimov, and A. Damascelli, "Spin-orbit-controlled metal–insulator transition in Sr_2IrO_4," *Nature Physics*, vol. 16, pp. 290–294, mar 2020.

[8] V. Brouet, P. Foulquier, A. Louat, F. Bertran, P. Le Fèvre, J. E. Rault, and D. Colson, "Origin of the different electronic structure of Rh- and Ru-doped Sr_2IrO_4," *Physical Review B*, vol. 104, p. L121104, sep 2021.

[9] P. Dutta, F. Parhizgar, and A. M. Black-Schaffer, "Superconductivity in spin-3/2 systems: Symmetry classification, odd-frequency pairs, and Bogoliubov Fermi surfaces," *Phys. Rev. Research*, vol. 3, p. 033255, Sep 2021.

[10] T. V. Bay, T. Naka, Y. K. Huang, and A. de Visser, "Superconductivity in noncentrosymmetric YPtBi under pressure," *Phys. Rev. B*, vol. 86, p. 064515, Aug 2012.

[11] H. Kim, K. Wang, Y. Nakajima, R. Hu, S. Ziemak, P. Syers, L. Wang, H. Hodovanets, J. D. Denlinger, P. M. R. Brydon, D. F. Agterberg, M. A. Tanatar, R. Prozorov, and J. Paglione, "Beyond triplet: Unconventional superconductivity in a spin-3/2 topological semimetal," *Science Advances*, vol. 4, no. 4, p. eaao4513, 2018.

[12] G. Cao, H. Zhao, B. Hu, N. Pellatz, D. Reznik, P. Schlottmann, and I. Kimchi, "Quest for quantum states via field-altering technology," *npj Quantum Materials*, vol. 5, p. 83, dec 2020.

[13] A. Seo, P. P. Stavropoulos, H. H. Kim, K. Fürsich, M. Souri, J. G. Connell, H. Gretarsson, M. Minola, H. Y. Kee, and B. Keimer, "Compressive strain induced enhancement of exchange interaction and short-range magnetic order in Sr_2IrO_4 investigated by Raman spectroscopy," *Physical Review B*, vol. 100, no. 16, pp. 1–7, 2019.

Chapter 8

Conclusion

This thesis has treated the subject of possible magnetic and superconducting orders in doped and strained Sr_2IrO_4 as an example of a multi-orbital system with strong spin-orbit coupling and interactions. The objective has been to describe the states that contribute to the magnetic order and to determine if a magnetic insulator/superconductor transition is possible. To fully capture the breadth of iridate physics the most realistic parameter ranges were considered as well as an extension to a broader range of values that could potentially be achieved.

The motivation for this approach is the observation that the magnetism is exceptionally sensitive to compressive strain in Sr_2IrO_4. Consequently, if superconductivity is mediated by magnetic fluctuations strain is a powerful tool for tuning the system. As superconductivity has been predicted in doped Sr_2IrO_4 and has not been confirmed in experiment, a compressive strain could be used as a tuning parameter to explore if the superconducting regions can be realized. If a model with multiple orbitals is used the multiple types of interaction can be taken into account and underlying fluctuations mediating the superconducting order can be explored. The objectives of this thesis were met by considering them in steps in Chapters 5 and 6:

The first step was to understand which degrees of freedom that are necessary to describe the bandstructure and possible orders of Sr_2IrO_4 under compressive strain, as well as a potential phase transition. In Chapter 5 magnetic orders were modeled via the mean field approximation for undoped Sr_2IrO_4 as a compressive strain was increased. Realistic values

for the interaction parameters and initial gap were chosen. A stain-induced transition is found for values beyond the epitaxial strain that has been achieved experimentally. This mean field model displays the same sensitivity of the canted antiferromagnet to compression as has been observed in experiment. The order remains of mainly $j = 1/2$ nature. By modeling an external magnetic field as a Zeeman coupling term the effect on the order in each orbital could be distinguished on both sides of the phase transition.

The second step was to expand the study to both doping and compressive epitaxial strain. The objective was to see if a stain-induced superconducting order is possible for realistic values, such that experiments can be more likely to observe the predicted $j = 1/2$ d-wave order under a combination of doping and compressive strain. In Chapter 6 superconductivity was modeled with an effective pairing interaction calculated via the random phase approximation, the effects of the magnetic order taken into account from Chapter 5. Strain-induced superconducting regions with a d-wave symmetry were found at a sufficiently low temperature and for a broad range of doping values. In the calculated phase diagram, the magnetic order was found via the Stoner criterion.

The final step was to explore a wider region of parameters to determine the symmetry of the order in any possible superconducting region. In Chapter 6 this objective was met by considering a range of higher Hund's coupling and lower SOC in additional phase diagrams. Orders that had previously been found for higher J_{H} were also found in this work. These are the multi-band $s_{\pm}$-wave, found in a large regime of doing and strain, and an odd parity p-wave, that here was found to be topologically trivial. Two anisotropic superconducting orders were for the first time predicted at high compressive strain and doping. To determine which fluctuations can mediate the orders the susceptibility peaks were tracked for changing doping and strain. For a Hund's coupling and SOC of comparable size several of the numerous susceptibility channels have large peaks. These peaks can be located at different momentum transfer $\boldsymbol{Q}$.

The findings of the thesis can be summarized as follows: a multi-orbital interacting model, with large SOC, can be tuned between a rich variety of competing phases by modifying the hopping amplitudes of each orbital via compressive strain. This is of particular relevance in potentially superconducting iridates, as their large spin-orbit coupling makes a simplified

model possible only in some parts of the phase diagram.

Many unanswered questions remain about the iridates and about the possibility of superconductivity in doped Sr_2IrO_4. As the result in this thesis predict that superconductivity can be present after a strain-induced transition, it seems to be a promising direction to combine compressive epitaxial strain with charge doping. Some potential research questions for future studies have been outlined in Chapter 7. There are also many unanswered questions about multi-orbital interactions and spin-orbit coupling. Many of the orders found in this iridate model appear in several other families of unconventional superconductors. The exact interplay between the different parameters and their contribution to a pairing mechanism is a complex problem. As this thesis has shown, the combination of multi-orbital interactions and spin-orbit coupling is a recipe for novel magnetic and superconducting orders.

Appendix A

The Gell-Mann Matrices

The Gell-Mann matrices [1] are given as 3×3 matrices in orbital space (d_{yz}, d_{xz}, d_{xy}) as

$$\lambda_1 = \begin{pmatrix} 0 & 1 & 0 \\ 1 & 0 & 0 \\ 0 & 0 & 0 \end{pmatrix}, \qquad \lambda_2 = \begin{pmatrix} 0 & -i & 0 \\ i & 0 & 0 \\ 0 & 0 & 0 \end{pmatrix}, \qquad \lambda_3 = \begin{pmatrix} 1 & 0 & 0 \\ 0 & -1 & 0 \\ 0 & 0 & 0 \end{pmatrix} \tag{A.1}$$

$$\lambda_4 = \begin{pmatrix} 0 & 0 & 1 \\ 0 & 0 & 0 \\ 1 & 0 & 0 \end{pmatrix}, \qquad \lambda_5 = \begin{pmatrix} 0 & 0 & -i \\ 0 & 0 & 0 \\ i & 0 & 0 \end{pmatrix}, \qquad \lambda_0 = \begin{pmatrix} 1 & 0 & 0 \\ 0 & 1 & 0 \\ 0 & 0 & 1 \end{pmatrix} \tag{A.2}$$

$$\lambda_6 = \begin{pmatrix} 0 & 0 & 0 \\ 0 & 0 & 1 \\ 0 & 1 & 0 \end{pmatrix}, \qquad \lambda_7 = \begin{pmatrix} 0 & 0 & 0 \\ 0 & 0 & -i \\ 0 & i & 0 \end{pmatrix}, \qquad \lambda_8 = \frac{1}{\sqrt{3}} \begin{pmatrix} 1 & 0 & 0 \\ 0 & 1 & 0 \\ 0 & 0 & -2 \end{pmatrix} \tag{A.3}$$

There are intraorbital matrices symmetric under exchange of orbitals $(\lambda_0, \lambda_3, \lambda_8)$ and interorbital both symmetric $(\lambda_1, \lambda_4, \lambda_6)$ and anti-symmetric $(\lambda_2, \lambda_5, \lambda_7)$ matrices.

Bibliography

[1] M. Gell-Mann, "The eightfold way: A theory of strong interaction symmetry," technical report, California Inst. of Tech., Pasadena. Synchrotron Lab., 3 1961.

Appendix B

Renormalized spin-orbit coupling

In the mean field calculations in Chapter 5 and 6, there are order parameters that renormalize the spin-orbit coupling. The resulting shift of the spin-orbit coupling is $\Delta\lambda$ and the effective $\tilde{\lambda} = \lambda + \Delta\lambda$. The value depends directly on the order parameters $\Delta\lambda = 2\mathrm{Im}\left[(J_\mathrm{H} - U')m_{(xz,\uparrow),(yz,\uparrow)} + J_\mathrm{H}\left(m_{(yz,\downarrow),(xz,\downarrow)} + m_{(xz,\downarrow),(yz,\downarrow)}\right)\right]$. If the symmetry is not spontaneously broken between orbitals: $\Delta\lambda = \mathrm{Im}\left[(U - 3J_\mathrm{H})\Lambda_A^z\right]$. The definition of Λ_A^z is given in Eq. (4.18). In Fig. B.1 the shift of the spin-orbit coupling is shown for $U = 1.4$eV, for a varying doping and compressive strain. Worth noting here is that $m_{(yz,\uparrow),(xz,\uparrow)}$ remains fairly constant with interaction strength U, meaning that $\Delta\lambda$ is directly proportional to the interactions as $\Delta\lambda \propto U(1 - 3J_\mathrm{H}/U)$. So, at the $U = 1.1$eV, $n = 5$, and $J_\mathrm{H}/U = 0.1$ the largest shift is expected to be $\Delta\lambda \approx 0.27$eV. An general trend is that $\Delta\lambda$ is increases close to a magnetic order, see the corresponding phase diagrams in section 6.A, and is larger for hole doping than for electron doping.

At an electron filling n, the states present at the Fermi surface is highly dependent on the strength of the spin-orbit coupling. As the $(3/2, \pm 1/2)$ states are located lower in energy than the others, they are always completely filled. For the other two states $(1/2, \pm 1/2)$ and $(3/2, \pm 3/2)$, the relative filling of each state depends on the positions and bandwidths of the bands. For example, when the size of a $(3/2, \pm 3/2)$ hole pocket increases the size of the $(3/2, \pm 3/2)$ electron pocket must increase. In therms of filling of each state, the filling $n_{3/2,3/2}$ decreases while the filling $n_{1/2}$ for this example. The filling of each state is defined with the order parameters in Eq. (5.16). At a fixed total electron filling n the

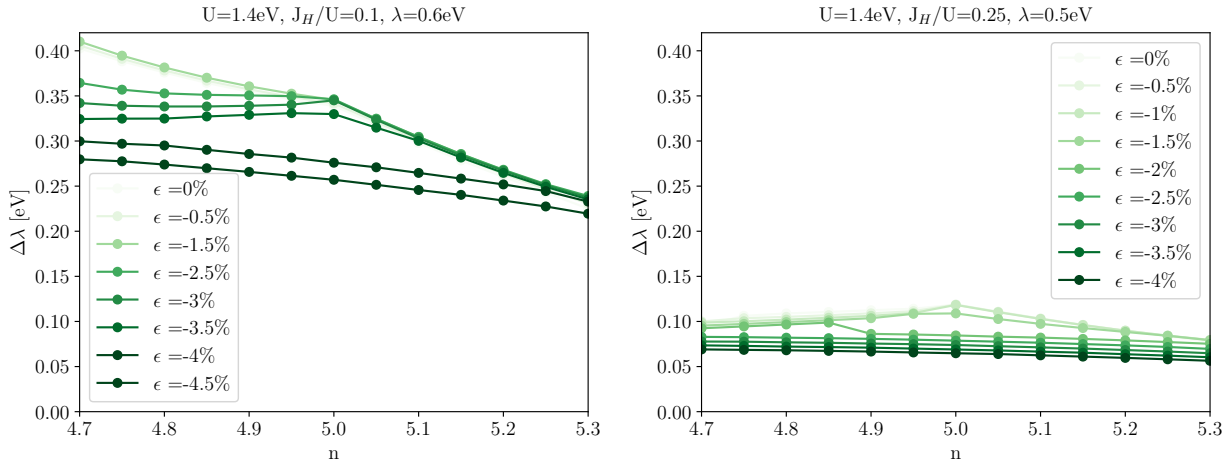

Figure B.1: The shift in spin-orbit coupling $\Delta\lambda$, as given by the mean field calculations in Chapters 5 and 6. The size of the shift is $\Delta\lambda \propto U(1 - 3J_{\mathrm{H}}/U)$ and the difference between the values at $J_{\mathrm{H}} = 0.1U$ and $J_{\mathrm{H}} = 0.25U$ is significant.

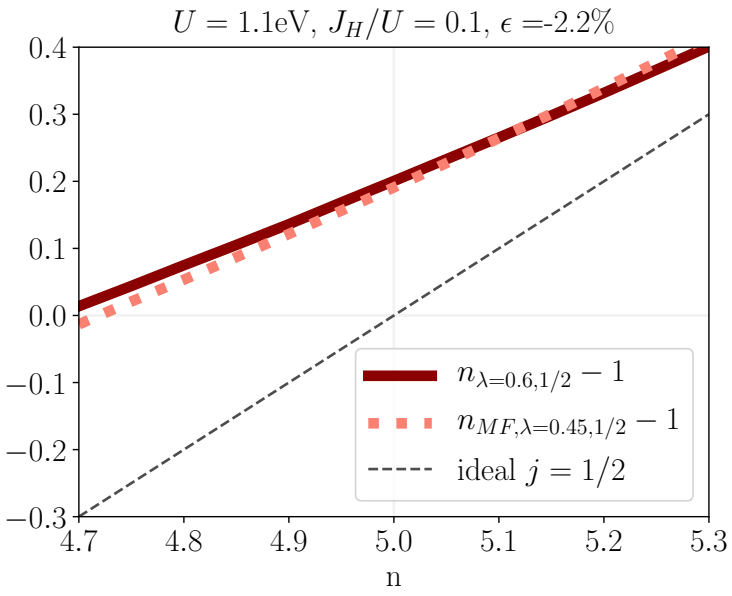

Figure B.2: The filling of the $j = 1/2$ states are shown at $\epsilon = -2.2\%$ for the two calculations in Fig.s 6.3 and 6.14. One calculation is for a non-interacting bandstructure while the other is a mean field calculation where the SOC has been renormalized. The effective doping is compared to a limit of a large SOC, where effectively only a $j = 1/2$ band is doped when the total filling n changes.

relative size of the hole pockets can increase by increasing the compressive strain. A general trend throughout the phase diagram is thus that for a fixed n the filling of the $j = 1/2$ states, $n_{1/2}$, increases with compressive strain. At a large SOC $\lambda \to \infty$ a change in the total filling n only changes the filling $n_{1/2}$, where the band is half-filled, $n_{1/2} = 1$, in the undoped compound $n = 5$. In Fig. B.2 the filling of the $j = 1/2$ states are shown for the compressing strain $\epsilon = -2.2\%$, a point where both the RPA and mean field calculation find a superconducting order, in Fig. 6.3. At this strain the $j = 1/2$ bands are effectively electron doped for all n considered. In addition to changing the shape of the pockets at the Fermi surface, compressive strain proves itself to be a tool for changing the relative filling of the different total angular momentum states.

Appendix C

J-state pairing symmetries

Two electrons, each with total angular momentum j_i and the projection j_i^z, can be paired together in a Cooper pair with a combined J, M. The possible values are $|j_1 - j_2| \leq J \leq (j_1 - j_2)$ and $M = j_1^z + j_2^z$. From standard angular momentum addition we have

$$\begin{aligned} \frac{1}{2} \otimes \frac{1}{2} &\rightarrow 0 \oplus 1 \\ \frac{1}{2} \otimes \frac{3}{2} &\rightarrow 1 \oplus 2 \\ \frac{3}{2} \otimes \frac{3}{2} &\rightarrow 0 \oplus 1 \quad \oplus 2 \oplus 3 \end{aligned} \tag{C.1}$$

The new total angular momentum state for the pair can be written in the old ones in terms of Clebsch-Gordon coefficients $\mathcal{C}^{J,M}_{j_1 j_2, j_1^z j_2^z}$:

$$|J, M\rangle = \sum_{j_1^z = -j_1}^{j_1} \sum_{j_2^z = -j_2}^{j_2} \langle j_1 j_2, j_1^z j_2^z | J, M \rangle | j_1 j_2, j_1^z j_2^z \rangle = \sum_{j_1^z, j_2^z} \mathcal{C}^{J,M}_{j_1 j_2, j_1^z j_2^z} | j_1 j_2, j_1^z j_2^z \rangle \tag{C.2}$$

In Fig.s C.1 and C.2 the found d- and $s_\pm$-wave parings analyzed in Chapter 6 is decomposed into total angular momentum J, M and the comparable size of the largest components are shown. The basis that the states are shown in are the representations of the O_h-group, as in [1].

$$J = 0 \rightarrow A_1, \qquad J = 1 \rightarrow T_1, \qquad J = 2 \rightarrow E \oplus T_2, \qquad J = 3 \rightarrow A_2 \oplus T_1 \oplus T_2 \tag{C.3}$$

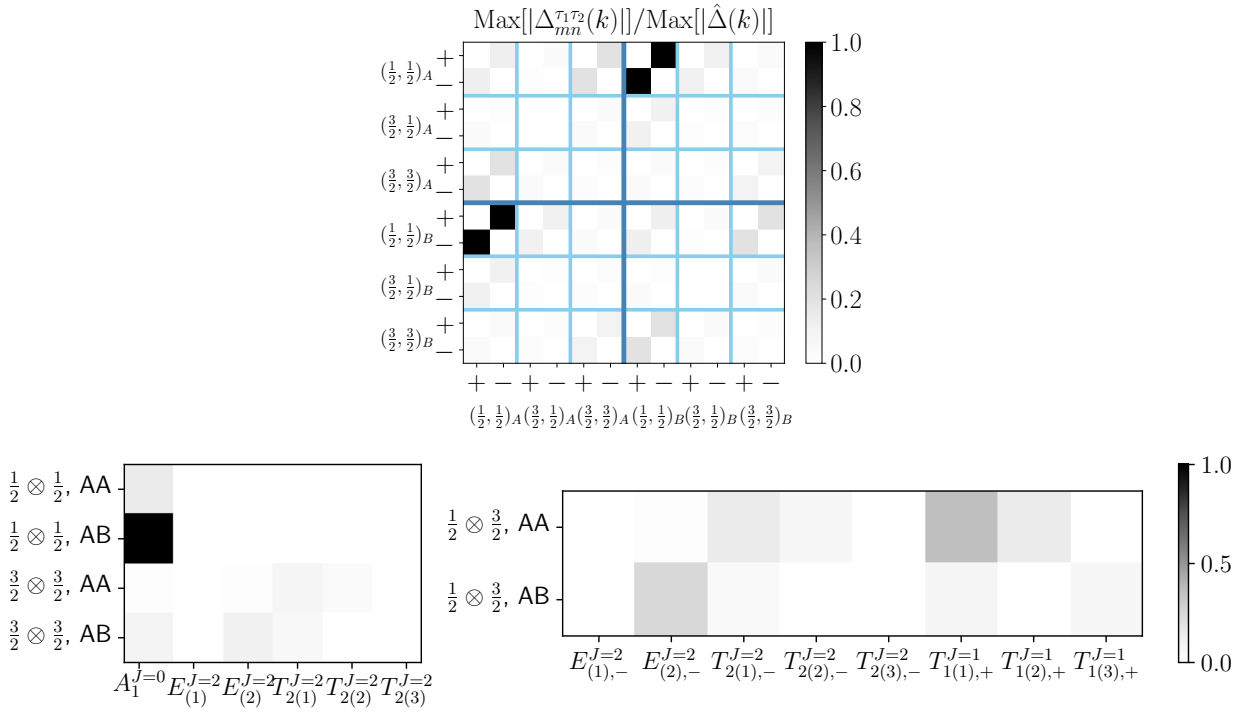

Figure C.1: The top panel shows the size of the components of the $d_{\pm}$-wave pairing in terms of the the total angular momentum of each electron, as in Fig. 6.18. In the lower panel the relative size of the pairing components are shown for the largest total angular momentum of the pair J, M in the basis given in Eq. (C.3).

where for example the $J = 2$ cases are the same as the e_g and t_{2g} orbital in Chapter 3:

$$\begin{aligned}
|E_{(1)}\rangle &= \frac{1}{\sqrt{2}}\left(|2,2\rangle + |2,-2\rangle\right) \\
|E_{(2)}\rangle &= |2,0\rangle \\
|T_{2^{(1)}}\rangle &= \frac{i}{\sqrt{2}}\left(|2,1\rangle + |2,-1\rangle\right) \\
|T_{2^{(2)}}\rangle &= \frac{1}{\sqrt{2}}\left(|2,1\rangle - |2,-1\rangle\right) \\
|T_{2^{(3)}}\rangle &= \frac{i}{\sqrt{2}}\left(|2,2\rangle - |2,-2\rangle\right)
\end{aligned} \tag{C.4}$$

This is just another basis for the spin-quintet states $J = 2, M = -2, -1, 0, 1, 2$ [2].

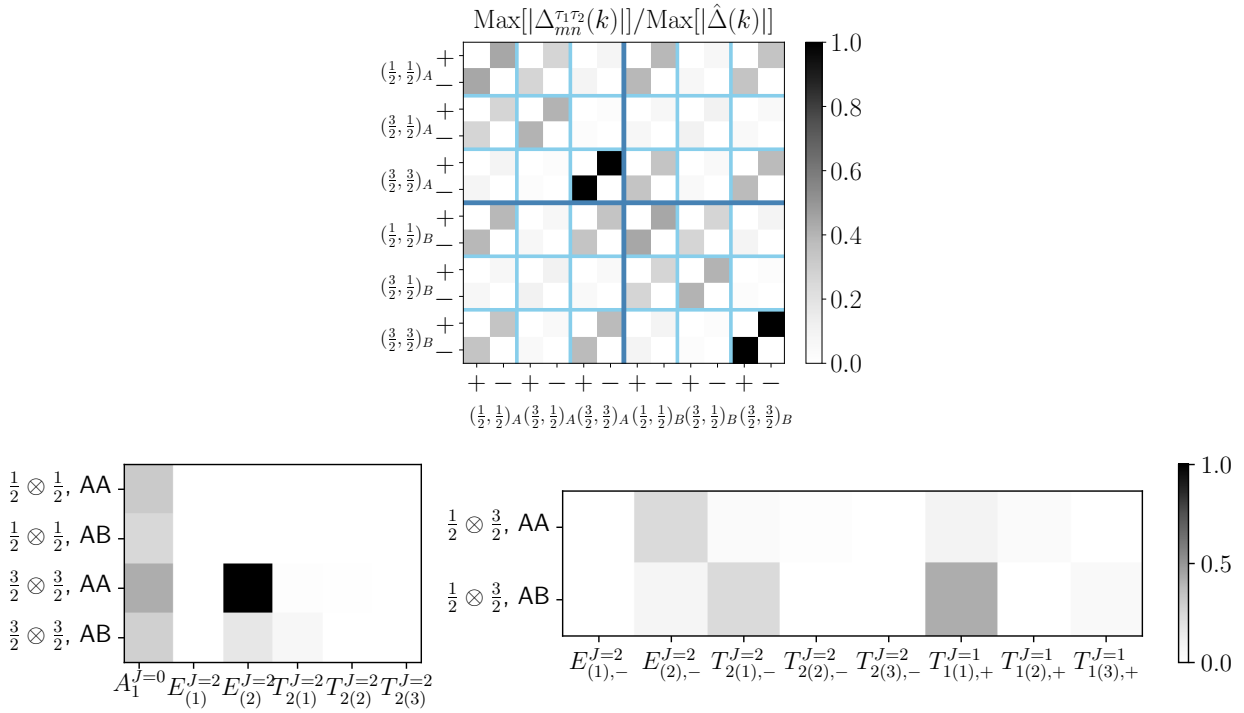

Figure C.2: The top panel shows the size of the components of the $s_{\pm}$-wave pairing in terms of the the total angular momentum of each electron, as in Fig. 6.19. Here the largest total angular momentum of the pair J, M, as in Eq. (C.3), has a largest component from the $E^J_{(2)}$-state originating from the $\frac{3}{2}\otimes\frac{3}{2}$-states. However, as we see from the top panel this state can be though of as a "singlet" within the $(3/2, \pm 3/2)$-states.

Bibliography

[1] A. S. Patri and Y. B. Kim, "Unconventional Superconductivity arising from Multipolar Kondo Interactions," *SciPost Phys.*, vol. 12, p. 057, 2022.

[2] P. Dutta, F. Parhizgar, and A. M. Black-Schaffer, "Superconductivity in spin-3/2 systems: Symmetry classification, odd-frequency pairs, and Bogoliubov Fermi surfaces," *Phys. Rev. Research*, vol. 3, p. 033255, Sep 2021.